



SAKARYA ÜNİVERSİTESİ

# FEN BİLİMLERİ ENSTİTÜSÜ DERGİSİ

Sakarya University Journal of Science (SAUJS)



SAKARYA  
ÜNİVERSİTESİ

e-issn: 2147-835X

SAÜ Fen Bil Der/SAUJS

Cilt/Volume: 25

Sayı/Issue: 5

Ekim/October 2021

---

---

**Sakarya Üniversitesi Fen Bilimleri Enstitüsü Dergisi**  
**(Sakarya University Journal of Science)**  
**Cilt/Volume: 25 No/ Issue:5 Ekim/October 2021**  
**Editör Kurulu/Editorial Boards**

---

---

### **Editor-in-Chief**

---

---

Davut Avci, Pyhsics, Sakarya University (Turkey)

### **Editors**

---

---

Alparslan Serhat Demir, Industrial Engineering, Sakarya University (Turkey)  
Asude Ateş, Environmental Engineering, Sakarya University (Turkey)  
Aysun Eğrisöğüt Tiryaki, Mechanical Engineering, Sakarya University (Turkey)  
Ertan Bol, Civil Engineering, Sakarya University (Turkey)  
Hüseyin Aksoy, Biology, Sakarya University (Turkey)  
M. Hilmi Nişancı, Electrical and Electronics Engineering, Sakarya University (Turkey)  
Mehmet Uysal, Metallurgical and Materials Engineering, Sakarya University (Turkey)  
Mehmet Nebioğlu, Chemistry, Sakarya University (Turkey)  
Muhammed Fatih Adak, Computer Engineering, Sakarya University (Turkey)  
Mustafa Gülfen, Chemistry, Sakarya University (Turkey)  
Murat Güzeltepe, Mathematics, Sakarya University (Turkey)  
Ömer Tamer, Physics, Sakarya University (Turkey)

### **Editorial Board**

---

---

Aliye Suna Erses Yay, Environmental Engineering, Sakarya University (Turkey)  
Aslı Uçar, Faculty of Health Sciences, Nutrition and dietetics, Ankara University (Turkey)  
Aykut Astam, Physics, Erzincan Binali Yıldırım University (Turkey)  
Burak Erkayman, Industrial Engineering, Atatürk University (Turkey)  
Cansu Akbulut, Biology, Sakarya University (Turkey)  
Caner Erden, International Trade and Finance, Sakarya University of Applied Sciences (Turkey)  
Can Serkan Keskin, Chemistry, Sakarya University (Turkey)  
Elif Büyük Öğüt, Mechanical and Metal Technologies, Kocaeli University (Turkey)  
Emrah Bulut, Chemistry, Sakarya University (Turkey)  
Emre Dil, Energy Systems Engineering, Beykent University (Turkey)  
Emre Tabar, Physics, Sakarya University (Turkey)  
Fahrettin Horasan, Computer Engineering, Kırıkkale University (Turkey)  
Faruk Fırat Çalım, Civil Engineering, Alparslan Türkeş University (Turkey)  
Gülnur Arabacı, Chemistry, Sakarya University (Turkey)

İrfan Yazıcı, Electrical and Electronics Engineering, Sakarya University (Turkey)  
İsmail Hakkı Demir, Architecture, Sakarya University (Turkey)  
Latif Kelebekli, Chemistry, Ordu University (Turkey)  
Mahmud Tokur, Metallurgical and Materials Engineering, Sakarya University (Turkey)  
Mevlüt Sami Aköz, Civil Engineering, Çukurova University (Turkey)  
Miraç Alaf, Metallurgical and Materials Engineering, Bilecik Şeyh Edebali University (Turkey)  
Muhammed Maruf Öztürk, Computer Engineering, Süleyman Demirel University (Turkey)  
Murat Sarduvan, Mathematics, Sakarya University (Turkey)  
Murat Tuna, Chemistry, Sakarya University (Turkey)  
Murat Utkucu, Geophysical Engineering , Sakarya University (Turkey)  
Mustafa Akpınar, Software Engineering, Sakarya University (Turkey)  
Nazan Deniz Yön Ertuğ, Biology, Sakarya University (Turkey)  
Nükheth Sazak, Electrical and Electronics Engineering, Sakarya University (Turkey)  
Osman Kırtel, Civil Engineering, Sakarya University of Applied Sciences (Turkey)  
Öznur Özkan Kılıç, Mathematics, Başkent University (Turkey)  
Rıfki Terzioğlu, Electrical and Electronics Engineering, Bolu Abant İzzet Baysal University, (Turkey)  
Sibel Güneş, Mechanical Engineering, Erciyes University (Turkey)  
Soley Ersoy, Mathematics, Sakarya University (Turkey)  
Tuğrul Çetinkaya, Metallurgical and Materials Engineering, Sakarya University (Turkey)  
Turgay Şişman, Biology, Atatürk University (Turkey)

## **English Language Editor**

---

Ömer Tamer, Physics, Sakarya University (Turkey)

SAKARYA ÜNİVERSİTESİ FEN BİLİMLERİ ENSTİTÜSÜ DERGİSİ  
(SAKARYA UNIVERSITY JOURNAL OF SCIENCE)  
İÇİNDEKİLER/CONTENTS  
Cilt/Volume: 25 – No/Issue5: (EKİM/OCTOBER-2021)

RESEARCH ARTICLES

Title	Authors	Pages
Position Estimation of In-Pipe Robot using Artificial Neural Network and Sensor Fusion	Abdullah Erhan AKKAYA, Muhammed Fatih TALU, Ömür AYDOĞMUŞ	1102-1120
Production and Purification of Peroxidase from Tissue Cultures of Cauliflower ( <i>Brassica oleracea</i> L. var. <i>Botrytis</i> )	Züleyha ALMAZ, Şeyma ÖNLÜ, Aykut ÖZTEKİN	1121-1128
Impact of Dehumidification Devices on Production Efficiency in Plastic Injection	M. Tahir OKTAÇ, Mustafa TİMUR, Halil KILIÇ	1129-1135
Effect of Grain Distribution on Resin Consumption and Mechanical Performance of GRP Pipes	Şevki EREN, Özcan ÇAĞLAR, Neslihan GÖKÇE, Azime SUBAŞI, Serkan SUBAŞI	1136-1147
Radical Scavenging and Antibacterial Activities of <i>Ruta buxbaumii</i> Poir. (Rutaceae) Growing in Raman Mountain-Batman	Alevcan KAPLAN	1148-1158
Development of Finite Element Model for a Special Lead Extrusion Damper	Ahmet GÜLLÜ, Furkan ÇALIM, Cihan SOYDAN, Ercan YÜKSEL	1159-1167
Investigation of a Perovskite Solar Cell and Various Parameters Impact on Its Layers and the Effect of Interface Modification by Using P3HT as an Ultrathin Polymeric Layer Through SCAPS-1D Simulation	Seyyedreza HOSSEİNİ, Mahsa BAHRAMGOUR, Nagihan DELİBAŞ, Aligholi NİAİE	1168-1179
On Generalized Recurrent and Generalized Concircularly Recurrent Weyl Manifolds	İlhan GÜL	1180-1188
Carbon Nanofibers Fabricated from Electrospun Nano-sized boron oxide/Polyacrylonitrile Nanofibers as electrode for Supercapacitors	Ümran KURTAN	1189-1196
Self-tuning fuzzy logic control of quarter car and bridge interaction model	Mustafa EROĞLU, Mehmet Akif KOÇ, Recep KOZAN, İsmail ESEN	1197-1209
Two-Dimensional Vector Boson Oscillator	Semra GÜRTAŞ DOĞAN	1210-1217
Effect of Heat Treatment on Microstructure of Zinc Aluminum Hybrid Composite Cast Alloys	Serdar ASLAN	1218-1234
Development of a Fluorescent Protein Based FRET Biosensor for Determination of Protease Activity	İbrahim İNCİR, Özlem KAPLAN, Sema BİLGİN, İsa GÖKÇE	1235-1244

The Investigation of Physical Properties of Composite  
Fertilizer Including Boron Micro Element

Havva MUMCU ŐİMŐEK, RvŐen  
GULIYEV

1245-1252



SAKARYA ÜNİVERSİTESİ

# FEN BİLİMLERİ ENSTİTÜSÜ DERGİSİ

Sakarya University Journal of Science  
SAUJS

e-ISSN: 2147-835X | Founded: 1997 | Period: Bimonthly | Publisher: Sakarya University |  
<http://www.saujs.sakarya.edu.tr/en/>

Title: Position Estimation of In-Pipe Robot using Artificial Neural Network and Sensor Fusion

Authors: Abdullah Erhan AKKAYA, Muhammed Fatih TALU, Ömür AYDOĞMUŞ

Received: 2021-03-16 16:46:59

Accepted: 2021-06-09 00:00:00

Article Type: Research Article

Volume: 25

Issue: 5

Month: October

Year: 2021

Pages: 1102-1120

How to cite

Abdullah Erhan AKKAYA, Muhammed Fatih TALU, Ömür AYDOĞMUŞ; (2021), Position Estimation of In-Pipe Robot using Artificial Neural Network and Sensor Fusion.

Sakarya University Journal of Science, 25(5), 1102-1120, DOI:

<https://doi.org/10.16984/saufenbilder.898072>

Access link

<http://www.saujs.sakarya.edu.tr/tr/pub/issue/65589/898072>

New submission to SAUJS

<http://dergipark.org.tr/en/journal/1115/submission/step/manuscript/new>

## Position Estimation of In-Pipe Robot Using Artificial Neural Network and Sensor Fusion

Abdullah Erhan AKKAYA\*<sup>1</sup>, Muhammed Fatih TALU<sup>1</sup>, Ömür AYDOĞMUŞ<sup>2</sup>

### Abstract

Automatic position detection of water leakage in water distribution pipelines is critical to minimize the loss of labour, time, money spent on exploration and excavation in pipe inspection procedures. Nevertheless, the main goal of detection is to prevent water loss. In this paper, accurate position detection, crack frequency band detection, and external sphere studies of an in-pipe robot prototype were presented. During the precise position estimation, classical Extended Kalman Filter (EKF), stationary region detection, and location estimation using Enhanced Heuristic Drift Elimination (EHDE) were performed with two different artificial neural networks (ANNs). In this way, online precise position estimation can be done on hardware with no sufficient computational power for indoor robotic studies. In addition, the sound characteristics resulting from the crack at different hole size and water pressure intensity levels were investigated. Finally, a new sealing sphere design was devised. Three different hydrophone sensor data were recorded on the SD card simultaneously. The results show that the proposed ANN method can work online and make a similar position estimation with the classical IMU position estimation method by 99%.

**Keywords:** Sensor Fusion, Artificial Neural Network, Inertial Navigation, Leak Detection

\* Corresponding author: erhan.akkaya@inonu.edu.tr

<sup>1</sup> Inonu University, Faculty of Engineering, Department of Computer Engineering, Malatya, Turkey.

E-Mail: erhan.akkaya@inonu.edu.tr; fatihtalu@gmail.com.

ORCID: <https://orcid.org/0000-0001-6193-5166>; <https://orcid.org/0000-0003-1166-8404>.

<sup>2</sup> Firat University, Faculty of Technology, Department of Mechatronic Engineering, Elazig, Turkey.

E-Mail: oaydogmus@firat.edu.tr.

ORCID: <https://orcid.org/0000-0001-8142-1146>.

## 1. INTRODUCTION

Water has great importance for the survival of living beings on earth and especially for the human species. Increasing the place of settlements in proportion to the human population also increases the water demand. Today's people should consume water cost-effectively for future generations to benefit from potable water resources. In many countries, serious policies have been developed, including water distribution systems for the conscious use of water [1]. According to World Bank, approximately 14.6 billion dollars of water is lost annually due to the cracks in the water pipes during transportation [2]. In another report prepared by the World Bank, two-thirds of the world's population will be going without water in 2025 unless the current water policies are taken under control [3]. In the U.S., approximately 240,000 water pipe cracks occur annually. These cracks are responsible for the loss of 2 trillion gallons of water that account for 15-25% of purified water [4].

One way of protecting water is by reducing water losses due to pipe cracks and faults in the pipelines in the distribution network. These faults should be identified and repaired to prevent loss of water and income. General pipe repairs have high costs in distribution networks. Finding the exact position of the fault and working in that area reduces the repair costs. Although surface pipe listening devices appear to be a solution to this need, they are not preferred because of influenced by external noise [5]. Moreover, the small scale of underground water leaks makes it very difficult to detect these leaks. Physical infrastructure failures, such as ageing, corrosion and mechanical stress, cause the water pipe to lose its thickness what causes cracking and water leakage due to pipe leaks/breaks [6]. Pipe maintenance must be carried out regularly to prevent damage. Traditional maintenance procedures have high costs as they require removal and excavation. Comprehensive pipe maintenance procedures include; (a) the detection of the amount of water lost in the pipes; (b) finding the location of the cracks in the pipeline that causing water loss; (c) the repair of the cracked areas in the detected position [7]. The amount of lost water is

determined by calculating the difference between the amount of water supplied to the grid and the amount used [8].

In the literature, there are many studies on distribution water leak detection and management. In monitoring and managing physical losses, various methods have been applied, such as the implementation of standard water balance and performance monitoring [9]–[12], monitoring of minimum night flow, determination of potentially preventable leaks daily [13], [14], implementation of pressure management [15], [16], pipe material management [17]–[19], in-pipe location detection robots that can find leak position [20]–[23]. In this preliminary study, a leak detection robot prototype, which can find the position of the pipe crack with high accuracy, was developed.

## 2. PRECISE POSITION ESTIMATION EXPERIMENTS

The operations were performed in the precise position estimation step are summarized as follows: (1) saving IMU data in navigation scenarios, (2) position estimation method, (3) Kuka experiments, (4) proposed artificial position estimation method.

### 2.1. Saving IMU Data in Navigation Scenarios

Navigation scenarios were carried out in a 20m<sup>2</sup> indoor space. There are eight different navigation scenarios, as shown in Figure 1. For the real-time recording of IMU data during navigation, Odroid XU3 and IMU sensor were connected. This navigation device was placed in a sphere-shaped housing produced by a 3D printer. IMU data was recorded between the nodes in the scenarios with the help of the navigation device. Figure 2 shows the navigation device and indoor space. An IMU that has nine degrees of freedom was used to collect the data. These nine degrees consists of a 3DOF accelerometer, 3DOF magnetometer and 3DOF gyroscope. The sensor data was read at 100Hz from the IMU sensor using virtual port listening software written in C++. The read data was transferred to the Odroid XU3 computer via

a USB port. Figure 3 shows the recorded IMU data for the navigation scenario.

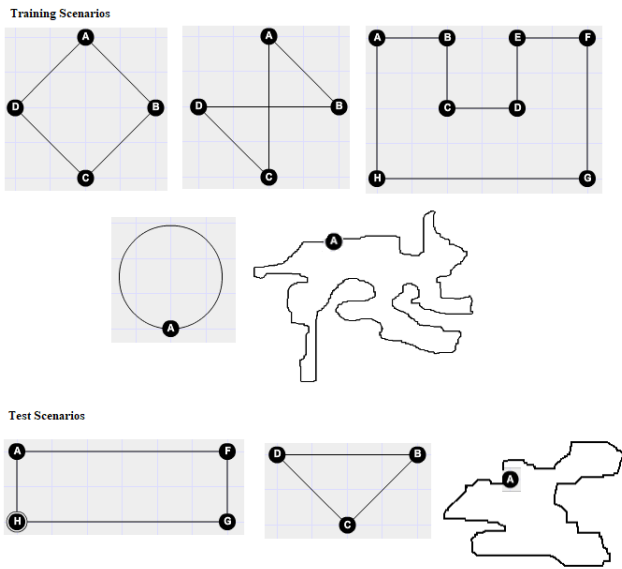


Figure 1 Navigation scenarios



Figure 2 Obtaining train and test data via IMU sensor that placed in 3D printed spherical ball

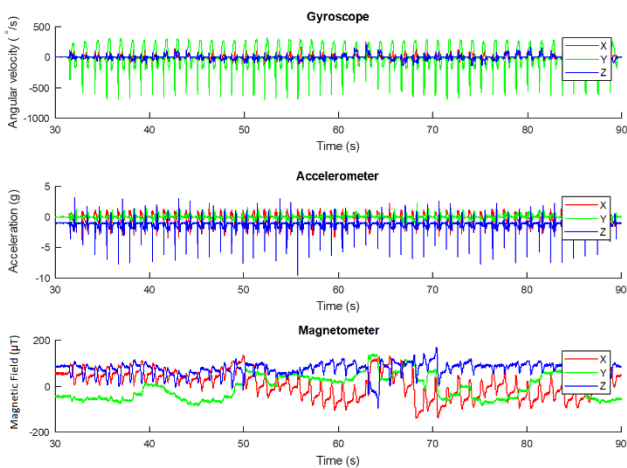


Figure 3 IMU data for a square navigation scenario

## 2.2. Position Estimation Method

Combining the data obtained from different sensors such as magnetometers, accelerometers, and gyroscopes, obtaining the measurement information with the smallest error is called sensor fusion [24]. The direct processing of raw IMU data results in an increase in cumulative error in the acceleration sensor data required for calculating the position, thereby decreasing position estimation accuracy. Therefore, data need to be filtered. Kalman filter has been used effectively in sensor fusion applications [25]–[28]. Rudolf Kalman, an American citizen of Hungarian origin, discovered The Kalman filter in 1960 [29]. First developed for linear systems, Kalman Filter is a recursive, least-squares algorithm in which weights are dynamically updated at each step. The Extended Kalman Filter (EKF) aims to apply the Kalman filter to a non-linear system [30].

In general, the Kalman filter is a filter that can predict the state of the system at the time  $t-1$  using the input and output information of a dynamic system. Kalman Filter is defined in Equation (1) and (2) [31]. At Equation (1),  $x$  represents the state vector,  $u$  control vector,  $w$  process noise,  $A$  state transition matrix,  $B$  control input matrix. The  $z$  value in Equation (2) represents the measurement vector,  $H$  the transformation matrix that maps the state vector parameters to the measurement region, and  $v$  represents the measurement noise.

$$x_t = A_t x_{t-1} + B_t u_t + w_t \quad (1)$$

$$z_t = H_t x_t + v_t \quad (2)$$

The state dynamics are not linear in many systems. In this case, the Kalman filter cannot be applied because the Kalman gain cannot be calculated. The standard Kalman filter has been used by calculating the Jacobian values of the functions to linearize the system's state dynamics and measurement function. Initially, the system state dynamics are linearized, followed by the measurement (system dynamics) update in the following step. In the third step, measurements are linearized, and the last step is updated. As a

result of this process, the Kalman filter transforms to the Extended Kalman Filter [30]. In the first step, the linearized state and measurement vectors are given in Equations (3) - (4).

$$x_{t+1} = f(x_t, u_t, w_t) \quad (3)$$

$$z_t = h(x_t, u_t, v_t) \quad (4)$$

The basic steps of the Extended Kalman Filter are listed below.

Step 1: Linearize measurements

$$H_t = \left. \frac{\partial h(x,u)}{\partial x} \right|_{x=\hat{x}_{t|t-1}} \quad (5)$$

Step 2: Update measurements (correction):

$$K_t = P_{t|t-1} H_t^T (H_t P_{t|t-1} H_t^T + R_t)^{-1} \quad (6)$$

$$\hat{x}_{t|t} = \hat{x}_{t|t-1} + K_t (z_t - H_t \hat{x}_{t|t-1}) \quad (7)$$

$$P_{t|t} = P_{t|t-1} - K_t H_t P_{t|t-1} \quad (8)$$

Step 3: Update measurements (correction):

$$F_t = \left. \frac{\partial f(x,u)}{\partial x} \right|_{x=\hat{x}_{t|t}} \quad (9)$$

Step 4: Time update (prediction) and return step1:

$$\hat{x}_{t+1|t} = f(\hat{x}_{t|t}, \hat{u}_t) \quad (10)$$

$$P_{t+1|t} = F_t P_{t|t} F_t^T + Q_t \quad (11)$$

In this study, 3DOF magnetic field sensor and 3DOF accelerometer sensors were used as complementary sensors [32]. A sensor fusion process was performed to correct the angular variation measured by a 3DOF gyroscope in the method used in leak detection. The integration step is the time update step which predicts the quaternion vector using the  $F_t$  transition matrix and the estimated error covariance matrix. The vector observation step optimizes the system state dynamics of the magnetic field sensor and the accelerometer data. The Kalman filter was applied at the final stage to minimize the error covariance, and the correction step is done. The noise characteristics of the sensors (acceleration,

rotation and magnetic field) were calculated by taking the mean and standard deviations of the data collected while the IMU was inactive [20].

The state vector of the generated filter system is defined in Equation (12).  $q_0$  is the real component,  $q_1$ ,  $q_2$ , and  $q_3$  are the virtual components of the quaternion vector.

$$x = [q_0 \quad q_1 \quad q_2 \quad q_3] \quad (12)$$

Euler angles have been calculated by passing the IMU data through the Extended Kalman Filter in classical studies. Since the rotation vector calculated by the Euler angle has the singularity problem, Quaternion vector  $q$  was calculated instead of the Euler angles. The following steps show the implementation of the Kalman Filter.

### 2.2.1. Integration Step

The gyroscope sensor measures the angular change in the X, Y and Z axes of the coordinate system in rad/s, the change in each axis is represented by  $\omega_x$ ,  $\omega_y$ ,  $\omega_z$ , respectively.  ${}^S\omega$  represents the gyroscope vector measured in all axes of the sensor coordinate system, eq. (13).

Equation (14) was used to calculate the quaternion derivative ( ${}^S\dot{q}$ ) which gives the amount of change from the global coordinate system to the sensor coordinate system [33].

$${}^S\omega = [0 \quad \omega_x \quad \omega_y \quad \omega_z] \quad (13)$$

$${}^S\dot{q} = \frac{1}{2} {}^S\hat{q} \otimes {}^S\omega \quad (14)$$

The quaternion derivative was calculated by multiplying the values read from the gyroscope sensor sequentially given in Equation (15).  ${}^S\omega_t$  represents the data read from the gyroscope at time  $t$ ,  ${}^S\hat{q}_{est,t-1}$  represents the previous quaternion vector. After these derivatives have added to the previous quaternion by multiplying by the sensor period  $\Delta t$  the quaternion, the orientation information has been obtained in Equation (16) [32].

$${}^S_G\dot{q}_{\omega,t} = \frac{1}{2} {}^S_G\hat{q}_{est,t-1} \otimes {}^S\omega_t \quad (15)$$

$${}^S_Gq_{\omega,t} = {}^S_G\dot{q}_{\omega,t}\Delta t + {}^S_G\hat{q}_{est,t-1} \quad (16)$$

Assume that the sensor operates at a frequency of 50Hz. In this case,  $\Delta t$  period value will be 0.02. In every 0.02 seconds, the current quaternion vector was multiplied by the gyroscope value  ${}^S\omega_t$  from the sensor to obtain the instant quaternion value. The effect of the calculated quaternion value on a total period of 1 second is 0,02. The quaternion was multiplied by this value and collected with the vector calculated in the previous step. As shown in Figure 4, the initial quaternion  $[1 \ 0 \ 0 \ 0]$  was rotated 90 degrees on the X-axis.

When the gyroscope process noise has added to the state equation, the general state equation of the system given in (17). The  $w_t$  value is the process noise defined by the covariance matrix  $Q$  of the gyroscope sensor [32].

$$x_t = f(x_{t-1}) + w_t \quad (17)$$

In principle, the  $Q$  covariance matrix and  $w_t$  are the same. The formulation is represented by the  $w_t$  in the optimization formulas and  $Q$  by the Kalman filter.  $Q$  covariance matrix is different even for the same brand sensor. When a sensor is stationary, it produces values unequal to zero due to external noise. After reading all these values for a certain period, the sensor's offset value was calculated by taking the arithmetic mean of the sensor data, Equation (18). In this paper, the offset value of the gyroscope sensor was added to the variance estimation algorithm. The variance vector of the sensor was calculated in (19). The variance vector  $Q$  is used in the construction of the covariance matrix.

$$offset = [[-0.1342 \ -0.0553 \ 0.1455]] \quad (18)$$

$$var = [0.0705 \ 0.0732 \ 0.0663] \quad (19)$$

When  ${}^S_G\dot{q}_{\omega,t}$  is replaced by Equation (15) in Equation(16), main quaternion equation is obtained [16], Equation (20).

$${}^S_Gq_{\omega,t} = \frac{1}{2} ({}^S_G\hat{q}_{est,t-1} \otimes {}^S\omega_t)\Delta t + {}^S_G\hat{q}_{est,t-1} \quad (20)$$

This equation which is estimated, is defined as the state equation in the Kalman filter. The  $x_t$  was calculated at the time  $t$  is also the predicted  ${}^S_G\hat{q}_{est,t-1}$  value in the previous step. When all these equations are combined, a Kalman filter state equation based on quaternion is defined in Equation (21). The state equation at time  $t$  is given in Equation (22).

$$f(x_{t-1}) = \frac{1}{2} (x_{t-1} \otimes {}^S\omega_t)\Delta t + x_{t-1} \quad (21)$$

$$x_{t|t-1} = f(x_{t-1|t-1}) \quad (22)$$

It is clear that the function  $f(x_t)$  is not linear. In this case, since the Kalman Filter cannot calculate the Kalman gain,  $F_t$  transition matrix should be computed using the Extended Kalman Filter. After  $x_{t-1} \otimes {}^S\omega_t$  quaternion production, Equation (23) is obtained [32].

$$x_{t-1} \otimes {}^S\omega_t = \begin{bmatrix} x_0 \cdot 0 - x_1\omega_x - x_2\omega_y - x_3\omega_z \\ x_0\omega_x + x_1 \cdot 0 + x_2\omega_z - x_3\omega_y \\ x_0\omega_y - x_1\omega_z + x_2 \cdot 0 + x_3\omega_x \\ x_0\omega_z + x_1\omega_y - x_2\omega_x + x_3 \cdot 0 \end{bmatrix} \quad (23)$$

In Equation (24), The Jacobian  $F_t$  transition matrix of the  $f(x_{t-1})$  function obtained when Equation (23) is replaced in Equation (21).

$$F_t = \left. \frac{\partial f(x_t)}{\partial x} \right|_{x=\hat{x}_{t-1|t-1}} = \begin{bmatrix} 1 & -\Delta t/2 \cdot \omega_x & -\Delta t/2 \cdot \omega_y & -\Delta t/2 \cdot \omega_z \\ \Delta t/2 \cdot \omega_x & 1 & \Delta t/2 \cdot \omega_z & -\Delta t/2 \cdot \omega_y \\ \Delta t/2 \cdot \omega_y & -\Delta t/2 \cdot \omega_z & 1 & \Delta t/2 \cdot \omega_x \\ \Delta t/2 \cdot \omega_z & \Delta t/2 \cdot \omega_y & -\Delta t/2 \cdot \omega_x & 1 \end{bmatrix} \quad (24)$$

The estimated quaternion vector is obtained by multiplying the initial quaternion value by  $F_t$ , in Equation (25).

$$x_{t|t-1} = F_t x_{t-1|t-1} \quad (25)$$

The final step of the integration step is the calculation of the estimated covariance matrix ( $P_{t|t-1}$ ) according to Equation (11) in the fourth step of the EKF.

### 2.2.2. Vector observation step

The observation step is the step in which the quaternion vector is optimized using auxiliary sensors. As a result of the optimization, the minimized quaternion,  $z_t$  observation vector was obtained.  ${}^S_G\hat{q}$ ,  ${}^G\hat{d}$  and  ${}^S\hat{s}$  represents the sensor orientation, the predefined reference direction on the earth, the data read from the sensor, respectively. The objective function to be minimized is defined by (26) [32].

$$\begin{aligned} \min_{{}^S_G\hat{q}} f({}^S_G\hat{q}, {}^G\hat{d}, {}^S\hat{s}) &\rightarrow f({}^S_G\hat{q}, {}^G\hat{d}, {}^S\hat{s}) \\ &= {}^S_G\hat{q}^* \otimes {}^G\hat{d} \otimes {}^S_G\hat{q} - {}^S\hat{s} \end{aligned} \quad (26)$$

Using the Gradient Descent method, the quaternion equation to be solved with  $\mu$  step size and the Jacobian matrix of the function indicating the direction of the error are given in the (27) and (28), respectively. The  $\nabla$  symbol indicates that the objective function is solved by the Gradient Descent method [32].

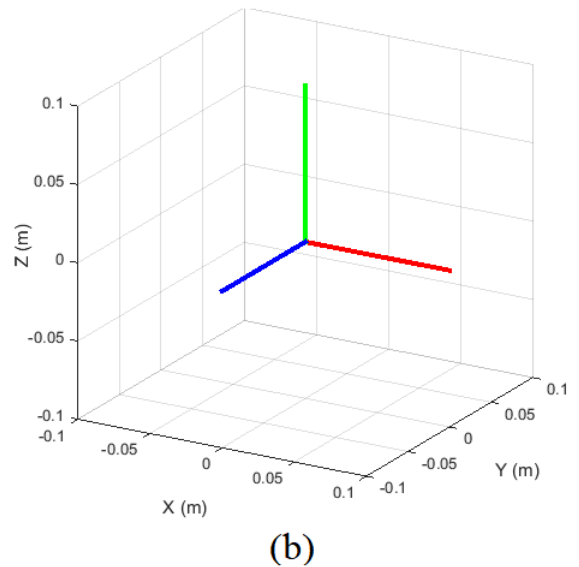
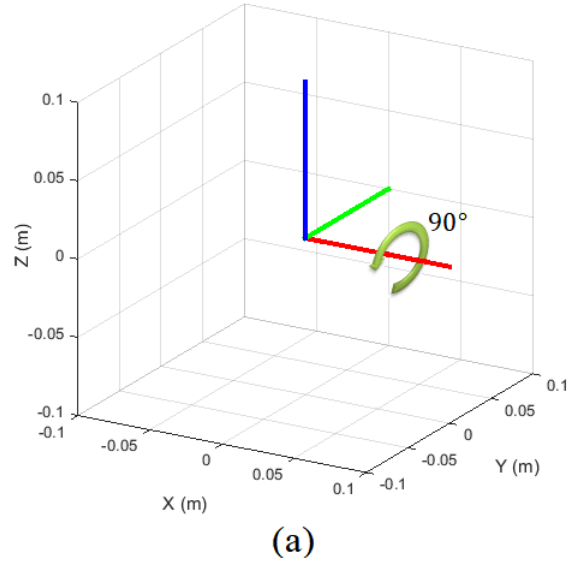


Figure 2 Rotating the IMU sensor around X-axis.

$${}^S_G\hat{q}_{k+1} = {}^S_G\hat{q}_k - \mu \frac{\nabla f({}^S_G\hat{q}_k, {}^G\hat{d}, {}^S\hat{s})}{\|\nabla f({}^S_G\hat{q}_k, {}^G\hat{d}, {}^S\hat{s})\|} \quad (27)$$

$$\nabla f({}^S_G\hat{q}_k, {}^G\hat{d}, {}^S\hat{s}) = J^T({}^S_G\hat{q}_k, {}^G\hat{d}) f({}^S_G\hat{q}_k, {}^G\hat{d}, {}^S\hat{s}) \quad (28)$$

The quaternion vector provides the coordinate transformation to be used in the calculations given in Equation (29). Given that the gravitational vector in the global coordinate system defines the Z-axis of the invariant gravity vector, the model refers to the angular change between the information coming from the accelerometer and

the gravity vector. In this case, the reference system defined as  ${}^G\hat{\mathbf{a}}$  in the objective function will be updated as  ${}^G\hat{\mathbf{g}}$ . The upper symbol defines the global coordinate system and  $\hat{\mathbf{g}}$  defines the gravity in Equation (30). If the accelerometer is to be used only in the quaternion update,  ${}^S\hat{\mathbf{a}}$  in Equation (28), the objective function of the optimization system to be installed according to Equation (26) and the Jacobian matrix are given in Equations (32) and (33). The orientation quaternion was calculated only by the accelerometer and gyroscope data [32]. This set of equations defines the Z-axis of the reference global coordinate system.

$${}^S\hat{\mathbf{q}} = [q_0 \quad q_1 \quad q_2 \quad q_3] \quad (29)$$

$${}^G\hat{\mathbf{g}} = [0 \quad 0 \quad 0 \quad 1] \quad (30)$$

$${}^S\hat{\mathbf{a}} = [0 \quad a_x \quad a_y \quad a_z] \quad (31)$$

$$f_g({}^S\hat{\mathbf{q}}, {}^S\hat{\mathbf{a}}) = \begin{bmatrix} 2(q_1q_3 - q_0q_2) - a_x \\ 2(q_0q_1 + q_2q_3) - a_y \\ 2\left(\frac{1}{2} - q_1^2 - q_2^2\right) - a_z \end{bmatrix} \quad (32)$$

$$J_g({}^S\hat{\mathbf{q}}) = \begin{bmatrix} -2q_2 & 2q_3 & -2q_0 & 2q_1 \\ 2q_1 & 2q_0 & 2q_3 & 2q_2 \\ 0 & -4q_1 & -4q_2 & 0 \end{bmatrix} \quad (33)$$

The quaternion vector calculated by the accelerometer only corrects the angle between the gravity vector, thus preventing angular orientation information from being updated in all three axes. In addition to gravity, when the magnetic axes present in the horizontal and vertical directions that define the X and Y axes of the global coordinate system are used, three orthogonal axes will be formed. Thus, three-dimensional angular orientation information was computed effectively. Equation (34) and (35) show that referenced magnetic field coordinate axes,  ${}^G\hat{\mathbf{b}}$  and magnetic field sensor data,  ${}^S\hat{\mathbf{m}}$ , respectively.

$${}^G\hat{\mathbf{b}} = [0 \quad b_x \quad 0 \quad b_z] \quad (34)$$

$${}^S\hat{\mathbf{m}} = [0 \quad m_x \quad m_y \quad m_z] \quad (35)$$

Magnetic field sensors can produce erroneous results influenced by all the magnetic field disturbers in the external environment, such as magnets and electrical appliances [34]. These waves, which have a disturbing effect around the sensor, have been described as *hard iron bias* [35]. The sensor must be calibrated to minimize ambient noise and increase the effectiveness of the magnetic field sensor output. In this calibration process, the quaternion multiplication between the predicted quaternion value and the data read from the sensor was performed, and the magnetic field direction  ${}^G\hat{\mathbf{h}}$  was measured (36). In the next step, the calibration of the reference magnetic field  ${}^G\hat{\mathbf{b}}$  of the algorithm was performed, (37). Thus, it was ensured that the error is limited only by the predicted quaternion orientation and does not spread to the whole system [36].

$${}^G\hat{\mathbf{h}}_t = [0 \quad h_x \quad h_y \quad h_z] = {}^S\hat{\mathbf{q}}_{est,t-1} \otimes {}^S\mathbf{m}_t \otimes {}^S\hat{\mathbf{q}}_{est,t-1}^* \quad (36)$$

$${}^G\hat{\mathbf{b}}_t = [0 \quad \sqrt{h_x^2 + h_y^2} \quad 0 \quad h_z] \quad (37)$$

The second cost function defines the X-Y axes of the global coordinate system, and the Jacobian matrix of this function is shown in Equations (38) and (39).

$$f_b({}^S\hat{\mathbf{q}}, {}^G\hat{\mathbf{b}}, {}^S\hat{\mathbf{m}}) = \quad (38)$$

$$\begin{bmatrix} 2b_x(0.5 - q_2^2 - q_3^2) + 2b_z(q_1q_3 - q_0q_2) - m_x \\ 2b_x(q_1q_2 - q_0q_3) + 2b_z(q_0q_1 + q_2q_3) - m_y \\ 2b_x(q_0q_2 + q_1q_3) + 2b_z(0.5 - q_1^2 - q_2^2) - m_z \end{bmatrix}$$

$$J_b({}^S\hat{\mathbf{q}}, {}^G\hat{\mathbf{b}}) = \begin{bmatrix} -2b_zq_2 & 2b_zq_3 \\ -2b_xq_3 + 2b_zq_1 & 2b_xq_2 + 2b_zq_0 \\ 2b_xq_2 & 2b_xq_3 - 4b_zq_1 \\ -4b_xq_2 - 2b_zq_0 & -4b_xq_3 + 2b_zq_1 \\ 2b_xq_1 + 2b_zq_3 & -2b_xq_0 + 2b_zq_2 \\ 2b_xq_0 - 4b_zq_2 & 2b_xq_1 \end{bmatrix} \quad (39)$$

The angular change values are calculated according to gravity, or magnetic axes alone do not give the orientation information of the sensor. A single solution surface must be formed by combining the objective functions defined by equations (32) and (38). Equations (40) and (41) combines objective functions and Jacobian matrices.

$$f_{g,b}({}^S\hat{q}, {}^S\hat{a}, {}^G\hat{b}, {}^S\hat{m}) = \begin{bmatrix} f_g({}^S\hat{q}, {}^S\hat{a}) \\ f_b({}^S\hat{q}, {}^G\hat{b}, {}^S\hat{m}) \end{bmatrix} \quad (40)$$

$$J_{g,b}({}^S\hat{q}, {}^G\hat{b}) = \begin{bmatrix} J_g^T({}^S\hat{q}) \\ J_b^T({}^S\hat{q}, {}^G\hat{b}) \end{bmatrix} \quad (41)$$

Once the equation systems to be optimized was defined, the sensor function to be used was selected in Equation (42). The quaternion value

was optimized for all three axes in the next step, and the vector observation step is completed in Equation (43). The  $\mu$  value is the step size, in Equation (44). The  $z_t$  measurement to be used in the next step was calculated by the observation vector in Equation (45).

$H$  represents the observability matrix, and  $v_t$  represents observation noise. The  $H$  matrix is the unit matrix,  $I_{4 \times 4}$ , because of containing the  $z_t$  quaternion information.

$$\nabla f = \begin{cases} J_g^T({}^S\hat{q}_{est,t-1}) \cdot f_g({}^S\hat{q}_{est,t-1}, {}^S\hat{a}_t) \\ J_{g,b}^T({}^S\hat{q}_{est,t-1}, {}^G\hat{b}) \cdot f_{g,b}({}^S\hat{q}_{est,t-1}, {}^S\hat{a}_t, {}^G\hat{b}, {}^S\hat{m}_t) \end{cases} \quad (42)$$

$${}^S q_{\nabla,t} = {}^S\hat{q}_{est,t-1} - \mu_t \frac{\nabla f}{\|\nabla f\|} \quad (43)$$

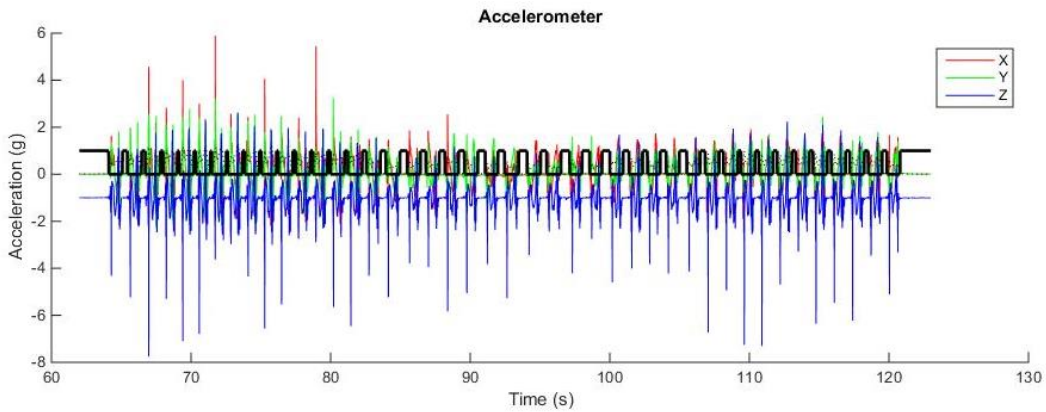


Figure 3 Determining the stationary region of the accelerometer using the Butterworth filter IMU data for a square navigation scenario

$$\mu_t = \alpha \left\| \frac{{}^S\dot{q}_{\omega,t}}{E} \right\| \Delta t, \quad \alpha > 1 \quad (44)$$

$$z_t = Hx_t + v_t = \frac{{}^S q_{\nabla,t}}{\|{}^S q_{\nabla,t}\|} \quad (45)$$

### 2.2.3. Kalman Filtering Step

Once the integration and vector observation steps are completed, the Kalman Filtering step starts. In this step, the Kalman gain was calculated using the estimated covariance matrix calculated in the integration step, the  $H$  observability matrix, and the  $R$  covariance matrix, Equation (46). The state correction and covariance matrix correction were performed with the calculated Kalman gain in Equations (47) and (48).

$$K_t = P_{t|t-1} H_t^T (H_t P_{t|t-1} H_t^T + R_t)^{-1} \quad (46)$$

$$\hat{x}_{t|t} = \hat{x}_{t|t-1} + K_t (z_t - H_t \hat{x}_{t|t-1}),$$

$${}^S\hat{q}_{est,t} = \hat{x}_{t|t} \quad (47)$$

$$P_{t|t} = P_{t|t-1} - K_t H_t P_{t|t-1} \quad (48)$$

The next step is the integration step. Estimated covariance matrix and estimated status update were performed. In the second stage, the  $z_t$  measurement vector was calculated using the Gradient Descent algorithm, and the Kalman filter was applied. The sensor fusion process ends after the vector observation step. Quaternion data were computed using an accelerometer, gyroscope and magnetic field sensors. The quaternion obtained

in the next step was used to compute the position. In order to be able to calculate the position correctly, it is necessary to eliminate the error in the accelerometer after calculating the quaternion vector by the sensor fusion process. First, using the quaternion values, the accelerometer values in the sensor coordinate system must be converted to the earth coordinate system [32], Equation (49).

$${}^G\hat{a} = ({}^S_G\hat{q} \otimes [0 \ a_x \ a_y \ a_z]) \otimes \hat{q}^* \quad (49)$$

After this process, the Butterworth filter was applied to the accelerometer data to determine the

sensor's fixed points and minimize the position offset. The Butterworth filter was preferred because it has a more linear frequency response than Chebyshev and the elliptical filters. Figure 5 shows the accelerometer data applied to the Butterworth filter. In the filter indicated by black, the regions with 0 value show the moving parts, and the regions with value 1 display the stationary areas. After determining the stationary regions, the velocity was calculated by integrating the accelerometer value in non-stationary regions.

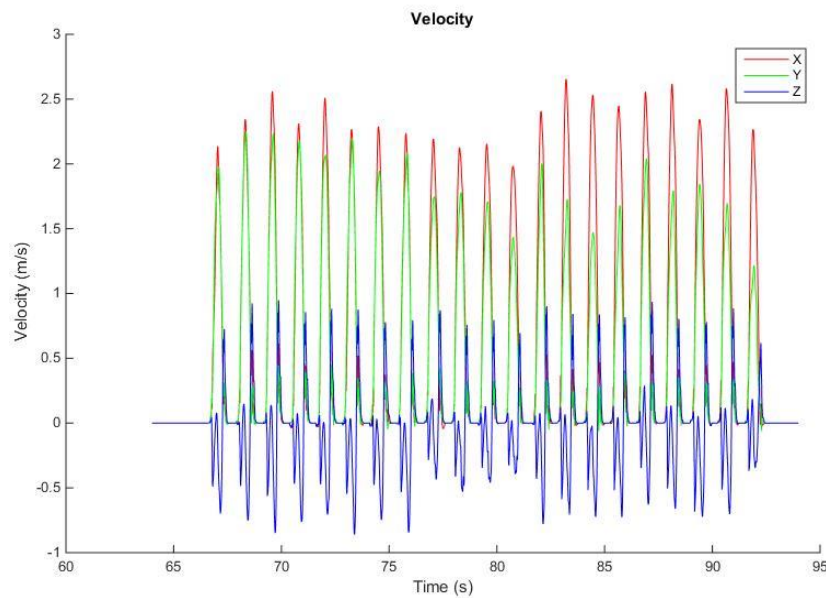


Figure 4 Sensor velocity graph resulting from the integration of accelerometer after a minute.

The calculated speed value was integrated into non-stationary regions, and the position information was calculated. The computed velocity is given in Figure 6.

#### 2.2.4. Enhanced Heuristic Drift Elimination (EHDE)

In the fourth and last stage, the first integral of the acceleration gives the sensor speed vector, and the second integral provides the position with information. For the square navigation data, the position graph obtained at the end of the four stages is shown in Figure 7a. Although the start and endpoint of the navigation are the same, the prediction error is high. Appear of this high error

is due to the cumulative growth of the error at each step. EHDE [37] method was used to reduce the cumulative error. This method filters the deviations in the sensor orientation. For this, a curve model is inserted into the last five measurement data and calculates the dominant sensor orientation. It then minimizes the error by subtracting the orientation difference between the model and the measurement from the current Quaternion vector. When we use EHDE in square navigation data, it is seen that the prediction error between the start and end points has dropped to 0.3m (see Figure 7b). This result is sufficient to continue the design.

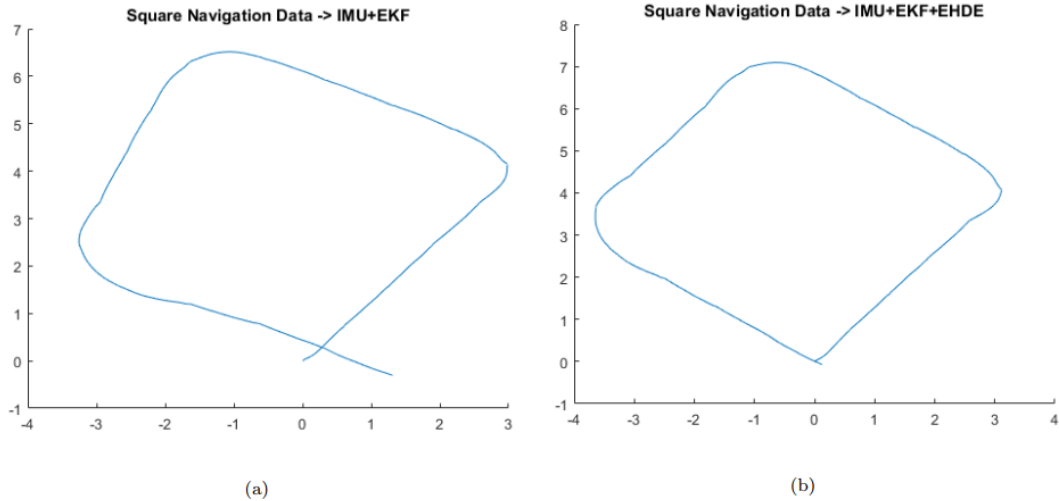


Figure 5 Position estimation results for square navigation data (a) IMU+EKF, (b) IMU + EKF + EHD

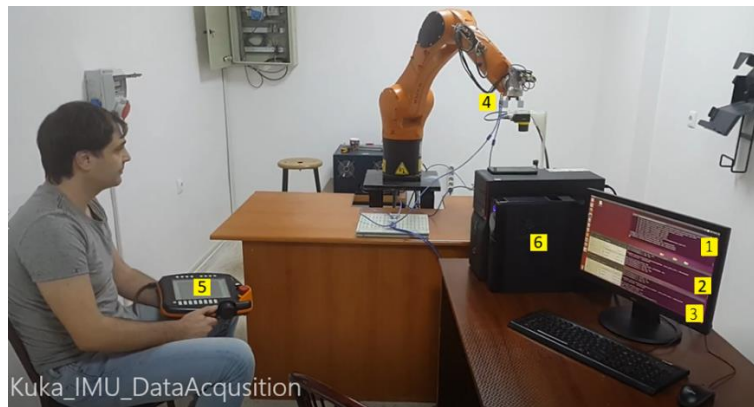


Figure 6 Experimental setup for simultaneous recording of Kuka and IMU data.

### 2.3. Kuka Experiments

In order to obtain the training set using Kuka Robot and IMU data, the simultaneous recording apparatus shown in Figure 8 was established. An artificial intelligence system was built to map the IMU sensor data using the precise position information obtained from the Kuka robot.

The components used in the recording device and numbered with yellow labels are listed below.

1. Software that records the XYZ position information of the robot end (JAVA)
2. Software that records the first IMU sensor data (C++)
3. Software that records the second IMU sensor data (C++)

4. Two IMU sensors placed at the end of the robot
5. Kuka robot controller
6. A computer that records the IMU and Kuka data synchronously.

Before the experiment, the Kuka robot movements were programmed by the operator using the control software interface and placed in the Kuka robot memory. In addition, both IMU sensors are fixed to the end of the Kuka. Necessary connections have been made for the flow of information from Kuka and IMUs to the computer. After the essential C++ and Java compilers were installed on the Ubuntu operating system, simultaneous data was recorded from the IMU sensors and the Kuka robot. The movements placed in the memory of the Kuka were performed at three different speeds, and during the arm

movements, Kuka/IMU data were recorded simultaneously (Figure 9a). Input and output data were trained using ANN, and the matching accuracy reached  $R = 0.902$  (see Figure 9b). Although this value seems acceptable, the accumulation of the error value of 0.098 in each measurement step results in unacceptable position estimation. For this reason, different methods were researched to make position estimation more accurate, and thus artificial location estimation method was applied.

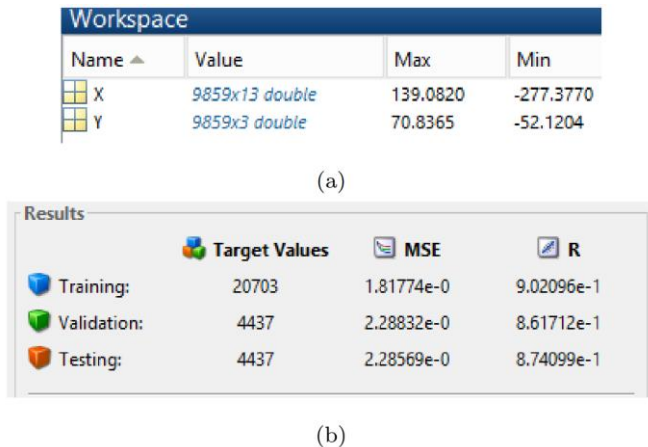


Figure 7 (a) Training data (X: input, Y: output);  
(b) Training results of Kuka data.

## 2.4. Proposed Artificial Position Estimation Method

In the proposed artificial position estimation method, two different artificial neural networks were created which mimic the classical position estimation. The first artificial neural network input and output consists of IMU sensor data and quaternion vectors, respectively.

The input of the second ANN is the quaternion vector, and the output is position information corrected by the EHDE algorithm. Thus, it is unnecessary to know the noise characteristics of the gyroscope, accelerometer and magnetometer sensors, the mathematical background required for EKF and EHDE, and Quaternion transformations for position estimation. The ANN directly converts the IMU sensor information to position information.

The first ANN is in the NARX architecture and has 4 cells in the input layer, 18 cells in the intermediate layer, and 4 cells in the output layer. System inputs and outputs are 9DOF IMU and 4D Quaternion data, respectively. The training, validation and test accuracy obtained from the training process is approximately 99.99% (see Figure 10).

Figure 11 shows classical and artificial methods that were used to estimate quaternion from the square navigation data. The 4D-Quaternion data are shown separately.

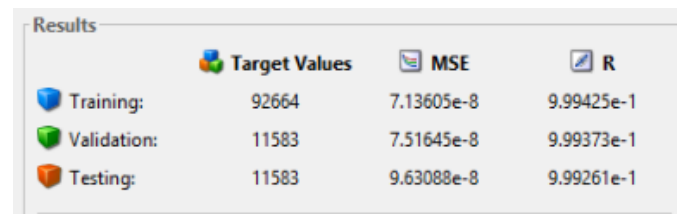


Figure 8 Training results of first ANN

It is seen that the artificial learning method produces almost the same results as the classical system has high accuracy.

Using the second ANN, the stationary zone detection and the noise elimination process performed by the EHDE method were imitated. Thus, IMU data was mapped to direct position information with two different ANNs. The fact that the location prediction process can be performed by an ANN method means that the network values can be transferred to an embedded system, and the position estimation can be run online. In this way, the online precision position estimation can be done in robotic studies (especially in the building) without sufficient speed and calculation power. Figure 12 shows the classical and recommended method results of eight different navigation positions. Since the results of two consecutive ANNs are the same as 99% of the classical method, the results are almost overlapping, as shown.

## 3. DETECTION OF LEAKAGE SOUND FREQUENCY BAND

The material type of the water pipe, the size of the crack and the severity of the water pressure causes

the sound from the pipe crack to be in different frequency bands. This experiment aims to examine the effect of crack hole diameter and pressure intensity on the frequency band and amplitude.

### 3.1. Preparing the Experiment Mechanism

Below are the different types of materials were used for the water pipe, the different sizes that the

crack may be and the different water pressure intensity values formed in the pipe.

Material Types: PCCP, RCCP, AC, PVC, HDPE, GRP, Steel, Cast Iron

Hole sizes: 2mm, 4mm, 6mm, 8mm

Water pressure intensity: 1bar, 2bar, 3bar, 4bar, 5bar

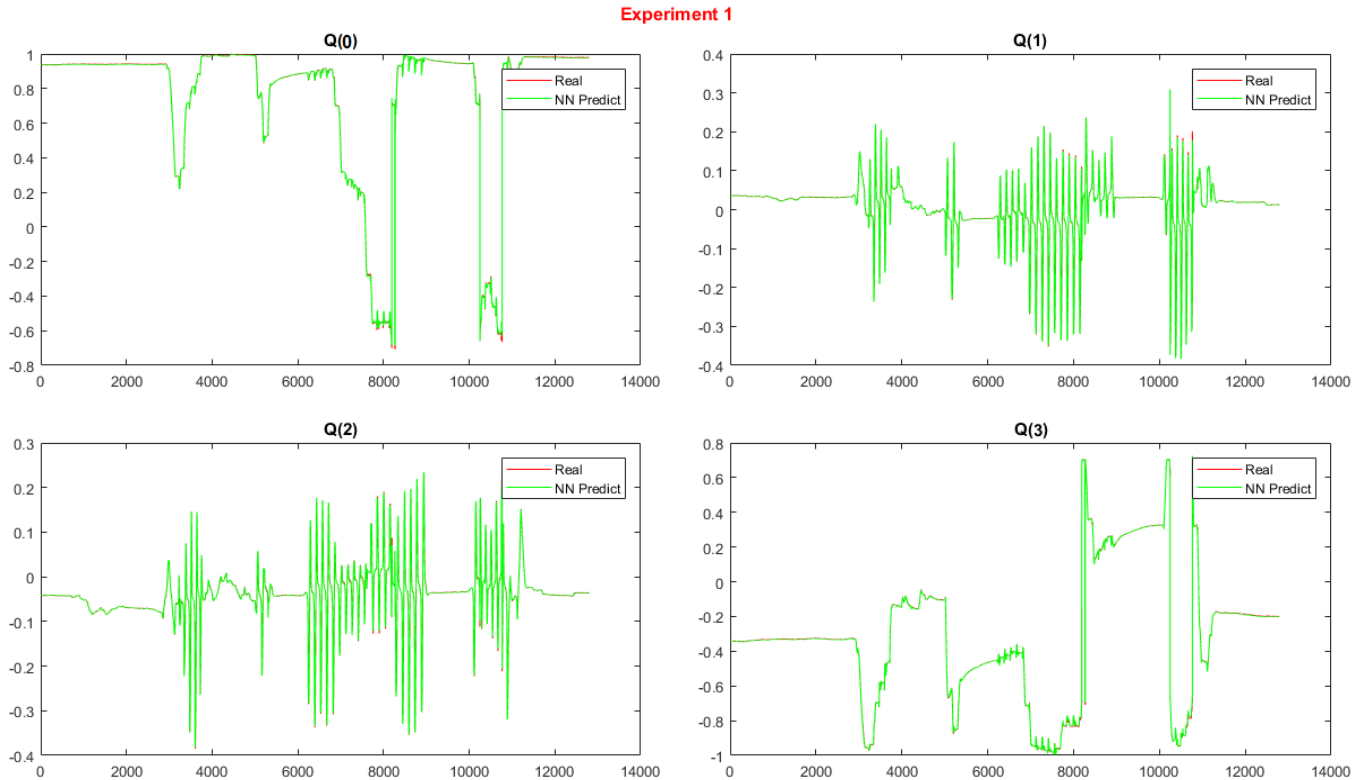


Figure 9 Training results of first ANN for  $x = [q_0; q_1; q_2; q_3]$  quaternion vector

As shown in Figure 13, a particular acoustic sound calibration device was prepared to record sound from crack for different hole sizes and pressure intensity. This apparatus comprises a 20cm diameter and 3m long tube with both ends closed. Water was pumped from one end of the pipe, and the water pressure level can be adjusted between 1 and 5 bar. The water pressure intensity can be seen with the pressure gauge at the pipe inlet. In order to measure the acoustic sound signal, a wired hydrophone was placed inwardly from the other end and positioned on the opening holes to record the voices. Measured acoustic data was amplified by the preamplifier, transferred to an oscilloscope for display and recording.

Two different types of pipes (PVC and Iron Casting) were used to apply the system. Images of both applications are shown in Figure 14. In the experiment where the PVC material was used, the end cap cover could not withstand the pressure and jumped 15 meters away from the pipe. Experiments to prevent this situation did not give any results, and the experiments with PVC pipe were terminated. The experiment was carried out successfully by using the iron casting material type (Figure 14b). The sound data in the pipe were recorded for different hole sizes and pressure intensities using the RESON hydrophone. Tektronix MSO-3014 digital oscilloscope was used to record the hydrophone data. In order to measure the water pressure in the metal pipe, a

manometer, which can measure up to 10 bar, was installed. Figure 15 shows the working environment in which the prepared sound system was tested. On the left, there is a sound recording device with an oscilloscope and preamplifiers.

The centre image shows the pool and the Iron Casting sound system used for water extraction and evacuation. When the metal pipe's water pressure increased to 4.8 bar, the water was discharged from the pipe via the outlet valve.

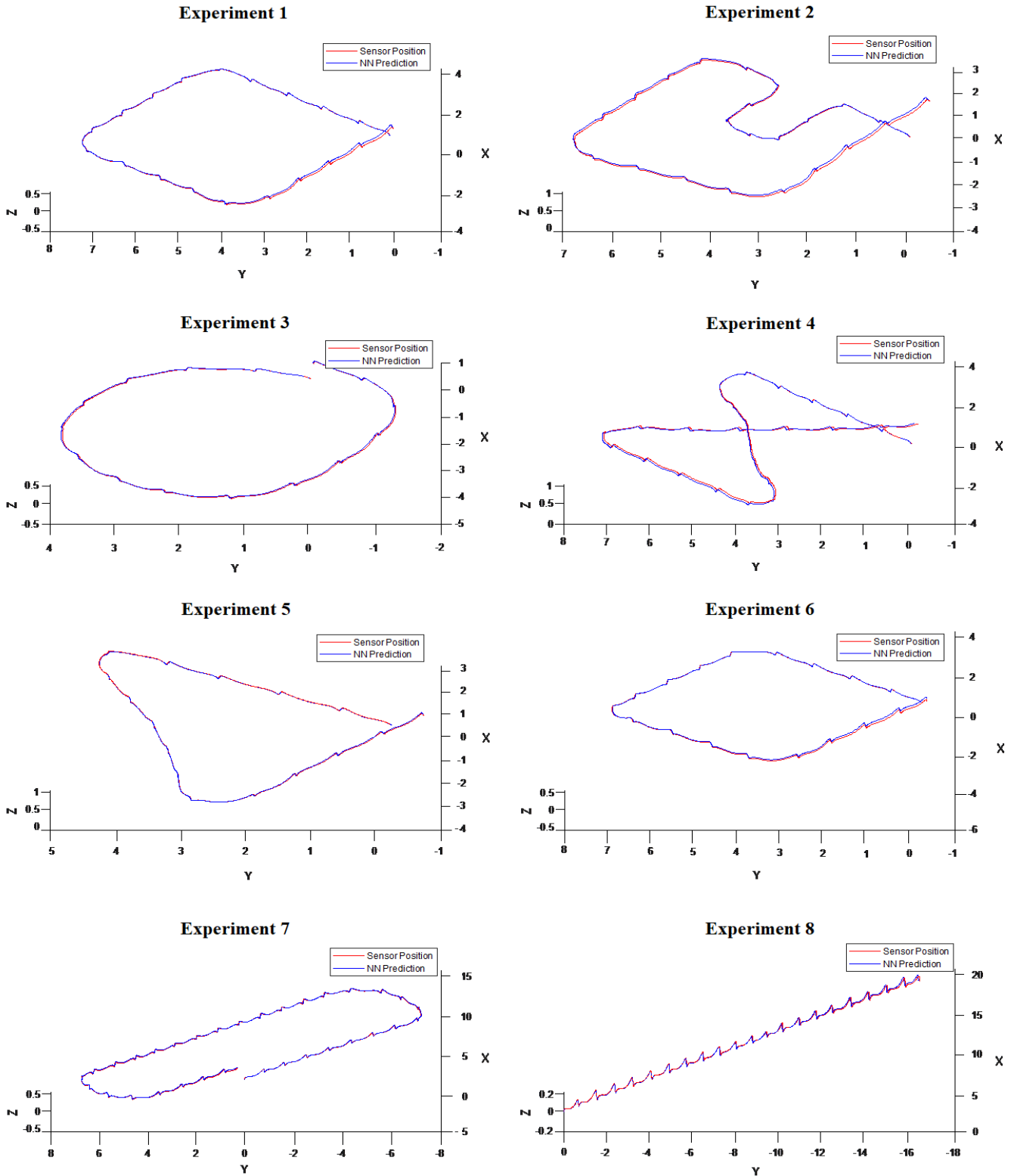


Figure 10 Estimation of navigation scenario locations by classical (red) and artificial learning method (blue).

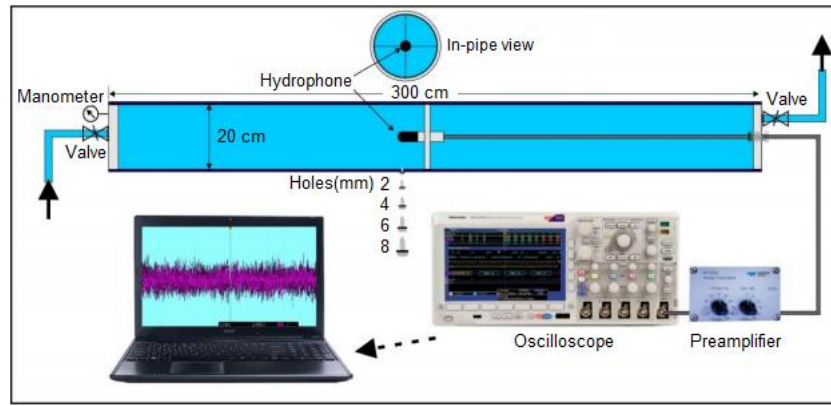


Figure 11 Sound calibration hardware.



Figure 12 Sound mechanisms (a) PVC pipe assembly (b) Iron Cast pipe assembly (c) Manometer.

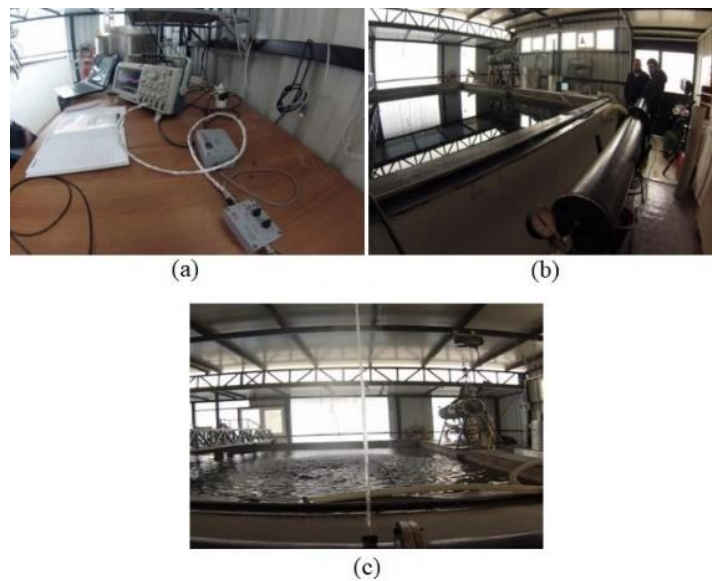


Figure 13 Experimental working environment (a) Sound recording device (b) Pool and perforated pipe (c) water jetting at 4.8bar pressure.

### 3.2. Measurements with Sound System

In experimental studies, the preamplifier's gain was set at 26dB, the value of the high-pass filter was set to 0.1Hz, and then measurements were performed. Each measurement was recorded numerically via the oscilloscope. The spectra in the frequency range of 0.1Hz-100kHz were visualized to see the frequency range of the sound characteristic from the crack. In order to understand the noise characteristic of the system, after the holes were closed, a pressure of 0-5bar was created in the pipe and measurements were completed (see Figure 16). Figure 17 illustrates how hole sizes and pressure intensity affect frequency and amplitude.

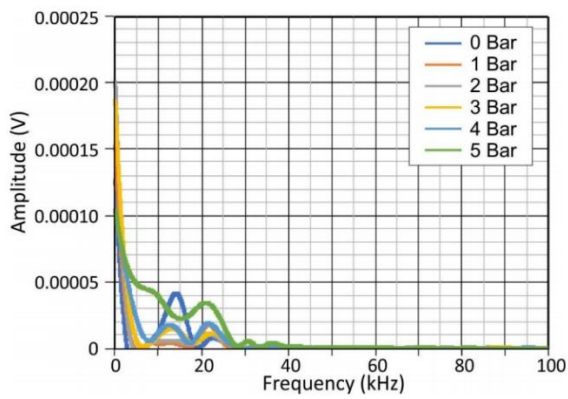


Figure 14 The noise characteristics of the system.

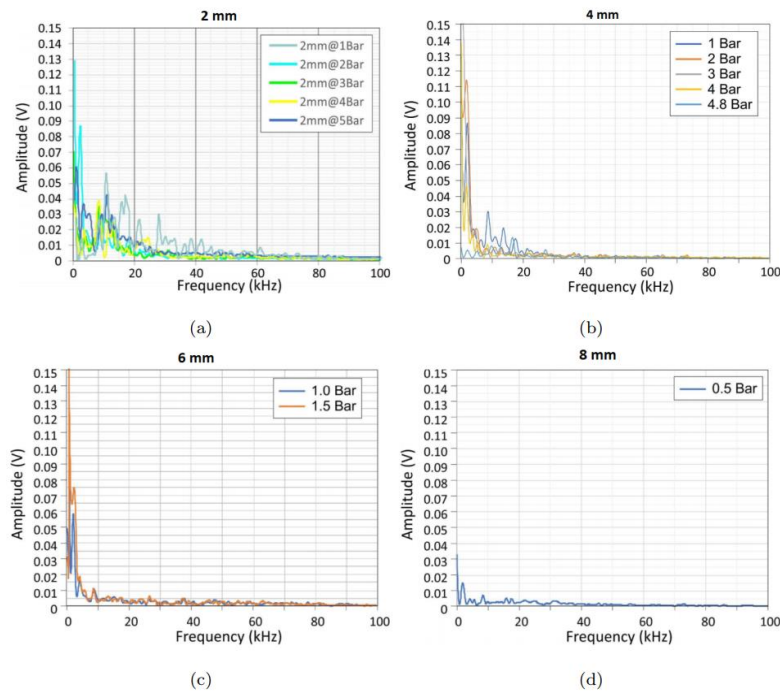


Figure 15 Effect of pressure magnitude on different hole sizes:(a)2mm; (b)4mm; (c)6mm; (d)8mm.

The following results were found after the graphs were evaluated:

- The cracked audio signal frequency was found in the 0.1Hz-40kHz band range.
- The cracked sound signal amplitude was found to be a maximum of 0.15V.
- The noise level of the system was found to be 0.0002V.
- It was seen that the oscillations were not reduced regularly as a result of the increase in pressure from 1Bar to 5Bar. This finding clearly shows that the system does not have a linear characteristic.
- It was seen that while the hole diameter increases, the acoustic signals are directed towards the low frequencies.
- It is foreseen that the same parameters can be used in the system to be designed because of the acceptable results obtained from the 26dB gain preamplifier and 0.1Hz high pass filter used during the measurements.

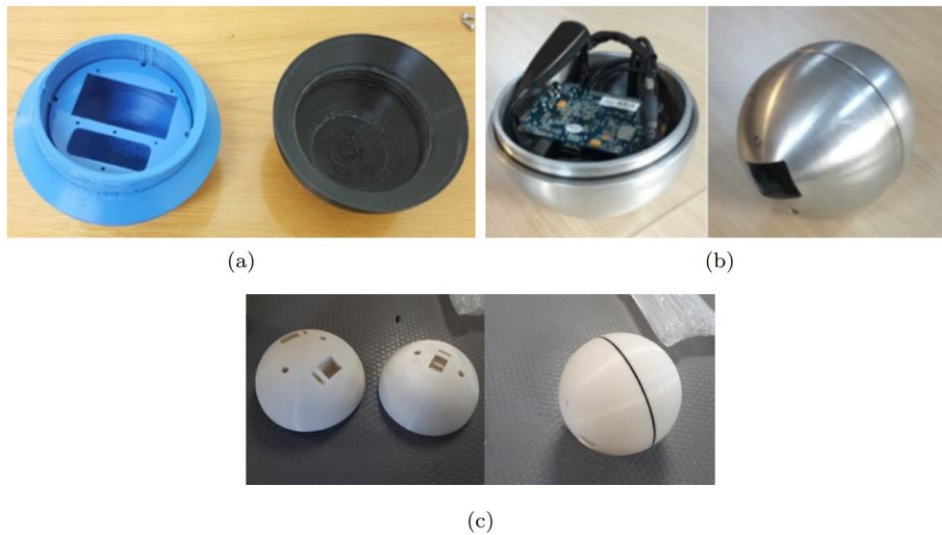


Figure 16 External sphere prototypes;(a) IMU only recording (b) IMU+single hydrophone recording, not circular;(c) IMU+three hydrophone recording, circular

#### 4. EXTERNAL SPHERE HOUSING STUDIES

In this study, the external sphere prototyping to maintain the electronic recording device (minicomputer, IMU, hydrophone, battery) was used and enabled independent data recording. Three different external sphere prototypes were produced. The first prototype was used to register IMU sensor data in walking scenarios (see Figure 18a). This prototype was only used on the ground because of having a water-permeable structure. A second external sphere design was needed to make the work on a basis similar to the water-filled pipes. Figure 18b shows the outer sphere prototype using metal material. However, the prototype's weight and the lack of a round geometry prevented the sphere from moving at the desired speed in the pipeline. In addition, the use of a single hydrophone for voice recording prevents the recording of sound equally in all directions. A third external sphere design was needed to overcome these problems (see Figure 18c). Because the last outer sphere is not metal, it is lighter and circular. There are three different hydrophone sensor locations on the sphere, allowing equal recording of the sound frequencies

in all directions. In addition, this sphere has a waterproof structure.

#### 5. CONCLUSION

In conclusion, a leak detection robot ball was designed to prevent water loss in distribution networks. Precise location estimation, sound frequency range discovery and external sphere studies of the ball was performed. In addition to classical studies, the artificial learning architecture was presented in the precise position estimation studies. The methods were compared using data from eight different motion scenarios. According to this, the proposed method performs online and have a 99% similar position estimation with the classical approach. Apart from classical pattern recognition and curve-fitting architectures, time-based NN architecture was applied. In the sound wave calibration step, two experimental setups, plastic and metal, were prepared. It was examined how different hole sizes (2mm-8mm) and different pressure intensity (0bar-5bar) change the sound of the crack using plastic and metal setups. Finally, a waterproof, external sphere design that uses three different hydrophones was produced.

### ***Funding***

This study was supported by The Scientific and Technological Research Council of Turkey (TUBITAK), Project Title: "Su Borularındaki Sızıntının Tespiti İçin Orta-Ölçekli Kapsül Robot Prototipinin Üretilmesi"; Project Number: 215E075.

### ***The Declaration of Conflict of Interest/ Common Interest***

No conflict of interest or common interest has been declared by the author.

### ***The Declaration of Ethics Committee Approval***

This study does not require ethics committee permission or any special permission.

### ***The Declaration of Research and Publication Ethics***

The author of the paper declare that they comply with the scientific, ethical and quotation rules of SAUJS in all processes of the paper and that they do not make any falsification on the data collected. In addition, they declare that Sakarya University Journal of Science and its editorial board have no responsibility for any ethical violations that may be encountered, and that this study has not been evaluated in any academic publication environment other than Sakarya University Journal of Science.

### ***Authors' Contribution***

The authors contributed equally to the study.

## **REFERENCES**

- [1] R. McKenzie and C. Seago, "Assessment of real losses in potable water distribution systems: Some recent developments," in *Water Science and Technology: Water Supply*, 2005, vol. 5, no. 1, pp. 33–40.
- [2] P. Marin, B. Kingdom, and R. Liemberger, "The challenge of reducing non-revenue water (NRW) in developing countries - how the private sector can help : a look at performance-based service contracting," Dec. 2006.
- [3] S. M. Hooda, "Rajasthan Water Assessment: Potential for Private Sector Interventions," New Delhi, © World Bank, 2017.
- [4] "Infrastructure Report Card 2017." [Online]. Available: <https://www.infrastructurereportcard.org/wp-content/uploads/2017/01/Drinking-Water-Final.pdf>. [Accessed: 20-May-2021].
- [5] N. Pizzi and W. Lauer, *Water distribution operator training handbook - Fourth Edition*, 3rd ed. American Water Works Association, 2013.
- [6] D. Misiunas, "Failure monitoring and asset condition assessment in water supply systems," Sweden, 2005.
- [7] O. Hunaidi, A. Wang, M. Bracken, T. Gambino, and C. Fricke, "Acoustic methods for locating leaks in municipal water pipe networks," 2004, pp. 1–14.
- [8] A.W.W.A., *Water Audits and Loss Control Programs(M36): AWWA Manual of Practice*, 4 edition. Denver: American Waterworks Association, 2016.
- [9] S. H. Zyoud, L. G. Kaufmann, H. Shaheen, S. Samhan, and D. Fuchs-Hanusch, "A framework for water loss management in developing countries under fuzzy environment: Integration of Fuzzy AHP with Fuzzy TOPSIS," *Expert Syst. Appl.*, vol. 61, pp. 86–105, Nov. 2016.
- [10] S. Eggimann *et al.*, "The Potential of Knowing More: A Review of Data-Driven Urban Water Management," *Environmental Science and Technology*, vol. 51, no. 5. American Chemical Society, pp. 2538–2553, 07-Mar-2017.
- [11] A. Gupta and K. D. Kulat, "A Selective Literature Review on Leak Management

- Techniques for Water Distribution System,” *Water Resources Management*, vol. 32, no. 10. Springer Netherlands, pp. 3247–3269, 01-Aug-2018.
- [12] M. FIRAT, S. YILMAZ, and C. ORHAN, “Su kayıp yönetimi için temel hesaplama araçlarının geliştirilmesi ve temel su kayıp bileşenlerinin analizi,” *Gümüşhane Üniversitesi Fen Bilim. Enstitüsü Derg.*, vol. 11, no. 2, pp. 405–416, Feb. 2021.
- [13] M. Eugene, “Predictive Leakage Estimation using the Cumulative Minimum Night Flow Approach,” *Am. J. Water Resour.*, vol. 5, no. 1, pp. 1–4, Jan. 2017.
- [14] E. Farah and I. Shahrour, “Leakage Detection Using Smart Water System: Combination of Water Balance and Automated Minimum Night Flow,” *Water Resour. Manag.*, vol. 31, no. 15, pp. 4821–4833, Dec. 2017.
- [15] E. Roshani and Y. Fillion, “WDS leakage management through pressure control and pipes rehabilitation using an optimization approach,” in *Procedia Engineering*, 2014, vol. 89, pp. 21–28.
- [16] N. Fontana, M. Giugni, L. Glielmo, G. Marini, and R. Zollo, “Real-Time Control of Pressure for Leakage Reduction in Water Distribution Network: Field Experiments,” *J. Water Resour. Plan. Manag.*, vol. 144, no. 3, p. 04017096, Mar. 2018.
- [17] Y. Kleiner, B. J. Adams, and J. S. Rogers, “Water distribution network renewal planning,” vol. 15, no. 1, pp. 15–26, Jan. 2001.
- [18] E. Mann and J. Frey, “Optimized pipe renewal programs ensure cost-effective asset management,” in *Pipelines 2011: A Sound Conduit for Sharing Solutions - Proceedings of the Pipelines 2011 Conference*, 2011, pp. 44–54.
- [19] I. Moslehi and M. Jalili\_Ghazizadeh, “Pressure-Pipe Breaks Relationship in Water Distribution Networks: A Statistical Analysis,” *Water Resour. Manag.*, vol. 34, no. 9, pp. 2851–2868, Jul. 2020.
- [20] A. E. Akkaya and M. F. Talu, “Extended kalman filter based IMU sensor fusion application for leakage position detection in water pipelines,” *J. Fac. Eng. Archit. Gazi Univ.*, vol. 32, no. 4, 2017.
- [21] C. Uyanik, E. Erdemir, E. Kaplanoglu, and A. Sekmen, “A deep learning approach for motion segment estimation for pipe leak detection robot,” in *Procedia Computer Science*, 2019, vol. 158, pp. 37–44.
- [22] S. Kazeminasab, V. Janfaza, M. Razavi, and M. K. Banks, “Smart Navigation for an In-pipe Robot Through Multi-phase Motion Control and Particle Filtering Method,” *CoRR*, vol. abs/2102.1, Feb. 2021.
- [23] S. Kazeminasab, R. Jafari, and M. Katherine Banks, “An LQR-assisted Control Algorithm for an Under-actuated In-pipe Robot in Water Distribution Systems,” in *Proceedings of the 36th Annual ACM Symposium on Applied Computing*, 2021.
- [24] W. Elmenreich, “Sensor Fusion in Time-Triggered Systems,” Austria, 2002.
- [25] C. Li, C. Yang, J. Wan, A. S. Annamalai, and A. Cangelosi, “Teleoperation control of Baxter robot using Kalman filter-based sensor fusion,” *Syst. Sci. Control Eng.*, vol. 5, no. 1, pp. 156–167, Jan. 2017.
- [26] T. Zhang and Y. Liao, “Attitude measure system based on extended Kalman filter for multi-rotors,” *Comput. Electron. Agric.*, vol. 134, pp. 19–26, Mar. 2017.
- [27] Y. Liu, S. Gong, and Y. Lu, “Estimation of inertial/magnetic sensor orientation for human-motion-capture system,” 2017, pp. 175–179.

- [28] S. Qiu, Z. Wang, H. Zhao, K. Qin, Z. Li, and H. Hu, "Inertial/magnetic sensors based pedestrian dead reckoning by means of multi-sensor fusion," *Inf. Fusion*, vol. 39, pp. 108–119, Jan. 2018.
- [29] R. Kalman, "A New Approach to Linear Filtering and Prediction Problems," *Trans. ASME – J. Basic Eng.*, no. 82 (Series D), pp. 35–45, 1960.
- [30] M. S. Grewal and A. P. Andrews, *Kalman Filtering: Theory and Practice Using MATLAB*, 3rd editio. Wiley-IEEE, 2008.
- [31] G. Bishop and G. Welch, "An Introduction to the Kalman Filter." University of North Carolina SIGGRAPH 2001 course notes. ACM Inc., North Carolina, 2001.
- [32] S. O. H. Madgwick, A. J. L. Harrison, and R. Vaidyanathan, "Estimation of IMU and MARG orientation using a gradient descent algorithm," 2011, pp. 1–7.
- [33] N. Trawny and S. I. Roumeliotis, "Indirect Kalman Filter for 3D Attitude Estimation A Tutorial for Quaternion Algebra Multiple Autonomous Robotic Systems Laboratory, Technical report," Mar. 2005.
- [34] W. H. K. de Vries, H. E. J. Veeger, C. T. M. Baten, and F. C. T. van der Helm, "Magnetic distortion in motion labs, implications for validating inertial magnetic sensors," *Gait Posture*, vol. 29, no. 4, pp. 535–541, Jun. 2009.
- [35] C. Wang, X. Qu, X. Zhang, W. Zhu, and G. Fang, "A Fast Calibration Method for Magnetometer Array and the Application of Ferromagnetic Target Localization," *IEEE Trans. Instrum. Meas.*, vol. 66, no. 7, pp. 1743–1750, Jul. 2017.
- [36] A. M. Sabatini, "Quaternion-based extended Kalman filter for determining orientation by inertial and magnetic sensing," *IEEE Trans. Biomed. Eng.*, vol. 53, no. 7, pp. 1346–1356, Jul. 2006.
- [37] Ruoyu Zhi, "A Drift Eliminated Attitude & Position Estimation Algorithm In 3D," The University of Vermont, 2016.



SAKARYA ÜNİVERSİTESİ

# FEN BİLİMLERİ ENSTİTÜSÜ DERGİSİ

Sakarya University Journal of Science  
SAUJS

e-ISSN: 2147-835X | Founded: 1997 | Period: Bimonthly | Publisher: Sakarya University |  
<http://www.saujs.sakarya.edu.tr/en/>

Title: Production and Purification of Peroxidase from Tissue Cultures of Cauliflower  
(*Brassica oleracea* L. var. *Botrytis*)

Authors: Züleyha ALMAZ, Şeyma ÖNLÜ, Aykut ÖZTEKİN

Received: 2020-12-21 00:00:00

Accepted: 2021-08-02 00:00:00

Article Type: Research Article

Volume: 25

Issue: 5

Month: October

Year: 2021

Pages: 1121-1128

How to cite

Züleyha ALMAZ, Şeyma ÖNLÜ, Aykut ÖZTEKİN; (2021), Production and Purification of Peroxidase from Tissue Cultures of Cauliflower (*Brassica oleracea* L. var. *Botrytis*). Sakarya University Journal of Science, 25(5), 1121-1128, DOI: <https://doi.org/10.16984/saufenbilder.844705>

Access link

<http://www.saujs.sakarya.edu.tr/tr/pub/issue/65589/844705>

New submission to SAUJS

<http://dergipark.org.tr/en/journal/1115/submission/step/manuscript/new>

## Production and Purification of Peroxidase from Tissue Cultures of Cauliflower (*Brassica oleracea* L. var. Botrytis)

Züleyha ALMAZ\*<sup>1</sup>, Şeyma ÖNLÜ<sup>1</sup>, Aykut ÖZTEKİN<sup>1</sup>

### Abstract

The plant peroxidases are remarkable enzymes due to their widespread use in industry. These enzymes, which are capable of catalysing the oxidation of various organic and inorganic substrates, have been used in clinical diagnosis, detoxification reactions and organic synthesis. In this study, in vitro production and purification of peroxidase enzyme from cauliflower plant was proposed. Firstly, sterile seedlings were obtained from MS/B5 nutrient medium without growth regulator from cauliflower seeds and calluses from medium containing 0.5 mg / L 2,4-D. Callus and seedlings were powdered with liquid nitrogen and then homogenized. Peroxidase enzymes were purified from these homogenates using affinity technique. SDS-PAGE electrophoresis was performed to determine the molecular weight of the purified enzymes and single bands was observed at approximately 46 kDa. In addition,  $K_M$  and  $V_{max}$  values of the callus peroxidase enzyme were determined for guaiacol, pyrogallol and  $H_2O_2$  substrates.

**Keywords:** Cauliflower (*brassica oleracea* l. var. botrytis), plant tissue culture, peroxidase purification.

### 1. INTRODUCTION

Enzymes are stable and specific biocatalysts for the processes in which they are used. Enzymes can be used as environmentally sensitive biotechnological approaches in various industrial processes. For this reason, the identification of enzymes and their sources that can be used in industry is of economic and environmental importance [1].

Peroxidases (E.C. 1.11.1.7) are mostly heme-group proteins containing protoporphyrin IX, and their molecular weight ranges from 30 kDa to 150 kDa [2]. It was found that peroxidases play an important role in cell wall formation, auxin

metabolism, lignification, removal of reactive oxygen species, fruit ripening and plant defence system [3].

Peroxidases are one of the major enzyme groups used in industrial production and applications. Peroxidases can oxidize many phenolic or non-phenolic substrates, so peroxidase enzymes are frequently used in oxidation reduction based biosensors [4], analytical and diagnostic kits [5, 6], degradation of phenolic compounds [7, 8], organic polymerization reactions [9], paper industry [1] and removal of industrial dyes [10]. In addition, peroxidase applications have been proposed in the medical, chemical and food industries [11]. Some of them relates to the

\* Corresponding author: z.turkoglu@alparslan.edu.tr

<sup>1</sup> Muş Alparslan University, Molecular Biology and Genetic.

E-Mail: s.sofuoglu@alparslan.edu.tr, aoztekin@agri.edu.tr

ORCID: <https://orcid.org/0000-0002-4532-4311>, <https://orcid.org/0000-0003-2005-1019>, <https://orcid.org/0000-0003-1418-179X>

quality and flavour of vegetative products in raw and processed foods [12].

Peroxidases are an important part of the world enzyme market. Therefore, they must be produced in large quantities. There are some difficulties in obtaining these enzymes from natural sources. For example, due to the unfavourable weather conditions, the yield is low and the process of growing the plant is long. In order to overcome all these difficulties, plants grown in vitro provides a great advantage to produce significant compounds and molecules [13]. It was aimed to produce peroxidase enzyme continuously by forming in vitro plant cell cultures [14]. The idea that different plant cells can produce more than the peroxidase produced by the roots; such as hairy root of horseradish [15, 16] and *Brassica napus* [17], callus and cell suspension culture of *Raphanus sativus* [18], is becoming more and more common.

In our previous study, peroxidase enzyme (POD) from radish species was successfully purified using Sepharose 4B-L-Tyrosine-4-amino 3-bromo benzohydrazide affinity chromatography [19]. In this study, peroxidase enzymes from cauliflower seedlings (S-POD) and calluses (C-POD) grown with tissue culture method were purified in a single step by Sepharose 4B-L-Tyrosine-4-amino 3-bromo benzohydrazide affinity gel. The purity of enzymes was controlled with sodium dodecyl sulfate polyacrylamide gel electrophoresis (SDS-PAGE). In addition,  $K_M$  and  $V_{max}$  values of the C-POD were determined for guaiacol, pyrogallol and  $H_2O_2$  substrates.

## 2. MATERIALS AND METHODS

### 2.1. Sterilization and Germination

Seeds of *Brassica oleracea* var. botrytis were surface sterilized 70 % EtOH for 1 min, then 20 % NaClO for 20 min, washed 3 times with sterile water. Germination medium was contained MS medium supplemented with B5 vitamins without plant growth regulators and pH of medium was adjusted 5.8 before autoclaving. Seed were germinated at  $24 \pm 2$  °C using a 16/8 photoperiod with a light intensity of  $50 \mu\text{mol m}^{-2} \text{s}^{-1}$  [16].

### 2.2. Callus Formation

After 15 days, sterile seedlings were obtained from seeds. The effect of growth regulators was tested using 2.4-D in different concentration (0.5, 1, 2, 3 mg/L) and axillary buds were used as explant from sterile seedlings. The best callus formation was obtained in 0.5 mg/L 2.4-D [18].

### 2.3. Chemicals

CNBr-Sepharose 4B, L-tyrosine and  $H_2O_2$  were obtained from Sigma–Aldrich Co. Methyl 4-amino-3-bromobenzoate from Alfa-Aesar and standard proteins from Thermo Scientific (26616) were purchased. If not explicitly mentioned, all other chemicals used for affinity gel synthesis, purification steps and kinetic determinations are analytical grade.

### 2.4. Synthesis of Sepharose 4B-based affinity gel

Methyl 4-amino 3-bromo benzoate was purchased and synthesized to benzohydrazide as our previous study described [19]. 1.5 g of CNBr-Sepharose-4B reacted with 30 mg of L-tyrosine to form Sepharose 4B-L-tyrosine. 15 mg of 4-amino-3-bromo benzohydrazide was diazotized and then coupled to the synthesized Sepharose 4B-L-tyrosine. The synthesized affinity gel was formed in three parts; Sepharose-4B (matrix), L-Tyrosine (spacer arm) and 4-amino 3-bromo benzohydrazide (ligand).

### 2.5. Activity Assay

Peroxidase activity at each step of purification was determined by monitoring the absorbance increase at 470 nm by coloured compounds formed by oxidation of guaiacol chromogenic substrate in the presence of  $H_2O_2$ . The reaction medium was formed from 15 mM guaiacol, 7.5 mM  $H_2O_2$ , 30 mM phosphate buffer (pH 6.0) and 10  $\mu\text{L}$  enzyme. Activity was defined as the amount of enzyme catalysing the one  $\mu\text{mol}$  coloured substance per minute. In kinetic studies with pyrogallol substrate, the method proposed by Bach was used [20].

## 2.6. Purification of Cauliflower S-POD and C-POD

Seedlings were separated from the stem and cut into small pieces. 5 g of these fractions and calluses were crushed in liquid nitrogen and dissolved in 20 ml of 0.3 M phosphate buffer (pH 7.0). Complete homogenization was achieved with ultraturax. It was then centrifuged at 15,000g at 4 °C for 20 minutes and pellet discarded. Supernatants were loaded onto the affinity columns (1\*10 cm) equilibrated with 10 mM phosphate buffer (pH 6.8). The excess substance was washed with 25 mM phosphate buffer and the peroxidase enzyme was eluted with 1 M NaCl / phosphate buffer. Protein amounts were measured by Bradford method at each step of purification [21].

## 2.7. SDS-PAGE

SDS-PAGE was performed under denaturing conditions to determine the molecular weight and purity of the purified Cauliflower S-POD and C-POD enzymes. Firstly, samples were loaded to stacking gel (3%) and electric current was applied until the line migrated to 0.5 cm from the bottom of the separation gel (10%) [22]. Then, protein bands were stained with Coomassie dye (R-250). Finally, excess dye was eluted with appropriate solvent and bands were made visible [23].

## 2.8. Determination of $K_M$ and $V_{max}$ values

The  $V_{max}$  and  $K_M$  values of the purified Cauliflower C-POD were calculated from the Lineweaver-Burk plots for the guaiacol and pyrogallol and  $H_2O_2$  substrates. Peroxidase activity was measured using 0.1 EU/mL enzyme solution at five different concentrations ranging from 1.8 mM to 32 mM for guaiacol and 0.5 mM to 10 mM for pyrogallol at 470 nm, during which  $H_2O_2$  concentration was kept saturated at 7.5 mM. In order to determine the affinity of C-POD enzyme to  $H_2O_2$ , activity measurements were made at varied  $H_2O_2$  concentration from 0.5 mM to 7.5 mM by keeping guaiacol concentration at 15 mM [24].

## 2.9. Optimum Parameters and Solvent Stability

For the estimation of optimum parameters and some solvents effected the C-POD activity, enzyme was assayed in varying pHs (4.5 to 9.0), different temperatures (10 to 80 °C) and activity was monitored in varied concentrations of methanol, ethanol and DMSO from 0.1 % to 10 % to investigate the enzyme's solvent stability. At the end of the reactions, all activity values were calculated as relative activity and highest was assigned as 100%.

## 3. RESULTS AND DISCUSSION

### 3.1. Purification of Peroxidase Enzymes

One of the important steps in the production of peroxidase is to use techniques such as callus, cell suspension and hairy root cultures which can be produced in a short time under sterile conditions instead of waiting for the product to grow in the field for a year.

As can be seen in detail in Table 1, using the Sepharose 4B-L-Tyrosine-4-amino 3-bromo affinity gel C-POD and S-POD were isolated from the seedlings and calluses of cauliflower with a yield of approximately 30-35% first time. In recent studies, peroxidases were purified using affinity chromatography, purification factors were founded as 665-fold with a yield of 55%, 613- fold with a yield of 34% for turnip and black radish respectively [19]. Using hydrophobic interaction chromatography, horseradish peroxidase was purified with a yield of 71.3% and a factor of 291 [25]. Using three steps, cauliflower peroxidase was purified as a value of 19.3-fold with a yield of 0.2%. The molecular weight of this enzyme was found to be 44 kDa by gel filtration chromatography method [26]. In our study, it is seen that Cauliflower seedlings and calluses have more enzymes than native cauliflower and tissue culture is advantageous in the production of peroxidase.

POD produced by Red beet (*Beta vulgaris* L.) hairy root was purified with 15-fold in a cell culture study and also the purified POD had a

molecular mass of 45 kDa as predicted by SDS-PAGE in the same research [27]. *Agrobacterium rhizogenes* transformed *Armoracia rusticana* L. tissue cultures of transformed roots were found to have 20 times higher activity than native horseradish plant [16]. In another study, peroxidase activity was found to be high in cell-free medium in cell suspension cultures of

*Raphanus sativus*. In addition, it has been reported that *Raphanus sativus* cell suspension cultures can produce peroxidase production as an alternative to horseradish roots [18]. It is supported by studies carried out in different plant groups where peroxidase can be produced and purified in different cultures in biotechnologically.

Table 1 Purification results of S-POD and C-POD from cauliflower seedling and callus by affinity chromatography

Source	STEP	T.V. <sup>a</sup> (mL)	Activity (EU/mL)	Protein (mg/mL)	T.A. <sup>b</sup> (EU)	T.P. <sup>c</sup> (mg)	S.A. <sup>d</sup> (EU/mg)	Yield (%)	Fold
Seedling	I	6	20.3	1.19	121.8	7.14	17.06	100	1
	II	1.5	23.8	0.0011	35.7	0.0017	21000	29.3	1230
Callus	I	6	30.6	1.57	183.6	9.42	19.5	100	1
	II	3	21.5	0.0015	64.5	0.0045	14300	35.1	734

Total volume<sup>a</sup>, Total activity<sup>b</sup>, Total protein<sup>c</sup>, Specific activity<sup>d</sup> Step I: Homogenate Step II: Purification with affinity chromatography

Cauliflower peroxidase, which is considered as an alternative to horseradish peroxidase, was rapidly propagated by tissue culture methods and this enzyme was purified from the obtained seedlings and calluses. According to this, 30% production of seedlings and 35% (Table 1.) production of calluses occurred. This study is one of the new-first studies that will be an example of peroxidase enzyme purified from seedling and callus growing by tissue culture methods in cauliflower plant.

### 3.2. SDS-PAGE

SDS-PAGE was performed to determine the purity and molecular weight of C-POD and S-POD enzymes isolated from cauliflower. The molecular weight (Mw) of these enzymes were found to be single bands at 46 kDa as shown in Figure 1.

Koksal and Gülçin determined the molecular weight of the purified POD enzyme from cauliflower to be 44 kDa [26]. Similarly, the molecular weight of the POD enzyme produced by the hairy root of beet (*Beta vulgaris* L.) was found to be 45 kDa by SDS-PAGE [27]. The fact that these values are consistent with the data in the literature is an indication of the successful purification of enzymes.

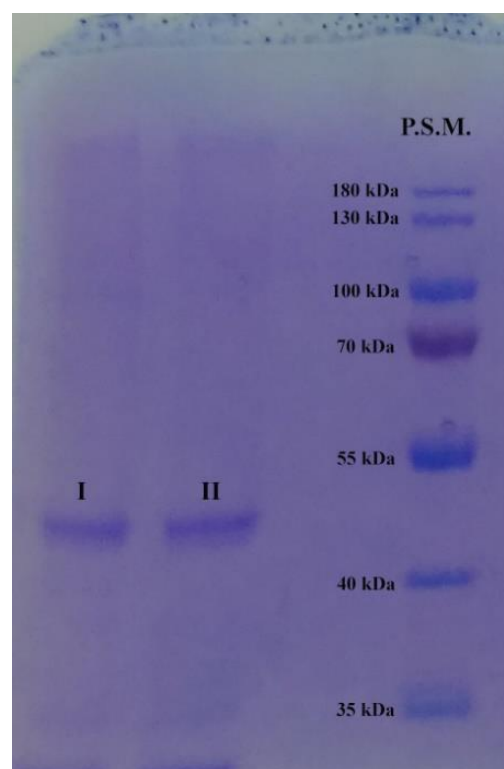


Figure 1 SDS-PAGE image of purified S-POD and C-POD enzyme. \*P.S.M.: Prestained protein markers, \*I: S-POD, \*II: C-POD

### 3.3. Determination of $K_M$ and $V_{max}$ values

Determining the kinetic parameters of the purified peroxidase enzyme in the presence of different substrates is one of the important data that should be obtained. These data help to determine the physiological role of the enzyme and whether it

can be used in vitro applications. For this reason, activity-concentration graphs were plotted for guaiacol, pyrogallol and  $H_2O_2$  substrates. Activity-concentration graphs were shown in Figure 2.  $K_M$ - $V_{max}$  values were calculated from these graphs for C-POD enzyme as 9.34 mM and 0.36 EU/mL.min, 1.8 mM and 0.3 EU/mL.min, 0.98 mM and 0.19 EU/mL.min respectively.

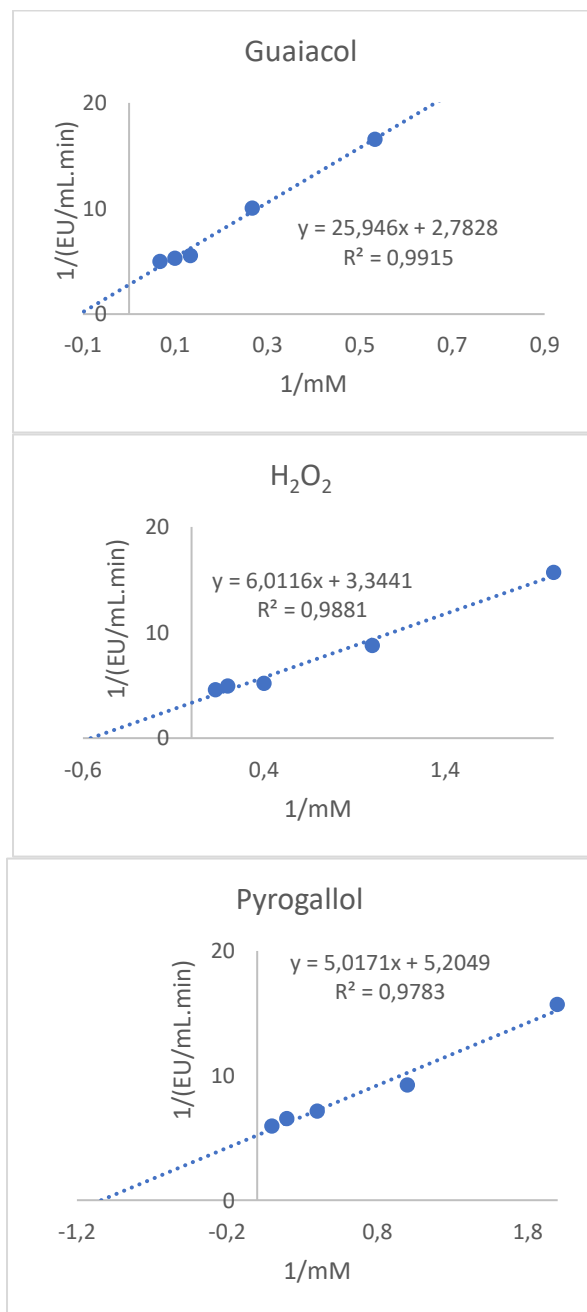


Figure 2 Activity-concentration graph plotted at five different guaiacol,  $H_2O_2$  and pyrogallol concentrations

In a study with native cauliflower peroxidase  $K_M$  affinity of POD for guaiacol and pyrogallol were determined as 141.64 mM and 1.1 mM respectively. [26]. In another study,  $K_M$  affinity and  $V_{max}$  values of *Beta vulgaris* L peroxidase for guaiacol were 98.61 mM and 0.107 EU/mL min, for orthodanisidine were 2.134 mM and 0.977 EU/mL min., for ABTS were 5.050 mM and 0.110 EU/mL, for  $H_2O_2$  were 0.113 mM and 1.389 EU/mL min [27].

When comparing the data in the literature and the data we obtained in our study, the substrate specificities of the peroxidase enzymes purified from different sources or from different regions of the same sources vary. Therefore, especially  $K_M$  value is an important indicator in determining whether the enzyme can be used in applications.

#### 3.4. Temperature, pH and Solvent Effects on Activity

The effects of temperature, pH and solvents on catalyst capacity of the enzyme were plotted as activity graphs (Figure 3). In obtained results, the maximum catalysing capacity of C-POD was observed at 60°C and pH 5.5. Moreover, the relative activity was recorded at 82%, 69% and 45% in the presence of %10 (w/w) methanol, ethanol and DMSO, respectively. It can be concluded that it is a great advantage that the C-POD enzyme obtained for the catalysis of reactions containing water-insoluble organic substrates is not affected much by the presence of these solvents (especially alcohols), which are frequently used in industrial processes.

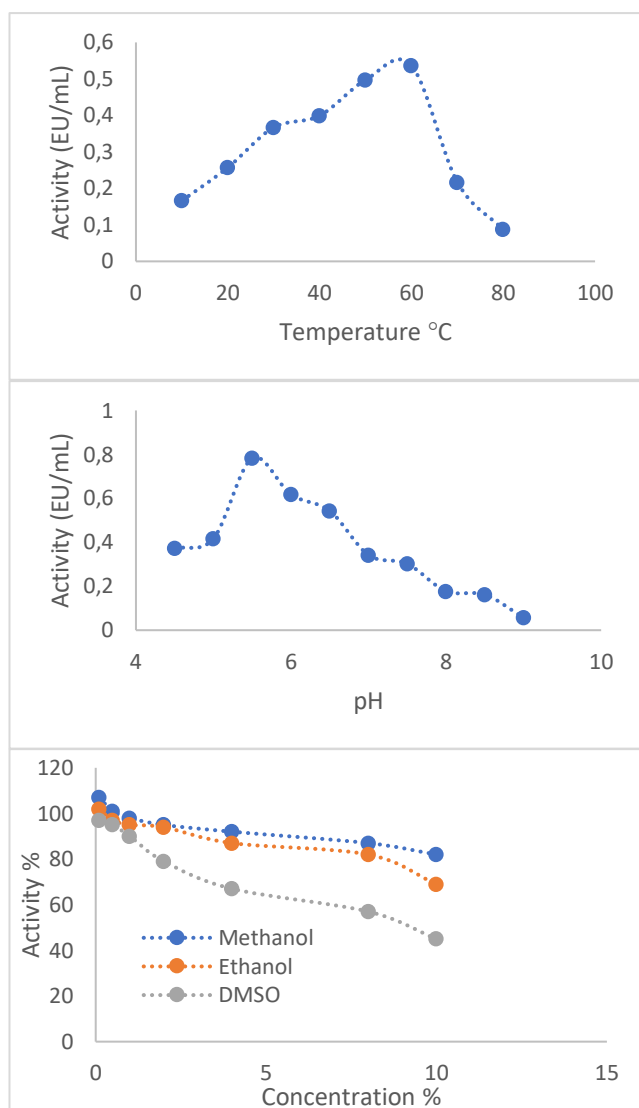


Figure 3 Activity graph plotted temperature, pH and solvents on catalyst capacity

#### 4. CONCLUSION

Peroxidases are important commercial enzymes. Therefore, there is a need to produce and purify peroxidases which can respond to different needs and are resistant to factors such as temperature, pH, salts, metals and organic solvents in the reaction medium. In this study, peroxidase enzymes were obtained from cauliflower seedlings and calluses for the first time. In addition, molecular weights of C-POD and S-POD enzymes and affinity of C-POD to  $H_2O_2$ , pyrogallol and guaiacol substrates were determined. Cauliflower plant callus can be easily modified, disease-free and sterile conditions; it is thought that large amounts of commercially

important peroxidase production can be realized by experimenting with different nutrient media and growth regulators.

#### *Funding*

The authors have not received any financial support for the research, authorship or publication of this study.

#### *The Declaration of Conflict of Interest/ Common Interest*

No conflict of interest or common interest has been declared by the authors.

#### *Authors' Contribution*

Under this heading, The authors contributed equally to the study

#### *The Declaration of Ethics Committee Approval*

This study does not require ethics committee permission or any special permission.

#### *The Declaration of Research and Publication Ethics*

The authors of the paper declare that they comply with the scientific, ethical and quotation rules of SAUJS in all processes of the paper and that they do not make any falsification on the data collected. In addition, they declare that Sakarya University Journal of Science and its editorial board have no responsibility for any ethical violations that may be encountered, and that this study has not been evaluated in any academic publication environment other than Sakarya University Journal of Science.

#### REFERENCES

- [1] V. P. Pandey, M. Awasthi, S. Singh, S. Tiwari, and U. N. Dwivedi, "A comprehensive review on function and application of plant peroxidases," *Biochemistry and Analytical Biochemistry*, vol. 6, no. 01, p. 308, 2017.

- [2] C. Regalado, B. E. García-Almendárez, and M. A. Duarte-Vázquez, "Biotechnological applications of peroxidases," *Phytochemistry Reviews*, vol. 3, no. 1-2, pp. 243-256, 2004.
- [3] F. Passardi, C. Cosio, C. Penel, and C. Dunand, "Peroxidases have more functions than a Swiss army knife," *Plant cell reports*, vol. 24, no. 5, pp. 255-265, 2005.
- [4] J. Jia, B. Wang, A. Wu, G. Cheng, Z. Li, and S. Dong, "A method to construct a third-generation horseradish peroxidase biosensor: self-assembling gold nanoparticles to three-dimensional sol-gel network," *Analytical Chemistry*, vol. 74, no. 9, pp. 2217-2223, 2002.
- [5] E. Agostini, J. Hernández-Ruiz, M. B. Arnao, S. R. Milrad, H. A. Tigier, and M. Acosta, "A peroxidase isoenzyme secreted by turnip (*Brassica napus*) hairy-root cultures: inactivation by hydrogen peroxide and application in diagnostic kits," *Biotechnology and applied biochemistry*, vol. 35, no. 1, pp. 1-7, 2002.
- [6] A. Heller and M. S. Vreeke, "Soybean peroxidase electrochemical sensor," ed: Google Patents, 1997.
- [7] A. Bhunia, S. Durani, and P. P. Wangikar, "Horseradish peroxidase catalyzed degradation of industrially important dyes," *Biotechnology and bioengineering*, vol. 72, no. 5, pp. 562-567, 2001.
- [8] K. Tatsumi, S. Wada, and H. Ichikawa, "Removal of chlorophenols from wastewater by immobilized horseradish peroxidase," *Biotechnology and Bioengineering*, vol. 51, no. 1, pp. 126-130, 1996.
- [9] J. Liu, L. Ye, and Y. Weiping, "Copolymerization of lignin with cresol catalysed by peroxidase in reversed micellar systems," *Electronic Journal of Biotechnology*, vol. 2, no. 2, pp. 7-8, 1999.
- [10] M. Chivukula, J. T. Spadaro, and V. Renganathan, "Lignin peroxidase-catalyzed oxidation of sulfonated azo dyes generates novel sulfophenyl hydroperoxides," *Biochemistry*, vol. 34, no. 23, pp. 7765-7772, 1995.
- [11] S.-S. Kwak, S.-K. Kim, I.-H. Park, and J. R. Liu, "Enhancement of peroxidase activity by stress-related chemicals in sweet potato," *Phytochemistry*, vol. 43, no. 3, pp. 565-568, 1996.
- [12] A. Cardinali *et al.*, "Purification and characterization of a cationic peroxidase from artichoke leaves," *Journal of the Science of Food and Agriculture*, vol. 87, no. 7, pp. 1417-1423, 2007.
- [13] G. Fernández and A. B. Pomilio, "Optimized growth conditions and determination of the catalytic type of the peptidase complex from a novel callus culture of pineapple (*Ananas comosus*)," *Mol Med Chem*, vol. 1, pp. 39-49, 2003.
- [14] N. González-Rábade, M. del Carmen Oliver-Salvador, E. Salgado-Manjarrez, and J. A. Badillo-Corona, "In vitro production of plant peroxidases—a review," *Applied biochemistry and biotechnology*, vol. 166, no. 7, pp. 1644-1660, 2012.
- [15] M. Parkinson, T. Cotter, and P. Dix, "Peroxidase production by cell suspension and hairy root cultures of horseradish (*Armoracia rusticana*)," *Plant Science*, vol. 66, no. 2, pp. 271-277, 1990.
- [16] P. Soudek, R. Podlipna, P. Marsik, and T. Vanek, "Optimization of the peroxidase production by tissue cultures of horseradish in vitro," *Biologia plantarum*, vol. 49, no. 4, pp. 487-492, 2005.
- [17] E. Agostini, S. M. de Forchetti, and H. A. Tigier, "Production of peroxidases by hairy roots of *Brassica napus*," *Plant cell, tissue and organ culture*, vol. 47, no. 2, pp. 177-182, 1997.

- [18] R. Vazquez-Duhalt, "Peroxidase activity in calluses and cell suspension cultures of radish *Raphanus sativus* var. Cherry Bell," *Plant cell, tissue and organ culture*, vol. 18, no. 3, pp. 321-327, 1989.
- [19] A. Oztekin *et al.*, "Purification of peroxidase enzyme from radish species in fast and high yield with affinity chromatography technique," *Journal of Chromatography B*, vol. 1114, pp. 86-92, 2019.
- [20] C. E. Bach *et al.*, "Measuring phenol oxidase and peroxidase activities with pyrogallol, L-DOPA, and ABTS: effect of assay conditions and soil type," *Soil Biology and Biochemistry*, vol. 67, pp. 183-191, 2013.
- [21] M. M. Bradford, "A rapid and sensitive method for the quantitation of microgram quantities of protein utilizing the principle of protein-dye binding," *Analytical biochemistry*, vol. 72, no. 1-2, pp. 248-254, 1976.
- [22] U. K. Laemmli, "Cleavage of structural proteins during the assembly of the head of bacteriophage T4," *nature*, vol. 227, no. 5259, p. 680, 1970.
- [23] C. R. Merril, "[36] Gel-staining techniques," in *Methods in enzymology*, vol. 182: Elsevier, 1990, pp. 477-488.
- [24] Y. Hu, J. Wu, P. Luo, and Y. Mo, "Purification and partial characterization of peroxidase from lettuce stems," *African Journal of Biotechnology*, vol. 11, no. 11, pp. 2752-2756, 2012.
- [25] C. B. Lavery *et al.*, "Purification of peroxidase from horseradish (*Armoracia rusticana*) roots," *Journal of agricultural and food chemistry*, vol. 58, no. 15, pp. 8471-8476, 2010.
- [26] E. Koksal and I. Gulcin, "Purification and characterization of peroxidase from cauliflower (*Brassica oleracea* L. var. botrytis) buds," *Protein and Peptide Letters*, vol. 15, no. 4, pp. 320-326, 2008.
- [27] T. Rudrappa, V. Lakshmanan, R. Kaunain, N. M. Singara, and B. Neelwarne, "Purification and characterization of an intracellular peroxidase from genetically transformed roots of red beet (*Beta vulgaris* L.)," *Food chemistry*, vol. 105, no. 3, pp. 1312-1320, 2007.



SAKARYA ÜNİVERSİTESİ

# FEN BİLİMLERİ ENSTİTÜSÜ DERGİSİ

Sakarya University Journal of Science  
SAUJS

e-ISSN: 2147-835X | Founded: 1997 | Period: Bimonthly | Publisher: Sakarya University |  
<http://www.saujs.sakarya.edu.tr/en/>

Title: Impact of Dehumidification Devices on Production Efficiency in Plastic Injection

Authors: M.Tahir OKTAÇ, Mustafa TİMUR, Halil KILIÇ

Received: 2021-02-18 00:00:00

Accepted: 2021-08-05 00:00:00

Article Type: Research Article

Volume: 25

Issue: 5

Month: October

Year: 2021

Pages: 1129-1135

How to cite

M.Tahir OKTAÇ, Mustafa TİMUR, Halil KILIÇ; (2021), Impact of Dehumidification  
Devices on Production Efficiency in Plastic Injection. Sakarya University

Journal of Science, 25(5), 1129-1135, DOI:

<https://doi.org/10.16984/saufenbilder.879543>

Access link

<http://www.saujs.sakarya.edu.tr/tr/pub/issue/65589/879543>

New submission to SAUJS

<http://dergipark.org.tr/en/journal/1115/submission/step/manuscript/new>



injection pressure, mold temperature, coolant temperature and the method of demolding. For the most part, mold cooling is performed by creating cooling grooves into the mold or core with some straight holes on the surface. However, the process is good for the production of the parts with a simple design and flat surface. For complex components with curved surfaces, straight perforated canals are not sufficient to cool the mold homogeneously [4]. As the cooling of the mold is not a uniform process, it causes defects such as distortion, warpage marks and welding lines. These defects reduce the quality of the product. With proper cooling in the molds and prevention of water droplets, the errors that will occur in the final products are reduced, thus increasing the quality of the product [5].

Systematic identification and elimination of losses to reduce operating and production costs are the main factors affecting production efficiency. When the production efficiency matters, internal audit is an important management function. Processes and equipment must be continuously optimized to profitably maintain the production of quality parts and competitiveness in their production. In the plastics sector, where raw materials and material costs are of great importance, the cost of raw materials could go up to 50% of the total cost of the final product. Especially if the raw material is imported, much attention should be given to material efficiency as well as the efficiency of other resources used in the production. When the quality of the resulting product changes, production costs will also change accordingly, and therefore, cost-related changes will also affect productivity changes. Design, cost calculation and manufacturing of plastic injection molds are one of the most important stages in the industry of mass production. The design of plastic injection molds is expensive and complex. The most important parameters affecting the production of plastic injection companies are the selection of machines and molds in the parts to be produced in line with the set criteria. Selection of improper machines has a big impact on the mold, production errors and therefore production-related cost [6]. The temperature of the manufactured product changes during the cooling

process. The design of the cooling system depends on the geometric structure of the injected plastic part. As the plastic melt material injected in the molding is hot, fast and smooth take-up must be ensured. The position of the cooling grooves should be designed in a position that can best transmit heat [7].

Desiccant dehumidification technology is emerging as a technically viable alternative to comfort conditioning in many commercial and institutional areas. Dehumidification systems are gaining popularity due to their ability to remove moisture from outside vent air while allowing traditional air conditioning systems to deal primarily with control temperature [8]. Dehumidification is an approach to space conditioning that offers solutions to many of the current economic, environmental and regulatory issues facing facility managers. Conveniently integrated desiccant dehumidification systems become cost-effective additions such as reduced dehumidification cost, energy savings and more comfortable air availability. In some ambient conditions, it may be necessary to dehumidify rather than cool the outdoor air used for ventilation [9].

Dehumidifiers work on the physical principle that they cool the flowing air below the dew threshold and draw moisture from the air by condensation onto a cold surface. For this reason, they are called refrigerated dehumidifiers. As the ambient air temperature rises, more surfaces are formed on which the moisture condenses again. Humidity does not disappear by simply cooling the air [10]. In the injection production processes in the industry, moist surfaces (water droplets) are formed on the molds with the increase in the ambient temperature. This situation adversely affects the properties of the final product and thus the production process. In order to continuously absorb the moisture contained in the ambient air, the technical solution has been to dehumidify by condensation.

Many studies conducted on plastic injection molding have focused on minimizing cycle time by improving cooling to improve the production rate and reduce the possibility of producing faulty parts. Since the cooling of the injection mold

takes up most of the cycle time, the literature reviewed is found to be mostly based on cooling systems. Sun et al. [3] conducted a study and proposed corrugated cooling grooves opened through the milling method. Using a sample door handle iron, they formed grooves opened with milling method in the core and mold. The cooling time for the milled grooves was shorter than for conventional straight-perforated grooves. It is stated that the cooling time can also be reduced by positioning the injection on the mold in the appropriate place [11]. Mercado et al.[12] developed a new algorithm for the automatic design of the cooling systems in injection molds based on the geometry of the plastic part. Li et al. [7] conducted a study on the optimal placement of cooling canals in plastic injection molds and developed a knowledge-based approach for the cooling system. Lin et al. [13] conducted research and created the optimal cooling system design for a free-form plastic product using the method of the neural network. Li et al. [14] conducted a study on the automatic placement of the cooling system in plastic injection molds. They created a computer-aided simulation of the cooling system of the TV panel mold.

These studies aimed to minimize the time losses during the production stage ensuring that the values regarding efficiency, temperature, humidity and mold parameters, etc. of the products made through plastic injection machines are in optimal conditions. Studies aiming to reduce the negative impacts of water droplets on injection molds under the influence of temperature are limited. In the literature review, different methods have been tried in the removal of water droplets in plastic injection molds, but the effect of dehumidifiers has not been directly observed. For this reason, studies examining the effect of dehumidifiers directly on plastic injection molds have not been found in literature research.

In this study, the effect of dehumidifiers on the production line was investigated as an innovative approach to reduce the negative effects of water droplets on plastic injection molds. For this purpose, dehumidifiers were placed in the injection molds in order to minimize the water

droplets formed in the molds during the plastic injection process in a company that produces plastic bottles in Lüleburgaz. Values regarding humidity and heat measurements during the production were monitored and recorded daily. The effect of using a dehumidifier in the production line on the production efficiency of injection machines is reported. The data obtained from this study will be useful in terms of the possibility of using dehumidifiers for applications of reducing water droplets in plastic injection molds.

## 2. MATERIAL METHOD

### 2.1. Injection Line

Within the scope of the study, the layout plan of the injection machines on the production line are shown in Figure 1, and the physical characteristics of the injection department in the enterprise is presented in Table 1. There are a total of 17 plastic injection benches in the region where the works are carried out. Experimental studies are based on this area. While the 1st hol in this area has a height of 3m, the 2nd hol has a height of 4m. Due to this height difference in the production area, the sections has examined separately.

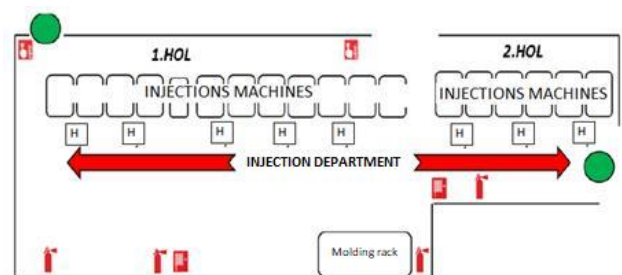


Figure 1 Layout plan of the injection department

Table 1 Physical properties of injection department

Area (m <sup>2</sup> )	Volume (m <sup>3</sup> )	Location	Height (m)	Machine (piece)
500	1750	1. Line	3	11
		2. Line	4	6

### 2.2. Dehumidification Device

Dehumidification is the process of removing water vapor from moist air. Too much water

vapor in the air could cause many problems. These include deterioration of comfort conditions, acceleration in metal corrosion, reduced impact properties of its materials, premature chemical degradation, and worsening of surface finishing. These are the systems or mechanisms designed to remove heat from an environment using a cooling cycle, remove excess moisture and provide fresh air to the environment. For this reason, it is not enough to cool the air only through air conditioners, the humidity must also be adjusted. In this study, the technical specifications of the dehumidification devices used in the injection department are listed in Table 2. 8 dehumidifiers are placed in the injection area, taking into account the circulation conditions.

Table 2 Technical specifications of the dehumidifier

Parameters	Value
Dehumidification capacity (L/D)	138
Voltage / frequency (V/Hz)	220/50
Air volume (m <sup>3</sup> /h)	1200
Power input (W)	1850
Operating temperature (°C)	5-35
Usable area (m <sup>2</sup> )	120-160

### 2.3. Production Efficiency

Efficiency in the technical sense is defined as "the number of goods and services produced and the ratio between the inputs used in the production of the amount of service in the production of these goods". Production efficiency means achieving optimum product quality with minimal unit cost. If it is the aim to achieve this goal, it is not enough to concentrate only on energy efficiency and machine technology. Instead, the whole value chain and all variables and the best possible solution should be discovered individually. Various factors such as cycle time, mold cavity number, cooling quality, mold life and strength, mold assembly status and production time, discards and energy have a significant effect on efficiency. For instance, Eq. (1) is used to calculate the injection production efficiency as follows [15]:

$$\text{Efficiency (\%)} = \left( \frac{\text{Theoretical hourly quantity of product}}{\text{Actual hourly production of the machine}} \right) \cdot 100 \quad (1)$$

### 3. EXPERIMENTAL STUDY

The experimental research started with the relevant environmental measurements before the dehumidification devices were placed in the injection line. As of 2019, ambient temperature and humidity were measured in the injection line for 16 days. The data obtained from the measurements are listed in Table 3. The obtained results from 1. hol and 2. hol regarding the changes in temperature and humidity are presented in Figure 2.

Table 3 Temperature and humidity values measured in the injection department

Day	1. Hol		2. Hol		Chiller Set Value (°C)	Water droplets	Environmental Air Cond.	
	Max Tem p. (°C)	Max Hum id. (%)	Max Tem p. (°C)	Max Hu mid (%)			Temp . (°C)	Humid (%)
1	36	57	38	29	24	No	27	48
2	35	57	37	28	24	No	28	49
3	35	57	38	28	12	Yes	27	50
4	33	53	35	30	15	No	27	51
5	Break							
6	33	52	38	28	15	No	27	57
7	35	55	39	27	14	No	27	55
8	37	43	38	26	13	No	30	59
9	32	46	36	27	12	Yes	28	60
10	34	48	37	29	14	No	31	65
11	34	57	37	32	14	No	33	69
12	Break							
13	34	58	36	30	14	No	30	65
14	34	59	40	27	13	Yes	32	64
15	34	58	41	26	15	No	31	64
16	34	55	42	25	15	No	32	63

During the production in the enterprise, 16-day ambient temperature and humidity values of the injection line was examined and it was found that; 1.hol the average temperature in the line was 34°C and humidity was 53.2 %.The average temperature in the line was found to be 38°C, and the humidity was found to be 28%.

It is predicted that the reason for the differences in the measurements performed in 1. hol and 2. hol in temperature and humidity could be the difference in machine capacities. As seen in Table 4, the changes in the measurements are affected by the changes in humidity and temperature in the air.

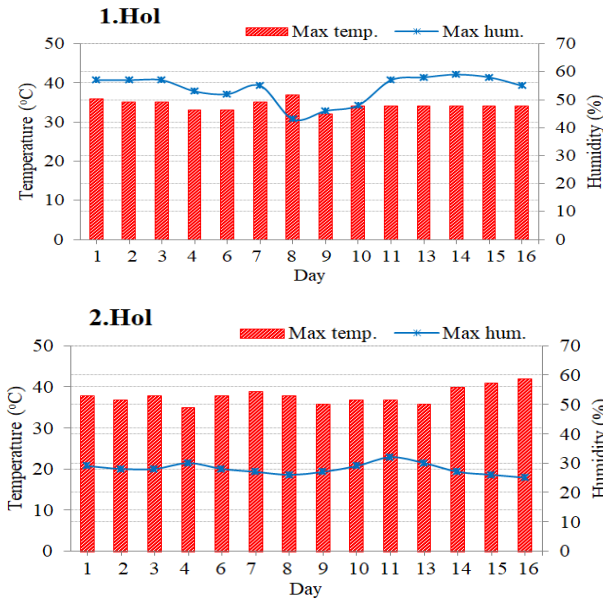


Figure 2 Temperature and humidity change in the injection environment

The amount of moisture in the environment decreases as the temperature increases. This is clearly seen in Figure 2. In an experimental study conducted with 8 dehumidifiers, it was found that the optimal temperature set value of the chiller cooling system was found to be 14°C.

It is a known fact that during the filling of the plastic injection mold, the hottest molten plastic was found to be at gate, and the coldest molten plastic was found to be at the farthest point from the input point of the mold. The temperature of the cooling water (chiller) increases as it passes through these canals, so to ensure equal cooling at the production stage, it is necessary to provide cooling water inlet to the hot areas of the mold and cooling water outlet to the cold areas of the mold. Increasing the temperature of the chiller is a factor that prevents optimal values in the production stage.

When Table 4 was examined, it was observed that chiller operating temperature values fell by 4.3°C in the summer when humidifier devices were active in injection machines and the machine operated at an average of 14.3°C. At these temperatures, no water droplet was observed on the surfaces of the injection mold. This confirms that the molds cool better, thus energy and production efficiency is increased. Under these conditions, when the humidity values on

dehumidifiers were examined, the machine was observed to have worked at an average 30% set value.

Table 4 Operating set values of chiller system regarding months June, July, August (°C)

2018	June	July	August	Average	Decrease
Injection machine (Inactive-dehumidifier)	18	19	19	18.6	-
2019	June	July	August	Average	Decrease
Injection machine (Active-dehumidifier)	15	14	14	14.3	4.3

In addition, efficiency results of injection production calculated based on the measurement data made in the months when the research was conducted are summarized in Table 5. It is possible to observe the average % efficiency of the machines in the injection line before and after the integration of dehumidifier into the system. Here, as a result of the effect of the dehumidifier on production, it is seen that the production efficiency has increased by ~ 8%. With the reduction of water droplets on the mold, a homogeneous temperature distribution occurs. Fault-free production is ensured by the fact that the temperature of the pet raw material at the injection point and the temperature value at the nozzle outlet end are the same. By adding dehumidifiers to the injection hall, the temperature balance on the mold was regulated and it was seen that it contributed positively to the production efficiency.

Table 5 Injection production efficiency obtained in June, July, August (%)

2018	June	July	August	Average	Increase
Injection machine (Inactive-dehumidifier)	79.02	77.44	78.11	78.19	-
2019	June	July	August	Average	Increase
Injection machine (Active-dehumidifier)	86.56	85.72	81	84.42	8

#### 4. CONCLUSIONS

The fact that the temperature exceeds the operating conditions during production has a negative impact on the production efficiency of injection machines and the performance of molds. To increase product quality for better, the machines were accelerated, but no successful results were obtained. At the same time, the rising temperature in the environment made the operating conditions difficult and created an unsuitable operation environment. This is also not ergonomically appropriate. For this purpose, dehumidifiers were integrated into the operating area manufacturing plastic injection. Humidity and heat values generated during the production were monitored daily and recorded.

The results revealed that setting the injection line to a fixed temperature and operating degrees will help prevent water droplets on the molds and also help increase the production efficiency by 8%. The decrease in the operating temperature of the chiller cooling system, compared to the figure of the former year, and the formation of effective cooling are thought to have eliminated water droplets. Integration of a humidifier device into the system helped the operation of the machines realize based on needs. Thus, with the more efficient operation of the machines and the elimination of water droplets on mold, the workload on the cooling was reduced. The findings suggest greater obtained efficiency, productivity, machine availability and quality. Besides, the study revealed that additional cooling applications are required in the injection operating environment to achieve a higher level of efficiency, especially at higher temperatures.

#### *Acknowledgments*

Authors would like to extend acknowledgement to the Plaş Plastic Package Corporation for the opportunity to conduct experimental studies.

#### *Funding*

The authors has no received any financial support for the research, authorship or publication of this study.

#### *The Declaration of Conflict of Interest/ Common Interest*

No conflict of interest or common interest has been declared by the authors.

#### *Authors' Contribution*

All authors have contributed in experimental study and writing of the manuscript equally.

#### *The Declaration of Ethics Committee Approval*

The authors declare that this work does not require an ethics committee approval or any special permission.

#### *The Declaration of Research and Publication Ethics*

The authors of the paper declare that they comply with the scientific, ethical and quotation rules of SAUJS in all processes of the paper and that they do not make any falsification on the data collected. In addition, they declare that Sakarya University Journal of Science and its editorial board have no responsibility for any ethical violations that may be encountered, and that this study has not been evaluated in any academic publication environment other than Sakarya University Journal of Science.

#### REFERENCES

- [1] D. V. Rosato, D. V. Rosato, and M.G. Rosato, "Injection Moulding Machines, In: *Injection Moulding,*" *Handbook.* Boston, MA, pp. 28-150, 2000.
- [2] D. Kozjek, R. Vrabič, D. Kralj, P. Butala, and N. Lavrač, "Data mining for fault diagnostics: A case for plastic injection moulding," In *Procedia CIRP*, vol. 81, pp. 809-814, 2019.

- [3] Y.F. Sun, K.S. Lee, and A.Y.C. Nee, "Design and FEM analysis of the milled groove insert method for cooling of plastic injection moulds," *The International Journal of Advanced Manufacturing Technology*, vol. 24, no. 9-10, pp. 715-726, 2004.
- [4] S.H. Tang, Y.M. Kong, S.M. Sapuan, R. Samin, and S. Sulaiman, "Design and thermal analysis of plastic injection mould," *Journal of Materials Processing Technology*, vol. 171 no. 2, pp. 259-267, 2006.
- [5] K.M. Au, and K.M. Yu, "A scaffolding architecture for conformal cooling design in rapid plastic injection moulding," *The International Journal of Advanced Manufacturing Technology*, vol. 34, no. 5-6, pp. 496-515, 2007.
- [6] M.W. Fu, J.Y.H. Fuh, and A.Y.C. Nee, "Undercut feature recognition in an injection mould design system," *Computer-Aided Design*, vol. 31, no. 12, pp. 777-790, 1999.
- [7] L.Q. Tang, C. Chassapis, and S. Manoochchri, "Optimal cooling system design for multi-cavity injection moulding," *Finite Elements in Analysis and Design*, vol. 26, no. 3, pp. 229-251, 1997.
- [8] A. Pesaran, T. Penney, A.W. Czanderna, "Desiccant cooling: state of the art Assessment", National Renewable Energy Laboratory, pp. 1-12, 1992.
- [9] B.R. Hughes, H.N Chaudhry, S.A. Ghani, "A review of sustainable cooling technologies in buildings," *Renewable and Sustainable Energy Reviews*, vol. 15, no. 6, pp. 3112-3120, 2011.
- [10] M. Sultan, I.I. El-Sharkawy, T. Miyazaki, B. B Saha, S. Koyama, d "An overview of solid desiccant dehumidification and air conditioning systems," *Renewable and Sustainable Energy Reviews*, vol. 46, pp. 16-29, 2015.
- [11] H.S. Park, and X.P. Dang, "Development of a smart plastic injection mould with conformal cooling channels" *Procedia Manufacturing*, vol. 10, pp. 48-59, 2017.
- [12] J.M. Mercado-Colmenero, M.A. Rubio-Paramio, J. J. Marquez-Sevillano, and C. Martin-Doñate, "A new method for the automated design of cooling systems in injection moulds," *Computer-Aided Design*, vol. 104, pp. 60-86, 2018.
- [13] J.C. Lin, "Optimum cooling system design of a free-form injection mould using an abductive network," *Journal of Materials Processing Technology*, vol. 120, no. 1-3, pp. 226-236, 2002.
- [14] H. Zhou, and D. Li, "Mould cooling simulation of the pressing process in TV panel production," *Simulation Modelling Practice and Theory*, vol. 13, no. 3, pp. 273-285, 2005.
- [15] Plaş Plastic Package Industry and Trade Inc. *Manufacturing Notes*, 2018.



SAKARYA ÜNİVERSİTESİ

# FEN BİLİMLERİ ENSTİTÜSÜ DERGİSİ

Sakarya University Journal of Science  
SAUJS

e-ISSN: 2147-835X | Founded: 1997 | Period: Bimonthly | Publisher: Sakarya University |  
<http://www.saujs.sakarya.edu.tr/en/>

Title: Effect of Grain Distribution on Resin Consumption and Mechanical Performance of GRP Pipes

Authors: Şevki EREN, Özcan ÇAĞLAR, Neslihan GÖKÇE, Azime SUBAŞI, Serkan SUBAŞI

Received: 2021-02-16 00:00:00

Accepted: 2021-08-15 00:00:00

Article Type: Research Article

Volume: 25

Issue: 5

Month: October

Year: 2021

Pages: 1136-1147

How to cite

Şevki EREN, Özcan ÇAĞLAR, Neslihan GÖKÇE, Azime SUBAŞI, Serkan SUBAŞI; (2021), Effect of Grain Distribution on Resin Consumption and Mechanical Performance of GRP Pipes. Sakarya University Journal of Science, 25(5), 1136-1147, DOI:

<https://doi.org/10.16984/saufenbilder.878809>

Access link

<http://www.saujs.sakarya.edu.tr/tr/pub/issue/65589/878809>

New submission to SAUJS

<http://dergipark.org.tr/en/journal/1115/submission/step/manuscript/new>

## Effect of Grain Distribution on Resin Consumption and Mechanical Performance of GRP Pipes

Şevki EREN\*<sup>1</sup>, Özcan ÇAĞLAR<sup>2</sup>, Neslihan GÖKÇE<sup>2</sup>, Azime SUBAŞI<sup>2</sup>, Serkan SUBAŞI<sup>2</sup>

### Abstract

It was aimed to produce glass fiber reinforced pipes (GRP), having less resin consumption and higher mechanical properties by changing the grain distribution of fillers used in the core region. American Foundry Society (AFS) grain fineness number currently used in GRP pipe production, and the grain distribution determined to the Fuller equation, the exponent of which is 0.8 (F 0.8), were used in the study. Chopped glass fibers, unsaturated polyester resin, and silica filler were used. It was manufactured three GRP pipes having 6 m length and nominal diameter (DN) of 350 mm by centrifugal casting technique. Initial specific ring stiffness and longitudinal tensile strength (LTS) tests were conducted on GRP pipes. After the longitudinal tensile tests of the produced GRP pipes, SEM images were taken from the core region and the morphological analyzes of the images were made. As a result of the study, when GRP pipes are produced incorporating 14 % less body resin in F 0.8 grain distribution, 44.11 % higher stiffness and 50.4 % higher LTS was obtained than the minimum value required in the standard.

**Keywords:** GRP pipe, filler materials, grain distribution, AFS grain fineness number, Fuller equation.

### 1. INTRODUCTION

Glass fiber reinforced pipes (GRP) are generally three-layered composite systems. These composite systems consist of thin FRP layers on the inner and outer surfaces of the pipe walls and a polymer mortar layer in the center [1],[2],[3]. These pipes are produced by centrifugal casting (CC) or filament winding (FW) methods [2],[3],[4],[5]. GRP pipes must provide certain design criteria, including short-term hydrostatic failure strength, representing the longitudinal

tensile strength (LTS) and initial specific ring stiffness [2],[5]. The primary purpose of fillers is to restrict the movement of the polymer chain, thereby increasing hardness, abrasion resistance, stiffness, and strength but reducing ductility [6], [7],[8]. Glass fiber reinforced polymer composite with particle-filled is formed by combining glass fiber and mineral aggregates with a resin system [9]. For this reason, GRP pipe manufacturers prefer to apply a filling layer impregnated between the FRP layers as an economical alternative method [2]. AFS grain fineness

\* Corresponding author: seren@ahievran.edu.tr

<sup>1</sup> Kırşehir Ahi Evran University.

ORCID: <https://0000-0003-0773-4034>,

<sup>2</sup> Duzce University

E-Mail: ocaglar@superlit.com, nesligke@gmail.com, azimesubasi@duzce.edu.tr, serkansubasi@duzce.edu.tr

ORCID: <https://0000-0002-6514-0691>, <https://0000-0001-5418-0551>, <https://0000-0002-1732-6686>, <https://0000-0001-7826-1348>

number is a grain distribution type used as a general indication of sand fineness by most foundries in the United States and calculated from the grain distribution determined by standard ASTM sieves [10]. Each fraction is multiplied with a weighting factor, the results are added together and divided by 100. AFS grain fineness number gets bigger as the average size decreases and is considered to be proportional to the number of grains per unit weight [11]. AFS 35 (390  $\mu\text{m}$ ), AFS 40 (340  $\mu\text{m}$ ), AFS 45 (300  $\mu\text{m}$ ), AFS 50 (280  $\mu\text{m}$ ), AFS 55 (240  $\mu\text{m}$ ), AFS 60 (220  $\mu\text{m}$ ), AFS 65 (210  $\mu\text{m}$ ), AFS 70 (195  $\mu\text{m}$ ), AFS 80 (170  $\mu\text{m}$ ), AFS 90 (150  $\mu\text{m}$ ), etc. different AFS grain fineness numbers have been currently using in the industry [10]. GRP pipes and grain distributions have been investigated by several researchers;

In the research conducted by Rafiee [2] it has been reported that the effect of adding sand filler into the polymer matrix as a core layer on the mechanical properties of GRP pipes has not been investigated enough by researchers. Kumar et al. [12] has selected the silica sand with the range of AFS 60-140 grain fineness number to explore its potential effects on tensile properties of Al-7 % Si alloy castings made by the EPC process. They determined that the grain fineness number and pouring temperature importantly affect the tensile strength and elongation percentage after a fracture. Fuller and Thompson [13] underlined the important effect of aggregate grain distribution on the physical and mechanical properties of concrete. The problem of the best possible grain distribution of aggregates and their contribution to optimum proportioning for the concrete mixture has been the issue of numerous experimental and theoretical investigations. Shi and Wei [14] examined the mechanical properties of glass fiber reinforced plastic mortar pipes with an inner diameter of 1500 mm under different loading conditions. In their study, ring and axial compressive strength and elastic modulus, stiffness and fatigue test were carried out. It was determined that the pipe stiffness was determined as 2.3 MPa. As a result, it was concluded that the composite with resin and quartz sand, increase the compression strength and the effect of quartz sand on compressive strength is more important than the resin and glass fiber. Rafiee and Reshadi [15]

simulated and analyzed the functional failure in composite pipes exposed to internal hydrostatic pressure. A progressive damage modeling was developed considering the effect of the core layer added for increasing the pipe stiffness. The effect of two primary parameters as core thickness and the winding angles of cross plies were studied. It was observed that first-ply-failure and functional failure pressures increase linearly as the core thickness increase. Gökçe et al. [16] analysed the effects of the type of resin and fiber on the mechanical behaviours of the polymer composite pipe manufactured by the CC technic. Isophthalic, orthophthalic, and vinyl ester resin were used as matrix material, E and ECR glass fiber were used as reinforcement material, and silica sand was used as filler material. As a result, it was found that the mechanical behaviours of the polymer composite pipes changed with different types of resin and fiber.

In this study, it was aimed to manufacture GRP pipes having less resin consumption and higher mechanical properties by changing the grain distribution of the fillers used in the core region.

## 2. EXPERIMENTAL

### 2.1. Matrix Materials

Orthophthalic body resin (Boytek BRE 310) and orthophthalic liner resin (BRE 816) were used in GRP pipe production. Cobalt octoate (Co: C<sub>16</sub>H<sub>30</sub>CoO<sub>4</sub>) (wt. 1 %) as an accelerator and methyl ethyl ketone peroxide (MEKP: C<sub>8</sub>H<sub>18</sub>O<sub>6</sub>) (wt. 1 %) as an initiator were used as additive materials. Some mechanical properties of orthophthalic body resin are given in Table 1.

Table 1 Physical and mechanical properties of orthophthalic body resin

Property	Unit	Orthophthalic Resin
Density	-	1.12
Viscosity	(cp)	250
Solid content	(%)	57
Tensile modulus	(MPa)	3550
Tensile strength	(MPa)	74
Flexural strength	(MPa)	125
Flexural modulus	(MPa)	3800
Elongation at Break (tensile)	(%)	3.15
Total volumetric shrinkage	(%)	8.0

## 2.2. Filling Materials

Silica sand with AFS 40-45 grain fineness number ( $\text{SiO}_2$ : 98.94 %;  $\text{Al}_2\text{O}_3$ : 0.08 %;  $\text{Fe}_2\text{O}_3$ : 0.1 %) currently used by Superlit Pipe Industry Inc. as filling material in GRP pipe production were used, and the grain distribution determined to the Fuller equation was used in the study. The physical properties of silica sand are given in Table 2.

Table 2 Physical properties of silica sand

Physical properties	Silica sand
Moisture content (%)	0.002
Relative density	2.55
Burning loss (%)	1.3
Dry specific gravity	2.55
Specific gravity saturated with water	2.61
Loose unit weight ( $\text{g}/\text{cm}^3$ )	1.616
Cramped unit weight ( $\text{g}/\text{cm}^3$ )	1.791
Water absorption (%)	2.03
Specific surface area ( $\text{m}^2/\text{kg}$ )	12.07
Average grain size (micron)	237

## 2.3. Fiber Materials

Chopped E-glass fiber was used in the study. The physical and mechanical properties of E-glass fiber are given in Table 3.

Table 3 Physical and mechanical properties of chopped E-glass fiber

Properties	Glass fiber
Moisture content (%)	0.92
Fiber weight ( $\text{g}/\text{km}$ )	2400
Binder content (%)	2.1
Number of ends	60
Fiber diameter (micron)	16-20
Specific weight	2.60
Tensile strength (MPa)	3400
Elasticity modulus (GPa)	77
Fiber length (mm)	50

## 2.4. Optimization of Filler Particle Distribution Used in GRP Pipe Production

Some early grain distribution design studies on polymer composites were performed using silica sands in different grain distributions determined according to the Fuller equation and also in AFS 40-45 grain fineness number. As a result of the tests on the polymer composites, the best grain distribution, which has the minimum resin consumption and the best compressive strength, was determined as F0.8 [17]. It has been concluded that the use of this distribution in GRP pipe production will be appropriate. The Fuller equation used in the study is given in Equation 1 [13].

$$P \% = (d / D)^n \quad (1)$$

P%: total percent of particles passing through (or finer than) sieve

d: diameter of the current sieve,

D: maximum size of aggregate (1000  $\mu\text{m}$ )

n: exponent of the equation, (n=0.8 for this study)

However, since F 0.8 grain distribution is not available in the market, silica sands with AFS 40-45 and AFS 110-140 grain fineness number that is available in the market were mixed to obtain F 0.8 grain distribution. For this reason, as a result of the grain distribution analysis, a new optimized mixture was formed by taking the proportion of 20 % of AFS 110-140 grain fineness number and 80 % of AFS 40-45 grain fineness number by weight and this mixture was called as F 0.8 (optimization 1). It was concluded that the new mixture optimized is the closest grain distribution to F 0.8 grain distribution. The grain sizes of the sands used are in the range of 0-1000 microns. F 0.8 filler grain-size distributions used in the study are represented in Table 4 and different AFS and F 0.8 (optimization 1) filler grain-size distributions are represented in Table 5. A visual of all filler grain-size distributions graphic used in the study are represented in Figure 1.

Table 4 F 0.8 filler grain-size distributions

Grain sizes ( $\mu\text{m}$ )	P, % F 0.8
1	0.4
10	2.5
100	15.8
150	21.9
180	25.4
250	33
300	38.2
500	57.4
600	66.5
710	76
850	87.8
1000	100

Table 5 Different AFS and F 0.8 (optimization 1) filler grain size distributions

Grain sizes ( $\mu\text{m}$ )	P, %		
	AFS 40-45	AFS 110-140	F0.8 (optimization 1) [AFS 110-140 (%20) + AFS 40-45 (%80)]
1	0	0	0
63	0	22	4
90	0	75	15
125	1	97	20
180	2	99.5	22
250	19	100	35
355	61	100	68
500	89	100	91
600	94	100	95
710	98	100	99
850	99	100	99
1000	100	100	100

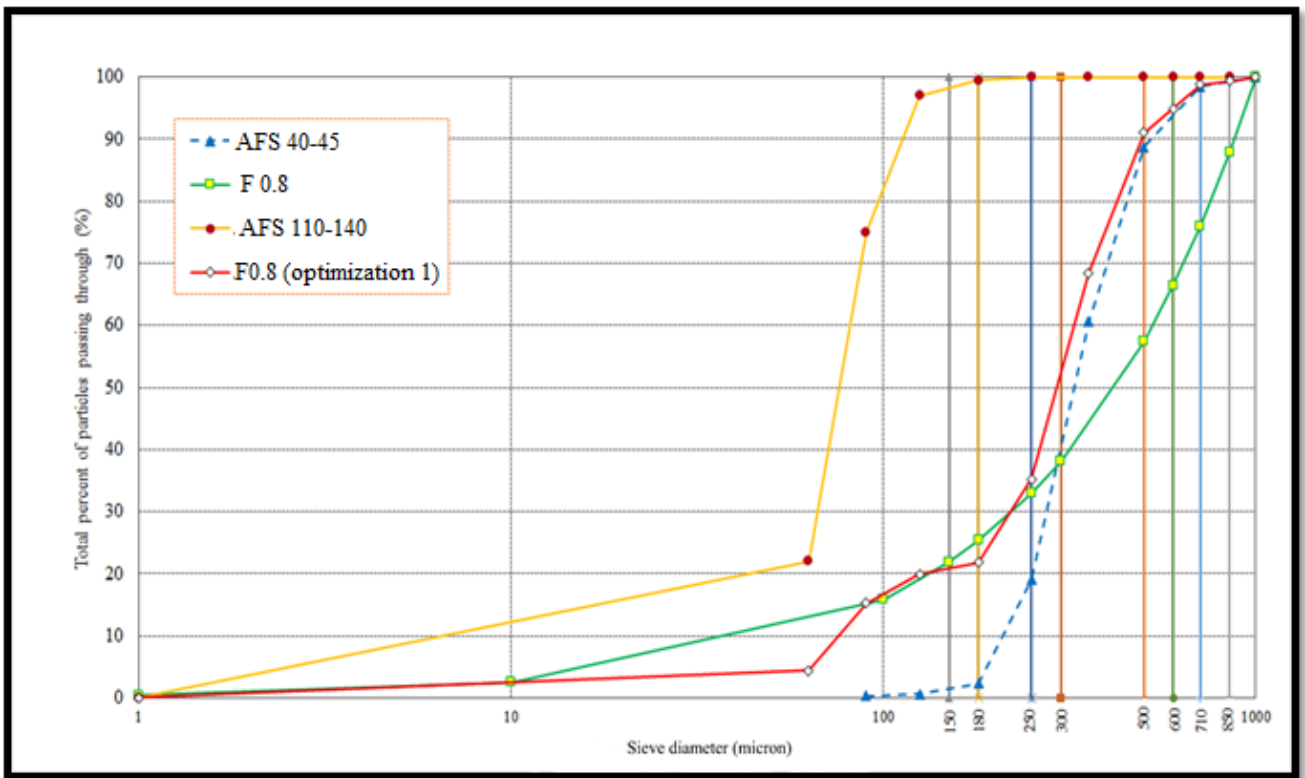


Figure 1 Different filler grain size distribution graphics used in the study

## 2.5. Manufacture of GRP Pipe

In this study, the CC method was preferred to produce GRP pipes in a standard way when the optimized mineral filling material mixture is started to mass production. It was produced three GRP pipes, having 6 m length and DN of 350 mm. GRP pipes were aimed to be exposed to a nominal pressure (PN) of 6 bar, have a nominal stiffness (SN) of at least 10.000 N/m<sup>2</sup>, and the LTS value of at least 135 N/mm. The pipe production process by the CC method can be seen in Figure 2.



Figure 2 GRP pipe production process by the CC method

Since the grain distributions of each pipe produced are different, the pipe types were numbered from 1 to 3. Necessary explanations regarding the raw material usage amounts of the

related pipes produced using different grain distributions are described below.

Pipe No (1) (Reference Pipe):

The reference pipe has been currently manufacturing by Superlit Pipe Industry Inc. chopped E-glass has been using as fiber reinforcement, and silica sand with AFS 40-45 grain fineness number has been using as filler material in this reference pipe production.

Pipe No (2):

In pipe no 2, chopped E-glass was used as fiber reinforcement, and silica sand with F0.8 (optimization 1) grain distribution was used as filler material. In this pipe type, the pipe production was carried out by incorporating 3.5 % less body resin than the amount of resin used in the reference pipe.

Pipe No (3):

In pipe no 3, chopped E-glass was used as fiber reinforcement, and F 0.8 (optimization 1) grain distributed silica sand was used as filler material. In this pipe type, the pipe production was carried out by incorporating 14 % less body resin than the amount of resin used in the reference pipe.

The pipe no 1 was called as the reference pipe. Initial specific ring stiffness and the LTS tests were performed on the produced pipes. The schematic representation of the pipe section produced by the CC method and a visual of the part cut from the produced pipes are shown in Figure 3. The duties of the layers specified in the pipe section are given in Table 6 [18].

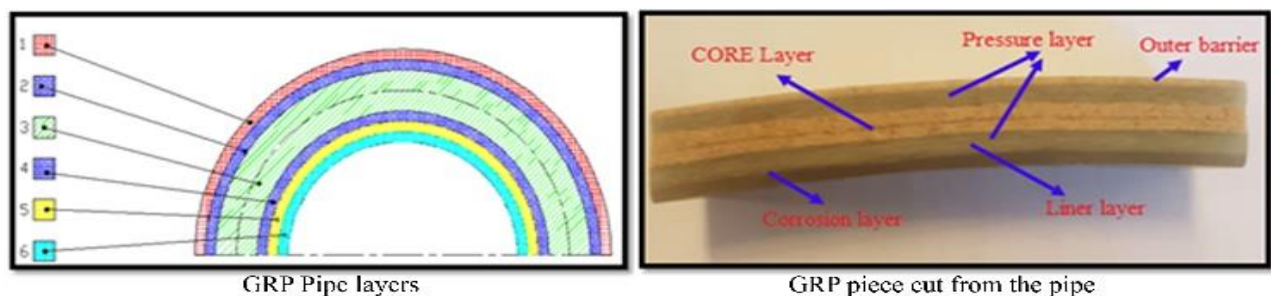


Figure 3 The schematic representation of the pipe section produced by the CC method and a visual of the part cut from the produced pipes

Table 6 Duties of the layers specified in the pipe section

Pipe Layer No	Function	Content	Thickness
1	An outer surface protective layer (outer barrier) (UV, chemicals, impact resistance, etc.)	Resin and sand	Min. 1 mm
2	Pressure layer	Resin and chopped fiber	While the wall thickness is increased to achieve high pressure, the thickness of the layers in this region is also increased.
3	CORE (filler zone) - stiffness zone	Resin, sand and small amount of chopped fiber	
4	Pressure layer	Resin and chopped fiber	While the wall thickness is increased to achieve high pressure, the thickness of the layers in this region is also increased.
5	Liner layer to ensure sealing	Resin and chopped fiber	
6	An inner surface protective layer (corrosion layer)	Pure Resin	Min. 1 mm

In GRP pipes, “resin + sand + chopped fiber” materials are used in the third layer, which is defined as the filling layer (CORE), to increase the stiffness performance. In these GRP pipes, the thicker pipe walls are necessary to increase the apparent pipe stiffness [2],[18].

**2.6. Initial Specific Ring Stiffness**

Initial specific ring stiffness test was carried out according to ISO 7685: 2019 was used as the reference specified in the relevant standard [19]. In the study, the stiffness samples were cut from the mold removal part and feeding part of GRP pipes. The outer diameter of the pipe was measured with a caliper on the stiffness samples and measurements were recorded. Subsequently, a deflection of 3 % was applied to the stiffness samples and deflection values recorded 2 minutes later and then the stiffness values were calculated.

The stiffness test samples of GRP pipes are given in Figure 4.



Figure 4 The stiffness test sample images of GRP pipes

**2.7. Longitudinal Tensile Strength Test**

ISO 8513: 2016 Method (A), was used to determine the LTS value of the pipe samples [20]. 5 longitudinal tensile test samples were cut in a longitudinal direction from GRP pipes, and the LTS test was carried out. A visual of specific ring stiffness and the LTS test is given in Figure 5.



Figure 5 A visual of the specific ring stiffness and the LTS test

### 3. RESULTS AND DISCUSSIONS

#### 3.1. Raw Material Usage Amounts in GRP Pipes

Raw material usage amounts according to pipe diameter and nominal pressure values of the GRP pipes are given in Table 7.

Table 7 Raw material usage amounts of GRP pipes

DN/PN/SN (mm/bar/N/m <sup>2</sup> )	Pipe No	Fiber	Grain Distribution Type	Body + Liner Resin (kg)	Total resin (kg)	Fiber amount (kg)	Filler amount (kg)	Total weight (kg)
350/06/10.000	Pipe No: (1) (Reference)	E- glass	AFS 40-45	29+14	43	16,6	77,1	136,7
	Pipe No: (2)	E- glass	Fuller 0.8	28+14 (incorporating 3,5% less body resin)	42	16,2	81	139,2
	Pipe No: (3)	E- glass	Fuller 0.8	25+14 (incorporating 14% less body resin)	39	16,2	79,8	135

Table 8 Average initial specific ring stiffness values of GRP pipes

DN/PN/SN (mm/bar/N/m <sup>2</sup> )	Pipe No	Fiber	Grain Distribution Type	Stiffness (N/m <sup>2</sup> )					
				Range	Min.	Max.	Std. Error	Std. Dev.	Average
350/06/10.000	Pipe No: (1) (Reference)	E glass	AFS 40-45	1626	14581	16207	334	668	15.369
	Pipe No: (2)	E glass	Fuller 0.8	2271	15361	17632	494	988	16.697
	Pipe No: (3)	E glass	Fuller 0.8	1710	13453	15163	339	758	14.411

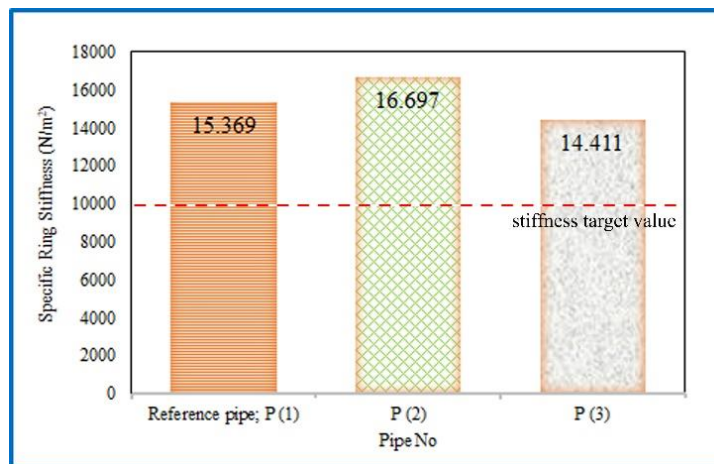


Figure 6 Change of the stiffness values according to the pipe type

It was determined that all GRP pipes produced within the scope of the study reached the

Resin reduction amounts were determined by foresight in this study. Of course, different resin reduction ratios can be used.

#### 3.2. Initial Specific Ring Stiffness Test Results

Average initial specific ring stiffness values of GRP pipes, which are produced in different filler grain distributions and numbered from 1 to 3, are given in Table 8 and Figure 6.

minimum stiffness value of 10.000 N/m<sup>2</sup> required in the standard and even higher stiffness values.

In the pipe number 2 with F 0.8 (optimization 1) grain distribution, which is used as an alternative to AFS 40-45 grain fineness number, 8.64 % higher stiffness was obtained by incorporating 3.5 % less body resin compared to the reference pipe production.

In the pipe number 3 with F 0.8 (optimization 1) grain distribution, a reduction of 6.23 % in the stiffness was obtained by incorporating 14 % less body resin compared to the reference pipe production, but 44.11 % higher stiffness value was obtained than the minimum stiffness value of 10.000 N/m<sup>2</sup> required in the standard.

As the stiffness test results, it was concluded that it is possible to produce GRP pipes with F 0.8 (optimization 1) grain distribution at a lower cost by providing up to the ratio of 14 % resin consumption.

### 3.3. LTS Test Results

Average LTS values of GRP pipes are given in Table 9 and Figure 7.

It was determined that all GRP pipes produced within the scope of the study reached the minimum LTS value of 135 N/mm required in the standard and even higher strength values.

Table 9 Average LTS values of GRP pipes

DN/PN/SN (mm/bar/N/m <sup>2</sup> )	Pipe No	Fiber	Grain Distribution Type	LTS (N/mm)					
				Range	Min.	Max.	Std. Error	Std. Dev.	Average
350/06/10.000	Pipe No: (1) (Reference)	E glass	AFS 40-45	57	190	247	16.895	29.263	214.97
	Pipe No: (2)	E glass	Fuller 0.8	32	199	231	8.010	16.020	212.98
	Pipe No: (3)	E glass	Fuller 0.8	26.1	185.8	211.9	8.6834	15.0401	203.167

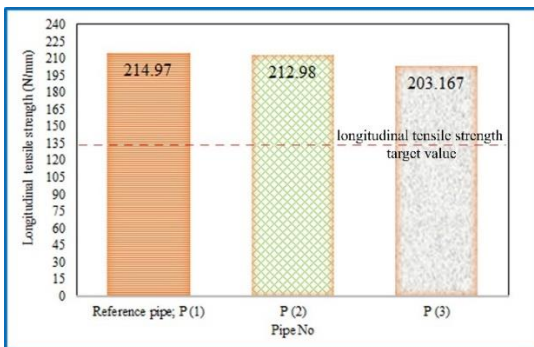


Figure 7 Change of the LTS values according to the pipe type

In pipe number 2 with F 0.8 (optimization 1) grain distribution, 57.8 % higher LTS value was obtained than the minimum LTS value of 135 N/mm required in the standard by incorporating 3.5 % less body resin.

In pipe number 3 with F0.8 (optimization 1) grain distribution, 50.4 % higher LTS value was obtained than the minimum LTS value of 135

N/mm required in the standard by incorporating 14 % less body resin.

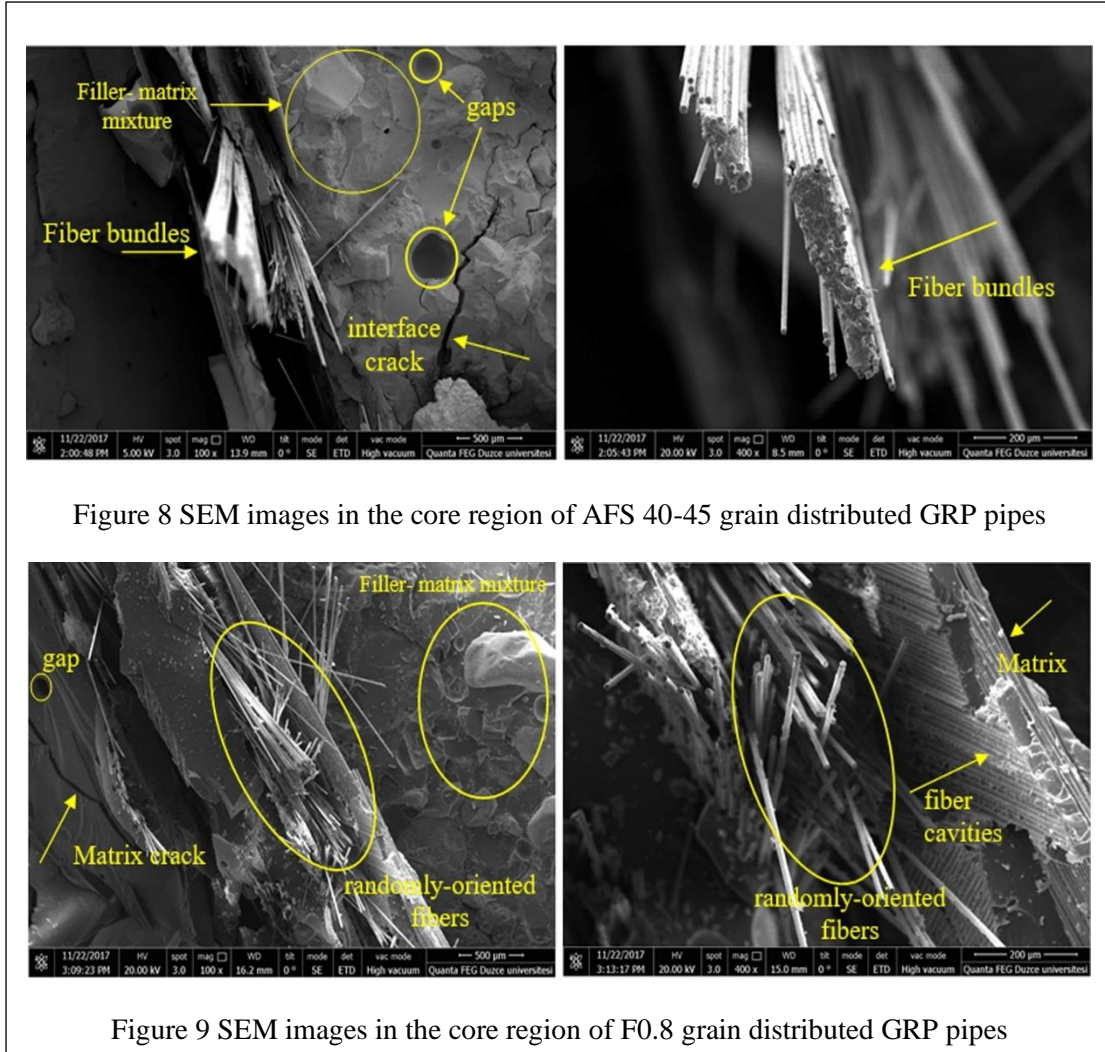
As the LTS test results, it was concluded that it is possible to produce GRP pipes with F 0.8 (optimization 1) grain distribution at a lower cost by providing up to the ratio of 14 % resin consumption.

Kumar et al. [12] determined that the grain fineness number and pouring temperature importantly affect the tensile strength. Fuller and Thompson [13] underlined the important effect of aggregate grain distribution on the physical and mechanical properties of concrete. In this study, a better grain distribution was obtained by using the F 0.8 (optimization 1) grain distribution in the core region in GRP pipe production and for this reason, it was concluded that F 0.8 (optimization 1) grain distribution is effective in reducing resin consumption.

### 3.4. SEM Images and Morphological Analysis of GRP Pipes

•After the longitudinal tensile tests of the produced GRP pipes, SEM images were taken

from the core region and the morphological analyzes of the images were made. SEM images in the core region of AFS 40-45 and F 0.8 (optimization 1) grain distributed GRP pipes are shown in Figure 8 and Figure 9 respectively.



When the SEM images in the core region of AFS 40-45 grain distributed GRP pipes in Figure 8 were examined, it was observed that there were air gaps and matrix cracks. However, it has been observed that the fillers are homogeneously distributed, and the random orientation of the fibers is good. The increase in tensile strength of composites is due to the increase in fiber content, due to the fact that fibers play an important role in tensile strength and their ability to resist crack propagation. When the Initial Specific Ring Stiffness and LTS test results of AFS 40-45 grain distributed GRP pipes are evaluated, it is thought

that the amount of fiber used for this mixture is enough to fulfill this task.

When the SEM images in the core region of F 0.8 (optimization 1) grain distributed GRP pipes in Figure 9 were examined, it was observed that the fillers were homogeneously distributed, and the random orientation of the fibers is good. In addition, it was observed that the matrix structure was adhered on the surface of the broken fiber pieces and fiber cavities were formed on the broken matrix surface. When this situation is evaluated together with the Initial Specific Ring Stiffness and LTS test results of GRP pipes with

F 0.8 (optimization 1) grain distribution, it is understood that the matrix and fiber interface bond strength is strong. Considering these results, it was concluded that it is possible to use lower rates of resin in GRP pipes with F 0.8 (optimization 1) grain distribution in this study.

#### 4. CONCLUSIONS

In this study, silica sands with AFS 40-45 grain fineness number currently used in GRP pipe production were used, and alternatively, F 0.8 grain distributions were used to reduce the resin consumption and increase the mechanical properties. As a result of the study;

It was determined that mechanical properties such as stiffness and longitudinal tensile strengths decreased as a result of reducing the amount of resin. However, all GRP pipes produced within the scope of the study reached the minimum stiffness, and the LTS value required in the standard and even higher values.

In the pipe number 2 with F 0.8 (optimization 1) grain distribution, 8.64 % higher stiffness was obtained compared to the reference GRP pipe production and 57.8 % higher LTS value was obtained than the minimum LTS value of 135 N/mm required in the standard by incorporating 3.5 % less resin.

In the pipe number 3 with F 0.8 (optimization 1) grain distribution, 44.11 % higher stiffness value was obtained than the minimum stiffness value of 10.000 N/m<sup>2</sup> and 50.4 % higher LTS value was obtained than the minimum LTS value of 135 N/mm required in the standard by incorporating 14 % less resin.

As a result of the study, when GRP pipes are produced incorporating 14 % less resin in F 0.8 (optimization 1) grain distribution, 44.11 % higher stiffness and 50.4 % higher LTS value was obtained than the minimum value required in the standard.

In other words, it was concluded that F 0.8 (optimization 1) grain distribution is effective in reducing resin consumption, and it is possible to produce GRP pipes with F 0.8 (optimization 1)

grain distribution at a lower cost by providing up to the ratio of 14 % resin consumption.

#### *Acknowledgments*

The authors gratefully acknowledge the financial support of the Scientific and Technological Research Council of Turkey (TUBITAK) and like to thank Superlit Pipe Industry Inc. for carrying out GRP pipe productions.

#### *Funding*

This work was supported by The Scientific and Technological Research Council of Turkey (TUBITAK), TUBITAK 1505: University-Industry Cooperation Project [Grant Number: 5140058], and GRP pipe productions were carried out by Superlit Pipe Industry Inc., at Kaynaşlı / DÜZCE factory in Turkey.

#### *The Declaration of Conflict of Interest/ Common Interest*

The authors declare that they have no known competing for financial interests or personal relationships that could have appeared to influence the work reported in this paper.

#### *Authors' Contribution*

The authors contributed to the study as follows. Şevki EREN: Investigation, Writing- Original draft preparation, Methodology, Formal analysis (35 %), Özcan ÇAĞLAR: Conceptualization, Methodology (20 %), Neslihan GÖKÇE: Conceptualization, Methodology (15 %), Azime SUBAŞI: review & editing, Visualization, Validation (15 %), Serkan SUBAŞI: Methodology, Supervision, Project administration (15 %).

#### *The Declaration of Ethics Committee Approval*

This study does not require ethics committee permission or any special permission.

### ***The Declaration of Research and Publication Ethics***

The authors of the paper declare that they comply with the scientific, ethical and quotation rules of SAUJS in all processes of the paper and that they do not make any falsification on the data collected. In addition, they declare that Sakarya University Journal of Science and its editorial board have no responsibility for any ethical violations that may be encountered, and that this study has not been evaluated in any academic publication environment.

### **REFERENCES**

- [1] Jin NJ, Hwang HG, Yeon JH, “Structural analysis and optimum design of GRP pipes based on properties of materials”, *Constr Build Mater.*, vol. 38, pp. 316–26, 2013. <https://doi.org/10.1016/j.conbuildmat..07.115>.
- [2] Rafiee R, “On the mechanical performance of glass-fibre-reinforced thermosetting-resin pipes: A review”, *Compos Struct.*, vol.143, pp. 151–64, 2016. <https://doi.org/10.1016/j.compstruct.2016.02.037>.
- [3] Zoghi M, “The International handbook of FRP composites in civil engineering”, CRC Press., 2013.
- [4] Farshad M, Neola A, “Strain corrosion of glass fibre-reinforced plastics pipes”, *Polym Test.*, vol.23, pp. 517–21, 2004. <https://doi.org/10.1016/j.polymertesting.2003.12.003>.
- [5] Faria H, Guedes RM, “Long-term behaviour of GFRP pipes: Reducing the prediction test duration”, *Polym Test.*, vol. 29, pp. 337–45, 2010. <https://doi.org/10.1016/j.polymertesting.2009.12.008>.
- [6] Road N, “A review of particulate reinforcement theories for polymer composites”, *Composites*, vol. 23, pp. 376, 1992. [https://doi.org/10.1016/0010-4361\(92\)90358-2](https://doi.org/10.1016/0010-4361(92)90358-2).
- [7] Mansour SH, Abd-El-Messieh SL, “Electrical and mechanical properties of some polymeric composites”, *J Appl Polym Sci.*, vol. 83, pp. 1167–80, 2002. <https://doi.org/10.1002/app.2283>.
- [8] Agarwal BD, Broutman LJ, Chandrashekhara K, “Analysis and performance of fiber composites”, John Wiley & Sons., 2006.
- [9] Guerrini GL, “Applications of high-performance fiber-reinforced cement-based composites”, *Appl Compos Mater.*, vol. 7, pp. 195–207, 2000. <https://doi.org/10.1023/A:1008994020916>.
- [10] Turkeli A, “Sand, sand additives, sand properties, and sand reclamation”, *Foundry Technology*, [http://mimoza.marmara.edu.tr/~altan.turkeli/files/cpt-2-sand\\_sand.pdf](http://mimoza.marmara.edu.tr/~altan.turkeli/files/cpt-2-sand_sand.pdf). (accessed 12/02/2021).
- [11] Molding sand: image analysis of molding sand particle sizing in the foundry industry. <https://www.microtrac.com/applications/knowledge-base/molding-sand/> (accessed 12/02/2021).
- [12] Kumar S, Kumar P, Shan HS, “Optimization of tensile properties of evaporative pattern casting process through Taguchi’s method”, *J Mater Process Technol.*, vol. 204, pp. 59–69, 2008. <https://doi.org/10.1016/j.jmatprotec.2007.10.075>.
- [13] Fuller WB, Thompson SE, “The laws of proportioning concrete”, *Trans Amer Soc Civ Engrs Bd.*, 1907.
- [14] Shi H, Wei L, “Laboratory evaluation on performance of glass fiber reinforced plastic mortar pipe culverts”, *Stavební Obz - Civ Eng J.*, vol. 27, pp. 60–71, 2018. <https://doi.org/10.14311/cej.2018.01.0006>.

- [15] Rafiee R, Reshadi F, “Simulation of functional failure in GRP mortar pipes”, *Compos Struct.*, vol. 113, pp.155–63, 2014. <https://doi.org/10.1016/j.compstruct.2014.03.024>.
- [16] Gokce N, Yilmazer U, Subasi S, “Effect of fiber and resin types on mechanical properties of fiber-reinforced composite pipe”, *Emerg Mater Res.*, vol. 8, pp. 452–8, 2019. <https://doi.org/10.1680/jemmr.18.00093>.
- [17] Ş. Eren, S. Subaşı, “A research on the production of hybrid fiber and mineral reinforced high-performance polymer composite material”, PhD Thesis, Duzce University, Institute of Science, Interdisciplinary Composite Materials Technologies Department, Düzce, Turkey, 2018.
- [18] CC (Savurma Döküm) - Superlit Boru San. A.Ş. <http://www.superlit.com/tr/teknoloji-ve-kalite/savurma-dokum-cc/> (accessed 12/02/2021).
- [19] ISO (2019) 7685: Plastics piping systems- Glass-reinforced thermosetting plastics (GRP) pipes — Determination of initial specific ring stiffness.
- [20] ISO (2016) 8513: Plastics piping systems — Glass-reinforced thermosetting plastics (GRP) pipes — Test methods for the determination of the initial longitudinal tensile strength.



SAKARYA ÜNİVERSİTESİ

# FEN BİLİMLERİ ENSTİTÜSÜ DERGİSİ

Sakarya University Journal of Science  
SAUJS

e-ISSN: 2147-835X | Founded: 1997 | Period: Bimonthly | Publisher: Sakarya University |  
<http://www.saujs.sakarya.edu.tr/en/>

Title: Radical Scavenging and Antibacterial Activities of *Ruta buxbaumii* Poir.  
(Rutaceae) Growing in Raman Mountain-Batman

Authors: Alevcan KAPLAN

Received: 2021-03-16 00:00:00

Accepted: 2021-08-18 00:00:00

Article Type: Research Article

Volume: 25

Issue: 5

Month: October

Year: 2021

Pages: 1148-1158

How to cite

Alevcan KAPLAN; (2021), Radical Scavenging and Antibacterial Activities of *Ruta buxbaumii* Poir. (Rutaceae) Growing in Raman Mountain-Batman. Sakarya University Journal of Science, 25(5), 1148-1158, DOI:

<https://doi.org/10.16984/saufenbilder.898031>

Access link

<http://www.saujs.sakarya.edu.tr/tr/pub/issue/65589/898031>

New submission to SAUJS

<http://dergipark.org.tr/en/journal/1115/submission/step/manuscript/new>

## Antibacterial and Radical Scavenging Activities of *Ruta buxbaumii* Poir. (Rutaceae) Growing in Raman Mountain-Batman

Alevcan KAPLAN\*<sup>1</sup>

### Abstract

The members of the Rutaceae genus have found a wide application area in traditional medicine in many countries from ancient times to today; they have been used for many purposes in Turkey. *Ruta* species have many pharmacological properties such as inducing abortion, antirheumatic, hypoglycemic, anthelmintic, antipyretic, antiepileptic, antidiabetic, against epilepsy, vertigo, headache and in eye diseases, anthelmintic and against poisoning. In this paper, it was aimed to determine the antimicrobial and radical scavenging activities of methanol (MeOH), petroleum ether (PE), ethyl acetate (EtOAc) and ethanol (EtOH) extracts of *Ruta buxbaumii* Poir. growing naturally in Raman mountain, Batman. Antimicrobial activities of extracts were evaluated using disc diffusion method. Two Gram-positive bacteria (*Staphylococcus aureus* ATCC 25923, *Streptococcus pyogenes* ATCC 19615) and two Gram-negative bacteria (*Pseudomonas aeruginosa* ATCC 27853, *Escherichia coli* ATCC 25922) were used to determine the antibacterial activity. Results demonstrated that although *R. buxbaumii* extracts showed close antibacterial effects, EtOAc extract showed the highest effect against *S. pyogenes* with  $23.5 \pm 1.2$  inhibition zones, while EtOH extract showed the lowest effect against *P. aeruginosa* with  $11.8 \pm 0.2$  inhibition zones. All the extracts showed no clearance of zone inhibition for against *E. coli*. Antioxidant properties and activities were evaluated by using total phenolic content (TPC), total flavonoid content (TFC), DPPH (2,2-diphenyl-1-picryl-hydrazyl-hydrate) free radical scavenging activity. The results showed that while activity of the EtOH extract of *R. buxbaumii* was the highest ( $54.10 \pm 0.13$  mg GAE/g extract) for total phenolic substance content, MeOH and EtOH extracts were found to be higher ( $47.52 \pm 0.19$  mg QE/g extract and  $46.86 \pm 0.16$  mg QE/g extract) for total flavonoid content, respectively. Also, radical scavenging activities such as (DPPH) of extracts were investigated, and it was revealed that EtOH extracts (73.6 %), MeOH (60 %), EtOAc (40 %) and PE extract (25 %), respectively. From these results indicates that this species can be used in the pharmaceutical application as a valuable bioproduct with new functional properties in foods.

**Keywords:** Antibacterial activity, DPPH, total flavonoid content, total phenolic content, *R. buxbaumii*.

### 1. INTRODUCTION

The use of herbs in treatment began with the history of humanity. Thousands of years ago, people realized the therapeutic power of herbs and

started benefiting them to sustain a healthy life. In Anatolia, where folk medicine practices are common, folk remedy practices have survived to the present day after long experiences. Many drugs used in modern medicine are also derived

\* Corresponding author: kaplanalevcan@gmail.com

<sup>1</sup> Batman University.

ORCID: <https://orcid.org/0000-0001-6738-7527>

from plants [1]. The therapeutic use of herbs varies according to the development level of the countries. In developing countries, 80% of the population benefit from herbal products for therapeutic purposes [2]. In some Asian, African, and Middle Eastern countries, this rate rises to 95%. In developed countries, this rate is less; 40-50% in Germany, 42% in the USA, 48% in Australia, and 49% in France [3]. The World Health Organization predicts that the treatment with medicinal plants will increase within the next years all over the world. Plants can produce secondary metabolites to protect them from natural enemies such as bacteria, viruses, fungi, and insects [4]. Medicinal plants are rich in chemical bioactive components such as terpenoids, phenolics, alkaloids, flavonoids, amino acids, saponins, glycosides, diterpenes and triterpenes [5].

The Rutaceae family is part of the order Sapindales, part of the Eurosid II group, which is part of the rosids in eudicots in cladistic studies based on DNA sequence analysis in angiosperms [6-7]. The Rutaceae family is a large family consisting of trees, shrubs, and woody species, containing 1600 species and ~155 genera, mostly tropical and subtropical [8-9]. The genus *Ruta* is represented by nine species all over the world; four species in the Mediterranean phytogeographic region, two species in Corsica, three species in the Canary Islands, and 55% of them are endemic [10]. The Rutaceae family includes species that are particularly appreciated in folk medicine for their numerous medicinal properties and benefits to human health. *Ruta* is one of the most well-known genera of the Rutaceae family, native to the Mediterranean region and known for its use in traditional medicine [11]. Today, this genus is cultivated in many parts of the world for its medicinal properties [12]. The most studied species of the genus *Ruta* in the world are *R. chalepensis* L., *R. graveolens* L., *R. montana* L. Extracts and essential oils of these species have a wide variety of medical uses such as gastric, diuretic, inflammatory, rheumatic disorders, anti-inflammatory, antioxidant, hypoglycemic, emmenagogue, spasmolytic, menstrual problems, as a sedative, antipyretic, antiplatelet and

anticholinesterase, an antibacterial, antifungal and as an anthelmintic agent and also as a food flavoring agent [13-14-15-16-17-18-19-20]. In their study on the genus *Ruta*, Coimbra et al. (2020) confirmed that different parts of the plant are used in folk medicine to treat a wide variety of diseases. Although its main use is in the gynecological field, it has also been described in the treatment of pain, fever, nausea, inflammation, infections, and nervous disorders. *Ruta* species contain many bioactive substances. The main classes of compounds are coumarins, alkaloids, terpenes, and flavonoids. Due to their wide range of biological abilities, the components of *Ruta* species are of great interest in medicinal chemistry, and many are used in medicine [22-23].

According to Townsend [24], the genus *Ruta* is represented by two species, *R. chalepensis*, and *R. montana*, in Turkey. However, in later studies, the genus *Ruta* is represented with six species such as *Ruta buxbaumii* (sin. *Haplophyllum buxbaumii*. Recently, several taxa from the genus *Haplophyllum* were transferred to *Ruta* and *R. buxbaumii* is one of them.), *R. chalepensis*, *R. montana*, *R. suaveolens*, *R. thesioides* and *R. villosa*. [25-26-27-28]. A literature review on *R. buxbaumii*, which grows on Mount Raman in Batman, one of the *Ruta* species traditionally known for its sedative and gas-digesting effects [29], reveals that there is no information about its biological properties. In addition, the region where medicinal and aromatic plants grow, climatic conditions, and soil properties directly affect plant components. The fact that Mount Raman is a unique region and there are not many studies in this sense reveals the necessity of this study. In line with this background, in the present study, the effect of the antibacterial and antioxidant activities of different extracts of the *R. buxbaumii* plant was investigated for the first time in this study.

## 2. MATERIALS AND METHOD

### 2.1. Source of Plant Material

The aerial parts of plant material was collected at flowering time in May 2020, from natural habitat

of Raman mountain (Batı Raman campus of Batman University). The taxonomical identity of the plant was confirmed by Dr. Alevcan Kaplan. Voucher specimens have been deposited at Batman University (voucher no. 2020/013).

## 2.2. Preparation of Plant Extract

The aerial parts of the plant were washed and dried in the shade at room temperature to remove contamination. The plants were dried at room temperature for two weeks. The samples were then ground with a blade-carbide grinding. The ground sample was macerated at room temperature using 1: 20 MeOH, EtOH, PE, EtOAc respectively to prepare various extracts. The beaker was covered with aluminum foil and shaken continuously using a rotary shaker at 100 rpm. The extraction process was performed in the dark for 3 days. New solvent volumes were changed until the color of the extract became colorless. The extracts were filtered through filter paper. The total volume of the extract was recorded. Subsequently, the extract solution was concentrated to dryness under vacuum and reduced pressure using a rotary evaporator at 60 °C to obtain concentrated extracts. These extracts were stored at 4°C for further bioassays [30-31].

## 2.3. Biological Evaluations

### 2.3.1. Antibacterial Screening

Disc diffusion method was performed according to Shryock et al. [32] with some changes. Four microbial strains were tested, including two Gram-positive bacteria (*S. aureus* ATCC 25923, *S. pyogenes* ATCC 19615) and two Gram-negative bacteria (*P. aeruginosa* ATCC 27853, *E. coli* ATCC 25922). The blank discs were filled with concentration of 5.0 mg/disc of extracts. Then, the petri dishes were incubated at 37 °C or 24 hours. The diameter of the inhibition zone around each disc was then measured. Antibacterial activity was determined by the diameter of the inhibition zones around the disc on the agar surface. All tests were performed in triplicate.

### 2.3.2. Determination of Total Phenolic Content (TPC)

The total phenolic content of the extracts were made according to the method of Singleton et al. [33]. 0.2 mL of sample solutions (2 mg/mL) prepared for the study were taken and after adding 9 ml of distilled water, 0.2 mL of Folin Ciocalteu reagent was added and left to stand for 3 minutes. Finally, 0.6 mL of Na<sub>2</sub>CO<sub>3</sub> (20%) was added and the total volume was adjusted to 10 ml. After incubating in the dark for 2 hours at room temperature, absorbance was measured at 760 nm. Gallic acid was used to create the standard calibration curve. 0.1 mg/mL was prepared as the master stock and seven different concentrations were obtained by dilution. 0.2 mL of sample solution was added for the control. According to the gallic acid standard, the total phenolic substance in all plant extracts was calculated as mg gallic acid equivalent (GAE)/g extract. The analysis was performed in triplicate.

### 2.3.3. Determination of Total Flavonoid Content (TFC)

The total flavonoid content of the extracts Arvouet-Grand et al. [34] was made according to the method. In the preparation of the experiment, 100 µl of 10% aluminum nitrate and 100 µl of 1 M potassium acetate were taken and the extract was added so that the final concentration of the plant extract was 100 µg/ml. The final volume of the experiment was completed to 5 mL with 99 % ethanol. After incubating in the dark for 40 minutes at room temperature, absorbance was measured at 417 nm. For control, 200 µl of the sample solution was added instead of extract. For the quercetin standard, master stock 0.5 mg/mL was prepared and eight different concentrations were obtained by dilution. The total flavonoid substance content was expressed as mg quercetin equivalent (QE)/g extract. The analysis was performed in triplicate.

## 2.4. Antioxidant Activity

### 2.4.1. Determination of DPPH Radical Scavenging Activity

Free radical activities of extracts were determined using DPPH free radical Gezer et al. [35]. For the experiment, the concentration was prepared by dissolving 4 mg DPPH in 100 mL methanol. For each sample, 3.2 mL DPPH radical and 200  $\mu$ L (500  $\mu$ g/mL) of extract solutions were added. After 30 minutes of incubation at room temperature in the dark, absorbance was measured at 517 nm. For control, 200  $\mu$ L extract solvent was added to the test tube. Analysis was performed in triplicate. The following formula was used to determine the % DPPH radical scavenger.

$$\% \text{ DPPH scavenging activity} = [(A_{\text{blank}} - A_{\text{extract}}) / A_{\text{blank}}] \times 100.$$

$A_{\text{blank}}$ : Absorbance of the control.

$A_{\text{extract}}$ : Absorbance of the reagent with extract.

## 2.5. Statistical Analysis

The analysis of variance of the data obtained was made according to the ANOVA procedure. The difference between the means was evaluated at the level of  $p < 0.05$  according to Duncan comparison test. The data obtained are given as mean  $\pm$  standard deviation. Data calculations were performed using SPSS for Windows (version 15.0, SPSS®, Chicago, USA).

## 3. RESULTS AND DISCUSSION

Plants have been used for centuries for medicinal purposes in the treatment of various diseases and enteritis [36-37]. The properties of plants that are lethal for microorganisms and important for human health have been investigated in laboratories since 1926. Recently, as well as all over the world, the use of plants found in the natural flora for different purposes such as treatment, food, tea, spice, paint, insecticide,

veterinary cure, resin, glue, essential oil, beverage, and cosmetics has become a part of our study area [1]. In this context, plant extracts are examined for their biological activities for the management of complex diseases. For instance, plant-based antioxidant compounds have been claimed to inhibit the oxidation process by reacting with free radicals, chelating catalytic metals, and scavenging oxygen molecules found in biological systems. Thus, in terms of biological activities, due to the pluripotential of plant extracts, including antioxidant, antimicrobial, antidiabetic properties, herbal extracts are paving the way for global recognition and inclusion in pharmaceutical drugs [38]. Antibacterial studies on medicinal plants are a rich source of antimicrobial agents. As synthetic and semi-synthetic antimicrobial drugs are abandoned on the market, there is a continuing need for new research to cope with the increasing evolution of many antimicrobial-resistant strains of organisms [39]. In this study carried out for this purpose, antibacterial and some biological activities of *R. buxbaumii* plant extracts were examined. The antibacterial activity of *R. buxbaumii* extracts was determined on four bacterial strains (Table 1). These selected microorganisms are known for their strong resistance, invasive and toxic powers, and are pathogenic in humans. They are frequently found in many infections that cause clinical and therapeutic problems in Turkey. The results of antibacterial screening of MeOH, PE, EtOAc and EtOH extract of *R. buxbaumii* are presented in Table 1. The antibacterial activity of the extracts was evaluated against streptomycin. All extracts exhibited strong antibacterial activity against Gram (+) strain *S. aureus* and *S. pyogenes*. On the other hand, weak to moderate antibacterial activity was found for the Gram (-) strain *P. aeruginosa*. Also, all the extracts showed no clearance of zone inhibition against the Gram (-) strain *E. coli*. EtOAc extract showed the highest zone of inhibition against *S. pyogenes* strains with  $23.5 \pm 1.2$  mm. EtOH extract showed the lowest zone of inhibition against *P. aeruginosa* strain with  $11.8 \pm 0.2$  mm. This suggests that it may have resulted from both the diversity of the compounds contained in the extracts and their synergistic interactions rather than individual activity.

Table 1 Antibacterial activity of the various solvent extracts from *R. buxbaumii* against human pathogenic bacteria.

Microorganisms	Inhibition zone (mm)				Antibiotic
	MeOH	EtOH	PE	EtOAc	Streptomycin
<i>S. aureus</i> ATCC 25923	21.3±0.5	21.6±0.0	22±0.5	21±0.0	27.0±0.1
<i>S. pyogenes</i> ATCC 19615	18±0.0	16.3±0.6	18.1±0.6	23.5±1.2	27.0±0.1
<i>P. aeruginosa</i> ATCC 27853	13.7±0.6	11.8±0.2	13±1.2	14± 1.1	27.0±0.1
<i>E. coli</i> ATCC 25922	na	na	na	na	na

\*na: not active

Antimicrobial activities of some species belonging to the genus *Ruta* have been reported by many researchers [22-23-40-41-42-16-43]. Bekkar et al. [20] reported that methanol extract had a strong antimicrobial effect against *S. enterica* ssp *arizonae*. The results of this study are in agreement with the report of Ivanova et al. [44] who confirmed that the different extracts of *R. graveolens* L., a related plant, have antimicrobial activity. Regarding antimicrobial activity, this study found inhibitory activity against *S. aureus* and *S. pyogenes* among the bacterial strains tested, while found no activity against *E. coli*. For *R. chalepensis* plant, antibacterial activity characteristics in the current experiment were close to the content reported by Ouerghemmi et al. [16]. In their study examining the antibacterial activity of the spontaneous and cultivated *R. chalepensis* plants in Tunisia, Ouerghemmi et al. [16] reported that while it exhibited moderate activity against the *S. aureus* strain, low or no activity against *P. aeruginosa* and *E. coli*. The effectiveness of these extracts against bacteria may be partly due to their phenolic composition. The studies of Nagarjuna and Al-Rajab [45] on *R. graveolens* was found antibacterial activity against gram-positive and gram-negative bacteria, resulting in several common human pathogenic bacteria, including methicillin-resistant *S. aureus* and the yeast *C. albicans*. Several studies have linked the inhibitory effect of plant extracts against bacterial pathogens to their phenolic composition [43-46-47]. The inhibitory effect of phenolic compounds can be explained by adsorption to cell membranes, interaction with enzymes, substrate, and metal ion deprivation [48]. Flavonoids and phenolic acids are very strong free radical scavengers. These compounds, taken

through food, largely eliminate the effects of oxygen radicals, which are called "oxidation stress", and adversely affect human health [49]. Table 2 shows the total phenolic (TPC) and total flavonoid content (TFC). The formation of blue density indicates the presence of phenolic compounds. Statistical differences were found between samples. The highest phenolic content of *R. buxbaumii* was  $54.10 \pm 0.13$  mg GAE/g extract in the EtOH extract and the lowest phenolic content of *R. buxbaumii* was  $34.12 \pm 1.2$  mg GAE/g extract in the PE. The phenolic substance content of the EtOAc extract was calculated as  $44.25 \pm 0.06$  mg GAE/g extract and was statistically significant. The highest flavonoid content of *R. buxbaumii* was  $47.52 \pm 0.19$  mg GAE/g extract in the MeOH extract and the lowest phenolic content of *R. buxbaumii* was  $18.94 \pm 0.24$  mg GAE/g extract in the PE. The levels of MeOH and EtOH extracts were high in terms of flavonoid but not significantly different between the extracts. The flavonoid substance content of the EtOAc extract was calculated as  $24.02 \pm 0.54$  mg QE/g extract and was statistically significant. As can be seen from the data, PE extract contains less amount of both phenolic and flavonoid substances than other extracts, and this was statistically significant. Total phenolic content (TPC) in this experiment was close to the content reported by Fakhfakh et al. [50]; they found phenolic content of  $54.13$  mg GAE/g extract in EtOH extract. Kacem et al. [16] obtained the highest TPC content of EtOH, water, hexane, EtOAc from EtOH extract with  $178$  mg GAE/g extract. Gali and Bedjou [30] found the highest TFC in butanol extract with  $210.00 \pm 4.93$   $\mu$ g GAE/mg extract, even reported that EtOAc extract was higher than EtOH ( $61.61 \pm 0.70$   $\mu$ g GAE/mg extract) extract. [51] found that the MeOH extract TFC  $1328.8$  mg GAE/100 g dry weight. Yaman et al. [52] examined the

antioxidant activities of MeOH and EtOH extracts of wild *R. chalepensis* L. (above-ground part) and *R. montana* L. (leaf-flower and stem parts). Total flavonoid content in dry weight of MeOH and EtOH extracts of *R. chalepensis* was found higher than other extracts except for MeOH leaves-flowers extract of *R. montana*. In their study on *in vitro*, antioxidant activity and total phenolic content of *R. montana* L., Merghem and Dahamna

[53] were found that EtOAc contained high amounts of total polyphenols ( $257.1 \pm 0.703 \mu\text{g}$  gallic acid equivalent/mg of extract), tannins ( $251 \pm 1.41 \mu\text{g}$  tannic acid equivalent /mg of extract), and flavonoids ( $117.4 \pm 3.451 \mu\text{g}$  quercetin equivalents/mg of extract), respectively. The differences between the values suggested that the plant species, locality, and extraction methods may cause this.

Table 2 Total phenolic and flavonoid contents of *R. buxbaumii* extracts.

Extracts	Total Phenolic Content (mg GAE/g extract)	Total Flavonoid Content (mg QE/g extract)
MeOH	49.60±0.17 <sup>b</sup>	47.52±0.19 <sup>a</sup>
EtOH	54.10±0.13 <sup>a</sup>	46.86±0.16 <sup>a</sup>
PE	34.12±1.2 <sup>d</sup>	18.94±0.24 <sup>c</sup>
EtOAc	44.25±0.06 <sup>c</sup>	24.02±0.54 <sup>b</sup>

\* Statistically, each column was evaluated separately and the differences were shown in lower case according to the  $p < 0.05$  level.

Various methods are widely used to measure the antioxidant capacity of extracts. Each method results in the generation or use of a different radical that is directly involved in the oxidative process through various mechanisms. Among the free radical scavenging methods, the DPPH method is fast, simple, and inexpensive compared to other test models. When the DPPH radical is scavenged with an antioxidant compound via hydrogen donation to form a stable DPPH-H molecule, the color of the solution changes from purple to yellow [54].

The results of the antioxidant properties of the crude extracts assessed by the DPPH• free radical scavenging method are shown in Figure 1. In general, the strongest activity was 73.6 % in EtOH extract, followed by 60 % in MeOH, 40 % in EtOAc, and 25 % in PE extract, respectively. Kacem et al. [16] examined the radical scavenging activity of *R. chalepensis* extracts at different concentrations and found that the 0.125 mg / mL sample of ethanol extract had inhibition of approximately 80-70 %. This value was found to be consistent with this study. More recently, Bekkar et al. [20] have reported an important antioxidant activity of *R. chalepensis*. Yaman et al. [52] examined the radical scavenging activities of the extracts such as DPPH and ABTS. It was observed that *R. chalepensis* extracts exhibited

higher activity when evaluated on a solvent basis. The studies of Merghem and Dahamna [53] on *R. montana* was found that EtOAc extract showed the highest scavenging capacity followed by MeOH, aqueous and chloroform extract. Ouerghemmi et al. [43] reported that the highest DPPH activity of *R. chalepensis* was in flower, leaf, and stem MeOH extracts, respectively. Kacem et al. [16] reported that the ethanol extract of the leaf-stem sample of *R. chalepensis* species had more radical scavenging activity than water, EtOAc and hexane extract, and even less aqueous extract activity than EtOAc. Antioxidant activities of extracts; It is due to reduction of hydroperoxides, inactivation of free radicals, complexation with metal ions or a combination of these. It is thought that some of the antioxidant activity provided by these mechanisms is due to flavonoids. Additionally, the antioxidant activities observed in plants may result from the synergistic interaction of two or more compounds in the plant. It has been reported that many natural antioxidant compounds generally act synergistically with each other, thus providing an effective defense against free radicals [55].

Due to the structural differences of herbal samples, it is not possible to talk about the use of a single solvent system for each sample in extraction methods. As the results clearly show, the analyzes by working with different solvents,

the most suitable solvent can be selected, so that accurate and high results can be obtained about the antioxidant capacity of the plants. According to the results, it was clearly seen that the differences in the phenolic content of the different extracts of the studied plant affected their antioxidant properties. Based on this, it can be said that the different antioxidant activities of the

extracts are due to the amount and chemical structure of phenols that can pass into the solvent during extraction. Lastly, the present study has found parallel results to other studies. It is clear that there is a positive correlation between total phenolic and flavonoid content and antioxidant activity.

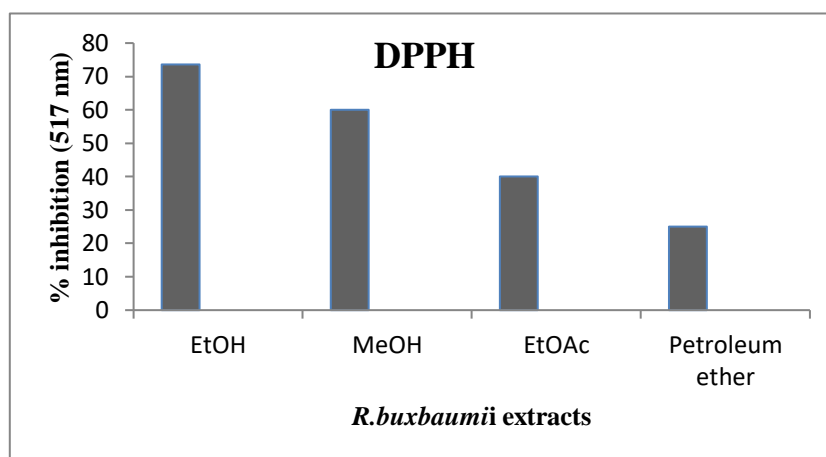


Figure 1 The DPPH free radical activities of the various solvent extracts from *R. buxbaumii*.

#### 4. CONCLUSION

This study showed that *R. buxbaumii* Poir. several extracts have significant antibacterial, antiradical activities and rich phenolic and flavonoid content. Results from experiments support biological activities. It was suggested that the variation of *R. buxbaumii* in this study may be due to differences affecting biochemical and physiological structures such as species, organ, physiological age, harvest time, and locality. Preliminary findings of our study suggest that *R. buxbaumii* Poir. could be used as a natural source of medicinal application for antimicrobial and antioxidant activities. However, further investigations on other species of the family Rutaceae are encouraged to determine their potential anti-agent (antimalarial, antifungal etc.) activities. In addition, the search for natural antioxidants that can replace synthetic antioxidants for the future continues rapidly. It is recommended to determine plant extracts with high antioxidant activity with such studies, to examine their antioxidant effects in food and health systems, and to ensure the continuity of studies to apply alternative ways to treat diseases.

#### Funding

The author received no financial support for this research, authorship, and/or publication of this paper.

#### The Declaration of Conflict of Interest/ Common Interest

No conflict of interest or common interest has been declared by the author.

#### The Declaration of Ethics Committee Approval

The author declares that this document does not require an ethics committee approval or any special permission.

#### The Declaration of Research and Publication Ethics

The author of the paper declares that he complies with the scientific, ethical and quotation rules of SAUJS in all processes of the paper and that he does not make any falsification on the data collected. In addition, he declares that Sakarya University Journal of Science and its editorial board have no responsibility for any ethical

violations that may be encountered, and that this study has not been evaluated in any academic publication environment other than Sakarya University Journal of Science.

## REFERENCES

- [1] E. Faydaoğlu and MS. Sürücüoğlu, “Geçmişten Günümüze Tıbbi ve Aromatik Bitkilerin Kullanılması ve Ekonomik Önemi”, Kastamonu Üniversitesi Orman Fakültesi Dergisi, vol.11, no. 1, pp.52-67, 2011.
- [2] WHO, “WHO Guidelines on Safety Monitoring of Herbal Medicines in Pharmacovigilance Systems”, Geneva, Switzerland: World Health Organization, 2004.
- [3] A. Titz, “Policy, Research & Development and Commercialisation Strategies, Scope for Diversified and Sustainable Extraction”, Bangalore, India, pp.72-80, 2004.
- [4] S. Erdem, P. Ata Eren, “Tedavi Amacıyla Kullanılan Bitkiler Ve Bitkisel Ürünlerin Yan Etkileri”, Türk Hijyen ve Deneysel Biyoloji Dergisi, vol. 66, no. 3, pp.133-141, 2009.
- [5] TG. Amabye and TM. Shalkh, “Phytochemical Screening and Evaluation of Antibacterial Activity of *Ruta graveolens* L. -A Medicinal Plant Grown around Mekelle, Tigray, Ethiopia”, Natural Products Chemistry and Research, vol. 3, no.6, 195, 2015.
- [6] APG, “The Angiosperm Phylogeny Group. An update of the Angiosperm Phylogeny Group classification for the orders and families of flowering plants: APG II”, Botanical Journal of Linnean Society, vol.141, pp. 399-436, 2003.
- [7] DE. Soltis, PS. Soltis, PK. Endress and MW. Chase, “Phylogeny and evolution of angiosperms”, Sunderland, MA, Sinauer, 2005.
- [8] L. Wei, YZ. Wang and ZY. Li, “Floral ontogeny of Ruteae (Rutaceae) and its systematic implications”, Plant Biology, vol. 14, pp.190-197, 2012.
- [9] MW. Chase, CM. Morton and JA. Kallunki, “Phylogenetic relationships of Rutaceae: a cladistic analysis of the subfamilies using evidence from *rbcL* and *atpB* sequence variation”, American Journal of Botany, vol. 86, pp.1191-1199, 1999.
- [10] G. Salvo, G. Bacchetta, F. Ghahremaninejad and E. Conti, “Phylogenetic relationships of Ruteae (Rutaceae): New evidence from the chloroplast genome and comparisons with non-molecular data”, Molecular Phylogenetic and Evolution, vol.49, pp. 736-748, 2008.
- [11] A. Pollio, A. De Natale, E. Appetiti, G. Aliotta and A. Touwaide, “Continuity and change in the Mediterranean medical tradition: *Ruta* spp.(rutaceae) in Hippocratic medicine and present practices”, Journal of Ethnopharmacology, vol.116, no.3, pp.469-482, 2008.
- [12] SA. Parray, JU. Bhat, G. Ahmad, N. Jahan, G. Sofi, SMF. Iqbal, “*Ruta graveolens*: from Traditional System of Medicine to Modern Pharmacology: an Overview”, American Journal of PharmTech Research, vol. 2, no. 2, 240-252, 2012.
- [13] K. Günaydin and S. Savca, “Phytochemical studies on *Ruta chalepensis* (LAM.) lamarck”, Natural Product Research, vol.19, no.3, pp. 203-210, 2006.
- [14] F. Haddouchi, TM. Chaouche, Y. Zaouali, R. Ksouri, A. Attou and A. Benmansour, “Chemical composition and antimicrobial activity of the essential oils from *Ruta* species growing in Algeria”, Food Chemistry, vol.141, no.1, pp.253- 258, 2013.

- [15] S. Bouajaj, A. Romane, A. Benyamna, I. Amri, M. Hanana, L. Hamrouni and M. Romdhane, "Essential oil composition, phytotoxic and antifungal activities of *Ruta chalepensis* L. leaves from High Atlas Mountains (Morocco)", *Natural Product Research*, vol. 28, no.21, pp. 1910-1914, 2014.
- [16] M. Kacem, I. Kacem, G. Simon, A. Benmansour, S. Chaabouni, A. Elfeki, M. Bouaziz, "Phytochemicals and bio-logical activities of *Ruta chalepensis* L. growing in Tunisia", *Food Bioscience*, vol. 12, pp. 73-83, 2015.
- [17] MR. Loizzo, T. Falco, M. Bonesi, V. Sicari, R. Tundis and M. Bruno, "*Ruta chalepensis* L. (Rutaceae) leaf extract: chemical composition, antioxidant and hypoglycaemic activities", *Natural Product Research*, vol. 32, no.5, pp.521-528, 2018.
- [18] S. Al Majmaie, L. Nahar, GP. Sharples, K. Wadi and SD. Sarker, "Isolation and Antimicrobial Activity of Rutin and its Derivatives from *Ruta chalepensis* (Rutaceae) Growing in Iraq". *Records of Natural Products*, vol.13, no.1, pp.64- 70, 2018.
- [19] L. Gali, F. Bedjou, "Antioxidant and anticholinesterase effects of the ethanol extract, ethanol extract fractions and total alkaloids from the cultivated *Ruta chalepensis*", *South African Journal of Botany*, vol. 120, pp.163-169, 2019.
- [20] NEH. Bekkar, B. Meddah, YS. Çakmak, B. Keskin, "Phenolic Composition, Antioxidant And Antimicrobial Activities of *Zizyphus lotus* L. and *Ruta chalepensis* L. Growing in Mascara (Western Algeria)", *Journal of Microbiology, Biotechnology, Food Science*, vol.10, no. 5, pp. 1-9, 2021.
- [21] AT. Coimbra, S. Ferreira and AP. Duarte, "Genus *Ruta*: A natural source of high value products with biological and pharmacological properties", *Journal of Ethnopharmacology*, 260, 2020.
- [22] IA. Kostova, A. Ivanova, B. Mikhova and I. Klaiber, "Alkaloids and coumarins from *Ruta graveolens*", *Monatshefte für Chemie*, vol. 130, pp. 703-707, 1999.
- [23] JF. Benazir, R. Suganthi, MR. Renjini Devi, K. Suganya, K. Monisha, KP. Ni-zar Ahamed, R. Santhi, "Phytochemical profiling, antimicrobial and cytotoxicity studies of methanolic extracts from *Ruta graveolens*", *Journal of Pharmacy Research*, vol.4, no.5, pp. 1407-1409. 2011.
- [24] CC. Townsend, "*Haplophyllum* A.Juss. In: Davis, P.H (Ed.) *Flora of Turkey and The Aegean Islands*", vol. 2, Edinburgh University Press, Edinburgh, pp. 496-506, 1967.
- [25] <http://www.bizimbitkiler.org.tr>, date of access, 11.03.2021.
- [26] <http://www.theplantlist.org>, date of access, 11.03.2021.
- [27] <http://www.ipni.org>, date of access, 11.03.2021.
- [28] O. Tugay, Rutaceae. Şu eserde: A. Güner, S. Aslan, T. Ekim, M. Vural, MT. Babaç, (edlr.) "Türkiye Bitkileri Listesi (Damarlı Bitkiler)", *Nezahat Gökyiğit Botanik Bahçesi ve Flora Araştırmaları Derneği Yayını*, İstanbul, 2012.
- [29] T. Baytop, "Türkiye'de Tıbbi bitkilerle Tedavi: Geçmişten Günümüze", *Sanal Basımevi*, İstanbul, pp.373-374,1984.
- [30] NA. Shuiba, A. Iqbal, FA. Sulaimana, I. Razaka, D. Susantic, "Antioxidant and Antibacterial Activities of *Ruta angustifolia* Extract", *Jurnal Teknologi (Sciences & Engineering)*, vol. 77, no.25, pp.101-105, 2015.
- [31] KM. Meepagala, KK. Schrader, DE. Wedge, SO. Duke, "Algicidal and antifungal compounds from the roots of *Ruta graveolens* and synthesis of their

- analogues”, *Phytochemistry*, vol. 66, pp. 2689-2695, 2005.
- [32] TR. Shryock, JM. Staples and DC. De Rosa, “Minimum Inhibitory Concentration Break Points and Disk Diffusion Inhibitory Zone Interpretive Criteria for Tilmicosin Susceptibility Testing Against *Pasteurella multocida* and *Actinobacillus pleuropneumoniae* Associated with Porcine Respiratory”, *Disease Journal of Veterinary Diagnosis Investigation*, vol.14, pp.389-395, 2002.
- [33] VL. Singleton, R. Orthofer, RM. Lamuela-Raventós, “Analysis of total phenols and other oxidation substrates and antioxidants by means of folin-ciocalteu reagent”, *Methods in Enzymology*, vol. 299, pp. 152-178, 1999.
- [34] A. Arvouet-Grand, B. Vennat, A. Pourrat and P. Legret, “Standardisation dun extrait de propolis et identification des principaux constituants”, *Journal de Pharmacie de Belgique*, vol. 49, pp. 462-468, 1994.
- [35] K. Gezer, ME. Duru, I. Kıvrak, A. Türkoğlu, N. Mercan, H. Türkoğlu, S. Gülcan, “Free-radical scavenging capacity and antimicrobial activity of wild edible mushroom from Turkey”, *African Journal of Biotechnology*, vol. 5, no. 20, pp. 1924-1928, 2006.
- [36] T. Essawi, M. Srour, “Screening of Some Palestinian Medicinal Plants for Antibacterial Activity”, *Journal of Ethnopharmacology*, vol. 70, pp. 343- 349, 2000.
- [37] Z. Özer, N. Tursun, H. Önen, “Yabancı Otlarla Sağlıklı Yaşam (Gıda ve Tedavi)”, Ankara, 4Renk Yayınları, pp.133, 2001.
- [38] Z. Gökhan, C. Ramazan, K. Jelena, M. Adriano, A. Abdurrahman, B. Tatjana, M. Sanja, M. Vladi-mir, S. Snezana, AE. Zaahira, Y. Mustafa Abdullah, M. Mohamad Fawzi, “Combining *in vitro*, *in vivo* and *in silico* approaches to evaluate nutraceutical potentials and chemical fingerprints of *Moltingia aurea* and *Moltingia coerulea*”, *Food and Chemical Toxicology*, vol. 107, pp. 540-553, 2017.
- [39] CA. Hart, S. Karriuri, “Anti-microbial resistant in developing country”, *British Medical Journal*, vol. 317, pp. 647-650, 1998.
- [40] A. Drioiche, A. Sanae, B. Salima, S. Soukaina, A. Atika, R. Rachid, M. Malika, EH, Fatima, M. Aicha, E. Bruno and Z. Touriya, “Antioxidant and Antimicrobial Activity of Essential Oils and Phenolic Extracts from the Aerial Parts of *Ruta montana* L. of the Middle Atlas Mountains-Morocco”, *Journal of Essential Oil Bearing Plants*, vol. 23, no. 5 pp. 902 - 917. 2020.
- [41] SM, Alotaibi, SS. Monerah, GAH. Jehan, “Phytochemical contents and biological evaluation of *Ruta chalepensis* L. growing in Saudi Arabia”, *Saudi Pharmaceutical Journal*, vol. 26, pp. 504-508, 2018.
- [42] H. Farah, MC. Tarik, Z. Yosr, K. Riadh, A. Amina, B. Abdelhafid, “Chemical composition and antimicrobial activity of the essential oils from four *Ruta* species growing in Algeria”, *Food Chemistry*, vol. 141, pp. 253-258, 2013.
- [43] I. Ouerghemmi, IB. Rebey, FZ. Rahali, S. Bourgou, L. Pistelli, R. Ksouri, B. Marzouk, MS. Tounsi, “Antioxidant and antimicrobial phenolic compounds from extracts of cultivated and wild-grown Tunisian *Ruta chalepensis*”, *Journal of Food and Drug Analysis*, vol. 25, no. 2, pp.350-359, 2017.
- [44] A. Ivanova, B. Mikhovaa, H. Najdenskib, I. Tsvetkovab, I. Kostova, “Antimicrobial and cytotoxic activity of *Ruta graveolens*”, *Fitoterapia*, vol.76, pp. 344-347, 2005.
- [45] RD.Nagarjuna and AJ. Al-Rajab, “Chemical composition, antibacterial and antifungal activities of *Ruta graveolens* L.

- volatile oils”, *Cogent Chemistry*, vol.2, 1220055, 2016.
- [46] BG. Nilgün, Ö. Gülcan, S. Osman, “Total phenolic contents and antibacterial activities of grape (*Vitis vinifera* L.) extracts”, *Food Control*, vol. 15, pp. 335-339, 2004.
- [47] MJ. Rodríguez Vaquero, A. Maria Rosa, MC. Manca de Nadra, “Antibacterial effect of phenolic compounds from different wines”, *Food Control*, vol. 18, no. 2, pp. 93-101, 2007.
- [48] A. Scalbert, “Antimicrobial Properties of Tannins”, *Phytochemistry*, vol. 30, pp. 3875-3883, 1991.
- [49] BG. Kaplan , “Patlıcanda (*Solanum melongena* L.) Aşı Kombinasyonlarının Bazı Biyokimyasal Bileşikler Üzerine Etkisi”, Doktora Tezi, Ankara Üniversitesi, Fen Bilimleri Enstitüsü, pp. 29, 2019.
- [50] N. Fakhfakh, S. Zouari, M. Zouari, C. Loussayef, N. Zouari, “Chemical composition of volatile compounds and antioxidant activities of essential oil, aqueous and ethanol extracts of wild Tunisian *Ruta chalepensis* L. (Rutaceae)”, *Journal of Medicinal Plant Research*, vol. 6, pp. 593-600, 2012.
- [51] KI. Ereifej, H. Feng, T. Rababah, A. Almajwal, M. Aludatt, SI. Gammoh, LI. Oweis, “Chemical composition, phenolics, anthocyanins concentration and antioxidant activity of ten wild edible plants”, *Food and Nutrition Sciences*, vol. 6, pp. 581-590, 2015.
- [52] C. Yaman, D. Ulukuş, O. Tugay, “Total Bioactive Contents and Radical Scavenging Activities of Some *Ruta* L. Extracts”, *KSU Journal of Agriculture and Nature*, vol. 22, no. 2, pp. 193-201, 2019.
- [53] M. Merghem, S. Dahamna, “ *In Vitro* Antioxidant Activity and Total Phenolic Content of *Ruta montana* L.”, *Journal of Drug Delivery and Therapeutics*, vol.10, no.2, pp. 69-75, 2020.
- [54] M. Gangwar, MK. Gautam, AK. Sharma, YB. Tripathi, RK. Goel, G. Nath, “Antioxidant Capacity and Radical Scavenging Effect of Polyphenol Rich *Mallotus philippensis* Fruit Extract on Human Erythrocytes: An *In Vitro* Study”, *Scientific World Journal*, vol. 12, pp. 2-12, 2014.
- [55] ZM. Zin, A. Abdul-Hamid, A. OSMAN, “Antioxidative activity of extracts from Mengkudu (*Morinda citrifolia* L.) root, fruit and leaf”, *Food Chemistry*, vol. 78, pp. 227-231, 2002.



SAKARYA ÜNİVERSİTESİ

# FEN BİLİMLERİ ENSTİTÜSÜ DERGİSİ

Sakarya University Journal of Science  
SAUJS

e-ISSN: 2147-835X | Founded: 1997 | Period: Bimonthly | Publisher: Sakarya University |  
<http://www.saujs.sakarya.edu.tr/en/>

Title: Development of Finite Element Model for a Special Lead Extrusion Damper

Authors: Ahmet GÜLLÜ, Furkan ÇALIM, Cihan SOYDAN, Ercan YÜKSEL

Received: 2020-10-09 00:00:00

Accepted: 2021-09-03 00:00:00

Article Type: Research Article

Volume: 25

Issue: 5

Month: October

Year: 2021

Pages: 1159-1167

How to cite

Ahmet GÜLLÜ, Furkan ÇALIM, Cihan SOYDAN, Ercan YÜKSEL; (2021), Development of Finite Element Model for a Special Lead Extrusion Damper. Sakarya University Journal of Science, 25(5), 1159-1167, DOI:

<https://doi.org/10.16984/saufenbilder.808517>

Access link

<http://www.saujs.sakarya.edu.tr/tr/pub/issue/65589/808517>

New submission to SAUJS

<http://dergipark.org.tr/en/journal/1115/submission/step/manuscript/new>

## Development of Finite Element Model for a Special Lead Extrusion Damper

Ahmet GÜLLÜ\*<sup>1</sup>, Furkan ÇALIM<sup>2</sup>, Cihan SOYDAN<sup>3</sup>, Ercan YÜKSEL<sup>2</sup>

### Abstract

A significant amount of seismic energy is imparted to the structures during earthquakes. The energy spreads within the structure and transforms in various energy forms as dissipated through the structure. The conventional seismic design provides specific ductile regions, namely plastic hinges, on structural elements. Therefore, the energy dissipation capacities of the structural elements and the structure enhance. However, this approach accepts that the deformations will concentrate on the plastic hinge zones and severe damage may occur on structural elements within deformation limits that are defined by the seismic codes. The modern seismic design aims to dissipate a large portion of the seismic input energy by installing energy dissipating devices (*EDDs*) to the structure. Thus, deformation concentrates on *EDDs* which can be replaced after an earthquake, and energy demand for structural elements is decreased. Lead extrusion damper (*LED*) is a passive *EDD* that utilizes the hysteretic behavior of lead. In this paper, the preliminary results of the developed three-dimensional finite element model (*FEM*) for a *LED* is presented. The results obtained from the finite element analysis (*FEA*) were compared with the experimental ones in which *LEDs* were exposed to sinusoidal displacements. Also, the applicability of the developed *FEM* was checked for different component dimensions given in the literature. The comparison study yielded a satisfactory consistency. Additionally, the maximum relative difference obtained for the literature devices was reduced to 12% from 39% by the developed *FEM*.

**Keywords:** Lead extrusion damper, Passive energy dissipater, Seismic energy dissipation, Finite element analysis.

### 1. INTRODUCTION

The energy released during earthquakes imparts to structures. This energy must be dissipated through the structure to prevent life and financial

losses. The conventional seismic design implicitly bases on the principle that structural elements dissipate the imparted energy by various mechanisms and limit displacement and deformation demands for structures. In the

\* Corresponding author: ahmgullu@gmail.com

<sup>1</sup> Istanbul Gedik University

ORCID: <https://orcid.org/0000-0001-6678-9372>

<sup>2</sup> Istanbul Technical University

E-Mail: calimf@itu.edu.tr yukselerc@itu.edu.tr

ORCID: <https://orcid.org/0000-0001-8365-9553>, <https://orcid.org/0000-0002-9741-1206>

<sup>3</sup> Namik Kemal University

E-Mail: csoydan@nku.edu.tr

ORCID: <https://orcid.org/0000-0003-3579-0033>

modern seismic design approach, a large portion of the imparted energy is expected to be dissipated through energy dissipation devices (*EDDs*). Many types of active [1-3] or passive [4-8] *EDDs* were designed and developed in academic and industrial areas to serve this purpose. Additional damping supplied by *EDDs* may reduce inter-story drifts and shear forces through the structure reasonably [9].

Being a soft metal with low yield strength and stiffness makes lead a desirable material for energy dissipation. Hence, it was also utilized in some base isolation systems [10-12]. Lead extrusion damper (*LED*) which is a passive *EDD* also benefits from the metallurgical properties of lead [13-19]. *LED* dissipates the energy by extrusion of lead through a hole or an orifice. The *LED* comprises lead, a tube, a cap, and a bulged shaft, Figure 1.

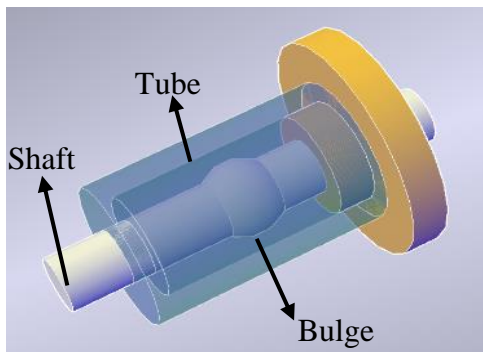


Figure 1 The lead extrusion damper

Even though the behavior of *LED* was determined experimentally in the literature [13-15], the finite element model of the damper is crucial for the prediction of behavior, especially for *LEDs* with distinct geometric dimensions. *LED* is difficult to model by finite elements since lead rapidly gains back its original characteristics, [20]. An effort has been paid on finite element modeling of *LED* by using simplified 2D elements, [21-22].

The rationale of the study is the development of a three-dimensional detailed finite element model of *LEDs* that were tested (*T-LED*), [13-19], and studied in the literature (*L-LED*), [21-22]. To this extent, numerically obtained force-displacement hysteresis of *T-LED* and the maximum force of *L-LED* were compared with the related experimental results.

## 2. MATERIAL AND METHOD

Finite element models of *T-LED* and *L-LED* were generated using the ABAQUS software package, [23].

### 2.1. Performed Experiments on T-LEDs

The *T-LED* was tested under various excitations (e.g. quasi-static, dynamic cyclic, and shaking table tests). The *T-LED* had a bulge on its shaft. The diameters of the bulge and the shaft were 44 and 32 mm, respectively. The surrounding tube had an interior diameter of 60 mm. The tube thickness was 12 mm. The closest distance between the bulge and the tube was 8mm. The displacement capacity of *T-LED* was  $\pm 33$  mm.

Initially, the behavior of *T-LED* was investigated using dynamic tests through sinusoidal excitations with various amplitudes and frequencies, [13]. The experimental setup is shown in Figure 2. It was stated that *T-LED* has almost rectangular load-displacement hysteresis with up to 50% equivalent damping ratio. Additionally, the damping ratio was found to be sensitive to displacement intensity and free from the loading frequency within the adopted displacement and frequency ranges.

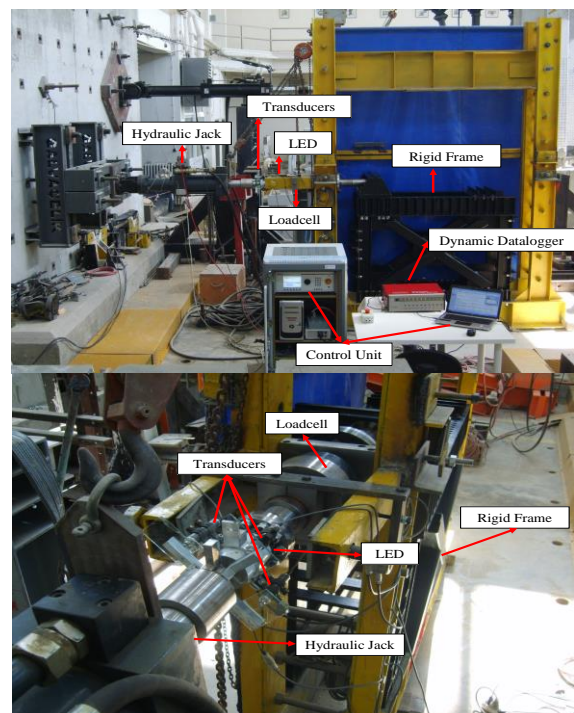


Figure 2 Dynamic tests on the developed *LED*, [13]

Hereafter, *T-LED* was inserted diagonally to a steel beam-to-column connection which was exposed to quasi-static cyclic displacement protocol, Figure 3.



Figure 3 Cyclic steel beam-column connection tests, [14].

The study revealed that the equivalent damping ratio of the connection equipped with *T-LED* was increased up to 6.5 times compared to the bare connection.

Finally, *T-LED* was installed diagonally to the beam-to-column connection of a precast RC frame, [18]. The bare specimen and the specimen equipped with *T-LED* were exposed to real ground motion records on the shake table, Figure 4.

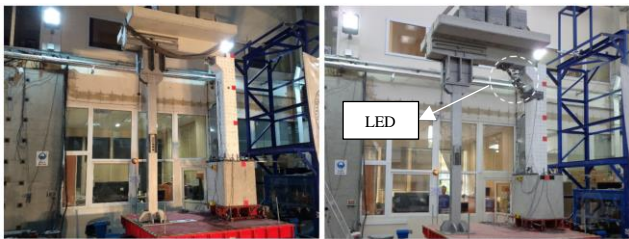


Figure 4 Precast RC beam-column connection shake table tests, [18]

The experimental study resulted that relative top displacement, deformations at the column base, and rotation of the connection joint were reduced up to 50%, 65%, and 30%, respectively by adding *T-LED* to the precast RC frame.

Since the effectiveness of *T-LED* was proven by various tests, a reliable and detailed 3D finite element model was generated to predict the behavioral characteristics of *T-LED* with distinct geometric properties.

## 2.2. Finite Element Model of *T-LED*

In this study, a three-dimensional (3D) finite element model (FEM) of *T-LED* was generated, Figure 5. The cap was not modeled for simplicity in the preliminary FEMs. Its effect on the behavior of the *T-LED* was considered through boundary conditions. Red, beige and, green parts represent shaft, lead, and tube, respectively, Figure 6.

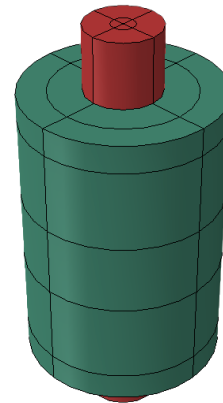


Figure 5 3D finite element model of *T-LED*

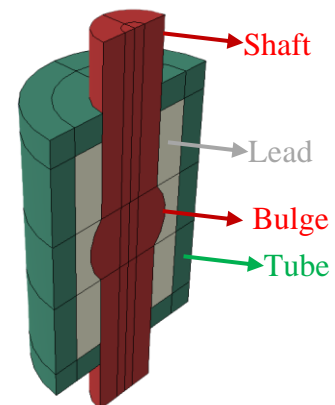


Figure 6 Parts of *T-LED*

An eight-node linear brick, reduced integration elements (C3D8R) were used for all parts of the *LED*. A total number of 33480 mesh elements (14400 elements on the shaft, 9000 elements on the lead, and 10080 elements on the tube) were generated on the instances, Figure 7.

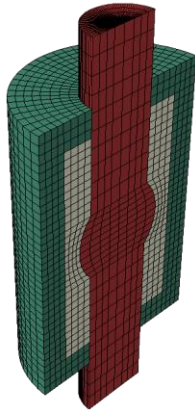
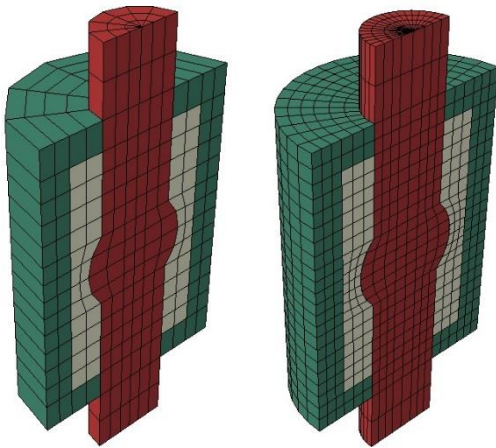


Figure 7 Meshing for FEM of T-LED

A convergence analysis was performed to evaluate the effect of mesh size. In order to serve this purpose, coarse meshing and nearly fine meshing were also applied to the numerical models, Figure 8. In these models, a total of 1320 and 9560 mesh elements were used, respectively.



a) Coarse

b) Nearly fine

Figure 8 Coarse and nearly fine meshing for convergence analyses.

Mechanical properties of the lead, which are available in the literature [21], were used in the preliminary models. The elasticity modulus, Poisson's ratio, and density of the lead were considered as 14 GPa, 0.44, and, 11350 kg/m<sup>3</sup>, respectively.

Surface-to-surface contacts were defined in the models. Contact between lead and steel was modeled by using tangential friction. Analyses were performed by defining a "Static, General" type step. The effects of nonlinearity caused by

both material and geometry are considered in the models.

The movement of the tube was restricted by assigning an encastre (fixed) type boundary condition to both ends of it. A sinusoidal displacement procedure was applied to the shaft, Figure 9. The amplitude of the sinusoidal loadings was 4.5 mm. The consistency of the numerical model was examined by using three cycles for the loading pattern.

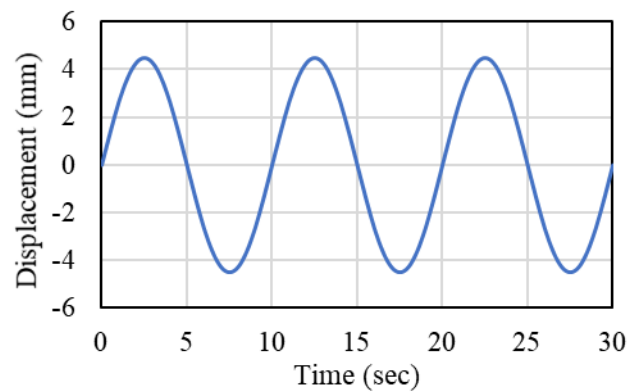


Figure 9 Applied sinusoidal displacement procedure for T-LED

### 2.3. Finite Element Model of L-LEDs

To check the applicability of the developed finite element model on different geometries of LED, FEMs of some selected LED geometries existing in the literature [21, 22] were generated by following the same steps with Chapter 2.2.

Three L-LED geometries with different cylinder, shaft, and bulge diameters ( $D_{cyl}$ ,  $D_{blg}$ ,  $D_{shaft}$ ) and lengths ( $L_{cyl}$ ,  $L_{blg}$ ,  $L_{blgshaft}$ ) were selected, Table 1. The selected geometries belong to the 4<sup>th</sup>, 17<sup>th</sup>, and 19<sup>th</sup> specimens of Vishnupriya [22].

Table 1 Geometric properties of L-LEDs [21, 22]

LED #	$D_{cyl}$ (mm)	$D_{blg}$ (mm)	$D_{shaft}$ (mm)	$L_{cyl}$ (mm)	$L_{blg}$ (mm)	$L_{blgshaft}$ (mm)
4	20	17	16	68	20	6
17	54	36	30	160	20	3
19	40	27	20	100	17	3

The prementioned study in the literature uses a two-dimensional finite element model and defines the shaft and tube as analytical rigid parts.

To represent the *LEDs* more realistically, all parts of *L-LEDs* were modeled as deformable parts.

In contradistinction to the finite element model for *T-LED* which was developed by the authors and discussed in Chapter 2.2, a monotonic displacement procedure with a loading rate of 0.5 mm/sec was applied to make a better comparison with the experiment results of *L-LEDs*, Figure 10.

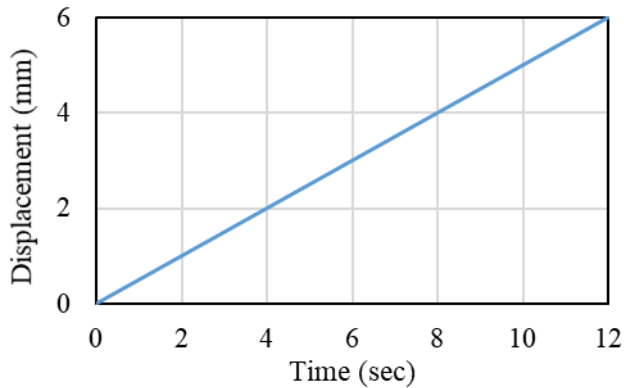


Figure 10 Ramp-type displacement procedure applied to *L-LEDs*

### 3. RESULTS AND DISCUSSION

The gap formation that occurs behind the bulge is one of the main issues with *LED*. It was satisfactorily observed by applying the cyclic displacement procedure in the developed *FEM*, Figure 11.

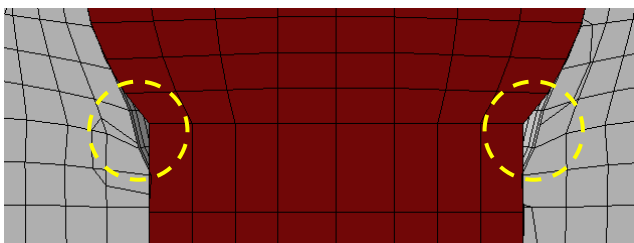


Figure 11. Gap formation at 4.5 mm (pull)

As the lead was pressurized and squeezed on one side by the movement of the shaft, out-of-plane stresses of the steel tube at that side increased, Figure 12. The highest levels of stress experienced by lead were observed to be around the shaft as expected, Figure 13. Stresses were accumulated at the front fibers of the bulge, Figure 14. All the stress distribution contours were plotted for the third cycle.

The change in the stresses observed on a mesh element in the lead throughout the analyses was plotted in Figure 15. The region of the selected finite element is shown in Figure 13. It can be stated that stress levels slightly increase with each cycle, which is also related to duration-based cumulative damage.

Steel members (tube and shaft) remained elastic even at maximum displacement levels of the shaft but plastic deformations were observed in the lead.

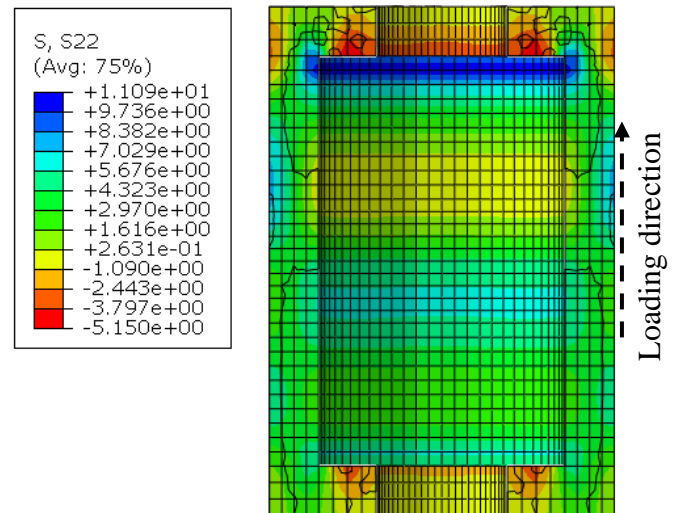


Figure 12 Stresses on the tube at 4.5 mm (pull)

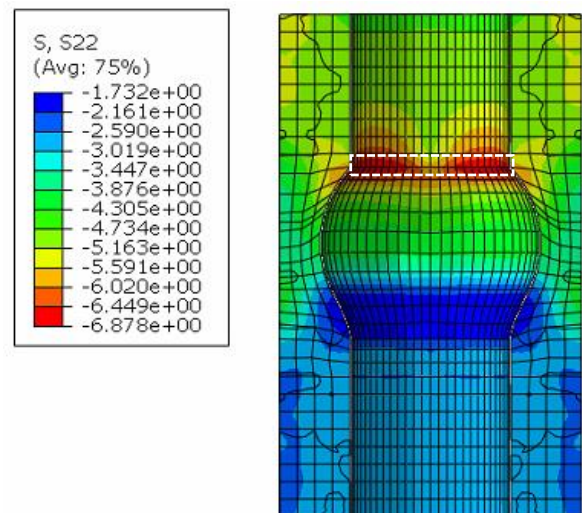


Figure 13 Stresses on the lead at 4.5 mm (pull)

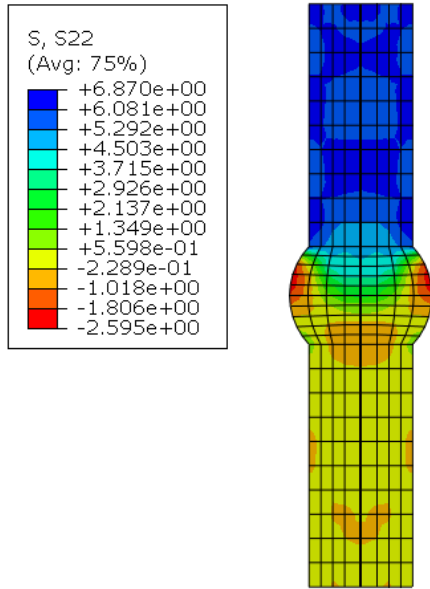


Figure 14 Stresses on the shaft at 4.5 mm (pull)

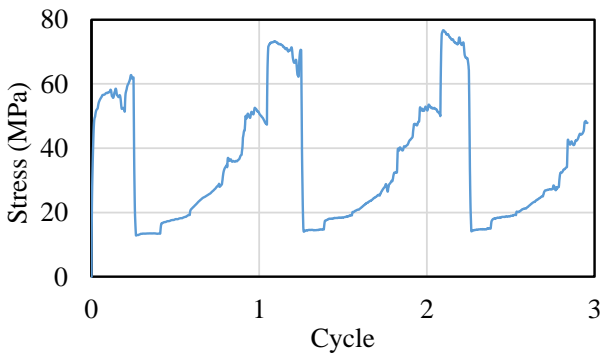


Figure 15 The change in the stress on lead.

### 3.1. Results for *T-LED*

As a result of the convergence analysis performed to investigate the mesh size effect, it was observed that the fine meshing yields better results in terms of the hysteresis shape, yield force, and maximum force values, Figure 16. Even though the computational time increases by the increasing number of mesh elements, fine meshing was selected for further analyses.

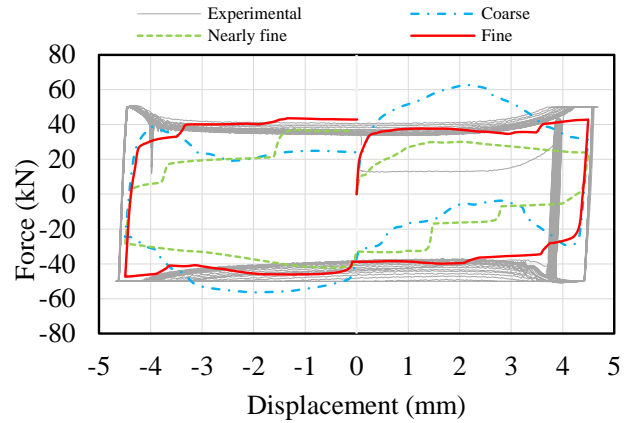


Figure 16 Convergence analysis for the mesh size

Numerically obtained force-displacement hysteresis from the preliminary *FEMs* was compared with the experimental result in Figure 17. While 30 cycles were performed in the experiments, this number was reduced to 3 cycles in numerical analyses to reduce computational time.

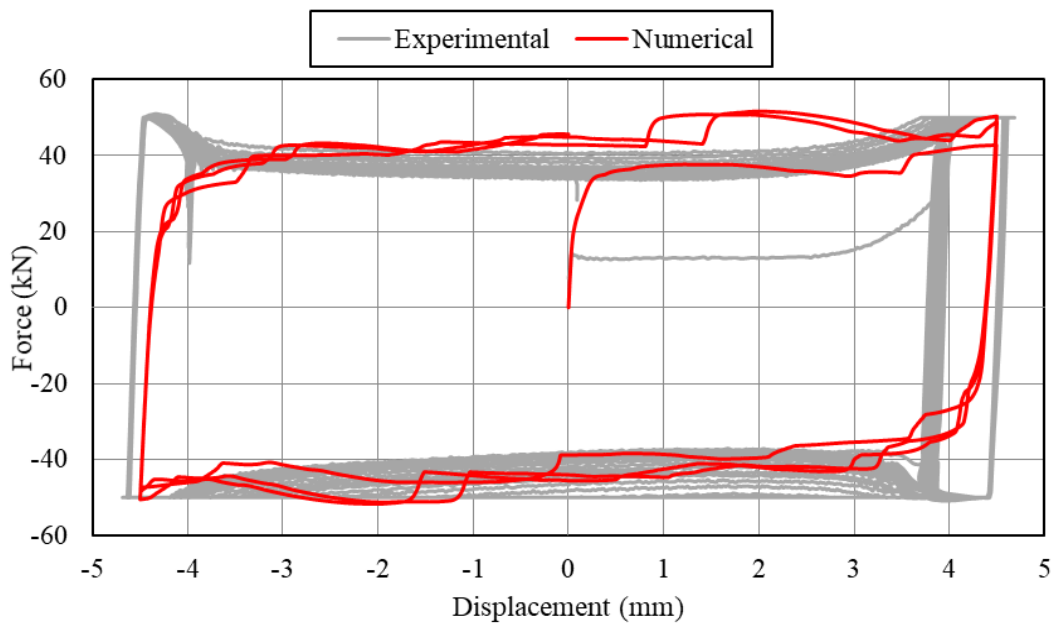


Figure 17 Comparison of experimental and numerical hysteresis of *T-LED*

Initial stiffness, force values, and loading/unloading paths were reasonably predicted by numerical analyses. Yet, there was a slight difference between experimental and numerical hysteresis. The reason for this might be the formation of air voids inside lead during the casting process. Besides, the softening of lead under repetitive cycles caused a slight decrement in yield force at each step. Air voids and softening of lead cannot be modeled through *FEMs*. Last but not the least, the mechanical properties of lead were adapted from literature.

### 3.2. Finite Element Analyses for the *L-LEDs*

In the literature study, only maximum reaction forces of *L-LEDs*, which resulted from a monotonic ramp type loading, obtained from experiments and 2D *FEAs* were compared. Hence, comparing only the maximum forces was possible in this study, also. The developed 3D *FEM* was much more efficient to predict the maximum forces.

It can be observed from Table 2 that the developed *FEM* predicts the maximum forces better. The relative difference was calculated by Equation (1). While the differences varied between 4-39% in the literature study, it was reduced to 2-12% by the developed model, Table 2.

$$Rel. Dif. = \frac{F_{num} - F_{exp}}{F_{exp}} \quad (1)$$

Table 2 Comparison of maximum forces and errors

<i>L-LED</i> #	$F_{exp}$ (kN)	Literature [21, 22]		This Study	
		$F_{num}$ (kN)	Rel. Dif. (%)	$F_{num}$ (kN)	Rel. Dif. (%)
4	85	52	39	75	12
17	200	220	-10	192	4
19	125	130	-4	123	2

## 4. CONCLUSIONS

In this study, finite element models of lead extrusion dampers (*LEDs*) were generated for numerical testing of the energy dissipating device.

The precision of the generated model was controlled by comparing the results of the geometrically updated model with the experimental results given in the literature. The following conclusions might be driven from the numerical studies:

- The gap formation behind the bulge of the shaft was satisfactorily captured by the *FEMs*. The energy dissipation capacity of the *LED* was reduced due to the existence of the gap. Developed *FEM* can be an efficient tool to reduce gap formation and enhance the performance of the *EDD*.
- Force-displacement hysteresis of the evaluated *T-LED* was successfully predicted by the developed *FEM*. The observed slight difference might be related to the air voids and softening of lead or the material properties taken from the literature.
- In the further step of the analyses, material tests will be performed on the lead, and experimentally obtained material properties will be defined in the *FEMs*.
- Air voids inside the lead should be minimized so pre-stressing can be an effective method in this regard. Pre-stressing may also be influential on gap formation behind the bulge of the shaft.
- The finite element model used in this study was shown to yield better results compared to the one used in the literature since *LEDs* were modeled more real-like (three-dimensional and deformable) in this study.

### Acknowledgments

The study was performed in the Structural and Earthquake Engineering Laboratory of Istanbul Technical University. The contribution of the laboratory staff is gratefully acknowledged.

### Research and Publication Ethics

This paper has been prepared within the scope of international research and publication ethics.

**Ethics Committee Approval**

This paper does not require any ethics committee permission or special permission.

**Conflict of Interest**

The authors declared no potential conflicts of interest with respect to the research, authorship, and/or publication of the paper.

**REFERENCES**

- [1] M. G. Soto, and H. Adeli, "Semi-active vibration control of smart isolated highway bridge structures using replicator dynamics," *Engineering Structures*, vol. 186, pp.536-552, 2019.
- [2] Y. Luo, X. Zhang, Y. Zhang, Y. Qu, M. Xu, K. Fu and L. Ye, "Active vibration control of a hoop truss structure with piezoelectric bending actuators based on fuzzy logic algorithm," *Smart Materials and Structures*, vol. 27, no.8, 085030, 2018.
- [3] X. Liu, G. Cai, F. Peng and H. Zhang, "Dynamic model and active vibration control of a membrane antenna structure," *Journal of Vibration and Control*, vol. 24, no. 18, pp. 4282-4296, 2017.
- [4] F. Karadoğan, E. Yüksel, A. Khajehdehi, H. Özkaynak, A. Güllü, and E. Şenol, "Cyclic behavior of reinforced concrete cladding panels connected with energy dissipative steel cushions," *Engineering Structures*, vol. 189, pp. 423-439, 2019.
- [5] E. Yüksel, F. Karadoğan, H. Özkaynak, A. Khajehdehi, A. Güllü, E. Smyrou and İ. E. Bal, "Behavior of steel cushions subjected to combined actions," *Bulletin of Earthquake Engineering*, vol. 16, no. 2, pp. 707-729, 2018.
- [6] H. Özkaynak, A. Khajehdehi, A. Güllü, F. Azizisales, E. Yüksel and F. Karadoğan, "Uni-axial behavior of energy dissipative steel cushions" *Steel and Composite Structures*, vol. 27, no. 6, pp. 661-674, 2018.
- [7] P. Saingam, F. Sütçü, Y. Terazawa, K. Fujishita, P. C. Lin, O. C. Çelik and T. Takeuchi, "Composite behavior in RC buildings retrofitted using buckling restrained braces with elastic steel frames," *Engineering Structures*, vol. 219, 110896, 2020.
- [8] A. Xhahysa, S. Kahraman and S. C. Girgin, "Flexure based energy dissipating device in self-centering braces," *Latin American Journal of Solids and Structures*, vol. 16, no. 8, e231, 2019.
- [9] T. T. Soong and B. F. Spencer, "Supplemental energy dissipation: state-of-the-art and state-of-the-practice," *Engineering Structures*, vol. 24, pp. 243-249, 2002.
- [10] P. Deng, Z. Gan, T. Hayashikawa and T. Matsumoto, "Seismic response of highway viaducts equipped with lead-rubber bearings under low temperature," *Engineering Structures*, vol. 209, 110008, 2020.
- [11] G. Özdemir and H. P. Gülkan, "Scaling legitimacy for design of lead rubber bearing isolated structures using a bounding analysis," *Earthquake Spectra*, vol. 32, no.1, pp. 345-366, 2016.
- [12] P. Shoaie, H. T. Orimi and S. M. Zahrai, "Seismic reliability-based design of inelastic base-isolated structures with lead-rubber bearing systems," *Soil Dynamics and Earthquake Engineering*, vol. 115, pp. 589-605, 2018.
- [13] C. Soydan, A. Güllü, O. E. Hepbostancı, E. Yüksel, and E. İrtem, "Design of a Special Lead Extrusion Damper", 15th World Conference on Earthquake Engineering, Lisboa, Portugal, September 24-28, 2012.
- [14] C. Soydan, E. Yüksel, and E. İrtem, "The Behavior of a Steel Connection Equipped

- with the Lead Extrusion Damper”, *Advances in Structural Engineering*, vol. 17, no. 1, pp. 25-40, 2014.
- [15] C. Soydan, E. Yüksel, and E. İrtem, “Determination of the characteristics of a specially designed lead extrusion damper”, 14th World Conference on Seismic Isolation, Energy Dissipation and Active Vibration Control of Structures, San Diego, USA September 9-11, 2015.
- [16] C. Soydan, “A new energy dissipating device and its application to pinned connections in precast structural systems”, Ph.D. thesis, Istanbul Technical University, Istanbul, Turkey, 2015.
- [17] C. Soydan, E. Yüksel, and E. İrtem, “Determination of the characteristics of a new prestressed lead extrusion damper”, 16th World Conference on Earthquake Engineering, Santiago, Chile, 2017.
- [18] C. Soydan, E. Yüksel, and E. İrtem, “Retrofitting of Pinned Beam–Column Connections in RC Precast Frames Using Lead Extrusion Dampers”. *Bulletin of Earthquake Engineering*, vol. 16, no. 3, pp. 1273–1292, 2017.
- [19] C. Soydan, E. Yüksel and E. İrtem, “Seismic performance improvement of single-storey precast reinforced concrete industrial buildings in use,” *Soil Dynamics and Earthquake Engineering*, vol. 135, 106167, 2020.
- [20] W. H. Robinson and L. R. Greenbank, “Properties of an extrusion energy absorber,” *Bulletin of New Zealand Society of Earthquake Engineering*, vol. 8, no. 3, pp. 187-191, 1975.
- [21] V. Vishnupriya, G. W. Rodgers, and J. G. Chase, “Finite element modelling of HF2V lead extrusion dampers for specific force capacities”, 2019 Pacific Conference on Earthquake Engineering, Auckland, New Zealand, April 4-6, 2019.
- [22] V. Vishnupriya, “Modelling force behaviour and contributions of metallic extrusion dampers for seismic energy dissipation”, Ph.D. thesis, University of Canterbury, Christchurch, New Zealand, 2019.
- [23] SIMULIA Abaqus/CAE (Version 2019) [Computer software]. Vélizy-Villacoublay: Dassault Systemes.



SAKARYA ÜNİVERSİTESİ

# FEN BİLİMLERİ ENSTİTÜSÜ DERGİSİ

Sakarya University Journal of Science  
SAUJS

e-ISSN: 2147-835X | Founded: 1997 | Period: Bimonthly | Publisher: Sakarya University |  
<http://www.saujs.sakarya.edu.tr/en/>

Title: Investigation of a Perovskite Solar Cell and Various Parameters Impact on Its Layers and the Effect of Interface Modification by Using P3HT as an Ultrathin Polymeric Layer Through SCAPS-1D Simulation

Authors: Seyyedreza HOSSEİNİ, Mahsa BAHRAMGOUR, Nagihan DELİBAŞ, Aligholi NİAİE

Received: 2021-06-03 00:00:00

Accepted: 2021-09-08 00:00:00

Article Type: Research Article

Volume: 25

Issue: 5

Month: October

Year: 2021

Pages: 1168-1179

How to cite

Seyyedreza HOSSEİNİ, Mahsa BAHRAMGOUR, Nagihan DELİBAŞ, Aligholi NİAİE; (2021), Investigation of a Perovskite Solar Cell and Various Parameters Impact on Its Layers and the Effect of Interface Modification by Using P3HT as an Ultrathin Polymeric Layer Through SCAPS-1D Simulation. Sakarya University Journal of Science, 25(5), 1168-1179, DOI: <https://doi.org/10.16984/saufenbilder.947735>

Access link

<http://www.saujs.sakarya.edu.tr/tr/pub/issue/65589/947735>

New submission to SAUJS

<http://dergipark.org.tr/en/journal/1115/submission/step/manuscript/new>

## Interface Modification by Using an Ultrathin P3HT Layer in a Custom Perovskite Solar Cell Through SCAPS-1D Simulation

Seyyedreza HOSSEİNİ<sup>1</sup>, Mahsa BAHRAMGOUR<sup>1</sup>, Nagihan DELİBAŞ<sup>2</sup>, Aligholi NİAİE\*<sup>1</sup>

### Abstract

Recently, renewable energy sources such as solar energy have gained much attention for electricity generation because of their easy access and infinite resources. Solar cells are a good choice for this goal. Among the various solar cells that have already been studied, perovskite solar cells (PSCs) have recently become an interesting issue for researchers due to their tremendous improvement in system performance and efficiency. This type of solar cell is divided into several layers, each of which has its role in the structure of the cell. “Front Contact/Electron transporting material/Absorber (perovskite)/Hole transporting layer/Back Contact”. The overall structure of these cells has shown a maximum efficiency of about 22% which is good efficiency for solar cells. However, this type of solar cell suffers from stability problems, especially at the junction point between the hole transporting layer (HTM) and the perovskite (absorber) layer, despite its cost-effectiveness advantages. To solve this problem, recent studies have been transferred to a study called interface engineering. In this study, the mentioned interfaces are modified by some materials that have regular and stable structures such as polymers. Many polymeric modifiers have been studied in recent years. Among them, P3HT (Poly(3-hexylthiophene-2,5-diyl)) has provided the best results. In this paper, first, the effect of different layer properties such as their thickness and charge carrier density were investigated and optimal parameters were obtained for each one using SCAPS-1D (Solar Cell Capacitance Simulator) software. Then we simulated the structure of a perovskite solar cell using a polymeric modifier in its structure. The results showed that by adding an ultrathin polymeric film as an interface between HTM and perovskite, the performance of the device was improved and its efficiency was enhanced. The final efficiency of the device with the optimal parameters was obtained about 26.5%.

**Keywords:** solar cells, perovskite, interface, modifiers, efficiency

### 1. INTRODUCTION

Electricity energy and the method of electricity generation have become a global issue and interest over the years. Nonrenewable energies

like fossil fuels are the largest sources of energy generation because of their high efficiency and good performance. Nowadays, the shortage of nonrenewable energy resources is an important problem because of their limited content and their

\* Corresponding author: aniaei@tabrizu.ac.ir

<sup>1</sup> Reactor & Catalyst Research lab., Department of chemical & petroleum Engineering, university of Tabriz, Iran.  
E-Mail: seyyedgrr@gmail.com, m\_bahramgur@outlook.com

ORCID: <https://orcid.org/0000-0002-0946-7489>, <https://orcid.org/0000-0002-2925-1538>, <https://orcid.org/0000-0001-5580-4266>

<sup>2</sup> Sakarya University, Faculty of Arts and Sciences, Department of Physics

ORCID: <https://orcid.org/0000-0001-5752-062X>

E-Mail: caylak@sakarya.edu.tr

environmental impacts like air pollution and releasing greenhouse gases. Despite these disadvantages, fossil fuels are still the common sources of energy generation; but usage of renewable energies like solar systems that have infinite sources, have progressed rapidly in recent decades. It was predicted that these energy resources will be responsible for most of the electricity generation since 2050 [1].

Solar cells are one of the hopeful resources of electricity generation because of their unique properties like global and overall distribution of sunlight and its low environmental impacts [1]. Generally, solar cells are divided into three common generations. Crystalline silicon was the first type of material that was used for solar cells because of their regular structures and high stability. Despite these good properties, their fabrication demanded high costs because of their relatively high thicknesses. Therefore, solar cell fabrication developed to a new generation that had low cost because of their thin layers. But their efficiency was not as well as the first generation. The final generation of solar cells has progressed to the third generation. Some common types of them are dye-sensitized solar cells (DSSC), Quantum dot solar cells, and perovskite solar cells (PSC).

Perovskite solar cells have become an interesting topic for researchers during the last decade because of their rapid growth in device performance over few years. They have some tremendous features such as tunable band gaps, low fabrication costs, easy fabrication process (for example they don't need high temperatures for their depositions), and acceptable efficiencies. The first study about these solar cells belongs to Miyasaka et al. in 2009 [2] that reached 3.8% efficiency utilizing  $\text{CH}_3\text{NH}_3\text{PbI}_3$  as an absorber layer with electrolytes used for charge-transporting layers. However, this was not the desired result and indicated low stability because corrosion occurred between absorber and electrolytes. Although, researches about perovskite solar cells continued and reached a structure with solid and relatively stable charge transporting materials in 2012. This study was done by Kim et al. [3] that reached an efficiency

of 9.7%. Over the years, studies about these cells continued and researchers have reached efficiencies of about 22%.

Perovskite solar cells structure generally consists of three types of layers. The most important layer is named absorber layer that is a perovskite material having a general formula of  $\text{MAX}_3$  that M, A, X is referred to as monovalent cation, a divalent cation, and a halide ion, respectively. According to carriers of these ions, perovskite is a generally inert material. This layer absorbs photon or light's energy and generates electrons and holes due to the concept of solid-state band theory and the electron-hole pair generation process in semiconductors. Other layers of PSC's structure are electron transporting material (ETM) and hole-transporting materials (HTM) that carry electrons and holes and transport them to counter electrodes, respectively. The total structure of these cells is shown in figure 1.

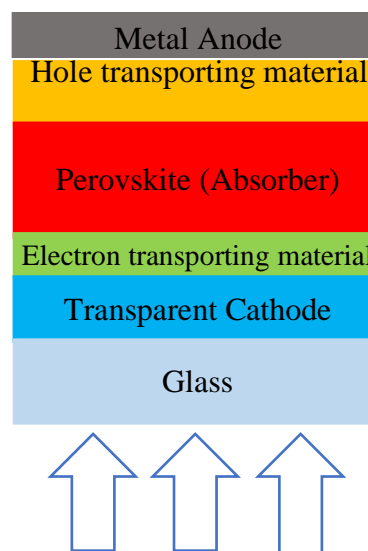


Figure 1 Perovskite solar cell's general structure [1]

Although perovskite solar cells have many advantages as mentioned above, they have some problems with stability issues. Charge recombination and corrosion at the interfaces of these cells especially at the interface between HTM and absorber layer leads to the unstable structure during the time. There have been some approaches for solving this problem in recent years. Some of them belong to a science named interface engineering that utilizes a material with more stable and regular structures like polymers to modify the surface and interfaces. Some

experimental studies have been performed to investigate the effect of the ultrathin polymeric layer in the interface between the absorber layer and charge transporting materials in recent years. All of them represented that the addition of polymeric modifiers led to an increment in both stability and efficiency indexes. Cai et al. in 2018 [4] investigated the effect of three different polymers including PMMA<sup>2</sup>, MEH-PPV<sup>3</sup> and PEG<sup>4</sup> on the PSC with TiO<sub>2</sub> layer; results indicated that by addition of these polymers not only stability improved but also efficiency increased from 15.49% to 17.15%, 17.09%, 16.96% for PMMA, MEH-PPV, PEG modifiers, respectively. In 2018 Du et al. [5] studied the effect of the addition of PTAA<sup>5</sup> to the PSC structure based on NiO<sub>x</sub>; results dedicated that the stability improved and efficiency increased from 13.2% for NiO<sub>x</sub>-based to 16.7% for PTAA/NiO<sub>x</sub> based PSC. Another empirical study was done by Hunag et al. in 2018 [6] that investigated the effect of utilizing P3HT<sup>6</sup>, PTAA, MEH-PPV, poly-TPD<sup>7</sup>, PBDTTT-CT<sup>8</sup> as the polymeric modifiers on the TiO<sub>2</sub>/perovskite/Spiro-OMeTAD structure; results indicated that the best performance was for the P3HT as the modifier that it improved the device efficiency from 15% for the simple structure to 19% for the P3HT-modified structure. In this study, we will investigate the effect of P3HT on the conventional TiO<sub>2</sub>/perovskite/Spiro-OMeTAD<sup>9</sup> structure in the simulation environment for the first time. Before this investigation, the effect of PSC's different layer properties and the optimum amount of each one will be investigated to improve the cell's efficiency.

## 2. GENERAL REQUIREMENTS

The simulation tool that was used in this work is software for solar cells named Solar Cell Capacitance Simulator in optical-electrical 1-

dimensional physics abbreviated as SCAPS-1D. This simulation tool was developed by Marc Burgelman et al. at the Department of Electronics and Information Systems (ELIS) of the University of Gent, Belgium. It can simulate up to seven layers (in addition to electrodes) with each one's properties like bandgap, electron affinity, defects, etc. SCAPS-1D can give us information about energy diagrams, recombination plots, and I-V (current-voltage) characteristics including VOC<sup>10</sup>, ISC<sup>11</sup>, FF<sup>12</sup>, PCE<sup>13</sup> (also called eta) and I-V curve. This software simulates the cell's structure and gives results by solving Poisson's equation and electron and hole continuity equations simultaneously [7]. The equations are as below:

$$\vec{\nabla} \cdot \vec{\nabla} \varphi = -q(p - n + N_D + -N_{A^-}) \quad (1)$$

$$\vec{\nabla} \cdot \vec{J}_n = q(R - G) + q \frac{\partial n}{\partial t} \quad (2)$$

$$-\vec{\nabla} \cdot \vec{J}_p = q(R - G) + q \frac{\partial p}{\partial t} \quad (3)$$

In these equations,  $\varphi$ ,  $\epsilon$ ,  $q$ ,  $p$ ,  $n$ ,  $N_D$ ,  $N_{A^-}$ ,  $\vec{J}_p$ ,  $\vec{J}_n$ ,  $G$ ,  $R$  refer to electrostatic potential, dielectric permittivity, electric charge, hole density, electron density, the dopant concentration of donor, dopant concentration of acceptor, hole current density, electron current density, charge generation rate, recombination rate, respectively.

In this work, two modified and simple optimized perovskite solar cell structures were simulated by SCAPS-1D. First, the Au/ Spiro-OMeTAD/ CH<sub>3</sub>NH<sub>3</sub>PbI<sub>3</sub>/ TiO<sub>2</sub>/ FTO<sup>14</sup> was investigated and its performance parameters were obtained. Then a modified Au/ Spiro-OMeTAD/ P3HT/ CH<sub>3</sub>NH<sub>3</sub>PbI<sub>3</sub>/ TiO<sub>2</sub>/ FTO with the ultrathin P3HT polymeric layer was simulated and its effect on

<sup>2</sup>Poly (methyl methacrylate)

<sup>3</sup>Poly[2-methoxy-5-(2-ethylhexyloxy)-1,4-phenylenevinylene]

<sup>4</sup>Polyethylene glycol

<sup>5</sup>Poly(triarylamine)

<sup>6</sup>Poly(3-hexylthiophene-2,5-diyl)

<sup>7</sup>Poly(4-butyl-N,N-diphenylamine)

<sup>8</sup>Poly[[4,8-bis[5-(2-ethylhexyl)-2-thienyl]benzo[1,2-b:4,5-b']dithiophene-2,6-diyl][2-(2-ethyl-1

oxohexyl)thieno[3,4-b]thiophenediyl]]

<sup>9</sup>N<sub>2</sub>,N<sub>2</sub>,N<sub>2</sub>',N<sub>2</sub>',N<sub>7</sub>,N<sub>7</sub>,N<sub>7</sub>',N<sub>7</sub>'-octakis(4-methoxyphenyl)-9,9'-spirobi[9H-fluorene]-2,2',7,7'-tetramine

<sup>10</sup>Open-circuit voltage

<sup>11</sup>Short-circuit current

<sup>12</sup>Fill Factor

<sup>13</sup>Power conversion efficiency

<sup>14</sup>Fluoridized tin-oxide

the efficiency of the system was investigated. To simulate the aforementioned structures, optical-electrical properties and characteristics of each layer are required. These properties are obtained from other researches and studies. Here, these properties were given in Table 1 [8-10]. The work function of the electrodes including gold (back contact) and FTO glass (front contact) were set in 5.1eV and 4.4eV, respectively. (Simulation was performed in the temperature of T=300 K, A.M.1.5 spectrum, and light power of 1000 W/m<sup>2</sup>)

Table 1 Material parameters used in the cells [8-10]

Properties	TiO <sub>2</sub>	CH <sub>3</sub> NH <sub>3</sub> PbI <sub>3</sub>	P3HT	Spiro-OMeTAD
Thickness (nm)	100	450	20	200
Bandgap (eV)	3.2	1.5	1.05	3.06
Electron Affinity (eV)	3.9	3.9	3.9	2.05
Dielectric Permittivity (Relative)	9	30	3	3
CB Effective Density of States (1/cm <sup>3</sup> )	1.00E+1	2.50E+2	1.00E+20	2.80E+19
VB Effective Density of States (1/cm <sup>3</sup> )	1.00E+1	2.50E+2	1.00E+20	1.00E+19
Thermal Velocity of Electron (cm/s)	1.00E+7	1.00E+7	1.00E+7	1.00E+7
Thermal Velocity of Hole (cm/s)	1.00E+7	1.00E+7	1.00E+7	1.00E+7
Mobility of Electron (cm <sup>2</sup> /Vs)	2.00E+1	5.00E+1	1.00E-4	1.00E+4
Mobility of Hole (cm <sup>2</sup> /Vs)	1.00E+1	5.00E+1	1.00E-4	2.00E+4
Dopant Concentration of Donor N <sub>D</sub> (1/cm <sup>3</sup> )	1.00E+1	0	0	0
Dopant Concentration of Acceptor N <sub>A</sub> (1/cm <sup>3</sup> )	0	1.00E+17	1.00E+16	1.00E+18
Defect Density N <sub>t</sub> (1/cm <sup>3</sup> )	0	1.00E+13	0	0

### 3. RESULTS AND DISCUSSION

The simulation was performed in two different structures including modified and simple structures. Figure 2 shows the structures of these two cells. Total results indicated that using a polymeric modifier improves the cell's efficiency. Before this investigation, for the goal of having an optimized cell, the impact of important layer properties containing thickness and charge density was investigated too. We will discuss these properties in the sections below.

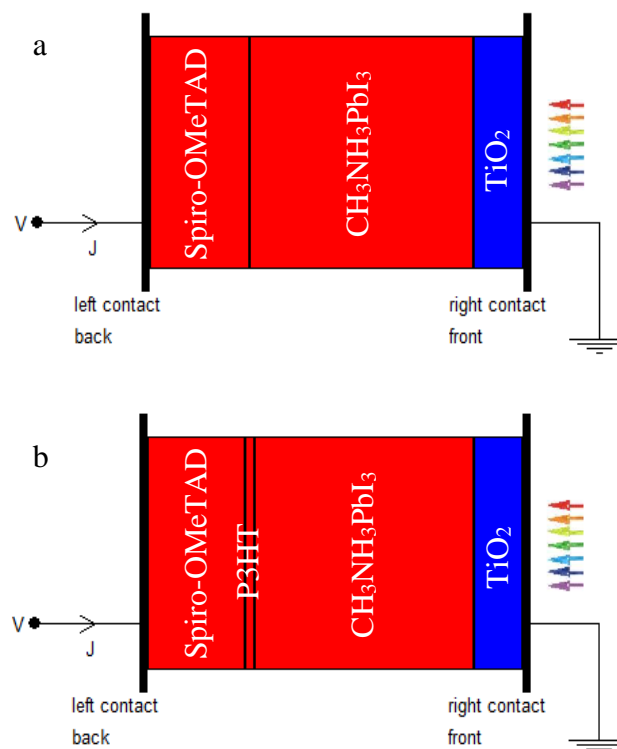


Figure 2 Perovskite solar cell (a) simple (b) modified structure used in this work

#### 3.1. Effect of thickness

##### 3.1.1. Effect of absorber layer thickness

The absorber layer thickness has an important impact on the cell's efficiency. Results indicated that by the increment of perovskite thickness, the cell's overall performance will be improved. Here the thickness was changed from 300-600 nm and results showed that the efficiency increased from 16.05% to 18.15%. This increase is probably due to the greater absorption of photons and the

consequent production of more charge carriers with increasing absorber thickness. In addition, from the plot that was represented in figure 3, it can be seen that the values of  $V_{OC}$  and FF have not changed significantly.  $J_{SC}$  of the cell increased from  $20.40 \text{ mA/cm}^2$  to  $23.51 \text{ mA/cm}^2$  and the cell generated more current as the thickness changed. Figure 3 illustrates the influence of changing the thickness of the perovskite layer (absorber) on the photovoltaic parameters of the simple perovskite solar cell that was used in this work.

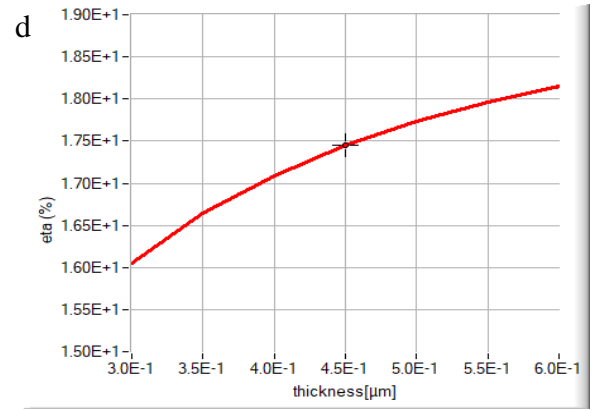
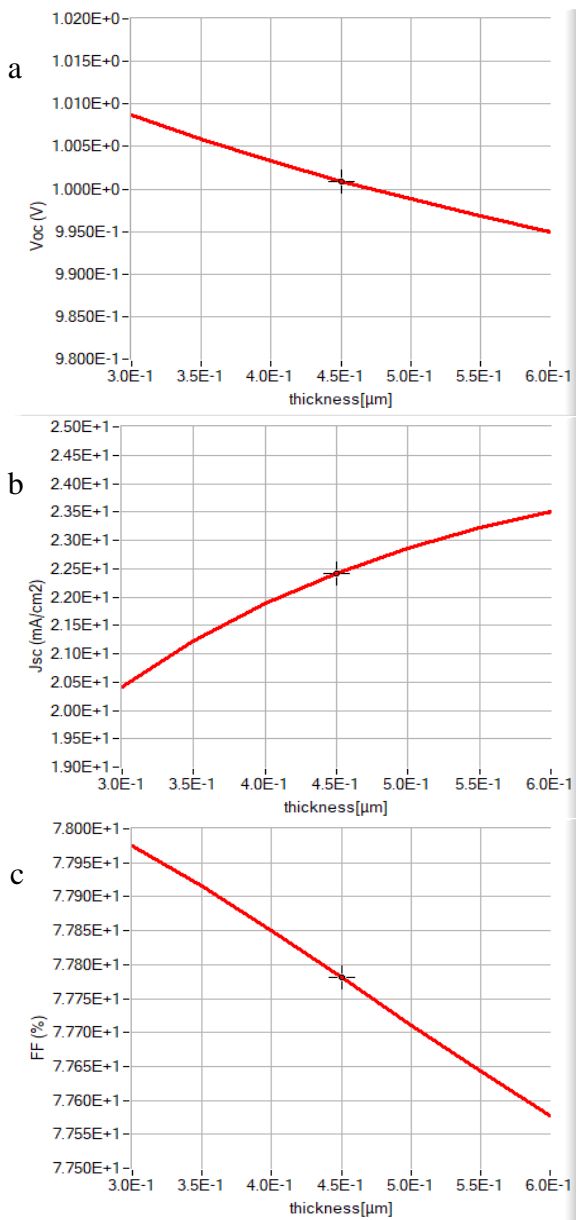


Figure 3 Variation of (a) open-circuit voltage (b) short-circuit current (c) fill-factor (d) power conversion efficiency (eta) by the increment of absorber thickness

### 3.1.2. Effect of ETM thickness

Generally, ETM's higher thickness harms the cell's performance. This can be observed from figure 4 that represents the effect of changing ETL's thickness from 50-150 nm vs. photovoltaic parameters of cell with the optimized thickness for absorber layer (600 nm) that was obtained in the previous section. However, as the results indicate, the change in thickness in this layer does not have a considerable impact on cell performance. The best performance was for the thickness of 50 nm with the photovoltaic parameters of  $V_{OC}= 0.996 \text{ V}$ ,  $J_{SC}= 23.52 \text{ mA/cm}^2$ ,  $FF= 78.35\%$ , and  $PCE= 18.36\%$ .

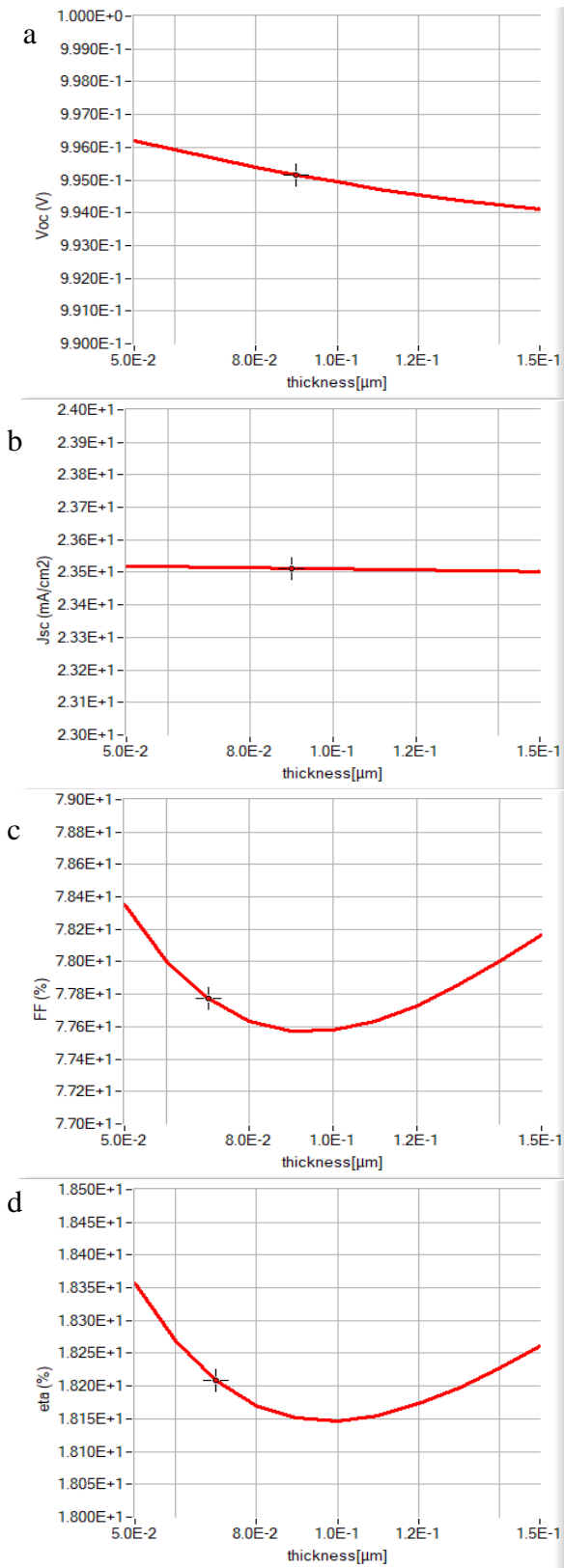


Figure 4 Variation of (a) open-circuit voltage (b) short-circuit current (c) fill-factor (d) power conversion efficiency by the increment of ETM thickness

### 3.1.3. Effect of HTM thickness

The HTM layer thickness change has some impacts on the cell's performance too. The plots of figure 5 confirm this subject. From the results, we can understand that thickness increment doesn't have any positive impact on a cell's efficiency. However, this amount shouldn't be less than a custom value. In this investigation, the thickness of the HTM layer was varied from 100-400 nm. Results indicated that the minimum thickness in this range showed the best performance with the optimum values of the layers in the previous sections. Cell parameters at this thickness were obtained at 0.996 V for  $V_{OC}$ , 23.52 mA/cm<sup>2</sup> for  $J_{SC}$ , 79.01% for FF, and 18.51% for efficiency.

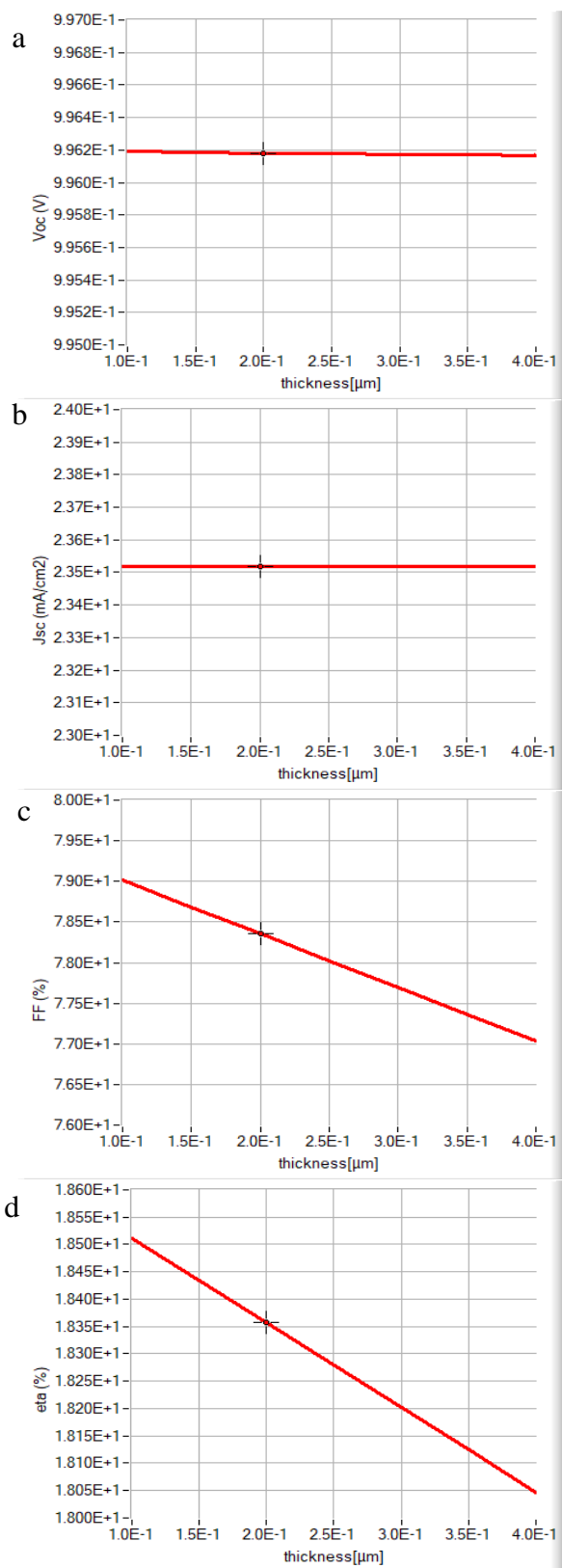


Figure 5 Variation of (a) open-circuit voltage (b) short-circuit current (c) fill-factor (d) power conversion efficiency (eta) by the increment of HTM thickness

### 3.2. Effect of dopant concentrations

The dopant concentration of layers indicates the density of charge carriers in a layer in solar cells. It is obvious that as this value was changed to a higher amount, the cell's efficiency will be improved. In the next three sections, this parameter was changed from  $10^{15}$ - $10^{19}$   $1/cm^3$  and the results were obtained with the optimal values for the layers' thicknesses. All of the optimal values were the maximum amount of dopant concentrations ranges ( $10^{19}$   $1/cm^3$ ). Each section was investigated with the optimum values of its previous sections.

#### 3.2.1. Effect of dopant concentrations of absorber

Figure 6 illustrates the photovoltaic parameters of the studied cell vs. changing dopant concentration of the perovskite layer. Plots indicated the efficiency of 16.18% and 21.50% for the minimum and maximum dopant concentration value of the absorber, respectively. This considerable change is probably because of perovskite's important role in the cell's performance and electricity generation. Results also dedicated that short-circuit current didn't change significantly in the mentioned range but the values of  $V_{oc}$  and FF underwent considerable changes.

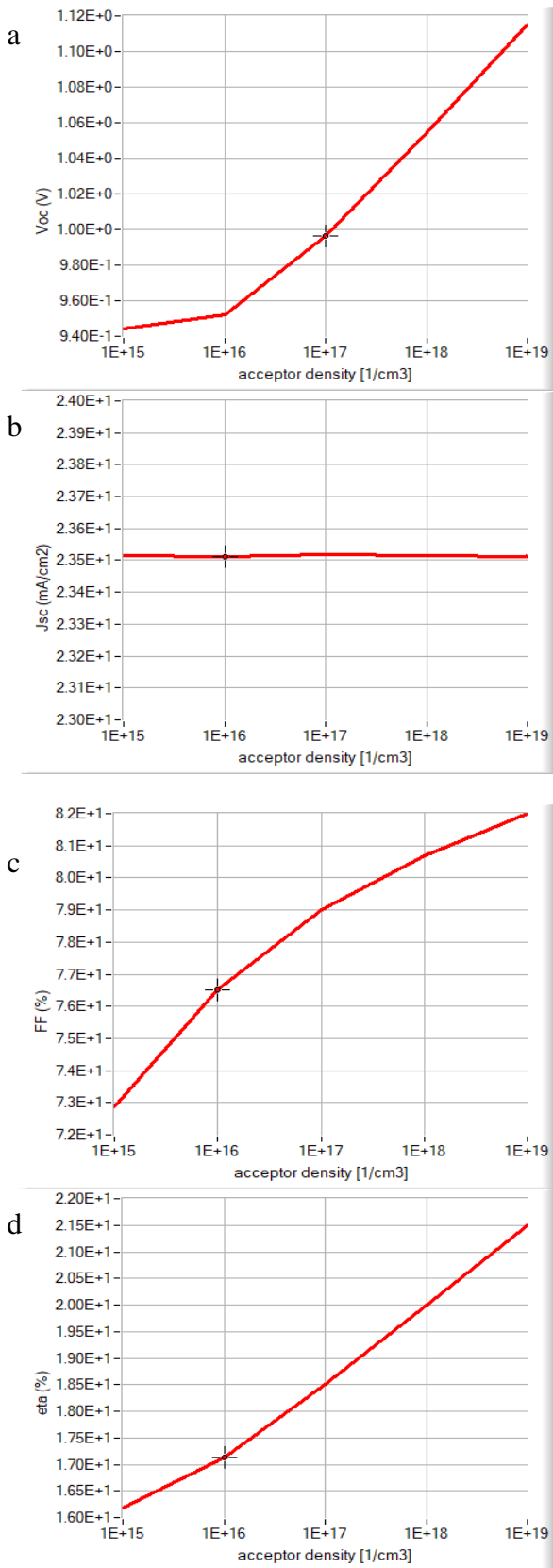
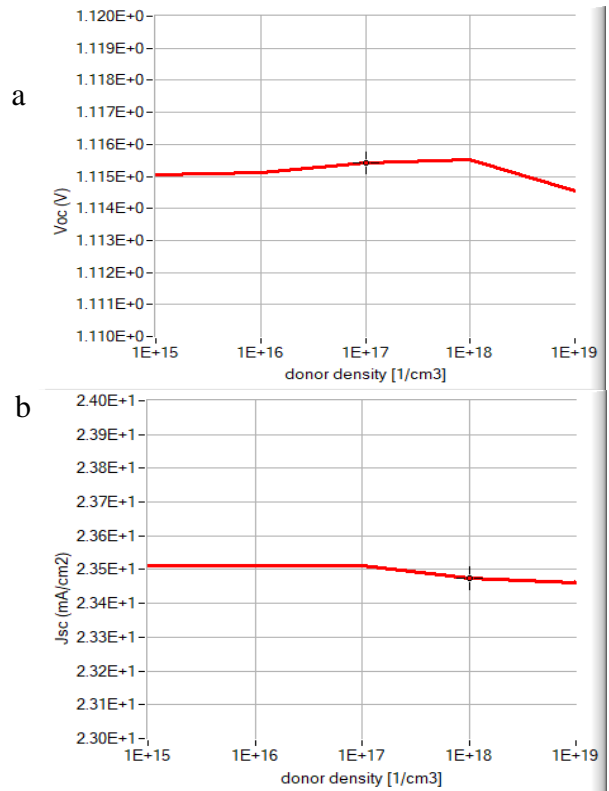


Figure 6 Variation of (a) open-circuit voltage (b) short-circuit current (c) fill-factor (d) power

conversion efficiency ( $\eta$ ) by the increment of dopant concentrations of absorber

### 3.2.2. Effect of dopant concentrations of ETM

Changes in the dopant concentration of the ETM layer, such as changes in thickness, do not have a significant effect on cell performance. This can be seen in figure 7. However, the main parameters of the cell with the optimal values of the previous sections were obtained in the values of  $V_{OC}=1.114V$ ,  $J_{SC}= 23.46 \text{ mA/cm}^2$ ,  $FF= 87.48\%$ , and  $PCE= 22.87\%$ .



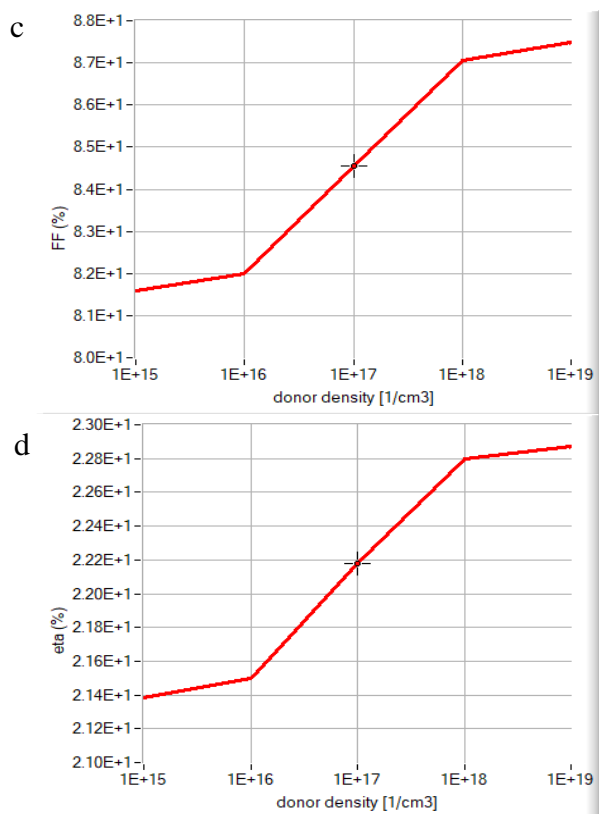


Figure 7 Variation of (a) open-circuit voltage (b) short-circuit current (c) fill-factor (d) power conversion efficiency (eta) by the increment of dopant concentrations of ETM

### 3.2.3. Effect of dopant concentrations of HTM

Figure 8 demonstrates the effect of variation of HTM's dopant concentration on the cell's performance with the previous optimal values. Results showed that  $V_{OC}$  and  $J_{SC}$  didn't undergo considerable changes in their values, but the amounts of FF and PCE indicated almost 30% and 8% in the variation range of dopant concentration, respectively. The optimum value for the acceptor density of HTM was obtained  $10^{19}$  1/cm<sup>3</sup> that represented the 23.02% value for efficiency.

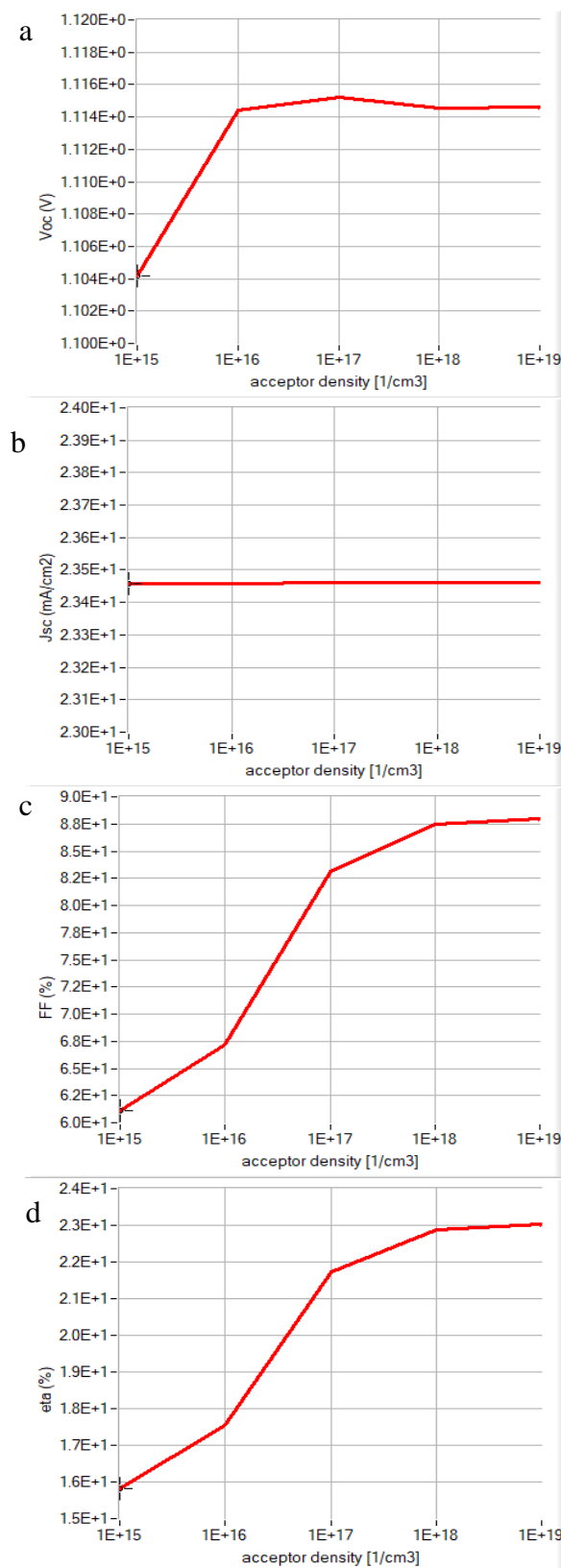


Figure 8 Variation of (a) open-circuit voltage (b) short-circuit current (c) fill-factor (d) power conversion efficiency (eta) by the increment of dopant concentrations of HTM

### 3.3. Effect of absorber defect density

Different defects of solar cells' layers always have negative impacts on the cell's performance. This is due to the trapping of charge carriers in the defect sites of the layers. Results of variation of photovoltaic parameters vs. the defect density increment in figure 9 confirm this subject too. Plots represent that there is a 10% difference between the efficiency of the highest and lowest value in the defect density range. The best result was for the density of  $10^{13}$   $1/cm^3$  with the previous optimized values and represents the efficiency of about 24.5%. Other photovoltaic parameters for this value were  $V_{OC}= 1.18$  V,  $J_{SC}= 23.47$   $mA/cm^2$ ,  $FF= 88.46\%$ .

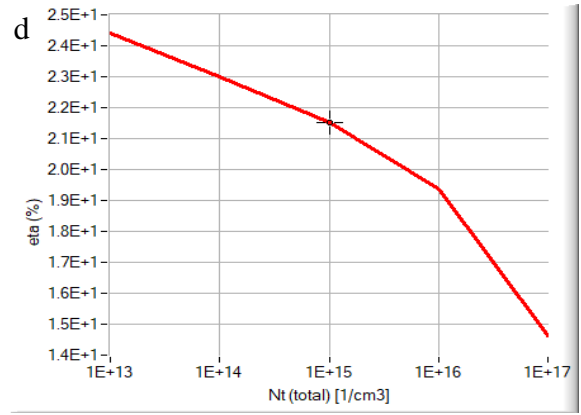
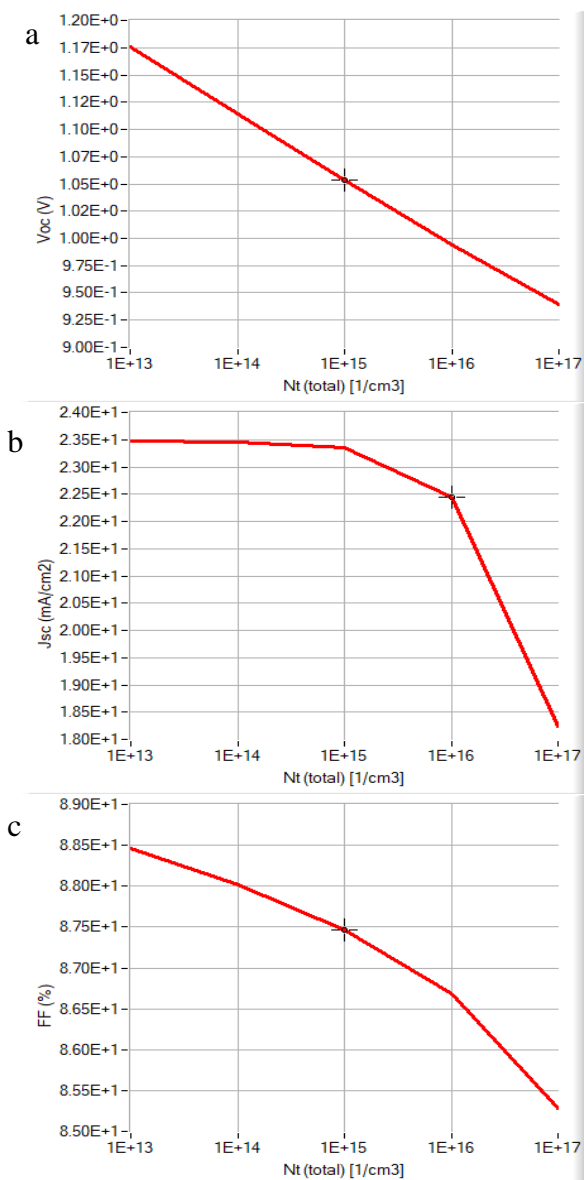


Figure 9 Variation of (a) open-circuit voltage (b) short-circuit current (c) fill-factor (d) power conversion efficiency by the increment of defect density of the absorber



### 3.4. Effect of interface modification

As it was mentioned in the previous sections, the addition of an ultrathin polymeric layer to the interface between the absorber layer and hole transporting material avoids corrosion among them and lessens the defects because of its regular structure. Besides the stability issue, it helps to improve the cell's efficiency because of less recombination in the interface layer. Our results in this study confirm this effect too. By using an ultrathin 20 nm polymeric P3HT layer in the perovskite and Spiro-OMeTAD layers' interface, the cell's efficiency increased from about 24.5% to 26.5%.

### 3.5. Final I-V curve

After optimizing all of the factors mentioned above, and the addition of the polymeric modifier to the cell's structure, the final current-voltage (I-V) curve of the modified perovskite solar cell was obtained. The curve was given in figure 10 with its corresponding photovoltaic parameters. Results were in good agreement with the experimental works [11-14]. The final results were represented in table 2.

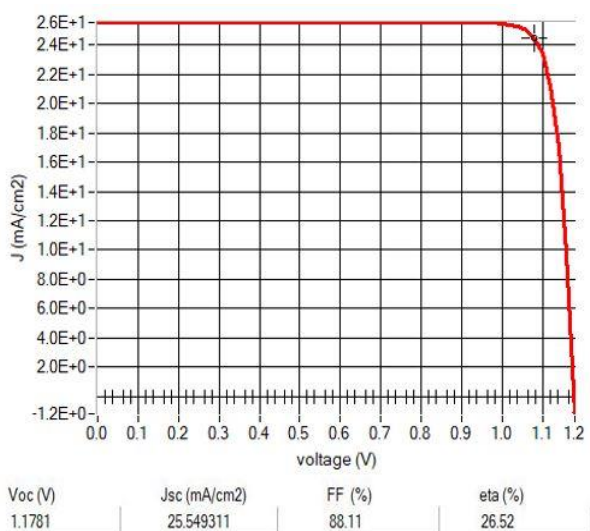


Figure 10 The final current-voltage curve of the modified cell by the optimized parameters

Table 2 Photovoltaic parameters of selected modified and single cells obtained by SCAPS software and their comparison with experimental works [11-14]

Cell's structure	Voc (V)	Isc (mA/cm2)	FF (%)	PCE (%)
Simple (SCAPS-1D)	1.18	23.47	88.46	24.41
Simple (experimental)	0.98	21.2	77.6	18.7
Modified (SCAPS-1D)	1.18	25.54	88.11	26.52
Modified (experimental)	1.13	-	-	20.8

#### 4. CONCLUSIONS

In this study, two simple and modified structures of a custom perovskite solar cell based on  $\text{CH}_3\text{NH}_3\text{PbI}_3$  were simulated by SCAPS-1D in two simple and modified cases and their performance was investigated separately with the optimized parameters for each layer. Results represented that the modified cell with P3HT as a polymeric interface between the perovskite and HTM layer indicated the best efficiency. The optimized thicknesses for the layers were 100 nm, 600 nm, 50 nm for HTM, absorber, ETM layers, respectively. The optimal value of dopant concentration of the mentioned layers was  $10^{19} \text{ 1/cm}^3$  for each layer. With the optimal values that were obtained, the final and best efficiency was about 26.5% for the modified cell.

#### Acknowledgments

The authors would like to thank the cooperation of the University of Tabriz, the University of Sakarya, and the School of Industrial and Information Engineering in Italy for the implementation of this project.

#### Funding

The authors have no received any financial support for the research, authorship, or publication of this study.

#### The Declaration of Conflict of Interest/ Common Interest

This study was produced from the Seyyed Reza Hosseini, Master thesis which was accepted on April 14, 2021, in the Department of Chemical Engineering, the University of Tabriz with supervisor Prof. Aligholi Niaei and advisor Dr. Nagihan Delibaş.

#### Authors' Contribution

Within this study, all authors were involved and cooperated in idea formation, simulation, evaluation of the data, and results.

#### The Declaration of Ethics Committee Approval

This study does not require ethics committee permission or any special permission.

#### The Declaration of Research and Publication Ethics

The authors of the paper declare that they comply with the scientific, ethical, and quotation rules of SAUJS in all processes of the paper and that they do not make any falsification on the data collected. In addition, they declare that Sakarya University Journal of Science and its editorial board have no responsibility for any ethical violations that may be encountered and that this study has not been evaluated in any academic publication environment other than Sakarya University Journal of Science.

## REFERENCES

- [1] Hussain I, Tran HP, Jaksik J, Moore J, Islam N, Uddin MJ. "Functional materials, device architecture, and flexibility of perovskite solar cell" *Emergent Materials*, vol. 1, no. 3, pp.54-133, 2018.
- [2] Kojima A, Teshima K, Shirai Y, Miyasaka T. "Organometal halide perovskites as visible-light sensitizers for photovoltaic cells" *Journal of the American Chemical Society*, vol. 131, no. 17, pp.1-6050, 2009.
- [3] Kim HS, Lee CR, Im JH, Lee KB, Moehl T, Marchioro A, Moon SJ, Humphry-Baker R, Yum JH, Moser JE, Grätzel M. "Lead iodide perovskite sensitized all-solid-state submicron thin film mesoscopic solar cell with efficiency exceeding 9%" *Scientific reports*, vol. 2, no. 1, pp.1-7, 2012.
- [4] Cai Y, Zhang Z, Zhou Y, Liu H, Qin Q, Lu X, Gao X, Shui L, Wu S, Liu J. "Enhancing the efficiency of low-temperature planar perovskite solar cells by modifying the interface between perovskite and hole transport layer with polymers" *Electrochimica Acta*, vol. 261, pp.53-445, 2018.
- [5] Du Y, Xin C, Huang W, Shi B, Ding Y, Wei C, Zhao Y, Li Y, Zhang X. "Polymeric surface modification of NiOx-based inverted planar perovskite solar cells with enhanced performance", *ACS Sustainable Chemistry & Engineering*, vol. 6, no. 12, pp.12-16806, 2018.
- [6] Huang LB, Su PY, Liu JM, Huang JF, Chen YF, Qin S, Guo J, Xu YW, Su CY. "Interface engineering of perovskite solar cells with multifunctional polymer interlayer toward improved performance and stability", *Journal of Power Sources*, vol. 378, pp.90-483, 2018.
- [7] Burgelman M, Nollet P, Degraeve S. "Modelling polycrystalline semiconductor solar cells. *Thin solid films*" vol. 361, pp.32-527, 2000.
- [8] Karimi E, Ghorashi SM. "Investigation of the influence of different hole-transporting materials on the performance of perovskite solar cells", *Optik*, vol. 130, pp.8-650, 2017.
- [9] Karimi E, Ghorashi SM. "Simulation of perovskite solar cell with P3HT hole-transporting materials", *Journal of Nanophotonics*, vol. 11, no. 3, pp. 032510, 2017.
- [10] Kim E, Bhattacharya I. "Material selection method for a perovskite solar cell design based on the genetic algorithm". In 2020 47th IEEE Photovoltaic Specialists Conference (PVSC), pp. 2631-2634, 2020.
- [11] Zhang F, Shi W, Luo J, Pellet N, Yi C, Li X, Zhao X, Dennis TJ, Li X, Wang S, Xiao Y. "Isomer-pure bis-PCBM-assisted crystal engineering of perovskite solar cells showing excellent efficiency and stability", *Advanced Materials*, vol. 29, no. 17, pp. 1606806, May 2017.
- [12] Kapur VK, Basol BM, Tseng ES. "Low cost methods for the production of semiconductor films for CuInSe<sub>2</sub>/CdS solar cells", *Solar cells*, vol. 21, no. 1-4, pp.65-72, June 1987.
- [13] Kapur VK, Bansal A, Le P, Asensio OI. "Non-vacuum processing of CuIn<sub>1-x</sub>Ga<sub>x</sub>Se<sub>2</sub> solar cells on rigid and flexible substrates using nanoparticle precursor inks". *Thin solid films*, vol. 431, pp.7-53, May 2003.
- [14] Dhere NG, Ghongadi SR, Pandit MB, Jahagirdar AH, Scheiman D. "CIGS<sub>2</sub> thin-film solar cells on flexible foils for space power", *Progress in Photovoltaics: Research and Applications*, vol. 10, no. 6, pp.16-407, September 2002.



SAKARYA ÜNİVERSİTESİ

# FEN BİLİMLERİ ENSTİTÜSÜ DERGİSİ

Sakarya University Journal of Science  
SAUJS

e-ISSN: 2147-835X | Founded: 1997 | Period: Bimonthly | Publisher: Sakarya University |  
<http://www.saujs.sakarya.edu.tr/en/>

Title: Carbon Nanofibers Fabricated from Electrospun Nano-sized boron oxide/Polyacrylonitrile Nanofibers as electrode for Supercapacitors

Authors: Ümran KURTAN

Received: 2021-02-09 00:00:00

Accepted: 2021-09-09 00:00:00

Article Type: Research Article

Volume: 25

Issue: 5

Month: October

Year: 2021

Pages: 1180-1188

How to cite

Ümran KURTAN; (2021), Carbon Nanofibers Fabricated from Electrospun Nano-sized boron oxide/Polyacrylonitrile Nanofibers as electrode for Supercapacitors.

Sakarya University Journal of Science, 25(5), 1180-1188, DOI:

<https://doi.org/10.16984/saufenbilder.877089>

Access link

<http://www.saujs.sakarya.edu.tr/tr/pub/issue/65589/877089>

New submission to SAUJS

<http://dergipark.org.tr/en/journal/1115/submission/step/manuscript/new>

## Carbon Nanofibers Fabricated from Electrospun Nano-sized Boron oxide/Polyacrylonitrile Nanofibers as Electrode for Supercapacitors

Ümran KURTAN\*<sup>1</sup>

### Abstract

Porous carbon nanofiber (CNF) composites are promising electrode materials for supercapacitor (SC) applications. In this research, to investigate the effect of nano-sized boron oxide ( $B_2O_3$ ) to CNF, PAN solutions introduced with nano-sized boron oxide ( $B_2O_3$ ) were electrospun then thermal treatment was applied at high temperature. The best electrochemical performance was found for the sample which was doped 1 wt% nano-sized boron oxide and a gradual decrease was seen when the content was increased from 1 to 5 wt%. 1BCNF electrodes prepared from 1 wt% nano-sized boron oxide with PAN show a remarkable specific capacitance of  $146 \text{ Fg}^{-1}$  at  $1 \text{ Ag}^{-1}$  compared to the pure CNF which is  $46 \text{ Fg}^{-1}$ . Also, 1BCNF composite has an excellent cycle life which is more than 90 % capacity retention after 6500 cycles. The results showed that 1BCNF composite is a promising potential electrode for supercapacitor applications due to the optimized pore structure and enhanced electrical conductivity.

**Keywords:** Electrospinning, nano-sized boron oxide, carbon nanofiber, supercapacitors.

### 1. INTRODUCTION

Supercapacitors are the subject of intense research in energy storage sector due to their high power density, rapid charge-discharge and superior cycle stability [1-4]. A supercapacitor (SC) has the electrical charge capacitance up to hundreds of times compared to the conventional capacitors and it stores energy electrostatically by charge accumulation at the electrode-electrolyte interface. As the key part of SCs, active electrode material is critical for high performance. To date, conductive polymers, transition metal compounds and carbon-based materials have received extensive attention as electrode materials. Carbon based nanomaterials such as activated carbon, graphene, carbon nanotube and carbon nanofibers

(CNFs) are commonly used as electrode materials for supercapacitor applications [5–7]. Graphene and CNTs are extensively investigated by the researchers but their close packing, entanglement and agglomeration problems can inhibit the practical applications in energy storage [8-11]. With respect to these considerations, carbon nanofibers with exceptional one dimensional (1D) nanostructure can have many inherent advantages for an electrode of a supercapacitor such as small number of defects low cost, excellent conductivity, ultrahigh power density and compact structure to construct flexible devices compared to graphene and CNTs [12]. On the other hand, pure CNFs still have disadvantages such as low hydrophilicity and low energy density

\* Corresponding author: umran.kurtan@istanbul.edu.tr

<sup>1</sup> Department of Materials and Materials Processing Technologies, Vocational School of Technical Sciences, Istanbul University-Cerrahpaşa, 34500, Istanbul/Turkey.

ORCID: <https://orcid.org/0000-0002-1279-7729>

thus it is still needed to be improved to enhance the properties of CNFs. Fortunately, modification the surface of CNFs such as heteroatom doping or surface activation is an alternative way to eliminate these disadvantages. Recently, heteroatoms doping is generally focused on to enhance the electrochemical properties and hydrophilicity of the carbon materials [6-8]. This study discusses design, fabrication and application of nano-sized  $B_2O_3$  loaded PAN nanofibers followed by carbonization for supercapacitor applications. The energy storage efficiency can be altered for the optimization of the electrochemical performance.

## 1. EXPERIMENTAL

### 1.1. Chemicals

Polyacrylonitrile (PAN), which has a molecular weight of  $150,000 \text{ gmol}^{-1}$  and N,N-Dimethylformamide (DMF) were supplied from Sigma-Aldrich; boron oxide ( $B_2O_3$ ) nanoparticles from SSNano, USA.

### 1.2. Fabrication of CNF composite electrodes

Firstly, 8 wt% of PAN polymer was dissolved in DMF by stirring. After, nano-sized boron oxide powder (1 and 5 wt% relative to PAN) were added into polymer solution and mixed together overnight at  $50^\circ\text{C}$  to obtain a uniform solution. The precursor solutions were electrospun with a 10-ml plastic syringe at an electrostatic voltage of 18 kV and the rate was  $1 \text{ mlh}^{-1}$ . Polymeric fibers were placed into a tube furnace and then stabilization was performed at  $250^\circ\text{C}$  ( $5^\circ\text{Cmin}^{-1}$ ) for 2h. After, carbonization was carried out by heating to  $800^\circ\text{C}$  ( $2^\circ\text{Cmin}^{-1}$ ) for 2 h under  $N_2$  flow to obtain CNFs. The activated samples, denoted as 1BCNF and 5BCNF, indicate concentrations of 1 and 5% nano-sized  $B_2O_3$  relative to PAN, respectively. Pure CNF without nano-sized  $B_2O_3$  was also prepared as shown in Figure 1.

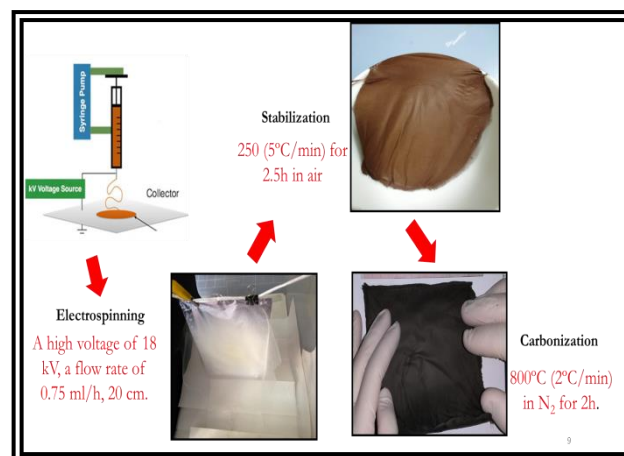


Figure 1 Schematic diagram of carbon nanofiber (CNF) formation.

### 1.3. Characterization

Fourier Transform Infrared (FTIR, Bruker) spectra of the nanofibers were taken by using a Bruker FTIR-ATR spectrometer in the range from  $4000$  to  $400 \text{ cm}^{-1}$ . The morphology of the carbonized fiber samples were observed by scanning electron microscope (JEOL JSM-7001F SEM). Electrochemical performance was evaluated with a two-electrode system. For this, the self-supported CNF electrodes were firstly cut into two pellet discs of 10 mm in diameter and sandwiched a Whatman glass fiber separator in a coin cell (CR2032). The electrolyte was 6M KOH solution. Cyclic voltammetry (CV) and electrochemical impedance spectroscopy (EIS) were performed using a Gamry potentiostat-galvanostat-ZRA Interface 1010B. The EIS test was performed with frequency rate from 20 kHz to 0.1Hz. Galvanic charge-discharge (GCD) measurements of the full cells were carried out using a battery test system (MTI).

In two-electrode model, the specific capacitance ( $C_{sp}$ ,  $\text{Fg}^{-1}$ ) could be estimated from GCD tests using the below formula [9-10]:

$$C_{sp} = (2 \times I \times \Delta t) / (m \times \Delta U) \quad (1)$$

where  $I$  is the constant current in GCD,  $t$  is the discharge time,  $\Delta U$  is the potential window and  $m$  is the mass of single electrode. Specific energy ( $E$ ,  $\text{Whkg}^{-1}$ ) and specific power ( $P$ ,  $\text{Wkg}^{-1}$ ) are calculated according to the following equations.

$$E = \frac{1}{3.6} \times \frac{1}{8} \times C_{sp} \times \Delta U^2 \quad (2)$$

$$P = \frac{3600E}{\Delta t} \quad (3)$$

## 2. RESULTS AND DISCUSSION

Chemical characteristics of all CNFs are firstly investigated by FT-IR spectra and shown in Figure 2. Two main absorption peaks at  $\sim 1100$  and  $1556 \text{ cm}^{-1}$  are observed due to the stretching band of C-C and C=C bonds, respectively. This implies that cyclization of nitrile groups of PAN takes place during stabilization and carbonization process. This phenomenon is similar to the previously reported articles in literature [18-19]. A new peak is appeared in the FT-IR spectrum of both 1BCNF and 5BCNF composites at around  $800 \text{ cm}^{-1}$  which is related to the activity of (O)BN functional groups. These results are evidence that CNF composites are synthesized successfully.

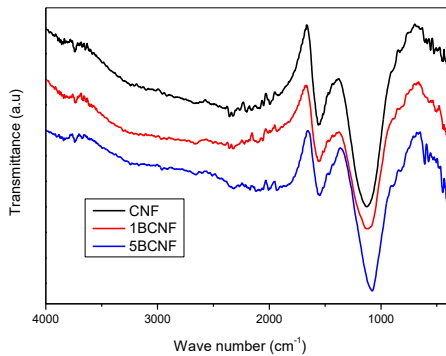


Figure 2 FT-IR spectra of pure CNF, 1BCNF and 5BCNF.

Exemplary SEM micrographs showing typical fiber morphologies are presented in Fig. 3a-c. The SEM images of the all CNFs display long and continuous interconnected morphologies. Fig. 3a shows the images of neat PAN-based CNFs which are a unique hierarchical porous network structure. When the nano-sized boron oxide amount is 1 wt%, more macropores are formed within the nanofibers, leading to a decrease in fiber diameter without any collapsing the fibrous morphology (Fig. 3b). But, when the nanosized boron oxide amount increases from 1 to 5 wt%, the fiber diameter decreases and shows a curved

morphology (Fig. 3c). From these results, we can hypothesize that the porosity is strongly dependent on the amount of added material and the nano-sized boron oxide can effectively create suitable pores during thermal treatment [19-20].

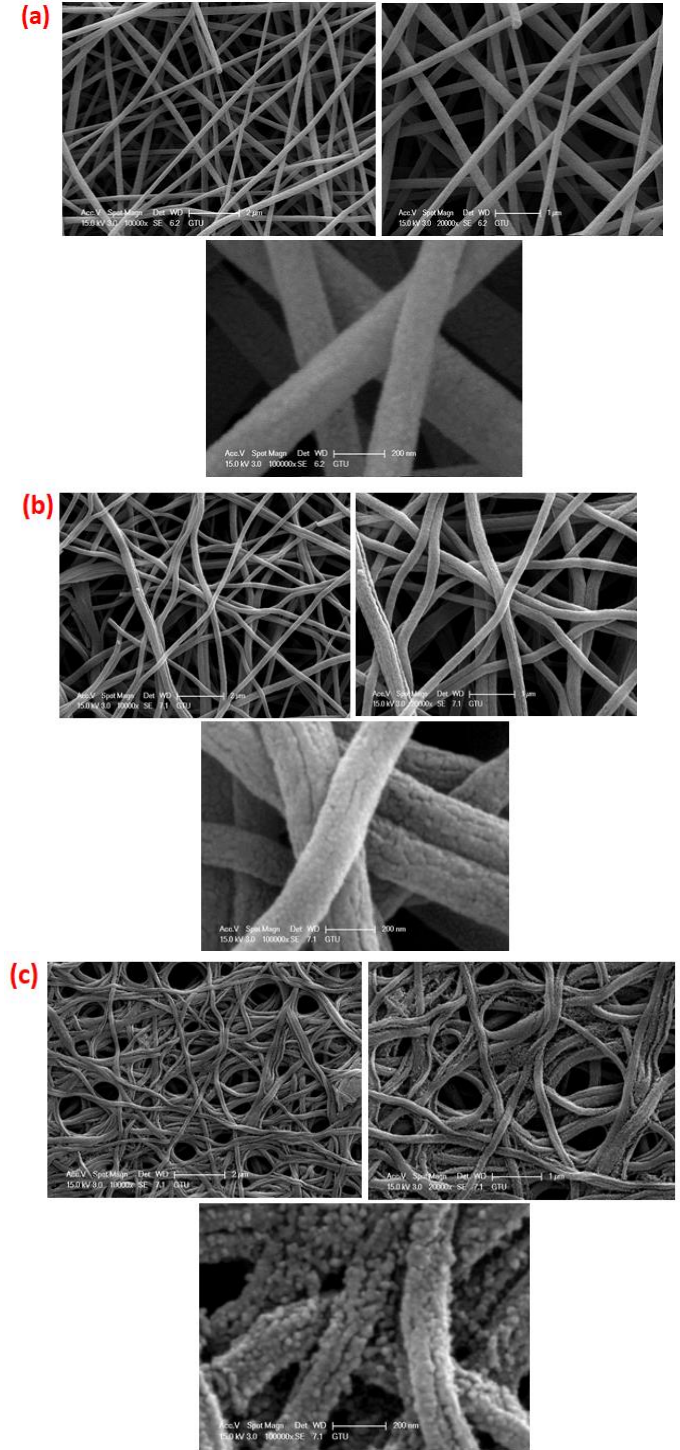


Figure 3 SEM images of (a) pure CNF, (b) 1BCNF and (c) 5BCNF.

### 2.1. Electrochemical Measurements

The electrochemical activities of the prepared electrodes were firstly investigated by CV analysis. Fig. 4 illustrates the CV plots of pure CNF, 1BCNF and 5BCNF with the potential window of 0-1V and ranging a scan rate of 10, 25, 50, 75, 100 and 200 mVs<sup>-1</sup> obtained by two-electrode cell measurement. The rectangular shape of CV curves was observed for 1BCNF and 5BCNF, which suggests a potential capacitive behavior comparing to pure CNF. High scan rates caused to decrease in specific capacitance since electrolyte cannot access the full surface of electrode [22, 23]. Notably, the shape of the CV graphs of 1BCNF are well maintained even at the scan rate of 200 mVs<sup>-1</sup>, indicating the good rate ability among all CNFs. 1BCNF electrode has highest current density which indicates a large increase in capacitance. These results indicate that 1BCNF electrode shows a typical SC behavior.

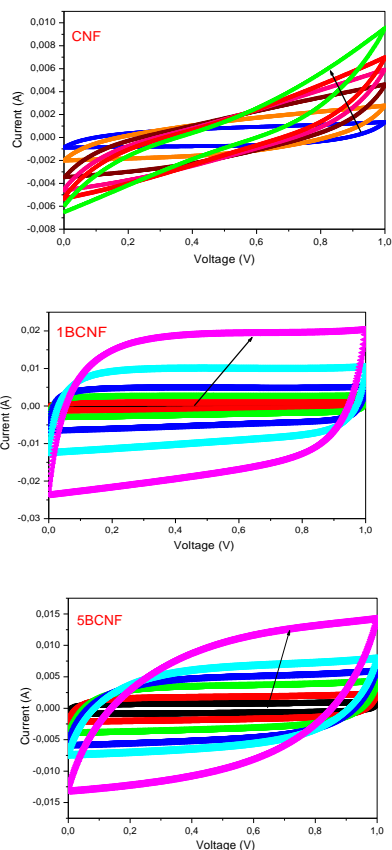


Figure 4 CV of CNF, 1BCNF and 5BCNF at different scan rates. The arrows mean the trend in CV with the increasing scan rates (from 10 to 200 mVs<sup>-1</sup>).

Figure 5a-c shows GCD curves of CNF, 1BCNF and 5BCNF at a current density of 0.5-5 Ag<sup>-1</sup>. It was noticed that there is a common trend in specific capacitance while current density increases, the specific decreases. Compared to the pure CNF, there is a big increase in the discharging time meaning that the introduction of nano-sized boron oxide enhances the electron mobility between carbon nanofibers. The discharge time is the longest for 1BCNF thus the highest specific capacitance it has. The lines are almost linear and symmetrical. It should be also noted that there is an IR drop in pure CNF electrodes but there is no such IR drop observed for 1BCNF and 5BCNF. This difference is due to the electrode microstructure.

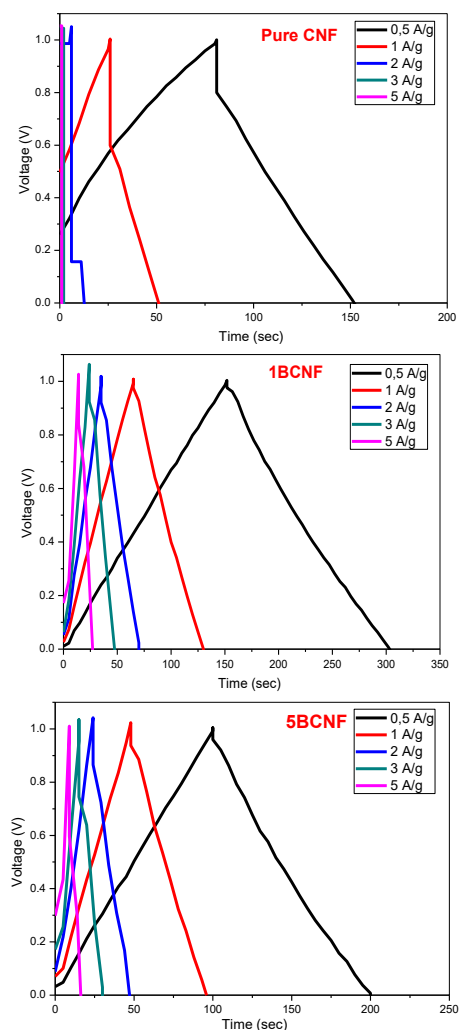


Figure 5 GCDs curves of SCs using CNF, 1BCNF and 5BCNF in 6M KOH electrolyte at different current densities.

The CV graphs of CNF based SC devices acquired at 50 mVs<sup>-1</sup> scan rate are presented in Fig. 6a. Nano-sized boron oxide added nanofibers, 1BCNF and 5BCNF, show a larger rectangle shape compared to the pure CNF, which means the expansion of the electrical double-layer area implying an ideal capacitive behavior. Specifically, 1BCNF has the largest integral area among all CNFs. This is ascribed to rapid diffusion of electrolyte within the electrode, 1BCNF, and the quick charge-discharge cycles.

Figure 6b shows specific capacitance values obtained at various current densities (0.5 to 5Ag<sup>-1</sup>). Among them, SC cell assembled with 1BCNF electrode showed the best specific capacitance. The specific capacitance value of 1BCNF was found as 150 Fg<sup>-1</sup> for at 0.5Ag<sup>-1</sup> and it still maintained by 86.7 % at 5Ag<sup>-1</sup>, providing an exceptional retention ability.

Fig. 6c indicates that the specific capacitances of CNF, 1BCNF and 5BCNF at 1 Ag<sup>-1</sup> are 46, 146 and 96 Fg<sup>-1</sup>, respectively (Table 1). The gravimetric specific capacitance value of 1BCNF is enhanced by a factor of about 3 compared to pure CNF which are comparable reported in the literature [14, 24, 25]. As expected from the results of the CV and GCD measurements, the specific capacitance increased as follows: CNF < 5BCNF < 1BCNF suggesting that lower amount of nano-sized boron oxide addition may provide fast ion channels and ion mobility.

Table 1 Gravimetric electrochemical performance of symmetric electrodes in 6M KOH electrolytes.

Sample	Specific Capacitance of the Electrode (F/g)		Energy and Power Density for the device		
	CV at 50mV/s	GCD at 1A/g	EIS (ohm) 0.1Hz to 1MHz	E(Wh/kg)	P(W/kg)
CNF	47	46	38	1.6	250
1BCNF	120	146	2.9	5.1	252
5BCNF	91	96	9.4	3.3	248

In order to better understand the electrochemical performance of the studied samples, EIS was employed. Fig. 6d presents the Nyquist plots for the studied electrodes. All impedance spectra of

CNF, 1BCNF and 5BCNF showed almost similar behavior, presenting a half semicircle at high frequencies and a straight line at low frequencies. SC from pure CNF exhibited a highest semicircle indicating a poor capacitive performance. For the device made of 1BCNF electrodes, the semicircle decreased clearly, suggesting the lower charge transfer resistance. In the presence of more nano-sized boron oxide addition, it is better than pure CNF but worse than 1BCNF, which is consistent with the little IR drop of the discharge curve. Based on these results, it is worth mentioning that the small amount of nano-size boron oxide doped interconnected carbon network can provide a continuous conducting paths for electron transfer as well as excellent structural stability during electrochemical process.

The specific energy (E) and specific power (P) are important parameters that characterize the performance of supercapacitors. Fig. 6e is a Ragone plot, which correlates the energy density and the power density of all supercapacitor. A symmetric SC based on the CNFs is compatible with the discharging time observed in GCD curves, where a longer discharging time indicates a better specific energy value. As expected, 1BCNF symmetric SC delivers a maximum specific energy of 5.2 Whkg<sup>-1</sup> at a specific power of 125 Wkg<sup>-1</sup>, and a maximum specific power of 1245 Wkg<sup>-1</sup> at a specific energy of 4.5 Whkg<sup>-1</sup>. 5BCNF possessed the specific energy of 3.5-2.8 Whkg<sup>-1</sup> while pure CNF exhibited a dramatical decrease in specific energy (2.5 Whkg<sup>-1</sup>) in the similar range of specific power range. These are close and even better values reported in previous studies [1, 26].

The long-term cycle stability test is a crucial factor in SC application. In this study, SC stability was evaluated by repeating the GCD measurements for 6500 cycles at a fixed current density of 1 Ag<sup>-1</sup>. The results are shown in Figure. 6f. The lowest capacitance retention is seen for pure CNF which can be explained by decomposition of electrode during charge/discharge process. On the other hand, 1BCNF shows a good cycling stability with a capacitance loss of 9.4 % after 6500 cycles. It confirms that its porous structure can offer more

channels for the electrolyte ions. Also, high porosity can easily relieve the internal stress during charging and discharging process, protecting the electrode from physical damage. Thus, the more fibrous an electrode, the better cycle stability is [6].

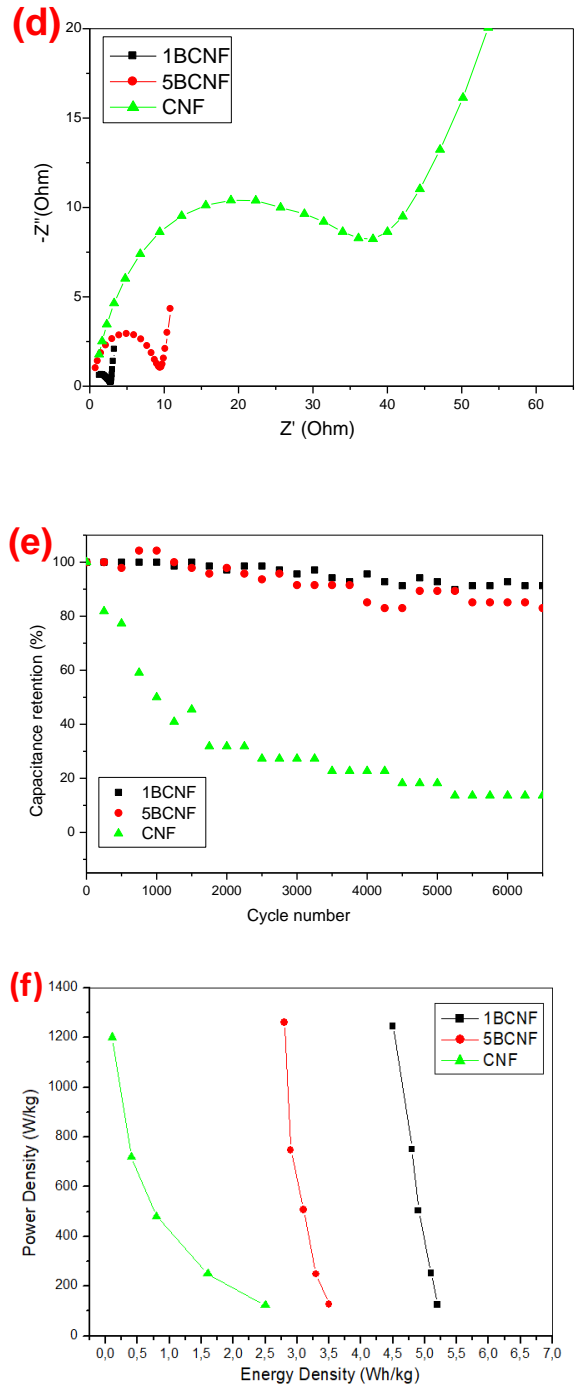
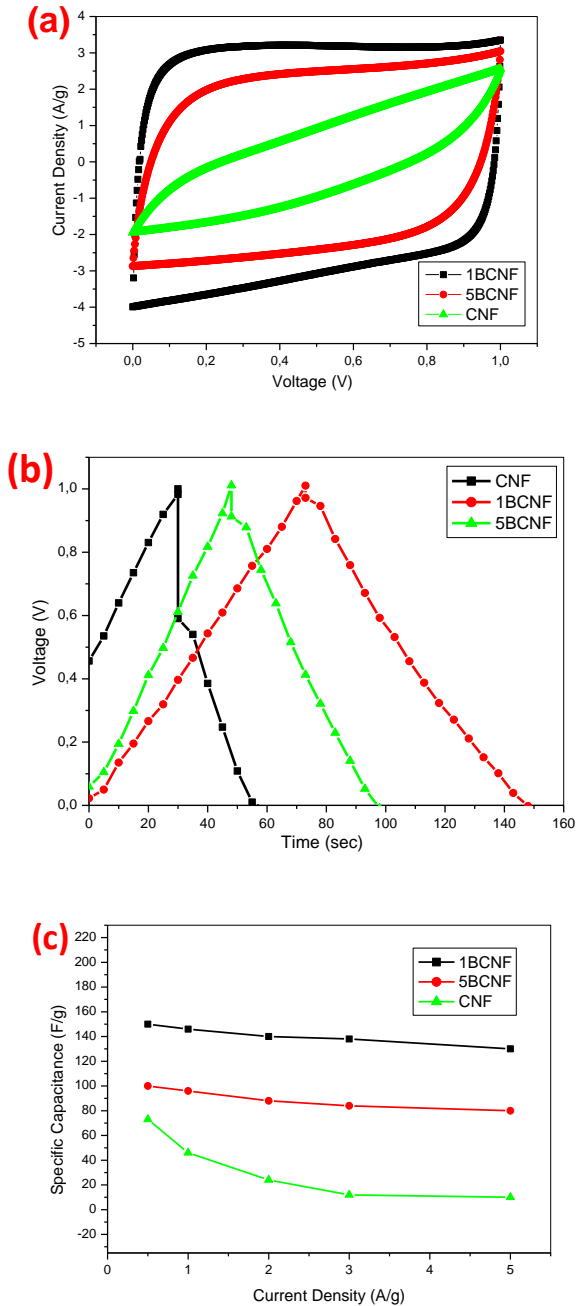


Figure 6 Electrochemical performance of CNF, 1BCNF and 5BCNF based SC cell of (a) CV plots at 50 mVs<sup>-1</sup>, (b) galvanic charge/discharge graphs at 1 Ag<sup>-1</sup>, (c) specific capacitance for various current densities, (d) Nyquist plots, (e) cycling performance test for 1 Ag<sup>-1</sup>, (f) Ragone plot.

In order to investigate the electrochemical stability of the as-fabricated supercapacitor, the device was cycled for 6500 cycles as depicted in Fig. 7a and 7b. Fig. 7a shows the Nyquist plots

obtained by EIS for the device composed of 1BCNF electrode. As can be seen, the semicircular diameter increased slightly after 6500 cycles which may be caused by the inferior ionic conductivity and ion diffusion rate. Fig. 7b shows the cycling stability of 1BCNF acquired by CV at  $200 \text{ mVs}^{-1}$ . Excitingly, CV plot did not change significantly and almost overlapped even after 6500 cycles, indicating the capacitance showed a low degradation and superior cycling reversibility. Thus, the cycle stability result reveals that 1BCNF is a suitable electrode for long term stability SC.

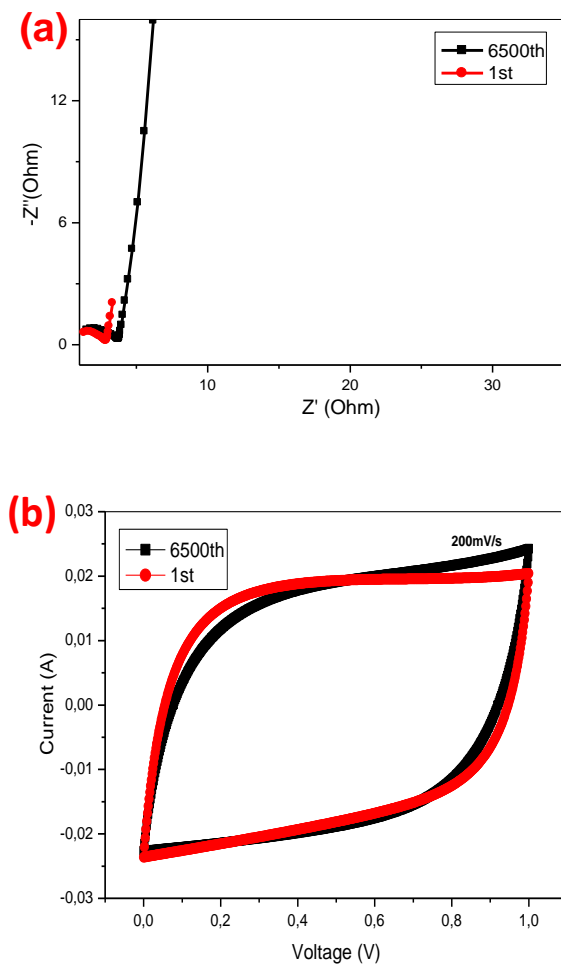


Figure 7 Electrochemical cycling stability test of symmetrical SC cells fabricated with identical 1BCNF electrodes before and after 6500 cycles, (a) EIS plots and (b) CV at  $200 \text{ mVs}^{-1}$

### 3. CONCLUSION

In summary, starting from electrospun PAN/nano-sized boron oxide composites, 1BCNF and 5BCNF were fabricated via oxidation and carbonization. CV and GCD results proved that 1BCNF electrode has the best electrochemical performance with respect to specific capacitance and energy density thus the optimum weight percentage of nanoparticles in PAN polymer was found to be 1. Additionally, 1BCNF supercapacitor exhibited an exceptional long cycle lives for at least 6500 charge/discharge cycles. It is expected to be a promising electrode material for application of energy storage.

#### *Acknowledgments*

I would like to acknowledge İstanbul University-Cerrahpaşa and Biyonanotronic Med. Müh. Ltd. Sti. for contribution to this work.

#### *The Declaration of Conflict of Interest/Common Interest*

The author declared no potential conflicts of interest with respect to the research, authorship, and/or publication of this paper.

#### *The Declaration of Ethics Committee Approval*

This paper does not require any ethics committee permission or special permission

#### *The Declaration of Research and Publication Ethics*

This paper has been prepared within the scope of international research and publication ethics. In addition, I declare that this study has not been evaluated in any academic publication environment other than Sakarya University Journal of Science.

## REFERENCES

- [1] X. Liu et al., "Flexible all-fiber electrospun supercapacitor," *Journal of Power Sources*, vol. 384, pp. 264–269, 2018.
- [2] H. Wang et al., "High Performance Supercapacitor Electrode Materials from Electrospun Carbon Nanofibers in Situ Activated by High Decomposition Temperature Polymer," *American Chemical Society Applied Energy Materials*, vol. 1, no. 2, pp. 431–439, 2018.
- [3] E. Lee, T. Lee, and B.-S. Kim, "Electrospun nanofiber of hybrid manganese oxides for supercapacitor: Relevance to mixed inorganic interfaces," *Journal of Power Sources*, vol. 255, pp. 335–340, 2014.
- [4] F. N. Tuzluca, Y. O. Yesilbag, and M. Ertugrul, "Synthesis of ultra-long boron nanowires as supercapacitor electrode material," *Applied Surface Science*, vol. 493, pp. 787–794, 2019.
- [5] Z. Çıplak, N. Yıldız, "The effect of Ag loading on supercapacitor performance of graphene based nanocomposites" *Fullerenes, Nanotubes Carbon Nanostructures* vol. 27, no. 1, pp. 65-76, 2019.
- [6] J. Liang et al., "Recent advances in electrospun nanofibers for supercapacitors," *Journal of Materials Chemistry A*, vol. 8, pp. 16747-16789 2020.
- [7] Y. Li, H. Xie, J. Li, Y. Bando, Y. Yamauchi, and J. Henzie, "High performance nanoporous carbon microsupercapacitors generated by a solvent-free MOF-CVD method," *Carbon N. Y.*, vol. 152, pp. 688–696, 2019.
- [8] C. Tran, V. Kalra, "Fabrication of porous carbon nanofibers with adjustable pore sizes as electrodes for supercapacitors" *Journal of Power Sources*, vol. 235, pp. 289-296, 2013.
- [9] K. Yang, K. Cho, D. S. Yoon, and S. Kim, "Bendable solid-state supercapacitors with Au nanoparticle-embedded graphene hydrogel films," *Scientific Reports*, vol. 7, pp. 2–9, 2017.
- [10] V. Thirumal, A. Pandurangan, R. Jayavel, and R. Ilangovan, "Synthesis and characterization of boron doped graphene nanosheets for supercapacitor applications," *Synthetic Metals*, vol. 220, pp. 524–532, 2016.
- [11] G. Wang, Y. Ling, F. Qian, X. Yang, X.-X. Liu, and Y. Li, "Enhanced capacitance in partially exfoliated multi-walled carbon nanotubes," *Journal of Power Sources*, vol. 196, no. 11, pp. 5209–5214, 2011.
- [12] U. Kurtan, U. Sahinturk, H. Aydın, D. Dursun, and A. Baykal, "CoFe Nanoparticles in Carbon Nanofibers as an Electrode for Ultra-Stable Supercapacitor," *Journal Inorganic and Organometallic Polymeric Materials*, vol. 30, pp. 3608-3616, 2020.
- [13] J. Lu et al., "Super flexible electrospun carbon/nickel nanofibrous film electrode for supercapacitors," *Journal of Alloys and Compounds*, vol. 774, pp. 593–600, 2019.
- [14] U. Kurtan, H. Aydın, B. Büyük, U. Şahintürk, MA Almessiere, A Baykal, "Freestanding electrospun carbon nanofibers uniformly decorated with bimetallic alloy nanoparticles as supercapacitor electrode," *Journal of Energy Storage*, vol. 32, p. 101671, 2020.
- [15] S. H. Kim and B. H. Kim, "Influence of boron content on the structure and capacitive properties of electrospun polyacrylonitrile/pitch-based carbon nanofiber composites," *Synthetic Metals*, vol. 242, pp. 1–7, 2018.
- [16] B. S. Mao, Z. Wen, Z. Bo, J. Chang, X. Huang, and J. Chen, "Hierarchical nanohybrids with porous CNT-networks decorated crumpled graphene balls for

- supercapacitors,” *ACS Applied Materials and Interfaces*, vol. 6, no. 12, pp. 9881–9889, 2014.
- [17] L. Qie, W.Chen, H.Xu, X.Xiong, Y.Jiang, F.Zou, X.Hu, Y.Xin, Z.Zhang and Y. Huang, “Synthesis of functionalized 3D hierarchical porous carbon for high-performance supercapacitors,” *Energy and Environmental Science*, vol. 6, no. 8, pp. 2497–2504, 2013.
- [18] H.Wang, W.Wang, H. Wang, X. Jin, H.Niu, H.Wang, H.Zhou and T.Lin, “High performance supercapacitor electrode materials from electrospun carbon nanofibers in situ activated by high decomposition temperature polymer,” *ACS Applied Energy and Materials*, vol. 1, no. 2, pp. 431–439, 2018.
- [19] J. Deng, C. He, Y. Peng, J.Wang, X. Long, P.Li, A.Chan, “Magnetic and conductive Fe<sub>3</sub>O<sub>4</sub>–polyaniline nanoparticles with core–shell structure,” *Synthetic Metals*, vol. 139, no. 2, pp. 295–301, 2003.
- [20] T. Lavanya and S. Ramaprabhu, “Copper nanoparticles incorporated porous carbon nanofibers as a freestanding binder-free electrode for symmetric supercapacitor with enhanced electrochemical performance,” *Materials Research Express*, vol. 6, no. 10, p. 105005, 2019.
- [21] B. H. Kim and K. S. Yang, “Enhanced electrical capacitance of porous carbon nanofibers derived from polyacrylonitrile and boron trioxide,” *Electrochimica Acta*, vol. 88, pp. 597–603, 2013.
- [22] İ. Yılmaz, A. Gelir, O. Yargi, U. Sahinturk, and O. K. Ozdemir, “Electrodeposition of zinc and reduced graphene oxide on porous nickel electrodes for high performance supercapacitors,” *Journal of Physical Chemistry and Solids*, vol. 138, p. 109307, 2020.
- [23] J. Ge, G.Fan, Y. Si, J. He, H. Kim, B.Ding, S. Al-Deyab, M. El-Newehy, and J. Yu, “Elastic and hierarchical porous carbon nanofibrous membranes incorporated with NiFe<sub>2</sub>O<sub>4</sub> nanocrystals for highly efficient capacitive energy storage,” *Nanoscale*, vol. 8, no. 4, pp. 2195–2204, 2016.
- [24] Z.-Y. Yu, L.-F. Chen, L.-T. Song, Y.-W. Zhu, H.-X. Ji, and S.-H. Yu, “Free-standing boron and oxygen co-doped carbon nanofiber films for large volumetric capacitance and high rate capability supercapacitors,” *Nano Energy*, vol. 15, pp. 235–243, 2015.
- [25] J. Kim, Y. J. Heo, J. Y. Hong, and S. K. Kim, “Preparation of porous carbon nanofibers with tailored porosity for electrochemical capacitor electrodes,” *Materials*, vol. 13, no. 13, p. 729, 2020.
- [26] Y. Yao, P. Liu, S. Zeng, T. Lan, H. Huang, X. Zeng and J. Zou, “Nitrogen-doped graphitic hierarchically porous carbon nanofibers obtained via bimetallic-coordination organic framework modification and their application in supercapacitors,” *Dalton Transactions*, vol. 47, no. 21, pp. 7316–7326, 2018.
- [27] X. Tian, N. Zhao, Y. Song, K. Wang, D. Xu, X. Li Q. Guo and L. Liu, “Synthesis of nitrogen-doped electrospun carbon nanofibers with superior performance as efficient supercapacitor electrodes in alkaline solution,” *Electrochimica Acta*, vol. 185, pp. 40–51, 2015.
- [28] Q. Xu, X. Yu, Q. Liang, Y. Bai, Z. H. Huang, and F. Kang, “Nitrogen-doped hollow activated carbon nanofibers as high performance supercapacitor electrodes,” *Journal of Electroanalytical and Chemistry*, vol. 739, pp. 84–88, 2015.



SAKARYA ÜNİVERSİTESİ

# FEN BİLİMLERİ ENSTİTÜSÜ DERGİSİ

Sakarya University Journal of Science  
SAUJS

e-ISSN: 2147-835X | Founded: 1997 | Period: Bimonthly | Publisher: Sakarya University |  
<http://www.saujs.sakarya.edu.tr/en/>

Title: On Generalized Recurrent and Generalized Concircularly Recurrent Weyl Manifolds

Authors: İlhan GÜL

Received: 2021-07-01 00:00:00

Accepted: 2021-09-09 00:00:00

Article Type: Research Article

Volume: 25

Issue: 5

Month: October

Year: 2021

Pages: 1189-1196

How to cite

İlhan GÜL; (2021), On Generalized Recurrent and Generalized Concircularly  
Recurrent Weyl Manifolds. Sakarya University Journal of Science, 25(5),  
1189-1196, DOI: <https://doi.org/10.16984/saufenbilder.960842>

Access link

<http://www.saujs.sakarya.edu.tr/tr/pub/issue/65589/960842>

New submission to SAUJS

<http://dergipark.org.tr/en/journal/1115/submission/step/manuscript/new>



$$\nabla_s \tilde{C}_{jkh}^i = A_s \tilde{C}_{jkh}^i + B_s (g_{jk} \delta_h^i - g_{jh} \delta_k^i), \quad (2)$$

where  $A_s$  and  $B_s$  are two 1-forms,  $B_s$  is non-zero. The concircular curvature tensor  $\tilde{C}_{jkh}^i$  is defined by

$$\tilde{C}_{jkh}^i = R_{jkh}^i - \frac{r}{n(n-1)} (g_{jk} \delta_h^i - g_{jh} \delta_k^i), \quad (3)$$

where  $r$  is the scalar curvature of the manifold.

If  $B_s = 0$ , then the manifold reduces to a concircularly recurrent manifold.

A non-flat Riemannian manifold of dimension ( $n > 2$ ) is called a generalized Ricci recurrent manifold if its Ricci tensor  $R_{ij}$  satisfies the condition

$$\nabla_s R_{ij} = A_s R_{ij} + B_s g_{ij}, \quad (4)$$

where  $A_s$  and  $B_s$  are two 1-forms,  $B_s$  is non-zero [8]. If  $B_s = 0$ , then the manifold reduces to a Ricci recurrent manifold.

A non-flat Riemannian manifold ( $n > 2$ ) is called a nearly quasi Einstein manifold if the components of its Ricci tensor  $R_{ij}$  are non-zero and satisfy the condition

$$R_{ij} = a g_{ij} + b E_{ij} \quad (5)$$

where  $a, b$  are scalars of which  $b \neq 0$  and  $E_{ij}$  is a symmetric (0,2) tensor [14].

The above definitions for Weyl manifolds are all given in the next section. In this paper, we investigate generalized recurrent and generalized concircularly recurrent Weyl manifolds.

## 2. PRELIMINARIES

An  $n$ -dimensional differentiable manifold  $M$  having a conformal metric tensor  $g$  and a torsion-free connection  $D$  satisfying the following condition

$$D_k g_{ij} = 2 \omega_k g_{ij}, \quad (6)$$

where  $\omega$  is a 1-form, is called a Weyl manifold and it is denoted by  $M_n(g, \omega)$ .

If  $\omega$  is locally a gradient,  $M_n(g, \omega)$  is conformal to a Riemannian manifold.

Under the conformal change of the metric tensor  $g$ ,

$$\tilde{g}_{ij} = \lambda^2 g_{ij}, \quad \lambda > 0 \text{ is a function,} \quad (7)$$

the 1-form  $\omega$  changes as follows:

$$\tilde{\omega}_k = \omega_k + D_k \ln \lambda. \quad (8)$$

It is not hard to see that  $M_n(\tilde{g}, \tilde{\omega})$  satisfies the equation (6) and therefore, we obtain the same Weyl manifold ([15]-[17]).

Throughout the paper, the Einstein convention of summing over the repeated indices will be adopted.

We have the following basic tensors for a Weyl manifold [18]:

$$v^j W_{jkl}^p = (D_k D_l - D_l D_k) v^p, \quad (9)$$

$$W_{h jkl} = g_{hp} W_{jkl}^p, \quad (10)$$

$$W_{ij} = W_{ijp}^p = g^{hk} W_{hijk}, \quad (11)$$

$$W = g^{ij} W_{ij}. \quad (12)$$

Here,  $W_{ij}$  and  $W$  represent the Ricci and the scalar curvature tensor, respectively.

From (9) it follows that

$$W_{jkl}^p = \partial_k \Gamma_{jl}^p - \partial_l \Gamma_{jk}^p + \Gamma_{hk}^p \Gamma_{jl}^h - \Gamma_{hl}^p \Gamma_{jk}^h, \quad (13)$$

where  $\partial_k = \frac{\partial}{\partial x^k}$  and  $\Gamma_{kl}^i$  are Weyl connection coefficients and defined by

$$\Gamma_{kl}^i = \left\{ \begin{matrix} i \\ kl \end{matrix} \right\} - g^{im} (g_{mk} \omega_l + g_{ml} \omega_k - g_{kl} \omega_m). \quad (14)$$

Here,  $\left\{ \begin{matrix} i \\ kl \end{matrix} \right\}$  are the Levi-Civita connection coefficients.

The following relations hold for a Weyl manifold [18]:

$$W_{ijkl} + W_{ijlk} = 0 \tag{15}$$

$$W_{ijkl} + W_{jikl} = 4g_{ij}D_{[l}\omega_{k]} \tag{16}$$

$$W_{[ij]} = n D_{[i}\omega_{j]}. \tag{17}$$

Here, brackets indicate the antisymmetric parts of the corresponding tensors.

A quantity  $A$  is called a satellite of  $g$  with weight  $p$  if it admits a transformation of the form

$$\tilde{A} = \lambda^p A, \tag{18}$$

under the change (7) of the metric tensor  $g$  [15].

The prolonged covariant derivative of a satellite  $A$  of  $g$  with weight  $p$  is defined by [15],

$$\dot{D}_k A = D_k A - p\omega_k A. \tag{19}$$

From (6) and (19) it follows that  $\dot{D}_k g_{ij} = 0$ .

We also note that the prolonged covariant differentiation preserves the weights of the satellites of  $g$ .

If the scalar curvature of a Weyl manifold is prolonged covariantly constant i.e.  $\dot{D}_i W = 0$ , and since the weight of  $W$  is  $-2$ , we get

$$\dot{D}_i W = D_i W + 2\omega_i W = 0. \tag{20}$$

Hence, we find

$$\omega_i = -\frac{D_i W}{2W}, \tag{21}$$

which means that  $\omega_i$  is locally a gradient. Therefore, the Weyl manifold is conformal to a Riemannian manifold.

**Definition 1** A Weyl manifold is said to be generalized concircularly recurrent if

$$\dot{D}_s Z_{jkh}^i = A_s Z_{jkh}^i + B_s (g_{jk}\delta_h^i - g_{jh}\delta_k^i), \tag{22}$$

where  $A_s$  and  $B_s$  are 1-forms of weight  $0$  and  $-2$ , respectively [13].

Here,  $Z_{jkh}^i$  is the concircular curvature tensor of a Weyl manifold which is given by [19]:

$$Z_{jkh}^i = W_{jkh}^i - \frac{W}{n(n-1)} (g_{jk}\delta_h^i - g_{jh}\delta_k^i). \tag{23}$$

If  $B_s = 0$  in (22), then the manifold is concircularly recurrent.

Using (23) in (22), we have the following equation:

$$\dot{D}_s W_{jkh}^i = A_s W_{jkh}^i + (g_{jk}\delta_h^i - g_{jh}\delta_k^i) \left( B_s - \frac{A_s W}{n(n-1)} + \frac{\dot{D}_s W}{n(n-1)} \right). \tag{24}$$

**Definition 2** A Weyl manifold is said to be generalized Ricci recurrent if

$$\dot{D}_s W_{ij} = A_s W_{ij} + B_s g_{ij}, \tag{25}$$

where  $A_s$  and  $B_s$  are 1-forms of weight  $0$  and  $-2$ , respectively [12]. If  $B_s = 0$  in (25), the manifold reduces to a Ricci recurrent manifold.

**Definition 3** A Weyl manifold is said to be generalized recurrent if

$$\dot{D}_s W_{jkh}^i = A_s W_{jkh}^i + B_s (g_{jk}\delta_h^i - g_{jh}\delta_k^i), \tag{26}$$

where  $A_s$  and  $B_s$  are 1-forms of weight  $0$  and  $-2$ , respectively [12]. In particular, if  $B_s = 0$  the manifold is recurrent.

**Definition 4** A Weyl manifold  $M_n(g, \omega)$  is said to be a nearly quasi-Einstein Weyl manifold if  $W_{(ij)}$ , the symmetric part of  $W_{ij}$ , satisfies the condition

$$W_{(ij)} = \alpha g_{ij} + \beta E_{ij}, \tag{27}$$

where  $\alpha$  is a function of weight  $-2$ , and the sum of the weight of the function  $\beta$  and the symmetric tensor  $E_{ij}$  is  $0$ .

**Example 1** Consider a 3-dimensional Weyl manifold  $M_3$  with a metric by,

$$ds^2 = g_{ij} dx^i dx^j = e^{x^1} [(dx^1)^2 + (dx^2)^2] + (dx^3)^2 \text{ and a 1-form } \omega = e^{x^1} dx^2 + dx^3. \text{ The nonzero Weyl connection coefficients are}$$

$$\begin{aligned} \Gamma_{11}^1 &= \frac{1}{2}, & \Gamma_{12}^1 &= \Gamma_{21}^1 = -e^{x^1}, \\ \Gamma_{13}^1 &= \Gamma_{31}^1 = -1, & \Gamma_{22}^1 &= -\frac{1}{2} \\ \Gamma_{11}^2 &= e^{x^1}, & \Gamma_{12}^2 &= \Gamma_{21}^2 = \frac{1}{2}, \\ \Gamma_{22}^2 &= -e^{x^1}, & \Gamma_{23}^2 &= \Gamma_{32}^2 = -1, \\ \Gamma_{33}^2 &= 1, & \Gamma_{11}^3 &= \Gamma_{22}^3 = e^{x^1}, \\ \Gamma_{23}^3 &= \Gamma_{32}^3 = -e^{x^1}, & \Gamma_{33}^3 &= -1. \end{aligned}$$

It is easy to see that  $M_3(g, \omega)$  is a Weyl manifold.

We can find the nonzero components of the Ricci tensor as follows:

$$\begin{aligned} W_{11} &= e^{x^1}(1 + e^{x^1}), W_{12} = -W_{21} = \frac{3}{2}e^{x^1}, \\ W_{22} &= e^{x^1}, W_{23} = W_{32} = -e^{x^1}, W_{33} = e^{x^1}. \end{aligned}$$

Moreover, we have

$$\begin{aligned} W_{(11)} &= e^{x^1}(1 + e^{x^1}), & W_{(22)} &= e^{x^1}, \\ W_{(23)} &= -e^{x^1}, W_{(33)} &= e^{x^1}, \\ W &= 2(1 + e^{x^1}). \end{aligned}$$

If  $\alpha = 1 + e^{x^1}$ ,  $\beta = -(1 + e^{x^1})$  and the components of the symmetric (0,2) tensor  $E_{ij}$  are

$$\begin{aligned} E_{11} &= E_{12} = E_{13} = E_{21} = E_{31} = 0, \\ E_{22} &= \frac{e^{2x^1}}{1 + e^{x^1}}, E_{33} = \frac{1}{1 + e^{x^1}}, \\ E_{23} &= E_{32} = \frac{e^{x^1}}{1 + e^{x^1}}, \end{aligned}$$

then, (27) holds.

Thus,  $M_3(g, \omega)$  is a nearly quasi-Einstein Weyl manifold.

### 3. GENERALIZED RECURRENT AND GENERALIZED CONCIRCULARLY RECURRENT WEYL MANIFOLDS

A generalized recurrent Weyl manifold is concircularly recurrent [13]. Conversely, assume that  $M_n(g, \omega)$  is concircularly recurrent i.e.

$$\dot{D}_s Z_{jkh}^i = A_s Z_{jkh}^i. \tag{28}$$

Then, using (23) in (28), we get

$$\begin{aligned} \dot{D}_s \left( W_{jkh}^i - \frac{W}{n(n-1)} (g_{jk} \delta_h^i - g_{jh} \delta_k^i) \right) &= \\ A_s \left( W_{jkh}^i - \frac{W}{n(n-1)} (g_{jk} \delta_h^i - g_{jh} \delta_k^i) \right). \end{aligned} \tag{29}$$

Now, the above equation can be written

$$\dot{D}_s W_{jkh}^i = A_s W_{jkh}^i + B_s (g_{jk} \delta_h^i - g_{jh} \delta_k^i), \tag{30}$$

where  $B_s = \frac{\dot{D}_s W - A_s W}{n(n-1)}$ . Therefore, we can state the following theorem:

**Theorem 1** A necessary and sufficient condition for  $M_n(g, \omega)$  to be generalized recurrent is that the  $M_n(g, \omega)$  is concircularly recurrent.

**Theorem 2** A generalized concircularly recurrent Weyl manifold is generalized recurrent.

*Proof.* Assume that  $M_n(g, \omega)$  is generalized concircularly recurrent. Then (24) can be written

$$\dot{D}_s W_{jkh}^i = A_s W_{jkh}^i + C_s (g_{jk} \delta_h^i - g_{jh} \delta_k^i), \tag{31}$$

where  $C_s = B_s - \frac{\dot{D}_s W - A_s W}{n(n-1)}$  from which we conclude that  $M_n(g, \omega)$  is generalized recurrent.

**Theorem 3** If a generalized recurrent Weyl manifold admits a special concircular vector field of weight -2, then the manifold is a nearly quasi-Einstein Weyl manifold.

*Proof.* A vector field  $\rho$  of weight -2 defined by  $A_j = \rho^i g_{ij}$  is said to be special concircular vector field if

$$\dot{D}_i A_j = \alpha g_{ij}, \tag{32}$$

where  $\alpha$  is a function of weight -2. It is easy to see that the weight of the 1-form  $A_j$  is 0.

Assume that a generalized recurrent Weyl manifold admits a special concircular vector field as defined in (32). Then applying the Ricci identity to (32) gives

$$\begin{aligned} A_s W_{kij}^s &= \dot{D}_i \dot{D}_j A_k - \dot{D}_j \dot{D}_i A_k \\ &= \dot{D}_i(\alpha g_{jk}) - \dot{D}_j(\alpha g_{ik}) \\ &= g_{jk} \dot{D}_i \alpha - g_{ik} \dot{D}_j \alpha. \end{aligned} \tag{33}$$

Transvecting (33) with  $g^{jk}$ , we get

$$A_s W_{kij}^s g^{jk} = (n-1) \dot{D}_i \alpha. \tag{34}$$

Now, taking the covariant derivative of (34), we have

$$\begin{aligned} (n-1) \dot{D}_r \dot{D}_i \alpha &= \dot{D}_r (A_s W_{kij}^s g^{jk}) = \\ A_s g^{jk} \dot{D}_r W_{kij}^s + W_{kij}^s g^{jk} \dot{D}_r A_s. \end{aligned} \tag{35}$$

If we use (26) and (32) in the above equation, we obtain

$$\begin{aligned} (n-1) \dot{D}_r \dot{D}_i \alpha &= A_s g^{jk} (A_r W_{kij}^s + B_r (g_{ik} \delta_j^s - g_{kj} \delta_i^s)) \\ &+ W_{kij}^s g^{jk} (\alpha g_{rs}) \\ &= A_r A_s W_{kij}^s g^{jk} + A_s B_r g^{jk} g_{ik} \delta_j^s \\ &- A_s B_r g^{jk} g_{kj} \delta_i^s + \alpha g_{rs} W_{kij}^s g^{jk} \\ &= A_r (n-1) \dot{D}_i \alpha + (1-n) A_i B_r \\ &+ \alpha g^{jk} g_{rs} W_{kij}^s, \end{aligned} \tag{36}$$

and hence we get

$$(n-1) (\dot{D}_r \dot{D}_i \alpha - A_r \dot{D}_i \alpha + A_i B_r) = \alpha g^{jk} W_{rkij}. \tag{37}$$

Now, transvecting (16) with  $g^{jk}$  gives

$$\begin{aligned} W_{rkij} g^{jk} &= -W_{krij} g^{jk} + 4g_{kr} D_{j[r} \omega_{i]} g^{jk} = \\ &-W_{ri} + 4D_{[r} \omega_{i]} \end{aligned} \tag{38}$$

Also, we have

$$A_r \dot{D}_i \alpha = \dot{D}_i (\alpha A_r) - \alpha \dot{D}_i A_r = \dot{D}_i (\alpha A_r) - \alpha^2 g_{ir}. \tag{39}$$

Using (38) and (39) in (37), we obtain

$$\begin{aligned} (n-1) (\dot{D}_r \dot{D}_i \alpha - \dot{D}_i (\alpha A_r) + \alpha^2 g_{ir} + A_i B_r) \\ = \alpha (-W_{ri} + 4D_{[r} \omega_{i]}), \end{aligned} \tag{40}$$

from which we get

$$\begin{aligned} W_{ri} &= (1-n) \alpha g_{ir} \\ &+ \left( \frac{1-n}{\alpha} \right) (\dot{D}_r \dot{D}_i \alpha - \dot{D}_i (\alpha A_r) \\ &+ A_i B_r) + 4D_{[r} \omega_{i]}. \end{aligned} \tag{41}$$

If we define a (0,2) tensor  $E_{ri}$  such that  $E_{ri} = \dot{D}_r \dot{D}_i \alpha - \dot{D}_i (\alpha A_r) + A_i B_r$ , then (41) can be written as follows:

$$W_{ri} = (1-n) \alpha g_{ir} + \left( \frac{1-n}{\alpha} \right) E_{ri} + 4D_{[r} \omega_{i]}.$$

Taking the symmetric part of the above equation, we find that

$$W_{(ri)} = \varphi g_{ri} + \phi E_{(ri)}, \tag{42}$$

where  $\varphi = (1-n)\alpha$ ,  $\phi = \frac{1-n}{\alpha}$  are functions of weight -2 and 2, respectively and  $E_{(ri)}$  is the symmetric part of  $E_{ri}$  with weight -2. Hence, the manifold is a nearly quasi-Einstein.

**Lemma 1** Scalar curvature tensor of a generalized concircularly recurrent Weyl manifold is prolonged covariantly constant if and only if  $A_s W = \frac{n}{2} (A^j W_{js} + A_i g^{jk} W_{jks}^i) - \frac{n(n-1)(n-2)}{2} B_s$ .

*Proof.* Suppose that the Weyl manifold is generalized concircularly recurrent. Permuting (24) cyclically with respect to  $s, k, h$ , we obtain two more equations such that

$$\begin{aligned} \dot{D}_k W_{jhs}^i &= A_k W_{jhs}^i + (g_{jh} \delta_s^i - g_{js} \delta_h^i) (B_k - \\ &\frac{A_k W}{n(n-1)} + \frac{\dot{D}_k W}{n(n-1)}), \end{aligned} \tag{43}$$

$$\begin{aligned} \dot{D}_h W_{jsk}^i &= A_h W_{jsk}^i + (g_{js} \delta_k^i - g_{jk} \delta_s^i) (B_h - \\ &\frac{A_h W}{n(n-1)} + \frac{\dot{D}_h W}{n(n-1)}), \end{aligned} \tag{44}$$

Now taking the sum of (24), (43), (44) and then applying second Bianchi Identity, we have

$$\begin{aligned}
 0 &= A_s W_{jkh}^i + A_k W_{jhs}^i + A_h W_{jks}^i \\
 &+ (g_{jk} \delta_h^i - g_{jh} \delta_k^i) \left( B_s - \frac{A_s W}{n(n-1)} + \frac{\dot{D}_s W}{n(n-1)} \right) \\
 &+ (g_{jh} \delta_s^i - g_{js} \delta_h^i) \left( B_k - \frac{A_k W}{n(n-1)} + \frac{\dot{D}_k W}{n(n-1)} \right) \\
 &+ (g_{js} \delta_k^i - g_{jk} \delta_s^i) \left( B_h - \frac{A_h W}{n(n-1)} + \frac{\dot{D}_h W}{n(n-1)} \right). \quad (45)
 \end{aligned}$$

Contracting the above equation with respect to  $i$  and  $h$ , we get

$$\begin{aligned}
 0 &= A_s W_{jk} - A_k W_{js} + A_i W_{jks}^i \\
 &+ (n-2) g_{jk} \left( B_s - \frac{A_s W}{n(n-1)} + \frac{\dot{D}_s W}{n(n-1)} \right) \\
 &+ (2-n) g_{js} \left( B_k - \frac{A_k W}{n(n-1)} + \frac{\dot{D}_k W}{n(n-1)} \right) \quad (46)
 \end{aligned}$$

Transvecting (46) with  $g^{jk}$  and using  $W_{jks}^i = -W_{jks}^i$  we find that

$$0 = A_s W - A^j W_{js} - g^{jk} A_i W_{jks}^i + (n-1)(n-2) \left( B_s - \frac{A_s W}{n(n-1)} + \frac{\dot{D}_s W}{n(n-1)} \right). \quad (47)$$

After rearranging the terms, we obtain the following equation

$$A_s W = \frac{n}{2} (A^j W_{js} + A_i g^{jk} W_{jks}^i) - \frac{n(n-1)(n-2)}{2} B_s - \left( \frac{n-2}{2} \right) \dot{D}_s W. \quad (48)$$

By hypothesis to be prolonged covariantly constant i.e.  $\dot{D}_s W = 0$ , we conclude the proof.

**Theorem 4** If the scalar curvature of a generalized concircularly recurrent Weyl manifold is prolonged covariantly constant, then the manifold reduces to a generalized Ricci recurrent manifold.

*Proof.* Contracting (24) with respect to  $i$  and  $h$ , we find that

$$\dot{D}_s W_{jk} = A_s W_{jk} + (n-1) g_{jk} \left( B_s - \frac{A_s W}{n(n-1)} + \frac{\dot{D}_s W}{n(n-1)} \right). \quad (49)$$

Using (48) and  $\dot{D}_s W = 0$  in the above equation, we get

$$\dot{D}_s W_{jk} = A_s W_{jk} + g_{jk} \left( \frac{n(n-1)}{2} B_s - \frac{1}{2} (A^j W_{js} + g^{jk} A_i W_{jks}^i) \right). \quad (50)$$

Hence the above equation can be written

$$\dot{D}_s W_{jk} = A_s W_{jk} + C_s g_{jk},$$

where  $C_s = \frac{n(n-1)}{2} B_s - \frac{1}{2} (A^j W_{js} + g^{jk} A_i W_{jks}^i)$  from which we conclude that the manifold is Ricci recurrent.

Here, we also note that the manifold under consideration is conformal to Riemannian manifold, since  $\dot{D}_s W = 0$ .

**Theorem 5** If a generalized concircularly recurrent Weyl manifold admits a special concircular vector field of weight -2, then the manifold is a nearly quasi-Einstein Weyl manifold.

*Proof.* Suppose that a generalized concircularly recurrent Weyl manifold admits a special concircular vector field of weight -2, then we have

$$\dot{D}_i A_j = \alpha g_{ij},$$

where  $\alpha$  is a function of weight -2. As in the proof of Theorem 3, if we apply the Ricci identity to the above equation, and then transvecting the resulted equation with  $g^{jk}$ , we get

$$A_s W_{kij}^s g^{jk} = (n-1) \dot{D}_i \alpha. \quad (51)$$

Now, the covariant derivative of the above equation gives

$$\begin{aligned}
 (n-1) \dot{D}_r \dot{D}_i \alpha &= \dot{D}_r (A_s W_{kij}^s g^{jk}) \\
 &= A_s g^{jk} \dot{D}_r W_{kij}^s + W_{kij}^s g^{jk} \dot{D}_r A_s.
 \end{aligned}$$

If we use (24) in the above equation, we obtain

$$\begin{aligned} (n-1)\dot{D}_r\dot{D}_i\alpha &= A_s g^{jk} \left( A_r W_{kij}^s + (g_{ki}\delta_j^s - g_{kj}\delta_i^s) \left( B_r - \frac{A_r W}{n(n-1)} + \frac{\dot{D}_r W}{n(n-1)} \right) \right) + \\ &W_{kij}^s g^{jk} (\alpha g_{rs}) \\ &= A_r (n-1)\dot{D}_i\alpha + (1-n)A_i \left( B_r - \frac{A_r W}{n(n-1)} + \frac{\dot{D}_r W}{n(n-1)} \right) + \alpha g_{rs} W_{kij}^s g^{jk}, \end{aligned}$$

and hence we get

$$(n-1) \left[ \dot{D}_r\dot{D}_i\alpha - A_r\dot{D}_i\alpha + A_i \left( B_r - \frac{A_r W}{n(n-1)} + \frac{\dot{D}_r W}{n(n-1)} \right) \right] = \alpha g^{jk} W_{rkij}. \tag{52}$$

Using (38) and (39) in (52), we obtain

$$\begin{aligned} (n-1) \left( \dot{D}_r\dot{D}_i\alpha - \dot{D}_i(\alpha A_r) + \alpha^2 g_{ri} + A_i \left( B_r - \frac{A_r W}{n(n-1)} + \frac{\dot{D}_r W}{n(n-1)} \right) \right) &= \alpha (-W_{ri} + \\ &4D_{[r}\omega_{i]}), \end{aligned}$$

from which we get

$$\begin{aligned} W_{ri} &= (1-n)\alpha g_{ir} + \left( \frac{1-n}{\alpha} \right) \left( \dot{D}_r\dot{D}_i\alpha - \dot{D}_i(\alpha A_r) + A_i \left( B_r - \frac{A_r W}{n(n-1)} + \frac{\dot{D}_r W}{n(n-1)} \right) \right) + \\ &4D_{[r}\omega_{i]}. \end{aligned} \tag{53}$$

If we define a (0,2) tensor  $\bar{E}_{ri}$  such that  $\bar{E}_{ri} = \dot{D}_r\dot{D}_i\alpha - \dot{D}_i(\alpha A_r) + A_i \left( B_r - \frac{A_r W}{n(n-1)} + \frac{\dot{D}_r W}{n(n-1)} \right)$ ,

then (53) can be written as follows:

$$W_{ri} = (1-n)\alpha g_{ir} + \left( \frac{1-n}{\alpha} \right) \bar{E}_{ri} + 4D_{[r}\omega_{i]}.$$

Taking the symmetric part of the above equation, we find that

$$W_{(ri)} = \varphi g_{ri} + \phi \bar{E}_{(ri)},$$

where  $\varphi = (1-n)\alpha$ ,  $\phi = \frac{1-n}{\alpha}$  are functions of weight -2 and 2, respectively and  $\bar{E}_{(ri)}$  is the

symmetric part of  $\bar{E}_{ri}$  with weight -2. Hence, the manifold is a nearly quasi-Einstein.

**Acknowledgments**

The author would like to thank the referee for a careful evaluation and pointing out some misprints.

**Funding**

The author has no received any financial support for the research, authorship or publication of this study.

**The Declaration of Conflict of Interest/ Common Interest**

No conflict of interest or common interest has been declared by the authors.

**The Declaration of Ethics Committee Approval**

This study does not require ethics committee permission or any special permission.

**The Declaration of Research and Publication Ethics**

The author of the paper declare that he comply with the scientific, ethical and quotation rules of SAUJS in all processes of the paper and that he does not make any falsification on the data collected. In addition, he declare that Sakarya University Journal of Science and its editorial board have no responsibility for any ethical violations that may be encountered, and that this study has not been evaluated in any academic publication environment other than Sakarya University Journal of Science.

**REFERENCES**

[1] H. Weyl, "Raum-Zeit-Materie", J. Springer, 1918.  
 [2] A. G. Walker, "On Ruse's spaces of recurrent curvature," Proc. Lond. Math., vol. 52, pp. 34-36, 1951.

- [3] U. C. De and N. Guha, "On generalized recurrent manifolds," J. National Academy of Math. India, vol. 9, pp. 85-92, 1991.
- [4] K. Arslan, U. C. De, C. Murathan and A. Yıldız, "On generalized recurrent Riemannian manifolds," Acta Math. Hungar., vol. 123 (1-2), pp. 27-39, 2009.
- [5] T. Miyazawa, "On Riemannian space admitting some recurrent tensor," Tru. Math. J., vol.2, pp. 11-18, 1996.
- [6] U. C. De and A. K. Gazi, "On generalized concircularly recurrent manifolds," Studia Scient. Math. Hungar., vol. 46(2), pp. 287-296, 2009.
- [7] E. M. Patterson, "Some theorems on Ricci-recurrent spaces," J. Lond. Math. Soc., vol. 27, pp. 287-295, 1952.
- [8] U. C. De, N. Guha and D. Kamilya, "On generalized Ricci recurrent manifolds," Tensor (NS), vol. 56, pp. 312-317, 1995.
- [9] A. A. Shaikh, I. Roy and H. Kundu, "On some generalized recurrent manifolds", Bull. Iranian Math. Soc., vol. 43(5), pp. 1209-1225, (2017).
- [10] S. A. Uysal and H. B. Yılmaz, "Some Properties of Generalized Einstein Tensor for a Pseudo-Ricci Symmetric Manifold," Advances in Mathematical Physics, vol. 2020, Article ID 6831650, 4 pages, 2020.
- [11] J. Kim, "On Almost Quasi Ricci Symmetric Manifolds," Commun. Korean Math. Soc. Vol. 35, No. 2, pp. 603-611, 2020.
- [12] E. Canfes, "On Generalized Recurrent Weyl Spaces and Wong's Conjecture," Differential Geometry and Dynamical Systems, vol. 8, pp. 34-42, 2006.
- [13] G. Gürpınar Arsan, G. Çivi Yıldırım, "Generalized concircular recurrent Weyl spaces," Proceedings of the 4th International Colloquium Mathematics in Engineering and Numerical Physics, pp. 6-8, 2006.
- [14] U. C. De and A. K. Gazi, "On nearly quasi Einstein manifolds," Novi Sad. J. Math., vol. 38(2), pp. 115-121, 2008.
- [15] V. Hlavaty, "Theorie d'immersion d'une  $W_m$  dans  $W_m$ ," Ann. Soc. Polon. Math., vol. 21, pp. 196-206, 1949.
- [16] A. Norden, "Affinely Connected Spaces," Nauka, Moscow, 1976.
- [17] G. Zlatanov, "Nets in the n-dimensional Space of Weyl," C. R. Acad. Bulgare Sci., vol. 41, no. 10, pp 29-32, 1988.
- [18] A. Özdeğer, "On sectional curvatures of Weyl manifolds," Proc. Japan Acad, vol. 82A, no. 8, pp. 123-125, 2006.
- [19] A. Özdeğer and Z. Şentürk, "Generalized Circles in Weyl spaces and their conformal mapping," Publ. Math. Debrecen, vol. 60, no. 1-2, pp. 75-87, 2002.



SAKARYA ÜNİVERSİTESİ

# FEN BİLİMLERİ ENSTİTÜSÜ DERGİSİ

Sakarya University Journal of Science  
SAUJS

e-ISSN: 2147-835X | Founded: 1997 | Period: Bimonthly | Publisher: Sakarya University |  
<http://www.saujs.sakarya.edu.tr/en/>

Title: Self-tuning fuzzy logic control of quarter car and bridge interaction model

Authors: Mustafa EROĞLU, Mehmet Akif KOÇ, Recep KOZAN, İsmail ESEN

Received: 2021-01-17 00:00:00

Accepted: 2021-09-20 00:00:00

Article Type: Research Article

Volume: 25

Issue: 5

Month: October

Year: 2021

Pages: 1197-1209

How to cite

Mustafa EROĞLU, Mehmet Akif KOÇ, Recep KOZAN, İsmail ESEN; (2021), Self-tuning fuzzy logic control of quarter car and bridge interaction model. Sakarya University Journal of Science, 25(5), 1197-1209, DOI:

<https://doi.org/10.16984/saufenbilder.863063>

Access link

<http://www.saujs.sakarya.edu.tr/tr/pub/issue/65589/863063>

New submission to SAUJS

<http://dergipark.org.tr/en/journal/1115/submission/step/manuscript/new>

## Self-tuning fuzzy logic control of quarter car and bridge interaction model

Mustafa EROĞLU\*<sup>1</sup>, Mehmet Akif KOÇ<sup>2</sup>, Recep KOZAN<sup>1</sup>, İsmail ESEN<sup>3</sup>

### Abstract

In this study, active suspension control of the interaction between the bridge can be modeled according to the Euler-Bernoulli beam theory, and the quarter car model with three degrees of freedom is studied. The active suspension system consists of a spring, damper, and linear actuator. The active suspension control is designed using classical PID and self-tuning fuzzy PID (STFPID) to reduce the vehicle body's disruptive effects. To determine the performance of the designed controllers, two different road profiles with the bridge oscillations caused by the bridge flexibility were considered as the disruptive effect of the vehicle. When the simulation results were examined in terms of passenger seat displacement and acceleration, the proposed STFPID method significantly increased road holding and ride comfort.

**Keywords:** Active vibration control, Quarter car model, Fuzzy logic, PID

### 1. INTRODUCTION

Suspension systems in vehicles are positioned between the wheels and the vehicle body. The suspension system generally consists of spring, damping, and their connections. The primary purpose of the suspension systems is to absorb the adverse effects that affect the vehicle. In this context, it is studied on the damping of vehicle vibrations in the automotive industry and academic studies. Car models can generally be modeled a quarter, half, and full car models. The suspension system can be divided into three categories: passive, semi-active, and active suspension. In classical passive suspensions,

spring and damping coefficients are constant, and they are successful to a limited extent. Therefore, an active suspension system is preferred for efficient damping in different conditions. Vehicle vibrations adversely affect passenger comfort and road holding. In order to improve these negatively affected parameters, active vibration control is performed with linear actuators added to the passive suspensions system. In the active vibration control, the system's acting force is determined and applied by the controller at the desired performance.

There are several approaches to increase the performance of the active controller. Many researchers have preferred PID control in the last

\* Corresponding author: mustafaeroglu@sakarya.edu.tr

<sup>1</sup> Sakarya University, Mechanical Engineering.

E-Mail: kazan@sakarya.edu.tr

ORCID: <https://orcid.org/0000-0002-1429-7656>, <https://orcid.org/0000-0001-8544-883X>

<sup>2</sup> Sakarya University of Applied Sciences, Faculty of Technology, Department of Mechatronics Engineering.

E-Mail: makoc@subu.edu.tr

ORCID: <https://orcid.org/0000-0001-7461-9795>

<sup>3</sup> Karabuk University, Faculty of Engineering, Mechanical Engineering.

E-Mail: iesen@karabuk.edu.tr

ORCID: <https://orcid.org/0000-0002-7853-1464>

decades, which ease to design and has good performance. Güçlü has used a PID controller to increase driving comfort in full car models that he modeled as linear and nonlinear [1]. In Koç's study, an active suspension system with fuzzy logic controller has been modeled to reduce excessive vibrations in the train component[2]. The PID controller can be used alone or together with other controllers to improve its performance. The most preferred of these is the Fuzzy PID controller, where the PID coefficients are determined by fuzzy logic. Khodadadi and Ghadiri used fuzzy logic self-tuning PID as active controllers in the active suspension half-car model and compared it with PID, fuzzy logic, and  $H_{\infty}$  controllers [3]. Swethamarai and Lakshmi are designed and compared to show the effect on vibration control, thereby increase ride quality for a 3 degree of freedom quarter car model[4]. Min et al. have performed the fuzzy adaptive output feedback control problem for the quarter-vehicle active suspension systems with electromagnetic actuator[5].

In one of their two different studies, Metin and Güçlü improved the passenger and driving comfort of 11 degrees of freedom rail car models with PID and fuzzy logic control separately[6], while in other studies, they compared PID and PID type fuzzy control in 6 degrees of freedom light rail transportation vehicles[7]. In many studies, PID and Fuzzy logic were used together or as separate controllers. In some studies, a hybrid controller that combines PID and fuzzy logic controllers have been used. Demir et al. ensured the ride comfort of the passenger in the half-car model by using a hybrid control approach[8]. Again using a hybrid control approach, Singh and Aggarwal have performed semi-active vibration control of passenger seat vibrations in the quarter car model[9]. Paksoy et al., using full car model with MR damper, performed semi-active control of vehicle vibrations with PID, fuzzy logic, and Self Tuning Fuzzy Logic controller (STFLC), which is a combination of both controllers, and the STFLC has given better results in vibration reduction performance compared to the other two controllers[10].

Another controller that draws attention in active vibration control studies is sliding mode control (SMC), which provides robustness against external and uncertain parameters. Zhang et al. and Bai and Guo showed that the SMC method proposed using a quarter car model achieved a good control performance for the active suspension system[11,12]. Du et al. proposed a terminal SMC approach to deal with the control issue for uncertain, full car active suspension systems [13]. Singh presented the effectiveness of a novel adaptive neuro-fuzzy inference system (ANFIS) based super twisting SMC in vibration suppression in an active quarter car model's suspension system[14].

Another control method is the Linear Quadratic Regulator (LQR). The LQR control theory, which is the optimal control theory, provides a dynamic system's best performance at minimum cost. In this regard, Ben et al. compared passive, semi-active, and active suspension systems in terms of driving safety and road holding using a half car model[15]. They used LQR in the control of the active suspension system and indicated that the proposed method gives better results against random disturbing road input. Agharkakli et al. applied the LQR control technique to the active suspension system using the quarter car model[16]. There has been an improvement in driving comfort and better handling, thanks to active vibration control against different bump inputs.

In addition, static output feedback control [17] and fuzzy logic controller based on particle swarm optimization controllers [18] can be used in the literature to provide vibration control and driving comfort in active suspension systems.

This study's main purpose is to provide active vibration control of the quarter car model with 3 degrees of freedom to increase the ride comfort and road holding by using PID and fuzzy logic. When the literature is examined, in studies conducted to determine vehicle models' dynamic responses, the flexibility of the ground, the vehicle passes through is generally neglected. In this study, the vehicle's passage over a flexible bridge and the disturbance effects on the car from the road while passing are also considered. The

mathematical model of 3 degrees of freedom quarter car model and Euler-Bernoulli bridge beam is obtained. Then, the first two natural frequency and mode shapes of the bridge beam were determined. The critical speeds of the vehicle corresponding to this natural frequency are calculated. The proposed active suspension control effect has been analyzed in detail, disturbing road input and vehicle speed. In this study, with the proposed method, the interaction between the flexible bridge and the car can be analyzed without the need for costly and time-consuming experimental studies.

## 2. MATHEMATICAL MODELING OF QUARTER CAR AND BRIDGE

In this study, the dynamic interaction between the quarter car model with 3 degrees of freedom and the bridge beam will be examined. Since the car's pitch motion and roll motion are not considered in this model, the quarter model is used, and only the vertical displacements are examined. The quarter car model consists of 3 parts: car body, wheel, and

passenger seat. The parameters  $m_p$ ,  $m_v$ , and  $m_w$  represent passenger seat mass, car body mass, and wheel mass, respectively. The spring coefficient between the passenger seat and the car body is defined as  $k_p$ , the damping coefficient is defined as  $c_p$ , the spring coefficient between the car body and the wheel is defined as  $k_v$ , the damping coefficient is defined as  $c_v$ , and the wheel spring coefficient is defined  $k_w$ . The vertical displacement of the passenger seat, the vertical displacement of the vehicle body, and the wheel's vertical displacement are represented as  $r_p$   $r_v$   $r_w$ , respectively. Here, the road disturbance is shown as  $r_d$ . The bridge beam's oscillations are also added together with the road disturbance as an input of the system. The vertical movement of the bridge,  $w_b(x,t)$ , represents the displacement of any  $x$  point of the bridge beam at any  $t$  time, regarding the point where the vehicle enters the bridge.  $V$  represents the speed of the vehicle, moving at a constant speed. In the model, there is an actuator that can apply vertical force between the car body and the wheel to increase passenger comfort and driving safety. The controller determines this actuator force shown as  $u$ .

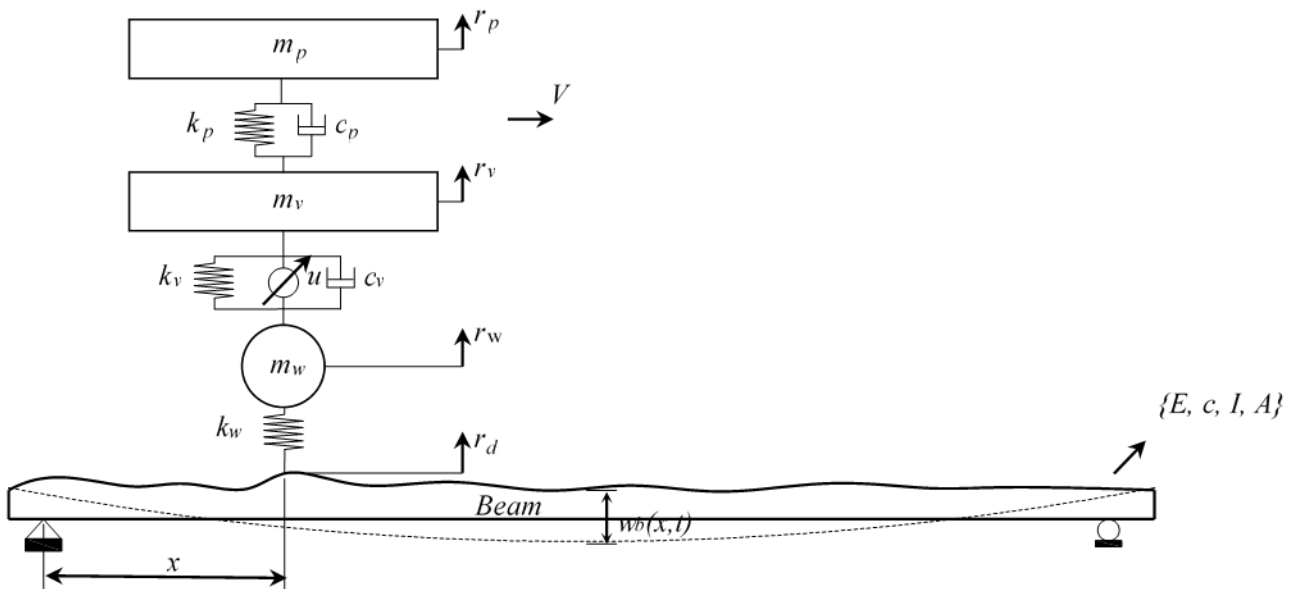


Figure 1 Physical model of the bridge and quarter car model with 3 degrees of freedom.

The natural frequency of vibration modes for the flexible bridge beam shown in Figure 1 is given as in Equation (1) [19].

$$w_j^2 = \frac{j^4 p^4 EI}{mL^4} \text{ (rad / s)} \tag{1}$$

In Equation (1), the parameter  $\omega_j$  is the circular natural frequency of the bridge beam (rad/s), parameter  $j$  represents a number of the mode, the parameter  $E$  represents the elastic modulus (N/m<sup>2</sup>) of the beam,  $I$  represent the moment of inertia (m<sup>4</sup>) of the cross-section of the beam. Using Equation (1), the natural frequency of a simply supported beam in Hz is expressed as follows:

$$f_j = \frac{\omega_j}{2\pi} = \frac{j^2 P}{2L^2} \frac{\alpha EI}{m}^{\frac{1}{2}} \quad (\text{Hz.}), \quad (2)$$

The excitation frequency of the vehicle moving on the bridge beam with  $\omega_j$  natural frequency is expressed as in Equation (3). Using Equation (2), the critical speed of the vehicle is determined as in Equation (4).

$$w = \frac{pv}{L} \quad (3)$$

$$v_{(cr)j} = 2f_j L = \frac{j^2 P}{L} \frac{\alpha EI}{m}^{\frac{1}{2}}, \quad (4)$$

The first two vibration modes of the flexible structure modeled as Euler-Bernoulli beam using the bridge parameters given in Table 1 are  $f_1=0.1852$  Hz,  $f_2=0.7407$  Hz. On the other hand, the vehicle's critical speeds corresponding to these frequencies were determined as  $V_{cr1}=22.22$  m/s,  $V_{cr2}=88.88$  m/s. The following assumptions were accepted in the quarter vehicle and bridge interaction analysis.

- Bridge beam is modeled as a simply-supported beam according to Euler-Bernoulli beam theory.
- Quarter car is modeled with 3 degrees of freedom.
- Only one vehicle passes over the bridge at constant  $v$  velocity.
- The car wheel is always in contact with the bridge beam and does not jump.

With these assumptions, the kinetic and potential energies of the quarter car and bridge interaction seen in Figure 1, as well as the damping function, are given in the equations below.

$$E_k = \frac{1}{2} \left[ \int_0^L \mu \dot{w}_b^2(x,t) dx + m_p \dot{r}_p^2 + m_v \dot{r}_v^2 + m_w \dot{r}_w^2 \right] \quad (5)$$

$$E_p = \frac{1}{2} \left[ \int_0^L EI [w_b''^2(x,t)] dx + k_p (r_p - r_c)^2 + k_v (r_c - r_w)^2 + k_w (r_w - w_b - r_d)^2 \right] \quad (6)$$

$$D = \frac{1}{2} \left[ \int_0^L c \dot{w}_b^2(x,t) dx + c_p (\dot{r}_p - \dot{r}_c)^2 + c_v (\dot{r}_c - \dot{r}_w)^2 \right] \quad (7)$$

In the Equations (5-7),  $\mu$  is the mass of the unit length of the beam, and  $EI$  is the flexural rigidity of the beam. The expression Galerkin for  $w_b(x,t)$ , which is the displacement of any  $x$  point on the beam at time  $t$ , is given below.

Here  $q_i$  represents the generalized coordinate representing the beam element's displacement,  $\varphi_i$  represents the oscillation form obtained with boundary conditions of the bridge beam, and  $\varphi_{ij}$  represents Kronecker delta. The conditions of orthogonality between these oscillation patterns are given in Equation (9). Rayleigh dissipation function for the combined car bridge system is presented in Equation (7). Here  $c$  is the equivalent viscous damping coefficient of the bridge beam.

$$\begin{aligned} \omega_b(x,t) &= \sum_{i=1}^n \varphi_i(x) q_i, \\ \dot{\omega}_b(x,t) &= \sum_{i=1}^n \varphi_i(x) \dot{q}_i, \\ \ddot{\omega}_b(x,t) &= \sum_{i=1}^n \ddot{\varphi}_i(x) q_i, \\ \varphi_i(x) &= \sqrt{\frac{2}{L}} \sin\left(\frac{i\pi x}{L}\right), \quad i = 1, 2, \dots, n. \end{aligned} \quad (8)$$

$$\int_0^L \mu \varphi_i(x) \varphi_j(x) dx = N_i \delta_{ij}, \quad \int_0^L EI \varphi_i''(x) \varphi_j''(x) dx = \Pi_i \delta_{ij} \quad (9)$$

Lagrange expression is the distinction between kinetic energy and potential energies obtained in Equations (5-6). Lagrange expression can be defined as ( $L=E_k-E_p$ ).

$$\frac{d}{dt} \left( \frac{\partial L}{\partial \dot{\eta}_k(t)} \right) - \frac{\partial L}{\partial \eta_k(t)} + \frac{\partial D}{\partial \dot{\eta}_k(t)} = 0, k=1,2,3 \quad (10)$$

$$\frac{d}{dt} \left( \frac{\partial L}{\partial \dot{q}_i(t)} \right) - \frac{\partial L}{\partial q_i(t)} + \frac{\partial D}{\partial \dot{q}_i(t)} = Q_i, i=1,2,3,4 \quad (11)$$

Generalized coordinates are given as in Equations (12-13).

$$\eta(t) = \{r_p, r_v, r_w\}^T, \quad (12)$$

$$q(t) = \{q_1(t), q_2(t), q_3(t), q_4(t)\}^T, \quad (13)$$

$$Q_i = \int_0^L \varphi_i(x) f_{ci}(x,t) dx, \quad i=1,\dots,4 \quad (14)$$

The motion equation of the 3 degrees of freedom quarter car model seen in Figure 1 was obtained using the orthogonality conditions given in Equation (9) and the Galerkin's approach of the beam displacement expressed in Equation (8). Equations of motion for the passenger seat, wheel, and bridge are given below.

$$m_p \ddot{r}_p + c_p (\dot{r}_p - \dot{r}_v) + k_p (r_p - r_v) = 0 \quad (15)$$

$$m_v \ddot{r}_v + c_v (\dot{r}_v - \dot{r}_w) - c_p (\dot{r}_p - \dot{r}_v) + k_v (r_v - r_w) - k_p (r_p - r_v) + u = 0 \quad (16)$$

$$m_w \ddot{r}_w - c_v (\dot{r}_v - \dot{r}_w) - k_v (r_v - r_w) - k_w (r_w - \varphi_i(x,t)q_i - r_d) - u = 0 \quad (17)$$

$$N \ddot{q}_{i(t)} + c \dot{q}_{i(t)} + S q_{i(t)} - k_w \varphi_i(x,t) (r_w - \sum_{i=1}^n \varphi_i(x,t) q_i - r_d) = f_g \varphi_i(x,t) \quad (18)$$

In Equation (18), the second-order equation of the bridge beam is given. Here,  $f_g$  value shows the static forces applied to the bridge beam by the car and is calculated as in Equation (19).

$$f_g = (m_p + m_v + m_w)g \quad (19)$$

Table 1 Quarter car and bridge parameters

Parameters of car	
Passenger seat mass ( $m_p$ )	80 kg
Car body mass ( $m_v$ )	350 kg
Wheel mass ( $m_w$ )	40 kg
Stiffness coefficient of primary suspension ( $k_p$ )	8000 N/m
Stiffness coefficient of secondary suspension ( $k_v$ )	20000 N/m
Tire stiffness ( $k_w$ )	180000 N/m
Damping coefficient of primary suspension ( $c_p$ )	800 Ns/m
Damping coefficient of secondary suspension ( $c_v$ )	1550 Ns/m
Parameters of bridge	
Elasticity module ( $E$ )	2.07 GPa
Bridge length ( $L$ )	60 m
Cross-section inertia moment ( $I$ )	0.17 m <sup>4</sup>
Mass of unit length ( $\mu$ )	2000 kg/m
Equivalent damping coefficient ( $c$ )	1750 Ns/m

The quarter car and bridge model's motion equations examined in this study are obtained by the Lagrange method given in Equations (10-11). A total of 7 second-order differential equations, 3 belonging to the car and 4 equations belonging to the bridge, are created. These equations are reduced to 14 first-order differential equations with the help of state-space forms. Then, to solve these equations, the fourth-order Runge Kutta method is used. The dynamic responses that occurred during the car's passage over the bridge, which can be modeled as the Euler-Bernoulli beam, are analyzed with the commercial analysis program MATLAB. The parameters of the car and bridge beam for analysis are given in Table 1.

In this study, an active suspension system is used to increase passenger comfort, which is adversely affected by road irregularity. Road disturbances that adversely affect the vehicle can be in different geometric shapes. In this study, two different road disturbances are added to the system as an input. These are in the form of hump and sinus.

### 3. DESIGN OF CONTROLLER

Control algorithms designed for active and semi-active suspension systems have been used

extensively in recent years. Active suspension systems are created by adding an actuator to passive suspension systems. The actuator represented by  $u$  in Figure 1 provides the necessary vertical force to the system. The controller force is given in Equations (16-17). In this study, car body displacement is used in system feedback to provide the desired performance. Here, car body displacement is expected to be zero displacements.

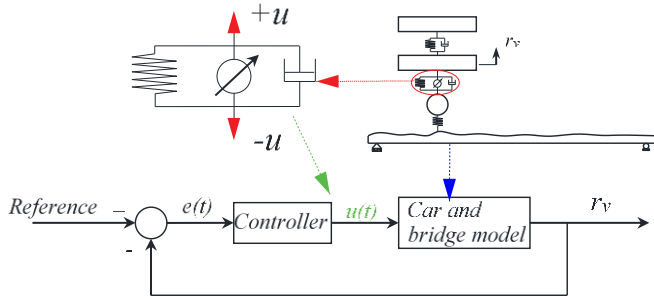


Figure 2 A simple controller design.

In this study, two different controller designs have been made and compared to reduce passenger seat vibrations and displacement in the quarter car model. The first of these is the classic PID controller, which is extensively used in the industry and provides easiness of design. In the classical PID controller,  $k_p$ ,  $k_i$ , and  $k_d$  gain parameter values are constant and does not change. The other controller is the Self-tuning Fuzzy PID (STFPID) controller, which allows the classical PID parameters to be adjusted according to stabilization.

### 3.1. PID Controller

The type of controller with the broadest usage area in the literature is the (Proportional-Integral-Derivative) PID type controller. The PID controller generates a control signal using the error signal of the system. The PID controller is expressed by the equation given in (20).

$$u = k_p e(t) + k_i \int_0^t e(t) dt + k_d \frac{de(t)}{dt} \tag{20}$$

$$e(t) = r_r(t) - r_v(t)$$

In the above equation,  $u$ ,  $e$ ,  $r_r$ , and  $r_v$  represent the control force, error signal, a reference displacement value, and actual car body displacement. The coefficients  $k_p$ ,  $k_i$ , and  $k_d$  represent the proportional gain, integral gain, and derivative gain of the PID controller.

There are several methods for determining PID controller coefficients. The well-known of these methods is the Ziegler-Nichols method. In this study, the parameters  $k_p=5*10^4$ ,  $k_i=1*10^4$ ,  $k_d=0.5*10^4$  are chosen to provide the desired settling time and short rising time.

The proportional gain in the PID control system decreases the rise time of the system, but it may create steady-state error. Integral control negatively affects the transient response while eliminating the steady-state error. Derivative control can predict the future state of the system and correct the transient response. While these controllers can be used alone, they are often used together to increase system stability.

### 3.2. Self-tuning Fuzzy PID controller

In this section, the self-tuning fuzzy PID (STFPID) controller, which allows the PID gains that determine the controller force to be updated within the system requirements' scope, will be examined. The control gains determined in classical PID control sometimes cannot provide the desired performance while controlling the system. Therefore, fuzzy logic is used to provide the appropriate gains while maintaining the system. In this study, the STFPID controller designed to control the vibration caused by the interaction between the quarter vehicle model and the bridge is shown in Figure 4.

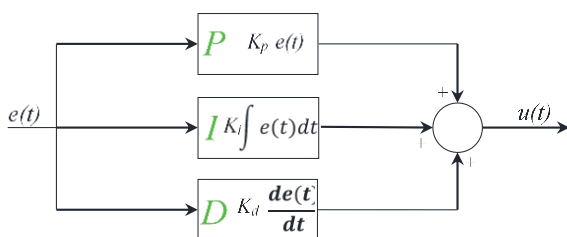


Figure 3 A simple controller design.

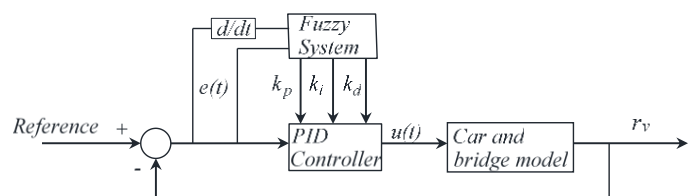


Figure 4 Structure of STFPID control.

The concept of fuzzy logic, which determines how to control a system with the intuitive knowledge of people, was first introduced by Lotfi Zadeh in 1965 [20]. Fuzzy logic consists of 3 different design stages: fuzzification, rule base, and defuzzification. In the fuzzification interface, appropriate linguistic variables are defined for the system inputs examined. The rule base is created by making use of expert experience. In the defuzzification interface, a precise control signal is provided to the active controller using the first two interfaces.

While the fuzzy logic shown in Figure 4 uses the vertical displacement of the vehicle body ( $e = r_r - r_v$ ) and its derivative ( $\dot{e} = \dot{r}_r - \dot{r}_v$ ) as input, it gives the PID parameters as output. Here, reference values ( $r_r, \dot{r}_r$ ) are desired to be zero.

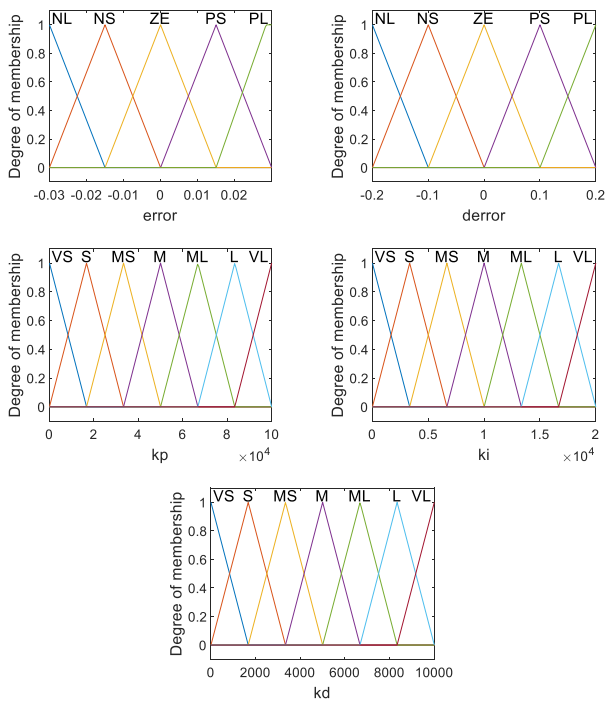


Figure 5 The membership functions of input and output parameters.

The membership functions created for the (STFPID) controller used in this study are shown in Figure 5. As seen in the figure, input values have been represented by five membership functions, namely NL (Negative Large), NS (Negative Small), ZE (Zero), PS (Positive Small), and PL (Positive Large). In comparison, output values have been represented by seven

membership functions, namely VS (Very Small), S (Small), MS (Middle Small), M (Medium), ML (Medium Large), L (Large), and VL (Very Large). All membership functions are selected in triangular geometry.

In the input variables given in Figure 5, the membership function of the error is selected in the intervals [-0.03, 0.03], while the change of the error was selected in the intervals of [-0.2, 0.2]. On the other hand, output variables  $k_p$ ,  $k_i$ , and  $k_d$  are determined in the ranges  $[0, 10^5]$ ,  $[0, 2 * 10^4]$ , and  $[0, 10^4]$ , respectively. The rule base defining the relationship between input and output of these membership functions is given in Table (2-4).

Table 2 Rule base for the  $k_p$

$k_p$		$\frac{de(t)}{dt}$				
		NL	NS	ZE	PS	PL
$e(t)$	NL	VL	VL	VL	VL	VL
	NS	VL	VL	M	VS	VS
	ZE	VL	ML	M	ML	VL
	PS	MS	M	VL	VL	VL
	PL	ML	L	VL	VL	VL

Table 3 Rule base for the  $k_i$

$k_i$		$\frac{de(t)}{dt}$				
		NL	NS	ZE	PS	PL
$e(t)$	NL	VL	VL	VL	VL	VL
	NS	VL	VL	ML	VS	VS
	ZE	VL	ML	M	ML	VL
	PS	MS	M	VL	VL	VL
	PL	ML	L	VL	VL	VL

Table 4 Rule base for the  $k_d$

$k_d$		$\frac{de(t)}{dt}$				
		NL	NS	ZE	PS	PL
$e(t)$	NL	VL	VL	VL	VL	VL
	NS	VL	VL	ML	S	VS
	ZE	VL	L	L	L	VL
	PS	S	M	VL	VL	VL
	PL	VL	VL	VL	VL	VL

#### 4. SIMULATION RESULTS AND DISCUSSION

In this section, the interaction between the quarter car model with 3 degrees of freedom and the bridge that can be modeled according to the simple supported Euler-Bernoulli beam theorem

is examined. For the simulation model, the differential equations given in Equations (15-18) Moreover, the parameters given in Table 1 are taken into account. In the quarter car model, the bridge beam's oscillation is added with two different road inputs as input for the system.

#### 4.1. Bridge displacement input

The bridge is forced to vibrate by the vehicle passing over it at a certain speed. Bridge vibrations also affect the dynamic behavior of the vehicle. In this section, only the bridge beam's oscillations were added to the quarter car as input, and active suspension control was not applied. The parameters of the bridge examined in the simulation are given in Table 1. The modes of the bridge beam, resonance frequencies, and critical speeds of the vehicle are provided in section 1.

In Figure 6, four different velocities,  $V=54$ ,  $V=108$ ,  $V=162$ ,  $V=216$  km/h, are examined. In Figure 6a, when the displacement of the bridge beam midpoint is reviewed, it is seen that the midpoint of the bridge beam makes more displacement at lower speeds of the vehicle. However, as vehicle speed increases, it takes more time for bridge oscillations to damping. In Figures 6b-c, the passenger seat displacement and acceleration values are given, respectively. While the passenger seat displacement values are similar to the bridge midpoint's displacement, the acceleration values and oscillations increase as the speed increases. It is seen that the maximum displacement time of the bridge and the passenger seat rises as the vehicle's speed increases. It is also observed that passenger vertical acceleration values due to bridge flexibility exceed the accepted comfort standards with the increase of vehicle speed. According to the ISO 2631 standard, the low comfort acceleration value that affects the human being is  $0.49 \text{ m/s}^2$ , and the medium comfortable acceleration value is  $0.37 \text{ m/s}^2$  [21].

Figure 7a shows the displacement of the midpoint of the bridge beam, the vertical displacement of the passenger seat, and the passenger seat's vertical acceleration when the vehicle speed changes from 1 m/s to 100 m/s in 1 m/s interval.

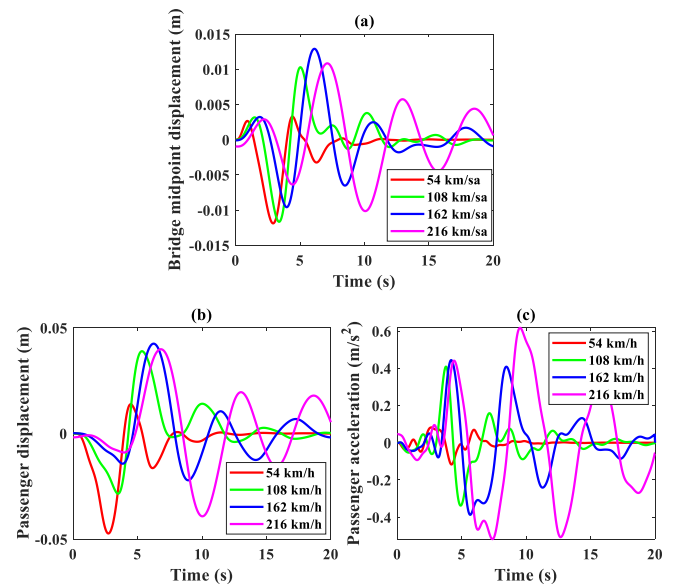


Figure 6 Dynamic responses of quarter car for bridge oscillation (a) Bridge midpoint displacement (b) Passenger displacement (c) Passenger acceleration.

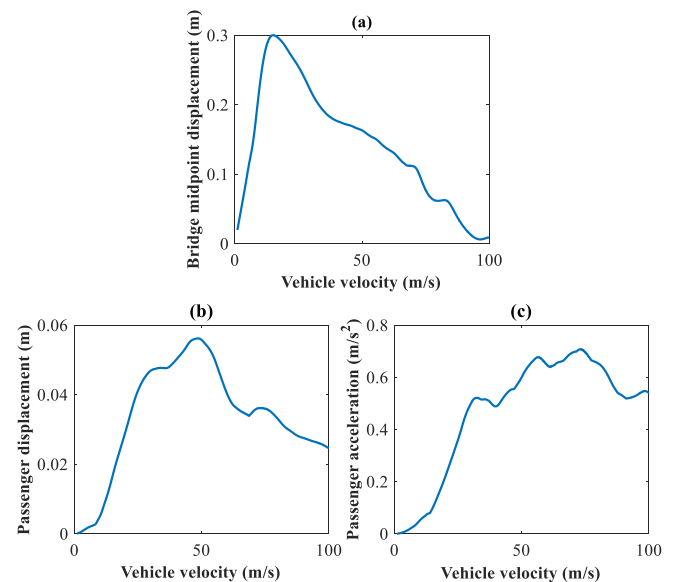


Figure 7 The effect of car velocity upon dynamic response (a) Bridge midpoint displacement (b) Passenger displacement (c) Passenger acceleration.

In Figure 7a, the maximum displacement of the bridge midpoint is determined as 0.3 m when the vehicle speed is 15 m/s. In Figure 7b, if the vehicle speed is approximately 50 m/s, the passenger seat displacement takes its maximum value. At more or less than this speed, the maximum displacement values decrease. In Figure 7c, as the vehicle speed increases, the passenger seat's acceleration values increase, and the acceleration values occurring at speeds above

40 m/s exceed the vibration values affecting humans according to ISO 2631 standard.

### 4.2. Sinusoidal input

As seen in Figure 8, a sinusoidal input with an amplitude of 0.02 m and a frequency of 3.14 rad/s is applied to the quarter car model for the vehicle's passage across the bridge of 60 m length. Sinusoidal input and bridge displacement input is given as disturbing input to the quarter car. The active controller's performance has been investigated using PID and STFPID controllers for passenger seat displacement and acceleration against disturbance input.

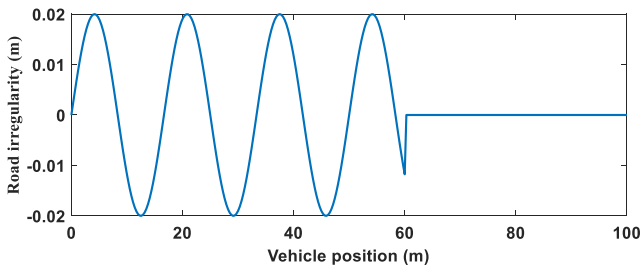


Figure 8. Sinusoidal input.

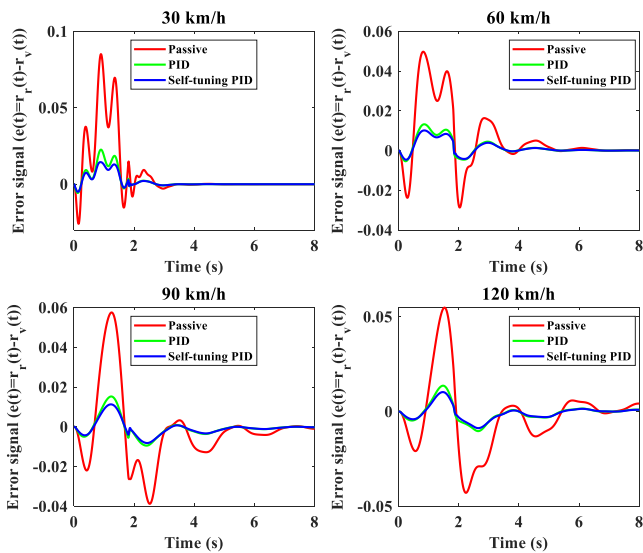


Figure 9 Error signal of car body for a sinusoidal input.

In order to increase passenger comfort in the 3 degree of freedom vehicle model, the vertical displacements of the vehicle body are aimed to be zero. Therefore, the control signal is generated by using the vertical displacements of the vehicle body. In Figure 9, the error signal graph obtained at different vehicle speeds for the sinusoidal input

is given. According to the graph, when PID and STFPID controllers are used, it is seen that the error signal value of the vehicle body is considerably reduced compared to the passive control.

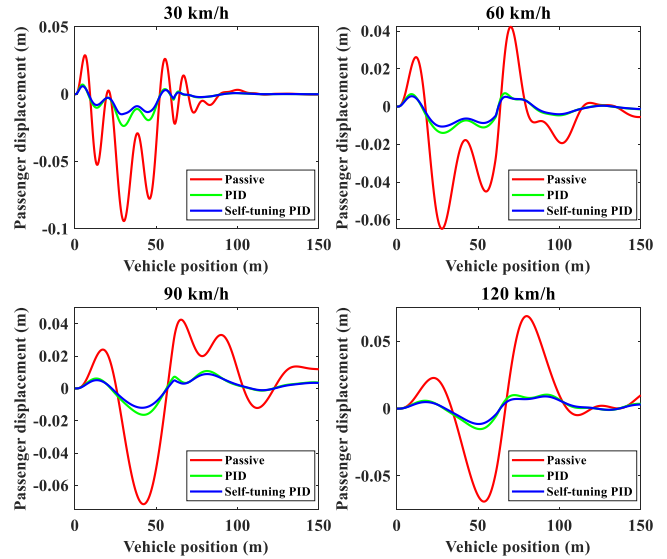


Figure 10 The response of passenger seat displacement for a sinusoidal input.

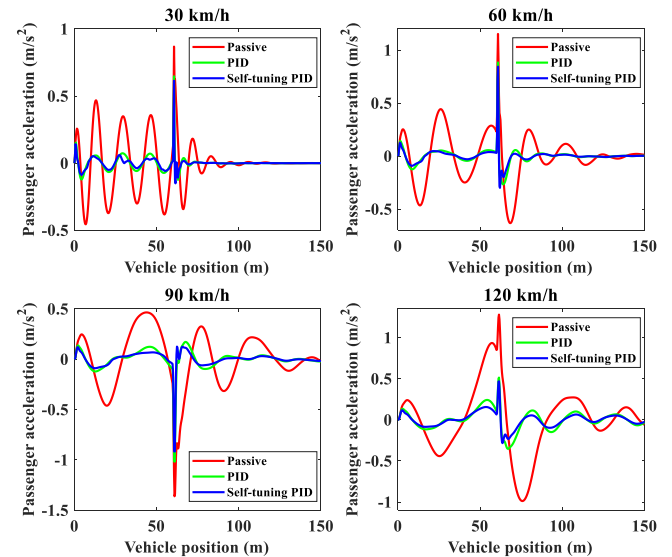


Figure 11 Response of passenger seat acceleration for sinusoidal input.

Figures 10-11 shows the effect of four different vehicle speeds, 30, 60, 90, and 120 km/h, on passenger seat displacement and acceleration. According to the graphics, it is seen that the STFPID controller gives better results than both the PID controller and the uncontrolled system. While the displacement values were relatively high in the simulation studies without a controller,

they decreased thanks to the PID, especially the STFPID controller. Also, in Figure 11, the passenger seat's acceleration values exceed the acceleration values affecting humans according to ISO 2631 standard. Figure 12 shows the control forces generated for STFPID and PID controllers.

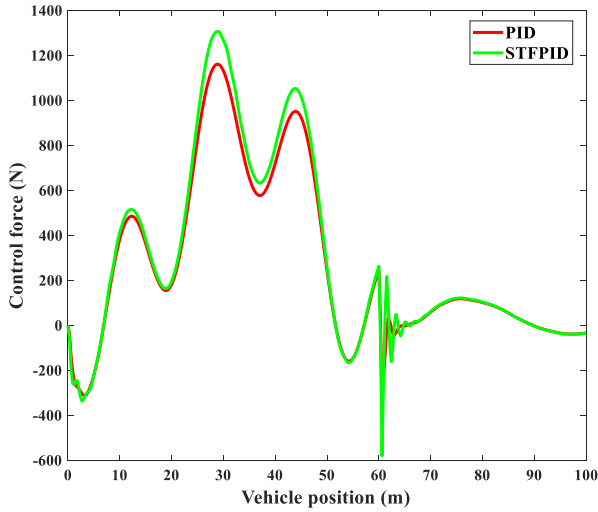


Figure 12 Control force for hump input.

### 4.3. Hump input

When the quarter car model with 3 degrees of freedom in Figure 1 passes over the bridge, it is exposed to two bumps with a height of 10 cm and a width of 5 m. These hump inputs shown in Figure 13 are located 20 m and 50 m away from the bridge's left reference. The equations of these inputs are determined according to the height and width of the hump and the vehicle's speed and are calculated in Equation (21). Here, the expression  $Y$  represents the height of the hump,  $\omega$  represents the angular frequency, and  $r_d$  represents the value of the hump at time  $t$ .  $T$  time is calculated as the time the vehicle passes the hump.

$$r_d = Y \sin(\omega t), \quad 0 \leq t \leq T, \quad T = \frac{L}{V} \quad (21)$$

In this case, the frequency of the sine wave given for the hump is as follows.

$$\omega = \frac{\pi V}{L} \quad (22)$$

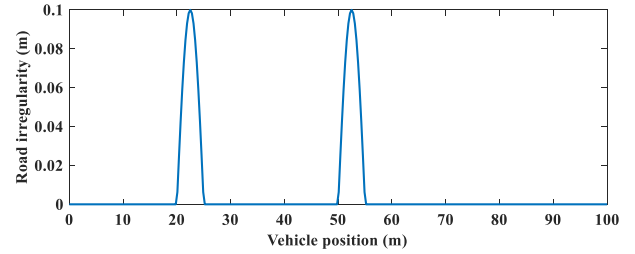


Figure 13 Hump input.

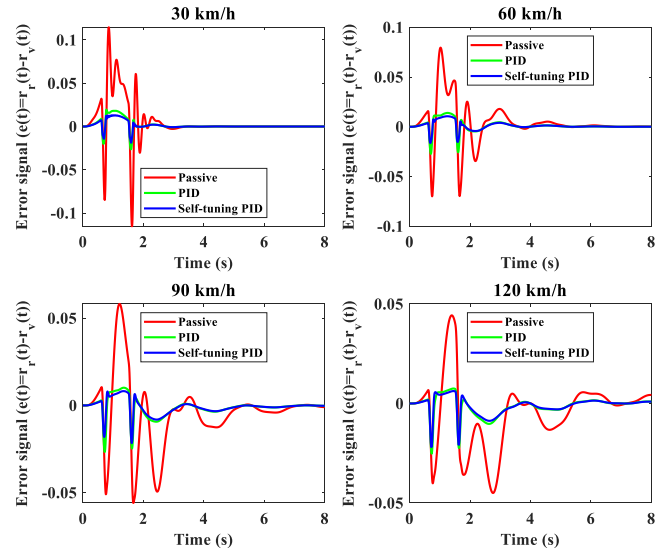


Figure 14 Error signal of car body for hump input.

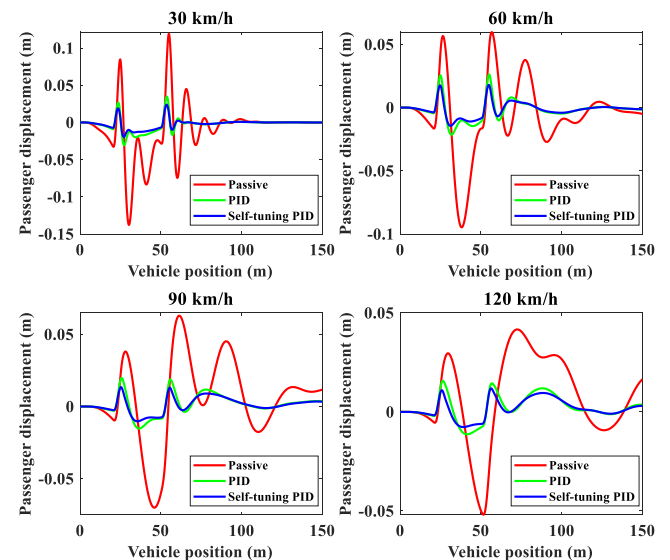


Figure 15 The response of passenger seat displacement for hump input.

In Figure 14, the error signal graph of the vehicle body is given for the hump input. According to the graph, if a controller is used, as in Figure 9, the error signal of the vehicle body is considerably reduced. In Figures 15-16, the controllers' performance proposed in this study for the hump input in passenger seat displacement and

acceleration values is examined. Like the sinusoidal input, four different speeds were evaluated and compared with STFPID and PID controllers. If the vehicle speed is 30 km/h, it is seen that the vertical displacement of the passenger seat is approximately 0.1 m, while it is about 0.05 m at other speeds. Thanks to the active suspension control, these relatively high displacement values have been reduced to very reasonable levels. In the case of increased vehicle speed, the passenger seat's vertical acceleration values also increase considerably. In Figure 17, both controller forces generated corresponding to the input values with hump and bridge displacement are given.

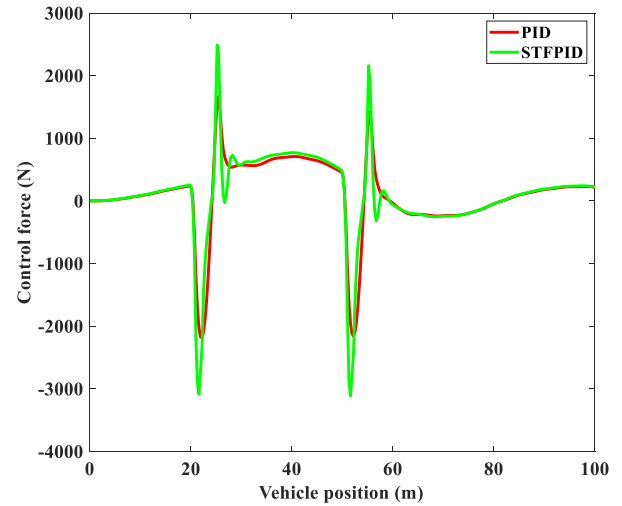


Figure 17 Control force for hump input.

### 5. CONCLUSION

In this study, it is investigated that disturbing road irregularities, which adversely affect the driving safety and passenger comfort parameters of the quarter car model, will be absorbed by the active suspension system. Modeled 3 degrees of the freedom car model were examined with uncontrolled and STFPID and PID type controllers. Uncontrolled and controlled systems are compared with each other using different system inputs. In the simulation results, it was determined that the STFPID controller performs much better than the others.

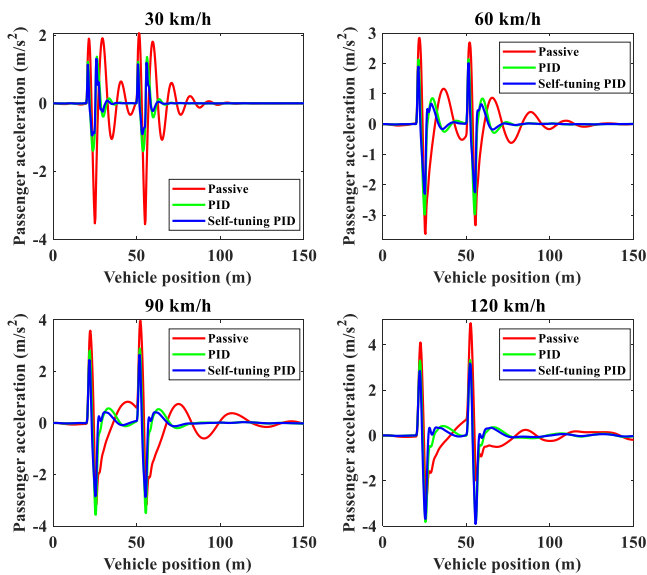


Figure 16 The response of passenger seat acceleration for hump input.

Table 5 RMS results for error signal ( $e(t)=r_r(t)-r_v(t)$ )

	Hump input (m)				Sinusoidal input (m)			
	30 km/h	60 km/h	90 km/h	120 km/h	30 km/h	60 km/h	90 km/h	120 km/h
Passive	0.0227	0.0189	0.0180	0.0163	0.0192	0.0156	0.0176	0.0181
PID	0.0055	0.0050	0.0048	0.0046	0.0052	0.0041	0.0045	0.0044
Self-tuning FPID	0.0039	0.0036	0.0039	0.0040	0.0038	0.0033	0.0036	0.0036
Improvement	27.96%	28.34%	18.72%	12.55%	27.56%	18.77%	18.93%	17.49%

Table 6. RMS results for passenger displacement

	Hump input (m)				Sinusoidal input (m)			
	30 km/h	60 km/h	90 km/h	120 km/h	30 km/h	60 km/h	90 km/h	120 km/h
Passive	0.0256	0.0205	0.0208	0.0167	0.0208	0.0178	0.0207	0.0234
PID	0.0064	0.0056	0.005	0.0047	0.0054	0.0043	0.0049	0.0049
Self-tuning FPID	0.0045	0.0041	0.0038	0.0037	0.0039	0.0035	0.0039	0.004
Improvement	29.3%	27.4%	24.3%	21.7%	28%	19.2%	20%	19.1%

Table 7 RMS results for passenger acceleration

	Hump input (m/s <sup>2</sup> )				Sinusoidal input (m/s <sup>2</sup> )			
	30 km/h	60 km/h	90 km/h	120 km/h	30 km/h	60 km/h	90 km/h	120 km/h
Passive	0.5161	0.5599	0.6503	0.6322	0.1345	0.1638	0.2071	0.3004
PID	0.2288	0.3865	0.5685	0.5327	0.0357	0.0567	0.0733	0.0872
Self-tuning FPID	0.1667	0.2987	0.3858	0.5021	0.0298	0.0493	0.06	0.0631
Improvement	27.2%	22.7%	17.6%	5.7%	16.3%	13.1%	17.2%	27.6%

This study's primary purpose is to reduce the passenger seat's displacement and acceleration values through controllers. In this context, error signal of car body, the passenger seat displacement, and acceleration values are compared under different speeds and disturbance inputs in Table (5-7). Root mean square (RMS) values of the uncontrolled results with both controllers are given in the table for comparison. After comparing the classical PID controller and the STFPID controller, the simulation results show that the STFPID controller has achieved more than 20% improvement over the classic PID controller.

## REFERENCES

- [1] R. Güçlü, "Active control of seat vibrations of a vehicle model using various suspension alternatives," *Turkish J. Eng. Environ. Sci.* 27 (2003) 361–373. <https://doi.org/10.3906/sag-1204-7>.
- [2] M.A. Koç, "Dynamic Response and Fuzzy Control of Half-Car High-Speed Train and Bridge Interaction," *Acad. Perspect. Procedia.* 3 (2020) 519–529. <https://doi.org/10.33793/acperpro.03.01.100>.
- [3] H. Khodadadi, and H. Ghadiri, "Self-tuning PID controller design using fuzzy logic for half car active suspension system," *Int. J. Dyn. Control.* 6 (2018) 224–232. <https://doi.org/10.1007/s40435-016-0291-5>.
- [4] P. Swethamarai, and P. Lakshmi, "Design and implementation of fuzzy-PID controller for an active quarter car driver model to minimize driver body acceleration," *IEEE Int. Syst. Conf.* (2019) 1–6. <https://doi.org/10.1109/SYSCON.2019.8836940>.
- [5] X. Min, Y. Li, and S. Tong, "Adaptive fuzzy output feedback inverse optimal control for vehicle active suspension systems," *Neurocomputing.* 403 (2020) 257–267. <https://doi.org/10.1016/j.neucom.2020.04.096>.
- [6] M. Metin, and R. Guclu, "Active vibration control with comparative algorithms of half rail vehicle model under various track irregularities," *JVC/Journal Vib. Control.* 17 (2011) 1525–1539. <https://doi.org/10.1177/1077546310381099>.
- [7] M. Metin, and R. Güçlü, "Vibrations control of light rail transportation vehicle via PID type fuzzy controller using parameters adaptive method," *Turkish J. Electr. Eng. Comput. Sci.* 19 (2011) 807–816. <https://doi.org/10.3906/elk-1001-394>.
- [8] O. Demir, I. Keskin, and S. Cetin, "Modeling and control of a nonlinear half-vehicle suspension system: A hybrid fuzzy logic approach," *Nonlinear Dyn.* 67 (2012) 2139–2151. <https://doi.org/10.1007/s11071-011-0135-y>.

- [9] D. Singh, and M.L. Aggarwal, "Passenger seat vibration control of a semi-active quarter car system with hybrid Fuzzy–PID approach", *Int. J. Dyn. Control.* 5 (2017) 287–296. <https://doi.org/10.1007/s40435-015-0175-0>.
- [10] M. Paksoy, R. Guclu, and S. Cetin, "Semiactive self-tuning fuzzy logic control of full vehicle model with MR damper," *Adv. Mech. Eng.* 2014 (2014). <https://doi.org/10.1155/2014/816813>.
- [11] Y.Q. Zhang, Y.S. Zhao, J. Yang, and L.P. Chen, "A dynamic sliding-mode controller with fuzzy adaptive tuning for an active suspension system," *Proc. Inst. Mech. Eng. Part D J. Automob. Eng.* 221 (2007) 417–428. <https://doi.org/10.1243/09544070JAUTO379>.
- [12] R. Bai, and D. Guo, "Sliding-mode control of the active suspension system with the dynamics of a hydraulic actuator," *Complexity.* 2018 (2018). <https://doi.org/10.1155/2018/5907208>.
- [13] M. Du, D. Zhao, B. Yang, and L. Wang, "Terminal sliding mode control for full vehicle active suspension systems," *J. Mech. Sci. Technol.* 32 (2018) 2851–2866. <https://doi.org/10.1007/s12206-018-0541-x>.
- [14] D. Singh, "Passenger body vibration control in active quarter car model using ANFIS based super twisting sliding mode controller," *Simul. Model. Pract. Theory.* 89 (2018) 100–118. <https://doi.org/10.1016/j.simpat.2018.09.010>.
- [15] L.Z. Ben, F. Hasbullah, and F.W. Faris, "A comparative ride performance of passive, semi-active and active suspension systems for off-road vehicles using half car model," *Int. J. Heavy Veh. Syst.* 21 (2014) 26–41. <https://doi.org/10.1504/IJHVS.2014.057827>.
- [16] A. Agharkakli, G.S. Sabet, and A. Barouz, "Simulation and Analysis of Passive and Active Suspension System Using Quarter Car Model for Different Road Profile," *Int. J. Eng. Trends Technol.* 3 (2012) 636–644.
- [17] J. Mrazgua, R. Chaibi, E.H. Tissir, and M. Ouahi, "Static output feedback stabilization of T-S fuzzy active suspension systems," *J. Terramechanics.* 97 (2021) 19–27. <https://doi.org/10.1016/j.jterra.2021.05.001>.
- [18] G.I.Y. Mustafa, H.P. Wang, and Y. Tian, "Vibration control of an active vehicle suspension systems using optimized model-free fuzzy logic controller based on time delay estimation," *Adv. Eng. Softw.* 127 (2019) 141–149. <https://doi.org/10.1016/j.advengsoft.2018.04.009>.
- [19] L. Frýba, "Vibration of Solids and Structures under Moving Loads," 3rd ed., Thomas Telford, London, ISBN 0-7277-2741-9, (1999).
- [20] L. A. Zadeh, "Fuzzy sets," *Information and Control* (1965) 338–353. <https://www.sciencedirect.com/science/article/pii/S001999586590241X>.
- [21] C. Mizrak, and I. Esen, "Determining Effects of Wagon Mass and Vehicle Velocity on Vertical Vibrations of a Rail Vehicle Moving with a Constant Acceleration on a Bridge Using Experimental and Numerical Methods," *Shock Vib.* 2015 (2015). <https://doi.org/10.1155/2015/183450>.



SAKARYA ÜNİVERSİTESİ

# FEN BİLİMLERİ ENSTİTÜSÜ DERGİSİ

Sakarya University Journal of Science  
SAUJS

e-ISSN: 2147-835X | Founded: 1997 | Period: Bimonthly | Publisher: Sakarya University |  
<http://www.saujs.sakarya.edu.tr/en/>

Title: Two-Dimensional Vector Boson Oscillator

Authors: Semra GÜRTAŞ DOĞAN

Received: 2021-05-18 00:00:00

Accepted: 2021-09-20 00:00:00

Article Type: Research Article

Volume: 25

Issue: 5

Month: October

Year: 2021

Pages: 1210-1217

How to cite

Semra GÜRTAŞ DOĞAN; (2021), Two-Dimensional Vector Boson Oscillator. Sakarya University Journal of Science, 25(5), 1210-1217, DOI:

<https://doi.org/10.16984/saufenbilder.938739>

Access link

<http://www.saujs.sakarya.edu.tr/tr/pub/issue/65589/938739>

New submission to SAUJS

<http://dergipark.org.tr/en/journal/1115/submission/step/manuscript/new>

## Two-Dimensional Vector Boson Oscillator

Semra GÜRTAŞ DOĞAN<sup>1</sup>

### Abstract

We introduce two-dimensional vector boson oscillator by using the generalized vector boson equation that derived as an excited of Zitterbewegung. We write the relativistic vector boson equation for a relativistic spin-1 particle and introduce the oscillator coupling via non-minimal substitutions. The corresponding equation gives a set of equations. By solving this equation set we obtain the components of the corresponding symmetric spinor and accordingly obtain the energy eigen-values for two-dimensional vector boson oscillator. This energy spectrum shows that the oscillator frequency couples with the spin of vector field in question and accordingly we discuss the results.

**Keywords:** Vector Boson Oscillator, Relativistic Quantum Mechanics, Quantum Oscillator

### 1. INTRODUCTION

It is well known that obtaining exact solutions of relativistic wave equations such as the Klein-Gordon equation (KGE), the Dirac equation, the Duffin-Kemmer-Petiau (DKP) equation and the well-established many-body equations are regarded as very important in the modern physics. Obtaining exact solutions for relativistic quantum oscillators such as Dirac oscillator (DO) [1], Klein-Gordon oscillator (KGO) [2], Duffin-Kemmer-Petiau oscillator (DKPO) [3,4] and relativistic spin-1 oscillator [5,6] can be considered between among them. The DO has been introduced in terms of a new type of interaction in the Dirac equation and corresponding form of this equation is linear in coordinate and momentum [1]. This form of the Dirac equation has provided the usual harmonic oscillator solution including strong spin-orbit coupling term in the non-relativistic limit. The DO name, which was coined by Moshinsky and Szczepaniak [1], originates from this fact. After

the DO oscillator was introduced, the electromagnetic potential associated with the DO interaction has been obtained and the results have shown that this type of interaction describes to the interaction of an anomalous magnetic moment with a linearly growing electric field [7]. Due to this linearly growing characteristic, the DO interaction has been considered to describe the dynamics of quarks [7, 8] and this interaction has been also considered in the context of the two-body systems consisting of fermion-antifermion pairs [9,10]. Furthermore, the DO system has been associated with the quantum optics models such as Jaynes-Cummings [11] (or anti Jaynes-Cummings [12]) model due to the mentioned spin-orbit coupling. In addition to these models, behavior of the DO system has been also investigated by considering the presence of a constant transverse magnetic field [13]. Experimentally, the first microwave realization of the one-dimensional DO has been performed [14] and it has been shown that the results agree well with the theoretical predictions for DO system [14]. Accordingly, the DO system has begun to

\* Corresponding author: semragurtas@yahoo.com

<sup>1</sup> Hakkari University, Vocational School of Health Services.

ORCID: <https://orcid.org/0000-0001-7345-3287>

widely studied by several research groups in many areas of the modern physics since this system has an important potential for several physical applications [7, 10, 15, 16, 17,18].

It is well known that the KGE is used to determine the relativistic dynamics of spinless relativistic particles. The KGO interaction, which was considered by inspiring from the DO, has been introduced as the interaction of a spinless relativistic particle (massive) with a complex linear vector potential [2]. This system has attracted a serious attention and has been investigated in many areas of the modern physics. For example, the KGO system has been studied in the presence of external magnetic field in cosmic string spacetime [19], it has been investigated in the presence of Coulomb type potential [20], this relativistic oscillator has been studied by considering the presence of position-dependent mass term [21] and it has been also used to determine the effects of geometric backgrounds having different physical properties on the corresponding physical systems. The studies based on the dynamics of KGO in the Gürses spacetime [22], in the cosmic string background in the context of Kaluza-Klein theory [23], and in the Som-Raychaudhuri spacetime [24] can be considered among such studies.

On the other hand, the DKP equation is used to describe the relativistic dynamics of both spin-0 and spin-1 particles [25, 26, 27]. Similar to the DO interaction, the DKPO system has been introduced via linear non-minimal substitution. This form of the equation has been used to determine the dynamics of spin-0 and spin-1 particles with a linearly varying non-minimal interaction. Several applications have been performed for this form of the DKP equation. For example, this system has been studied under the influence of an external magnetic field [28,29,30], it has been considered in a non-commutative phase space [31,32]. The DKPO has been studied in the context of the minimal length scenarios [33] and it has been investigated by considering the presence of minimal uncertainty in momentum [34]. In three-dimensions, spin-1 sector of the DKP equation has been derived as excited state of Zitterbewegung by considering the associated spinor is a symmetric spinor of rank-two [35].

This spinor, which does not include the spin-zero sector, is constructed by a direct product of two Dirac spinors [36-38]. The vector boson equation (VBE) corresponds to the spin-1 sector of the DKP equation (see also [39]) in 2+1 dimensions [35, 36, 40, 41] and it has been studied in the several contexts of modern physics [5,38-44]. Also, the relativistic oscillator systems are the most useful tools of the mathematical physics, since they are exactly solvable problems, in general. This fact provides to analyse the effects of spacetime topologies on the dynamics of the corresponding physical systems [6,45].

In this research, our aim is to obtain exact results for the two-dimensional vector boson oscillator (VBO), without considering any external effect, in order to discuss the fundamental properties of the system. To achieve this we have used the generalized VBE. We have written this equation in three dimensions in terms of cartesian coordinates and then we have introduced the two-dimensional VBO through non-minimal substitutions. We have solved the corresponding equation by exploiting the angular symmetry of the polar coordinates and have obtained exact results for this relativistic oscillator.

This paper is organized as follows: in section 2, we have written the VBE in three dimensional flat geometric background and have introduced the oscillator coupling, in section 3, by exploiting the angular symmetry of the polar background, we have obtained a set of coupled equations and accordingly we have acquired an exact energy spectrum for this investigated system. Then, in section 4, we have discussed the fundamental properties of this system, such as spin coupling dependence of the spectra and have discussed the behavior of energy levels with respect to the strength of non-minimal coupling.

## 2. THE VECTOR BOSON EQUATION

In 2 + 1-dimensional flat spacetime background, the VBE can be written in terms of cartesian coordinates as the following [5,35], without considering the existence of any external electromagnetic field,

$$\left\{ \frac{1}{2} (\gamma^\mu \otimes I_2 + I_2 \otimes \gamma^\mu) \partial_\mu + i \frac{m_b c}{\hbar} I_4 \right\} \varphi(\mathbf{x}) = 0, \quad (1)$$

( $\mu = 0,1,2$ ).

In Eq. (1),  $\gamma^\mu$ ,  $I_2$ ,  $I_4$ ,  $m_b$ ,  $c$ ,  $\hbar$ ,  $\varphi$  and  $\mathbf{x}$  are the Dirac matrices,  $2 \times 2$  dimensional unit matrix,  $4 \times 4$  dimensional unit matrix, rest mass of the vector boson, speed of the light in vacuum, the reduced Planck constant, symmetric spinor and spacetime position vector, respectively. Also, in Eq. (1) the symbol  $\otimes$  indicates the direct product. In terms of the cartesian coordinates the 2+1-dimensional spacetime background is given by the following metric (with negative signature) [46],

$$ds^2 = c^2 dt^2 - dx^2 - dy^2. \quad (2)$$

According to signature of Eq. (2) the Dirac matrices can be chosen as the following [47],

$$\gamma^t = \frac{1}{c} \sigma^z, \gamma^x = i \sigma^x, \gamma^y = i \sigma^y, \quad (3)$$

where,  $\sigma^x, \sigma^y, \sigma^z$  are the well-known Pauli spin matrices. Now, we can introduce the two dimensional vector oscillator through the following non-minimal substitutions,

$$\begin{aligned} \delta_x &\rightarrow \partial_x + \frac{m_b \omega}{\hbar} (\sigma^z \otimes \sigma^z) x, \\ \delta_y &\rightarrow \partial_y + \frac{m_b \omega}{\hbar} (\sigma^z \otimes \sigma^z) y, \end{aligned} \quad (4)$$

in which  $\omega$  is the oscillator frequency [5,9]. By assuming the interaction is time-independent we can define the spinor,  $\varphi(\mathbf{x})$ , as  $\varphi(\mathbf{x}) = e^{-i \frac{E}{\hbar} t} \Xi(\vec{\mathbf{x}})$ , in which  $E$  is the total energy of the investigated spin-1 field. Under this assumption, by substituting Eq. (3) and Eq. (4) into the Eq. (1) one can obtain the following matrix equation,

$$\left\{ 2 \begin{pmatrix} \mathcal{E} - \mathcal{M} & -\hat{\Pi}^* & -\hat{\Pi}^* & 0 \\ -\hat{\Pi} & -\mathcal{M} & 0 & -\hat{\Pi}^* \\ -\hat{\Pi} & 0 & -\mathcal{M} & -\hat{\Pi}^* \\ 0 & -\hat{\Pi} & -\hat{\Pi} & -\mathcal{E} - \mathcal{M} \end{pmatrix} + \kappa \begin{pmatrix} 0 & \mathcal{Z}^* & \mathcal{Z}^* & 0 \\ -\mathcal{Z} & 0 & 0 & -\mathcal{Z}^* \\ -\mathcal{Z} & 0 & 0 & -\mathcal{Z}^* \\ 0 & \mathcal{Z} & \mathcal{Z} & 0 \end{pmatrix} \right\} \Xi(\vec{\mathbf{x}}) = 0, \quad (5)$$

where,

$$\begin{aligned} \mathcal{E} &= \frac{E}{\hbar c}, \quad \kappa = \frac{m_b \omega}{\hbar}, \quad \mathcal{M} = \frac{m_b c}{\hbar}, \\ \hat{\Pi} &= \frac{1}{2} (\partial_x + i \partial_y), \quad \hat{\Pi}^* = \frac{1}{2} (\partial_x - i \partial_y), \\ \mathcal{Z} &= x + iy, \quad \mathcal{Z}^* = x - iy. \end{aligned}$$

To exploit the angular symmetry, we transform the background into the polar coordinates through the following relations [31,46],

$$\begin{aligned} \partial_x \pm i \partial_y &= e^{\pm i \phi} \left( \pm \frac{i}{r} \partial_\phi + \partial_r \right), \\ x \pm iy &= r e^{\pm i \phi}, \end{aligned} \quad (6)$$

and in terms of the new coordinates spatial part of the spinor,  $\Xi(\vec{\mathbf{x}})$ , can be defined as follows,

$$\Xi(\vec{\mathbf{x}}) = \begin{pmatrix} \psi_1(r) e^{i(s-1)\phi} \\ \psi_2(r) e^{is\phi} \\ \psi_3(r) e^{is\phi} \\ \psi_4(r) e^{i(s+1)\phi} \end{pmatrix} \quad (7)$$

which includes all possible spin eigenstates ( $s = \pm 1, 0$ ) of the considered vector field.

### 3. ENERGY SPECTRUM OF TWO-DIMENSIONAL VBO

In this section, we obtain an exact energy spectrum of two-dimensional VBO. Here we should notice that  $\psi_2(r) e^{is\phi} = \psi_3(r) e^{is\phi}$  (see Eq. (5) and Eq. (7)). By substituting Eq. (6) and Eq. (7) into the Eq. (5) and then by defining a dimensionless independent variable,  $\eta = \kappa r^2$ , one can obtain the following equations,

$$\begin{aligned} \mathcal{E} \psi_+(\eta) - \mathcal{M} \psi_-(\eta) - \frac{s}{\sqrt{\frac{\eta}{\kappa}}} \psi_0(\eta) &= 0, \\ \mathcal{M} \psi_0(\eta) - \frac{s}{\sqrt{\frac{\eta}{\kappa}}} \psi_-(\eta) + \left( \frac{1}{\sqrt{\frac{\eta}{\kappa}}} + 2\kappa \sqrt{\frac{\eta}{\kappa}} \frac{d}{d\eta} \right) &+ \\ \kappa \sqrt{\frac{\eta}{\kappa}} \psi_+(\eta) &= 0, \\ \mathcal{E} \psi_-(\eta) - \mathcal{M} \psi_+(\eta) + \kappa \left( \sqrt{\frac{\eta}{\kappa}} - 2 \sqrt{\frac{\eta}{\kappa}} \frac{d}{d\eta} \right) \psi_0(\eta) &= 0, \end{aligned} \quad (8)$$

where,  $\psi_\mp(\eta) = \psi_1(\eta) \mp \psi_4(\eta)$  and  $\psi_0(\eta) = 2\psi_2(\eta)$ . By solving these equations for  $\psi_0(\eta)$  we obtain a  $2^{nd}$  order wave equation which can be reduced into a well-known form by considering an ansatz function, reads as  $\psi_0(\eta) = \eta^{-\frac{1}{2}} \psi(\eta)$ ,

$$\frac{d^2}{d\eta^2} \psi(\eta) + \left[ \frac{\delta}{\eta} - \frac{1}{4} + \frac{1-\xi^2}{\eta^2} \right] \psi(\eta) = 0, \quad (9)$$

$$\delta = \frac{\mathcal{E}^2 - \mathcal{M}^2}{4\kappa} + \frac{\mathcal{E}s}{2\mathcal{M}} - \frac{1}{2}, \quad \xi = \frac{s}{2}.$$

Eq. (9) is in the form of the well-known Whittaker differential equation [40]. Solution function of this equation is obtained as  $\psi(\eta) = \mathcal{N}\mathcal{W}_{\delta,\xi}(\eta)$ , in which  $\mathcal{N}$  is an arbitrary constant and  $\mathcal{W}_{\delta,\xi}(\eta)$  is the Whittaker function which can be re-expressed in terms of the generalized Laguerre polynomials (see [48,49]). By using the solution function,  $\psi(\eta) = \mathcal{N}\mathcal{W}_{\delta,\xi}(\eta)$ , the defined forms of the components in Eq. (8) are obtained

$$\begin{pmatrix} \psi_+(\eta) \\ \psi_0(\eta) \\ \psi_-(\eta) \end{pmatrix} = \begin{pmatrix} \frac{\mathcal{N}\sqrt{\kappa}}{\eta(\mathcal{E}^2 - \mathcal{M}^2)}(\mathcal{M}(1 + 2\delta) - s\mathcal{E})\mathcal{W}_{\delta,\xi}(\eta) + 2\mathcal{M}\mathcal{W}_{\delta+1,\xi}(\eta) \\ \mathcal{N}\eta^{\frac{1}{2}}\mathcal{W}_{\delta,\xi}(\eta) \\ \frac{\mathcal{N}\sqrt{\kappa}}{\eta(\mathcal{E}^2 - \mathcal{M}^2)}(\mathcal{E}(1 + 2\delta) - s\mathcal{M})\mathcal{W}_{\delta,\xi}(\eta) + 2\mathcal{E}\mathcal{W}_{\delta+1,\xi}(\eta) \end{pmatrix}$$

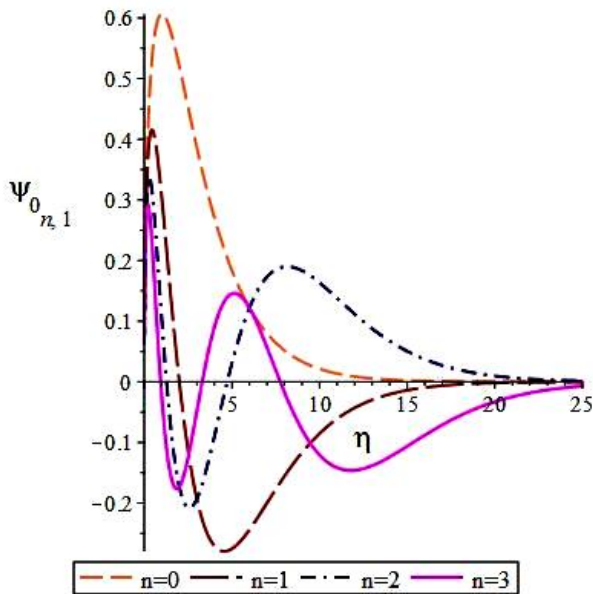


Figure 1 Behaviour of the function  $\psi_0(\eta)$  with respect to the varying values of the space coordinate  $\eta$  for a few quantum states. Here we get  $m = c = \hbar = \omega = 1$ .

To be polynomial condition of the solution function,  $\psi(\eta)$ , is  $\frac{1}{2} + \xi - \delta = -n$ . This relation gives the following spectrum of energy,

$$E_{n,s} = \mp \omega \hbar s \pm m_b c^2 \sqrt{1 + \frac{4\omega \hbar}{m_b c^2} \left(n + 1 + \frac{s}{2}\right) + \left(\frac{\omega \hbar s}{m_b c^2}\right)^2}. \quad (10)$$

The Eq. (10) gives the exact results of one-dimensional Kemmer oscillator [50] (see also

[12]) when  $s = 0$ . For this case ( $s = 0$ ), it is very interesting that the result in Eq. (10) agrees well with the recently published results for a fermion-antifermion pair holding via DO coupling [9]. Eq. (10) shows that the oscillator frequency couples with spin of the vector boson. Here, we have seen also that the total energy becomes equal to the rest mass energy of the vector boson when  $\omega = 0$ .

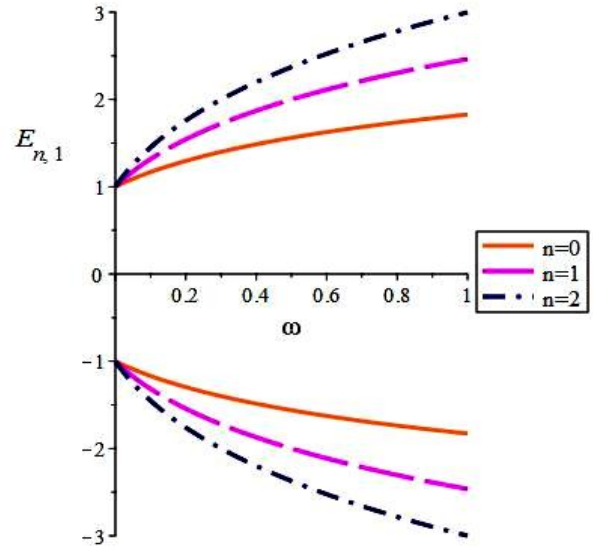


Figure 2 Dependence of the energy levels on the oscillator frequency for  $m = c = \hbar = 1$

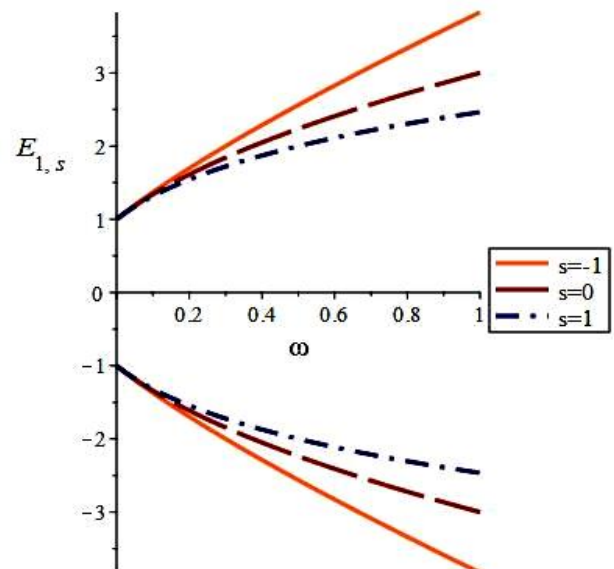


Figure 3 Dependence of the energy levels associated with possible spin eigen-states on the oscillator frequency for  $m = c = \hbar = 1$

#### 4. RESULTS AND DISCUSSIONS

In this study, we have investigated the relativistic dynamics of two-dimensional VBO by using the VBE. In order to arrive at non-perturbative results for the system in question, we have solved the corresponding form of VBE by defining the oscillator coupling through non-minimal substitutions. The corresponding equation has provided a matrix equation and by solving this equation we have obtained an exact energy spectrum for two-dimensional VBO. This energy expression is given in Eq. (10) and this result agrees well with previously announced results in the literature when the spin coupling vanishes. This fact can be seen by comparing the result in Eq. (10) and the published results in [9,50]. The result in Eq. (10) explicitly shows that the oscillator frequency couples with the spin of vector boson particle. This nature of the considered system has provided to discuss whether the corresponding energy levels can be degenerated or not. The behaviour of the energy levels can be seen in the Figure 2 and Figure 3. We can observe in Figure 3 that there is no any degeneracy in the energy levels associated with the possible spin eigen-states of the VBO. According to the result in Eq. (10) we can see that this spin-1 oscillator does not stop oscillating since there is no physical reason that imposes to stop the oscillation even for the ground state of the system, except for  $\omega = 0$ . Of course, such a physical reason may occur in the presence of external electromagnetic fields. We have also observed that total energy of the VBO closes to rest mass energy ( $E \approx \pm m_b c^2$ ) of the considered vector field when  $\omega \approx 0$ . By using the solution function of wave equation in Eq. (9) and the obtained non-perturbative energy expression in Eq. (10) we have shown the behaviour of wave functions, associated with the ground state and a few excited states of the considered system, with respect to the varying values of the defined space coordinate  $\eta$  in Figure 1. In this figure, we can see that amplitude of the wave function(s) closes to zero in the limits of both  $\eta \rightarrow 0$  and  $\eta \rightarrow \infty$ . Therefore, we can also infer that behaviour of the probability density function, for example  $|\psi_0(\eta)|^2$  associated with the solution function, shows similar behaviour. Here, we should also

notice that strength of the considered interaction closes to zero when the radial coordinate  $\eta$  (note that  $r \propto \sqrt{\eta}$ ) closes to zero.

##### *Funding*

The author has no received any financial support for this research.

##### *The Declaration of Conflict of Interest/ Common Interest*

No conflict of interest or common interest has been declared by the author. The author has fully disclosed conflict of interest situations to the journal.

##### *Author' Contribution*

This paper has been prepared by the author.

##### *The Declaration of Ethics Committee Approval*

This study does not require ethics committee permission. This study also does not require any special permission.

##### *The Declaration of Research and Publication Ethics*

The author declares that she complies with the scientific, ethical and quotation rules of SAUJS in all processes of the present paper and that she does not make any falsification on the data collected. Also, the author declares that Sakarya University Journal of Science and its editorial board have no responsibility for any ethical violations that may be encountered, and that the present study has not been evaluated in any academic publication environment other than Sakarya University Journal of Science.

#### REFERENCES

- [1] M. Moshinsky, A. Szczepaniak, "The Dirac oscillator." *Journal of Physics A: Mathematical and General*, vol. 22, no. 17, pp. L817-L819, 1989.
- [2] S. Bruce and P. Minning, "The Klein-Gordon oscillator," *Il Nuovo Cimento A*, vol. 106, no. 5, pp. 711–713, 1993.
- [3] N. Debergh, J. Ndimubandi, and D. Strivay, "On relativistic scalar and vector mesons with harmonic oscillator - like interactions,"

- Zeitschrift für Physik C Particles and Fields  
", vol. 56, pp. 421–425, 1992.
- [4] Y. Nedjadi and R. C. Barrett, "The Duffin-Kemmer-Petiau oscillator," *Journal of Physics A: Mathematical and General*, vol. 27, no. 12, pp. 4301–4315, 1994.
- [5] A. Guvendi, S. Zare and H. Hassanabadi "Vector boson oscillator in the spiral dislocation spacetime", *The European Physical Journal A*, vol. 57, no. 6, pp. 1-6, 2021.
- [6] A. Guvendi, and H. Hassanabadi "Relativistic vector Bosons with Non-minimal coupling in the Spinning Cosmic String Spacetime", *The European Physical Journal A*, vol. 62, no. 3, pp. 1-8, 2021.
- [7] J. Benitez, R. P. Martinez y Romero, H. N. Nuez-Yépez, and A. L. Salas-Brito, "Solution and hidden supersymmetry of a Dirac oscillator," *Physical Review Letters*, vol. 64, no. 14, pp. 1643–1645, 1990.
- [8] M. Moreno and A. Zentella, "Covariance, CPT and the FoldyWouthuysen transformation for the Dirac oscillator," *Journal of Physics A: Mathematical and General*, vol. 22, no. 17, pp. L821, 1989.
- [9] A. Guvendi, Relativistic Landau levels for a fermion-antifermion pair interacting through Dirac oscillator interaction. *European Physical Journal C*, vol. 81, no. 2, pp.1-7, 2021.
- [10] A. Guvendi, "Dynamics of a composite system in a point source-induced space-time", *International Journal of modern Physics A*, vol. 36, no. 19, pp.2150144, 2021.
- [11] A. Bermudez, M.A. Martin-Delgado, E. Solano, Exact mapping of the 2+ 1 Dirac oscillator onto the Jaynes-Cummings model: Iontrap experimental proposal, *Physical Review A*, vol.76, no. 4, pp. 041801, 2007.
- [12] Y. Luo, Y. Cui, Z. Long, and J. Jing, "2+1 Dimensional Noncommutative Dirac Oscillator and (Anti)-JaynesCummings Models," *International Journal of Theoretical Physics*, vol. 50, no. 10, pp. 2992–3000, 2011.
- [13] Y. Chargui and A. Dhahbi, "On the q-deformed Dirac oscillator in (2+1)-dimensional space-time", *Annals of Physics*, vol.428, pp. 168430, 2021.
- [14] M. H. Pacheco, R. R. Landim and C. A. S. Almeida, "One-dimensional Dirac oscillator in a thermal bath," *Physics Letters A*, vol. 311, no. 2-3. pp 93-96, 2003.
- [15] M. Moshinsky, Y.F. Smirnov, "The Harmonic Oscillator in Modern Physics", vol. 9, pp. 414, CRC Press, Boca Raton, 1996.
- [16] M. Moshinsky, G. Loyola, "Barut equation for the particle antiparticle system with a Dirac oscillator interaction". *Found. Phys.* Vol.23, 197–210, 1993.
- [17] J. Carvalho, C. Furtado and F. Moreas, "Dirac oscillator interacting with a topological defect," *Physical Review A*, vol. 84, no. 3. pp. 032109, 2011.
- [18] M. M. Cunha, H. S. Dias, and E. O. Silva, "Dirac oscillator in a spinning cosmic string spacetime in external magnetic fields: Investigation of the energy spectrum and the connection with condensed matter" *Physical Review D*, vol.102, no.10, pp. 105020, 2020.
- [19] A. Boumali and N. Messai, "Klein–Gordon oscillator under a uniform magnetic field in cosmic string space-time," *Canadian Journal of Physics*, vol. 92, no. 11, pp. 1460–1463, 2014.
- [20] K. Bakke and C. Furtado, "On the Klein-Gordon oscillator subject to a Coulomb-type potential," *Annalen der Physik*, vol. 355, pp. 48–54, 2015.

- [21] R. L. L. Vitória, C. Furtado, and K. Bakke, "On a relativistic particle and a relativistic position-dependent mass particle subject to the Klein-Gordon oscillator and the Coulomb potential," *Annals of Physics*, vol. 370, pp. 128–136, 2016.
- [22] F. Ahmed, "The Klein-Gordon oscillator in (1+2)-dimensions Gurses space-time backgrounds," *Annals of Physics*, vol. 404, pp. 1-9, 2019.
- [23] F. Ahmed, "The generalized Klein--Gordon oscillator in the background of cosmic string space-time with a linear potential in the Kaluza--Klein theory," *The European Physical Journal C*, vol. 80, pp. 1-12, 2020.
- [24] L. Zhong, H. Chen, Z. W. Long, C. Y. Long, and H. Hassanabadi, "The study of the generalized Klein--Gordon oscillator in the context of the Som--Raychaudhuri space--time," *International Journal of Modern Physics A*, pp. 2150129, 2021.
- [25] R. J. Duffin, "On the characteristic matrices of covariant systems," *Physical Review A: Atomic, Molecular and Optical Physics*, vol. 54, no. 12, pp. 1114, 1938.
- [26] N. Kemmer, "The particle aspect of meson theory," *Proceedings of the Royal Society A Mathematical, Physical and Engineering Sciences*, vol. 173, no. 952, pp. 91–116, 1939.
- [27] G. Petiau, "Contribution à la théorie des équations d'ondes corpusculaires," *Mémoires de l'Académie Royale de Belgique, Classe des*, vol. 8, no. 2, pp. 16, 1936.
- [28] A Boumali, L Chetouani, H Hassanabadi, *Canadian Journal of Physics*, "Two-dimensional Duffin–Kemmer–Petiau oscillator under an external magnetic field" "vol. 91, no.1, pp. 1-11, 2013.
- [29] M. Falek, M. Merad, and M. Moumni "Bosonic oscillator under a uniform magnetic field with Snyder-de Sitter algebra" *Journal of Mathematical Physics*, vol. 60, no.1, pp. 013505, 2019.
- [30] I.S. Gomez and E. S. Santos and O. Abla, *Physics Letters A* , "Splitting frequency of the (2 + 1)-dimensional Duffin-Kemmer-Petiau oscillator in an external magnetic field ", vol. 384, no.27, pp. 126706, 2020.
- [31] Z.-H. Yang, C.-Y. Long, S.-J. Qin, and Z.-W. Long "DKP oscillator with spin-0 in three-dimensional noncommutative phase space," *International Journal of Teoretical Physics*, vol. 49, no. 3, pp. 644–651, 2010.
- [32] M. Falek and M. Merad, "DKP oscillator in a non-commutative space," *Communications in Teoretical Physics*, vol. 50, no. 3, pp. 587–592, 2008.
- [33] M. Falek and M. Merad, "Bosonic oscillator in the presence of minimal length," *Journal of Mathematical Physics, Journal of Mathematical Physics*, vol.50, no.2, pp. 023508, 2009.
- [34] B. Hamil, and M. Merad and T. Birkandan, "The Duffin-Kemmer-Petiau oscillator in the presence of minimal uncertainty in momentum" , *Physica Scripta*, vol. 95, no.7, pp. 075309, 2020.
- [35] A. O. Barut, "Excited states of zitterbewegung," *Physics Letters B*, vol. 237, no. 3, pp. 436-439, 1990.
- [36] N. Ünal, "A simple model of the classical zitterbewegung: photon wave function", *Foundations of Physics*, vol. 27, no. 5. pp 731-746, 1997.
- [37] N. Ünal, "Path Integral Quantization of a Spinning Particle" *Foundations of Physics*, vol. 28 no.5, pp.755–762. 1998.
- [38] A. Guvendi, R. Sahin and Y. Sucu, "Exact solution of an exciton energy for a monolayer medium," *Scientific Reports*, vol. 9, no. 1. pp 1-6, 2019.

- [39] A. Guvendi and Y. Sucu, “An interacting fermion-antifermion pair in the spacetime background generated by static cosmic string,” *Physics Letters B*, vol. 811, no. 135960. pp 135960, 2020.
- [40] M. Dernek and S. G. Doğan and Y. Sucu and N. Ünal, “Relativistic quantum mechanical spin-1 wave equation in 2+1 dimensional spacetime,” *Turkish Journal of Physics*, vol. 42, no. 5. pp 509-526, 2018.
- [41] Y. Sucu and C. Tekincay, “Photon in the Earth-ionosphere cavity: Schumann resonances,” *Astrophysics and Space Science*, vol. 364, no. 4. pp 1-7, 2019.
- [42] G. Gecim and Y. Sucu, “The GUP effect on tunneling of massive vector bosons from the 2+1 dimensional blackhole,” *Advances in High Energy Physics*, vol. 2018, no. 8. pp 1-8, 2018.
- [43] Y. Sucu and N. Ünal, “Vector bosons in the expanding universe,” *The European Physical Journal C*, vol. 44, no. 2. pp 287-291, 2005.
- [44] R. E. Kozack, B. C. Clark, S. Hama, V. K. Mishra, R. L. Mercer, and L. Ray, “Spin-one Kemmer-Duffin-Petiau equations and intermediate-energy deuteron-nucleus scattering,” *Physical Review C*, vol. 40, no. 5, pp. 2181–2194, 1989.
- [45] M. Hosseinpour, H. Hassanabadi and F. M. Andrade, “The DKP oscillator with a linear interaction in the cosmic string space-time,” *The European Physical Journal C*, vol. 78, no. 2. pp 1-7, 2018
- [46] A. Guvendi and S. G. Doğan, “Relativistic Dynamics of Oppositely charged Two Fermions Interacting with External Uniform Magnetic Field,” *Few-Body Systems*, vol. 62, no. 1. pp 1-8, 2021.
- [47] A. Guvendi, R. Sahin and Y. Sucu, “Binding energy and decaytime of exciton in dielectric medium,” *The European Physical Journal B*, vol. 94, no. 1. pp 1-7, 2021.
- [48] C. Tezcan and R. Sever, “A General Approach for the Exact Solution of the Schrodinger Equation” *Int. J. Theor. Phys.* vol. 48, no. 2, pp. 337, 2009.
- [49] A.F. Nikiforov and V.B. Uvarov, “Special Functions of Mathematical Physics”, Birkhauser, Basel vol.205, pp. 427, 1988.
- [50] A. Boumali, “One-dimensional thermal properties of the Kemmer oscillator,” *Physica Scripta*, vol. 76, no. 6. pp 669, 2007.



SAKARYA ÜNİVERSİTESİ

# FEN BİLİMLERİ ENSTİTÜSÜ DERGİSİ

Sakarya University Journal of Science  
SAUJS

e-ISSN: 2147-835X | Founded: 1997 | Period: Bimonthly | Publisher: Sakarya University |  
<http://www.saujs.sakarya.edu.tr/en/>

Title: Effect of Heat Treatment on Microstructure of Zinc Aluminum Hybrid Composite Cast Alloys

Authors: Serdar ASLAN

Received: 2021-08-14 00:00:00

Accepted: 2021-09-27 00:00:00

Article Type: Research Article

Volume: 25

Issue: 5

Month: October

Year: 2021

Pages: 1218-1234

How to cite

Serdar ASLAN; (2021), Effect of Heat Treatment on Microstructure of Zinc Aluminum Hybrid Composite Cast Alloys. Sakarya University Journal of Science, 25(5), 1218-1234, DOI: <https://doi.org/10.16984/soaufenbilder.982948>

Access link

<http://www.saujs.sakarya.edu.tr/tr/pub/issue/65589/982948>

New submission to SAUJS

<http://dergipark.org.tr/en/journal/1115/submission/step/manuscript/new>

## Effect of Heat Treatment on Microstructure of Zinc-Aluminum Hybrid Composite Cast Alloys

Serdar ASLAN\*<sup>1</sup>

### Abstract

The matrix material ZA-27 alloy was used in the production of metal matrix composite material. SiC and graphite were used as reinforcement materials in the study. ZA27 alloy with 10% SiC, 2.5% , 5% , 7.5% and 10% graphite and 10% SiC + 2.5% , 5%, 7.5%, 10% graphite reinforcement by weight hybrid composite material was produced. The microstructures were examined by SEM and EDS and the results were discussed. In the investigations, SiC and graphites had a heterogeneous nucleating effect during the solidification of the alloy. In addition, thin dendrites showed a tendency to become spherical by heat treatment.

**Keywords:** ZA alloy casting, Heat Treatment, Composite, Hybrid Casting

### 1. INTRODUCTION

In 1979, a unique family of alloys, hypereutectic zinc-aluminum alloys with high aluminum and copper contents, were developed from Zamak alloys that widely used. ZA-27 is the recently developed Zn-Al based alloy [1].

Zinc aluminum (ZA) alloys are the alloys containing zinc as the base metal with higher aluminum concentrations compared to conventional zinc alloys (ZAMAK). Other metals found in these alloys are magnesium and copper.

Zinc aluminum alloys are high performance metallic composites thanks to their good strength, good hardness, high corrosion resistance under atmospheric conditions, excellent casting properties, easy processing and good tribological properties. Some of the zinc aluminum alloys are

ZA8, ZA12 and ZA27, the numbers in these expressions indicate the aluminum concentration.

ZA27 alloy is a lightweight alloy suitable for applications requiring optimum strength. It exhibits good strength, stiffness, maximum friction and creep resistances [2-3].

Zinc-aluminum based alloys have many advantages over some ferrous and non-ferrous alloys [1]. Among these advantages are ideal casting properties, requiring little additional processing after casting, high specific strength (strength/density ratio), wear resistance and corrosion resistance. The composite's alloying elements are cheap and easy to obtain which shows they are financially affordable and environment friendly. ZA alloys were developed as replacements for bronze during periods when the copper content was insufficient [4]. The addition of copper, aluminum and silicon enabled zinc-based alloys to exhibit low coefficient of

\* Corresponding author: saslan@sakarya.edu.tr

<sup>1</sup> Sakarya University, Engineering Faculty, Department of Metallurgical and Materials Engineering.

ORCID: <https://orcid.org/0000-0001-5061-6338>

friction and high wear resistance properties in lubricated medium. Although copper showed a better effect than silicon in case of increased strength, it did not show the same effect in terms of increased wear resistance. Because zinc aluminum alloys contain copper and silicon, their use as bearing materials has gained commercial importance. Bearings made of these alloys are widely used in plain bearings with low speed and high load [5]. However, the limited operating temperature of 100 °C and the low impact resistance are among the factors limiting the use of this alloy. These considerations have led to studies to determine the appropriate composition, heat treatment and the addition of second particles [5].

In general, zinc aluminum alloys are used in many engineering fields such as construction machines, lathes, hydraulic lift cylinders, water pumps, automobile and textile industry [6]. Zamak alloys, which have a very high usage area in the construction and automotive industry electronic devices; household goods, ready-to-wear; toys, sports, office machinery; hardware, tools used in agriculture and mining which are frequently preferred as raw materials. Especially thanks to the high strength Zamak2 [7] exhibits, it can be used in shaft bearings as well as metal plates, where the wear effect is high. Zamak2, which is used in plastic injection equipment, metal forming molds, is the best example of this [8]. Finally, Zamak5 alloy, which is preferred in the areas of usage where tensile performance is important, is also used in areas where slightly higher performance is expected compared to Zamak3 [8].

## 2. EXPERIMENTAL STUDIES

### 2.1. Matrix and Reinforcement Materials

The matrix material used in the production of the metal matrix composite in this present work was

ZA-27 alloy. In the production of ZA-27 matrix alloy, 99.99% pure Zn, Cu, and Mg and 99.95% pure Al were used and the prepared matrix alloy composition was poured into a permanent mold. The melting process was carried out under argon gas in a graphite crucible in an electric resistance furnace. The chemical analysis of the produced alloy in the absorption device is as follow; 26.7% Al, 2.1% Cu, 0.03% Mg, 0.035% Fe, 71.135% Zn by weight (w/w). SiC and graphite were used as reinforcement materials into the previously prepared matrix alloy during the experimental work. Together with ZA-27 alloy, hybrid composite materials (HCM) consisting of 10% SiC+2.5%, 5%, 7.5% and 10% graphite reinforcements by weight were produced. The diameter of SiC particles used in the production of composites and hybrid composites is 62.5 µm, and the diameter of graphite particles is about 40-90 µm. Despite a tough addition of graphite particles into the matrix is well-known in the literature due to the high surface tension between ZA 27 alloy and graphite, copper metal coating on graphite particles was performed to control surface tension of graphite particles to make them suitable for hybrid composite production. In order to reduce a surface tension, the graphite particles were coated with copper metal.

The purpose of the coating is the metal/reinforcement phase interface structure; converting from graphite/metal to metal/metal. Surfaces of graphite particles were activated by addition of 0.2 M CuSO<sub>4</sub>.5H<sub>2</sub>O solution in a 380 °C furnace and a thin copper layer was formed on the particle surface based on the cementation of copper [9]. The surface and cross-sectional images of the coated graphite particles are given in Figure 1.

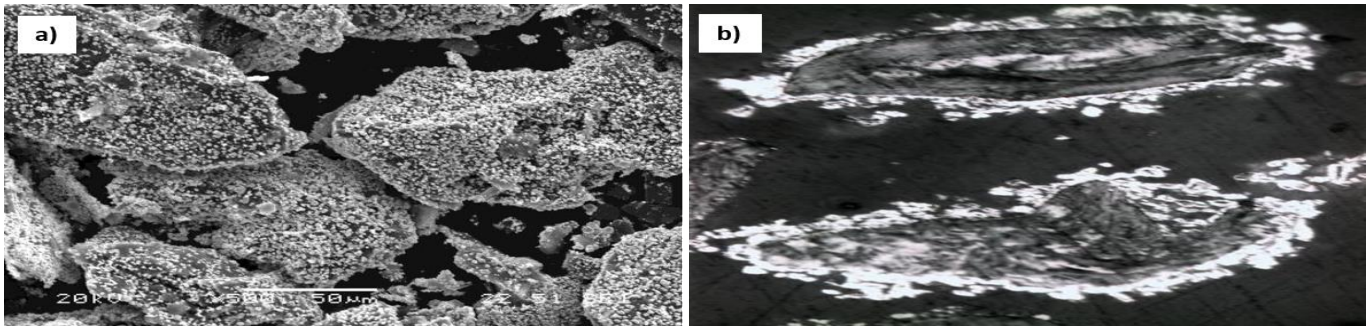


Figure 1 SEM micrograph of the graphite particles coated with Cu: a) surface image of starting graphites, b) cross sectional image of the graphite with Cu coating layer.

## 2.2. Heat Treatment of the Composite Materials Produced

The samples prepared for heat treatment were placed in an oven and subsequently the temperature inside was set at 330 °C and kept constant for 5 hours, and then the specimens were cooled in water.

## 2.3. Metallographic Studies

The samples to be used for metallographic investigation after casting and heat treatment were first prepared by cutting with a diamond disc with the help of a cutting device.

Unlike ZA 27, while composite materials consist of two components, hybrid composite materials consist of three main components: matrix, graphite particles and hard ceramic SiC particles. The metallographic preparation of these materials is a difficult process, since each of these components has their own unique hardness. Sanding and polishing processes must be done very sensitively so that the soft graphite particles and the hard and brittle ceramic reinforcement phases are not removed from the matrix by the abrasive. Specimens used for this examination were sanded in accordance with standard sample preparation methods. The specimens, which were cleaned from abrasives that may come from the sanding step by washing thoroughly, were polished with 1µm alumina.

The dried samples were etched in Keller's solution (1cm<sup>3</sup> hydrofluoric acid; 1.5 cm<sup>3</sup> chloric acid; 2.5 nitric acid; 95 cm<sup>3</sup> water) for optical and SEM examination with EDS analysis. After etching, the

specimens were washed and dried again, and SEM examinations were made.

## 3. CONCLUSIONS AND DISCUSSIONS

### 3.1. Microstructure of the ZA-27 Alloy, Reinforcement Materials and the Hybrid Composites Produced

SEM image of the microstructure of the ZA-27 alloy after casting is given in Figure 2a. In Figure 2b, the microstructure image of the ZA alloy after heat treatment is given. The particle visible in Figure 2b is the  $\eta$  phase, which is rich in net region consisting of black thin lines, and the very thin  $\epsilon$ s in this phase are in the ground.

In ZA 27 alloy, unlike other alloys, peritectic and eutectic and eutectoid reactions are seen together. During the solidification process, aluminum-rich  $\alpha$  phase occurs in the liquid first. At 443 °C,  $\alpha$  dendrites form a peritectic reaction with the liquid. During the formation of  $\alpha$  dendrites containing 60% aluminum in the structure, the liquid phase becomes enriched with zinc. As a result of peritectic reaction of  $\alpha$  dendrites with the liquid at 443 °C, zinc-rich  $\beta$  phases form around the dendrites. The  $\alpha$  and  $\beta$  phases are in FCC structure and differ in terms of composition and lattice parameter [5]. Solidification is completed by the eutectic transformation of the remaining zinc-rich liquid. As a result of the eutectic reaction at 377 °C; aluminum-rich  $\alpha$  phase, zinc-rich  $\eta$  phase and intermetallic (CuZn<sub>4</sub>)  $\epsilon$  phases are formed. This  $\epsilon$  (CuZn<sub>4</sub>) phase in the ZA 27 alloy is in a metastable state intermetallic. This phase, which is present in  $\eta$  as precipitate particles, contributes to the mechanical properties

positively. At 268 °C, the triple stable phase of  $Al_4Cu_3Zn$  ( $T'$ ) occurs as  $\epsilon + \alpha \rightarrow \eta + T'$  [5,18].  $Al_4Cu_3Zn(T')$  phase contains 12.7% Zn, 31.6% Al and 55.7% Cu in content and has a rhombohedral structure. The aluminum-rich  $\beta$  phase, which is unstable under 275 °C, forms the  $\alpha$  and  $\eta$  stable phases as a result of the eutectoid reaction. Figure 2a and 2b show the microstructures of the ZA 27 alloy after casting and heat treatment, respectively. When the cast structure is investigated, it is seen that the  $\beta$  phase formed as a result of the peritectic reaction

surrounds the first formed  $\alpha$  dendrites. It is known that the dark colored part in the microstructures contains the  $\alpha$ ,  $\eta$  and  $\epsilon$  phases formed as a result of the eutectic reaction of the final liquid [15]

When the heat treated microstructures in Figure 2b are investigated, It is seen that the alloy structure becomes homogeneous and the  $\alpha$  dendrites become spherical and coarse. A similar situation has been observed in the heat treatment of Altupak's short fiber reinforced Al alloy and composites [16].

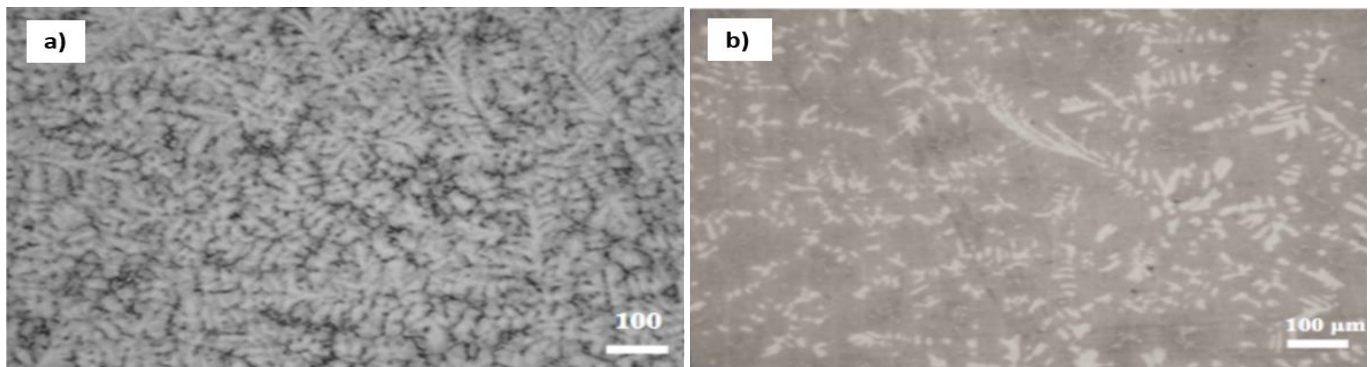


Figure 2 a) ZA 27 alloy casting state, b) thermal post heat treatment microstructure micrographs

In Figure 3, the microstructures of SiC reinforced composite materials (SRC) after casting and heat treatment are given. The matrix in the SRC casting structure is similar to the microstructure of the alloy given in Figure 2. SiC particles are homogeneously dispersed in the structure.

It is seen that the matrix microstructure of the heat-treated SRC material in Figure 2b degenerates compared to the cast structure in Figure 2a, and the dendrites are thinner.

Figure 4–7 shows the microstructures of graphite reinforced composite (GRC) materials containing 2.5-5-7.5-10% graphite by weight, after casting and post heat treatment, respectively. Due to the increase in graphite percent, segregation did not occur in 5, 7.5 and 10% graphite by weight reinforced composites. The difference in crystallization system, density difference and high surface tension between graphite and metal prevents the metal from wetting the graphite and thus forming a good bond [9]. Thanks to the copper coating, the metal and graphite bond is very well. Since the bond structure of graphite in

the c direction has Van der Waals bond structure, weak bonds in this direction were broken as a result of squeeze casting and liquid metal was filled in this region. In Figure 4a-5a, this structure is seen on graphite. Figure 6a-6b show the microstructures of casting and post-heat treatment of graphite reinforced composite (GRC) materials containing 2.5, 5, 7.5 and 10 % graphite by weight, respectively. Due to the increase in graphite percent, segregation did not occur in 5, 7.5 and 10% by weight reinforced composites. The difference in crystallization system, density difference and high surface tension between graphite and metal prevents the metal from wetting the graphite and thus forming a good bond [9].

Thanks to the copper coating, the metal and graphite bond very well. Since the bond structure of graphite in the c direction has Van der Waals bond structure, weak bonds in this direction were broken as a result of squeeze casting and liquid metal was filled in this region. Figure 4a-5a shows this structure on graphite.

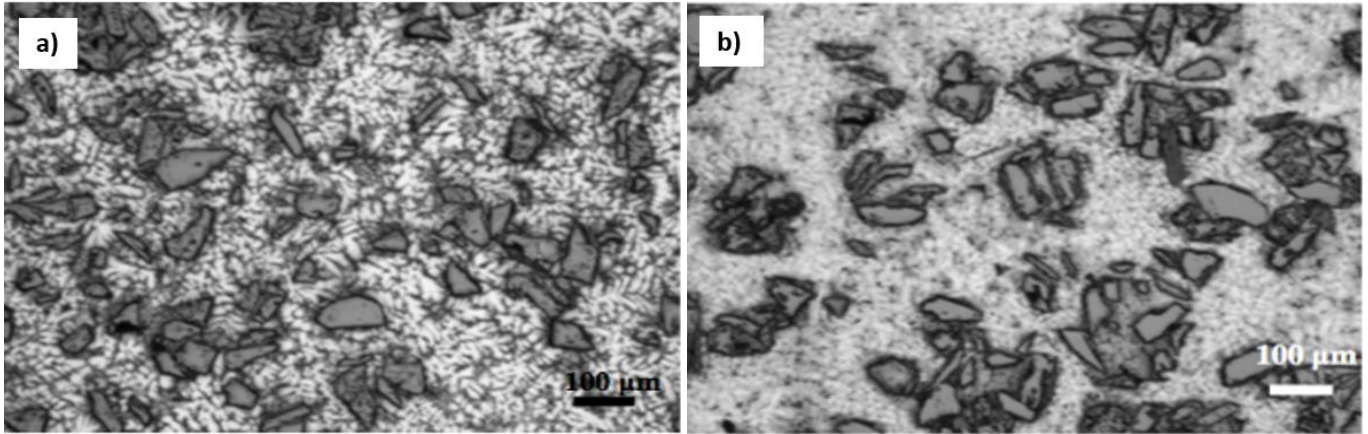


Figure 3 Microstructure photographs of a) casting state of 10% SiC reinforced composite, b) post heat treated graphite reinforced composite

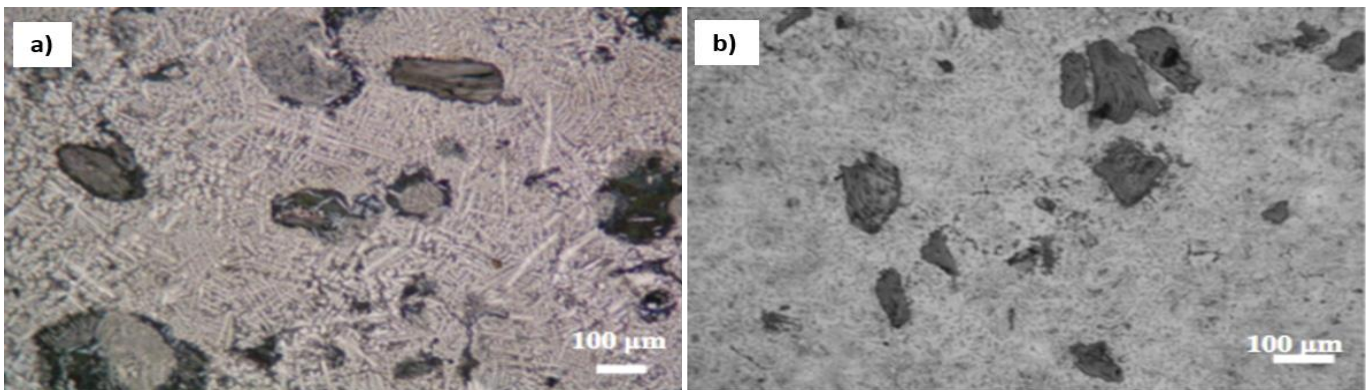


Figure 4 Microstructure pictures of a) casting of 2.5% graphite reinforced composite b) post heat treated graphite reinforced composite

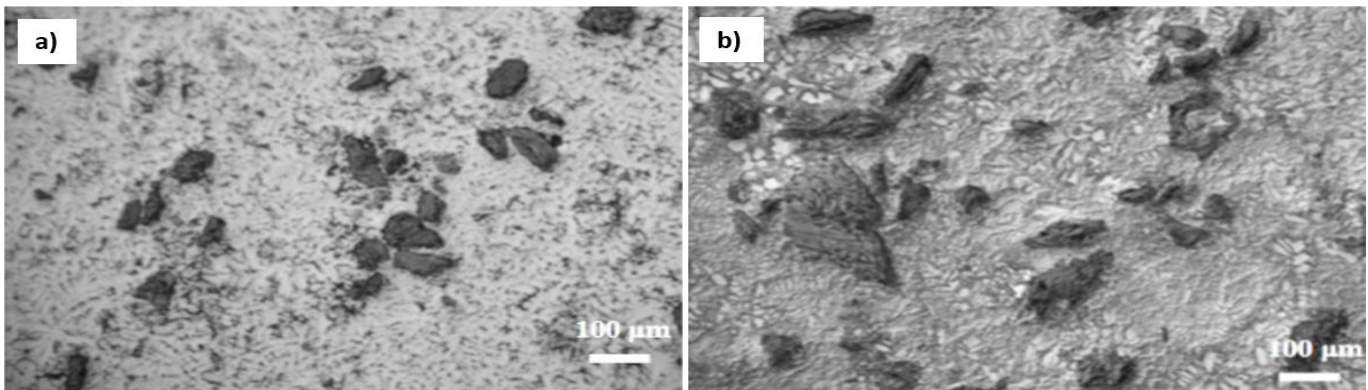


Figure 5 Microstructure photographs of a) casting state of 5% graphite reinforced composite, b) post heat treated graphite reinforced composite

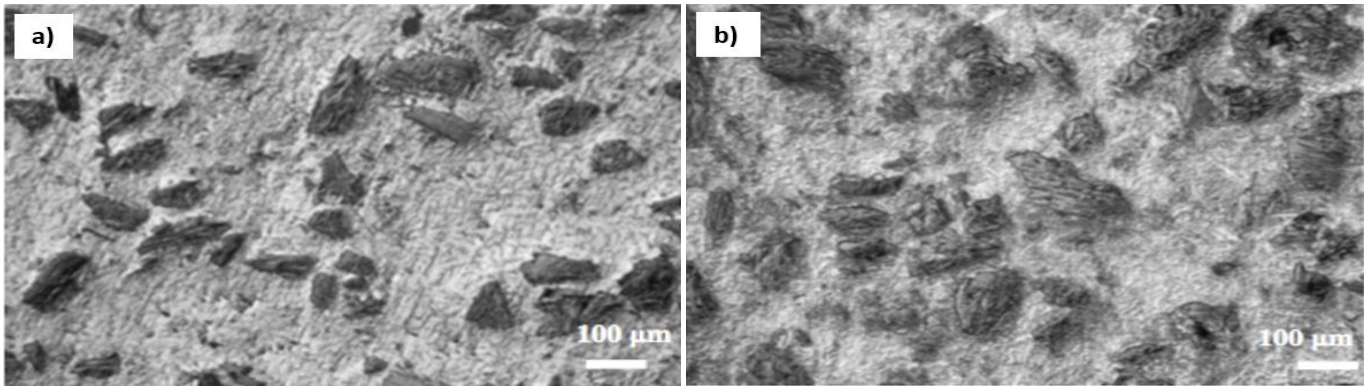


Figure 6 Microstructure photographs of a) casting state of 7.5% graphite reinforced composite, b) post heat treated graphite reinforced composite heat

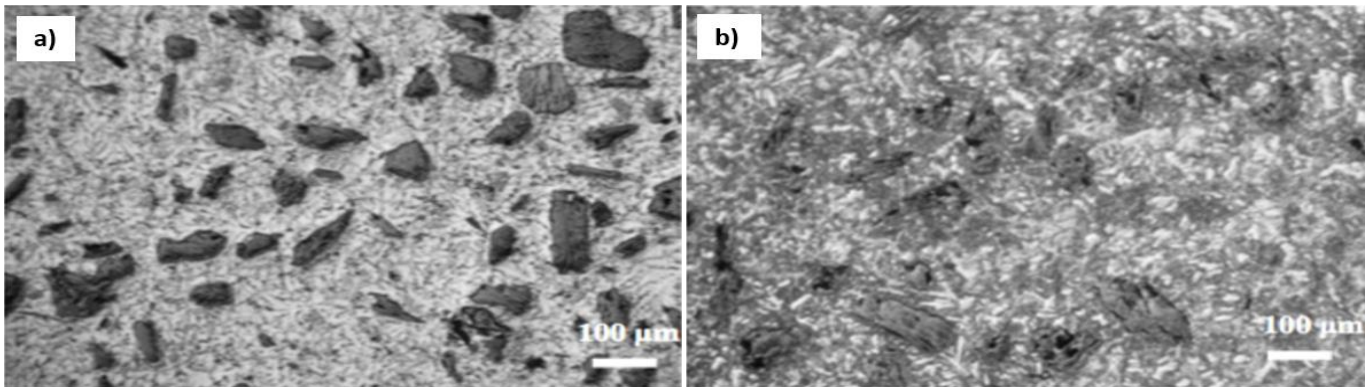


Figure 7 microstructure pictures of a) 10% graphite reinforced composite casting state, b) post heat treated graphite reinforced composite

In Figure 8-11, casting and heat treated microstructures of hybrid composite (HCM) materials containing 10% SiC and 2.5-5-7.5-10% graphite by weight respectively, are given. In addition, in Figure 9a and 10a, finer dendritic structure is seen around graphite with much higher heat conductivity, while coarser dendrites grow around SiC. Figure 8b-10b clearly shows the microstructure formed post heat treatment. The resulting white areas are primary  $\alpha$  and around

them  $\alpha+\eta$  structure is seen. After heat treatment, primary  $\alpha$  phases in the form of dendrites become spherical. In the HCMs in Figure 8-11, this spheroidization size is at a lower order compared to the heat-treated microstructure of the alloy in Figure 2b. The same behavior was detected in 10% SiC reinforced and graphite reinforced materials. Increasing reinforcement ratio prevents coarsening of primary  $\alpha$  dendrites.

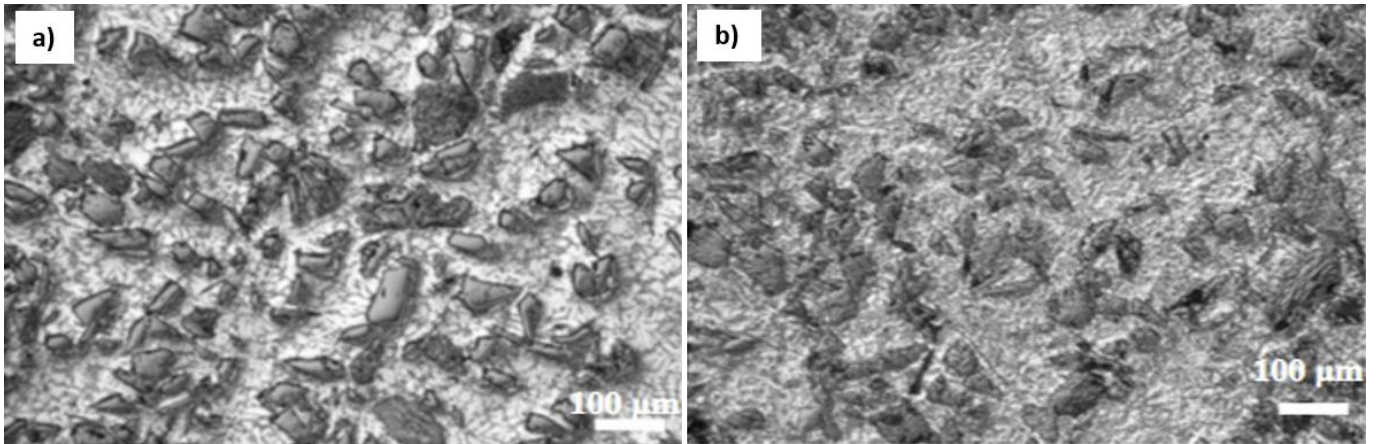


Figure 8 Microstructure photographs of a) casting state of 10% SiC + 2.5% graphite by weight reinforced hybrid composite b) heat treated state

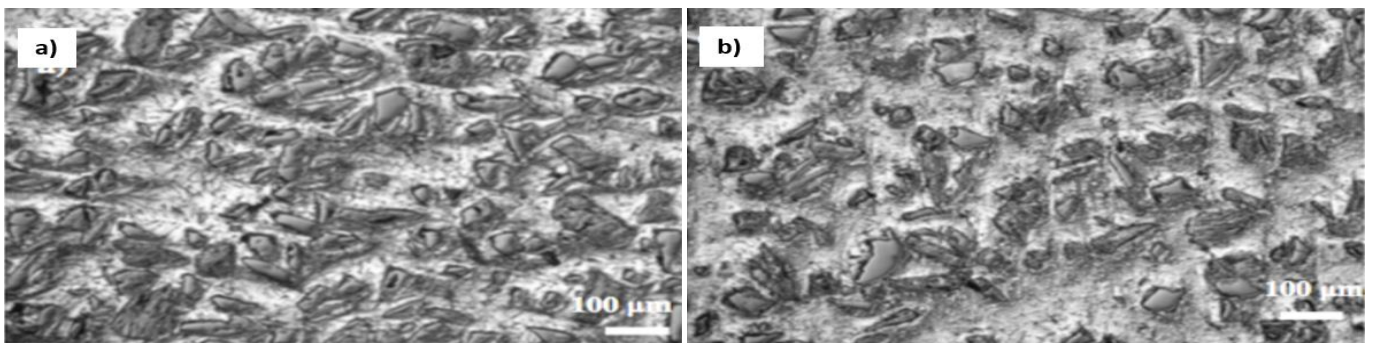


Figure 9 Microstructure photographs of a) 10% SiC + 5% by weight graphite reinforced hybrid composite as casting, b) heat treated state

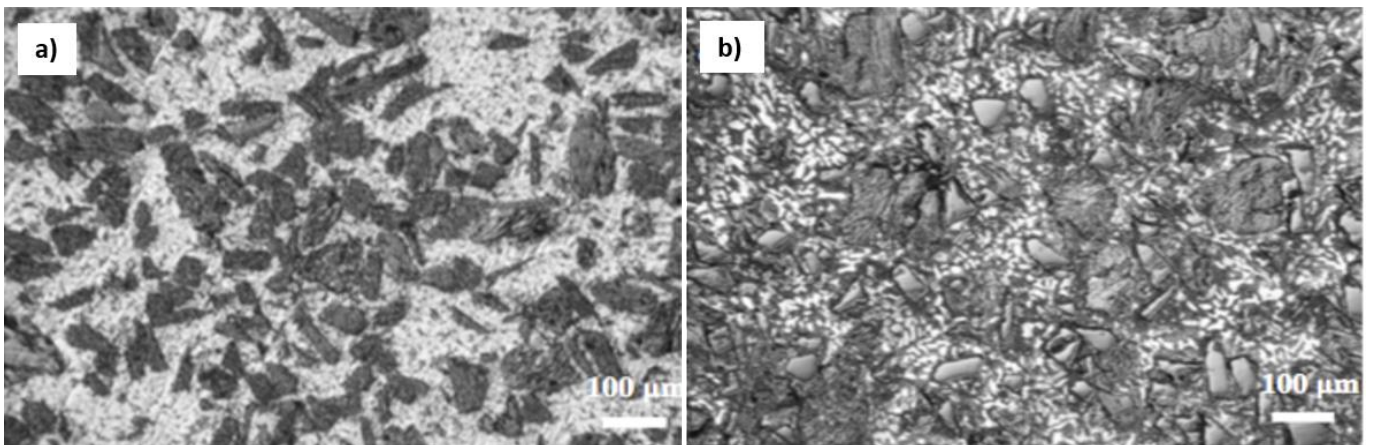


Figure 10 Microstructure photographs of a) 10% SiC + 7.5% by weight graphite reinforced hybrid composite casting state, b) heat treated state

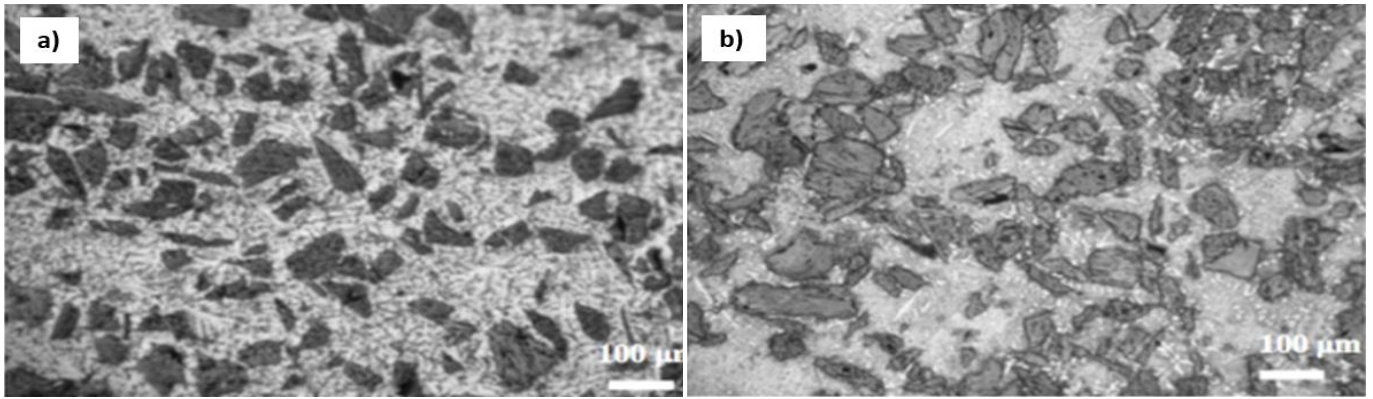


Figure 11 Microstructure photographs of a) 10% SiC + 10% by weight graphite reinforced hybrid composite casting state, b) heat treated state

Electron microscope images of ZA 27 alloy, SRC, GRC and HCM and EDS analysis of these images are given in Figure 12-24. In electron microscope (SEM) images, Zn-rich phases were detected in light tones, while Al-rich phases were detected in dark tones. Durman and Murphy [17] showed that the  $\epsilon$  phase contains 84% Zn and 14.8% Cu by weight. In our study, EDS analyzes taken from the  $\epsilon$  phase in electron microscope images give 82-85% Zn and 14-15% Cu content by weight, in accordance with the literature. Durman and Murphy, in their studies, showed that Cu in the alloy in the metastable  $\epsilon$  phase, Zn rich eutectic  $\eta$  and high temperature phase  $\beta$  precipitated as very small particles in the  $\eta$  matrix formed as a result

of the eutectoid transformation and preserved its metastable existence for a very long time, for more than five years. It has been proven in the examinations made on samples aged at room temperature. The  $\epsilon$  phase is not stable at temperatures below 268 °C and must be transformed into the T' phase. The T' phase consists of 58% Cu, 30% Al and 12% Zn, and accordingly, the transformation of the  $\epsilon$  phase to the stable T' phase requires diffusion of aluminum into the  $\epsilon$  phase. However, due to the very low aluminum solubility in the  $\eta$  matrix and the similar crystal structures of the  $\eta$  and  $\epsilon$  phases, it can maintain its metastable existence in the  $\epsilon$  phase and  $\eta$  matrix for long periods of time

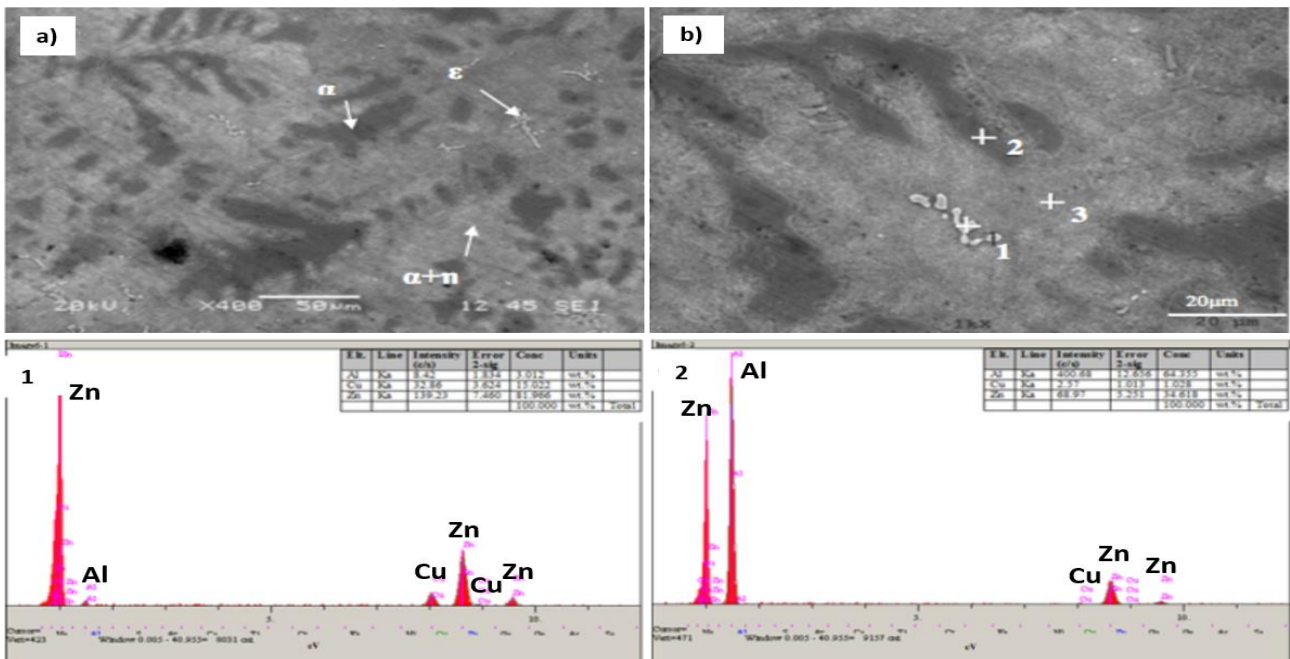


Figure 12 a-b) SEM structure of cast ZA 27 alloy, 1-2) EDS analysis of cast ZA 27 alloy

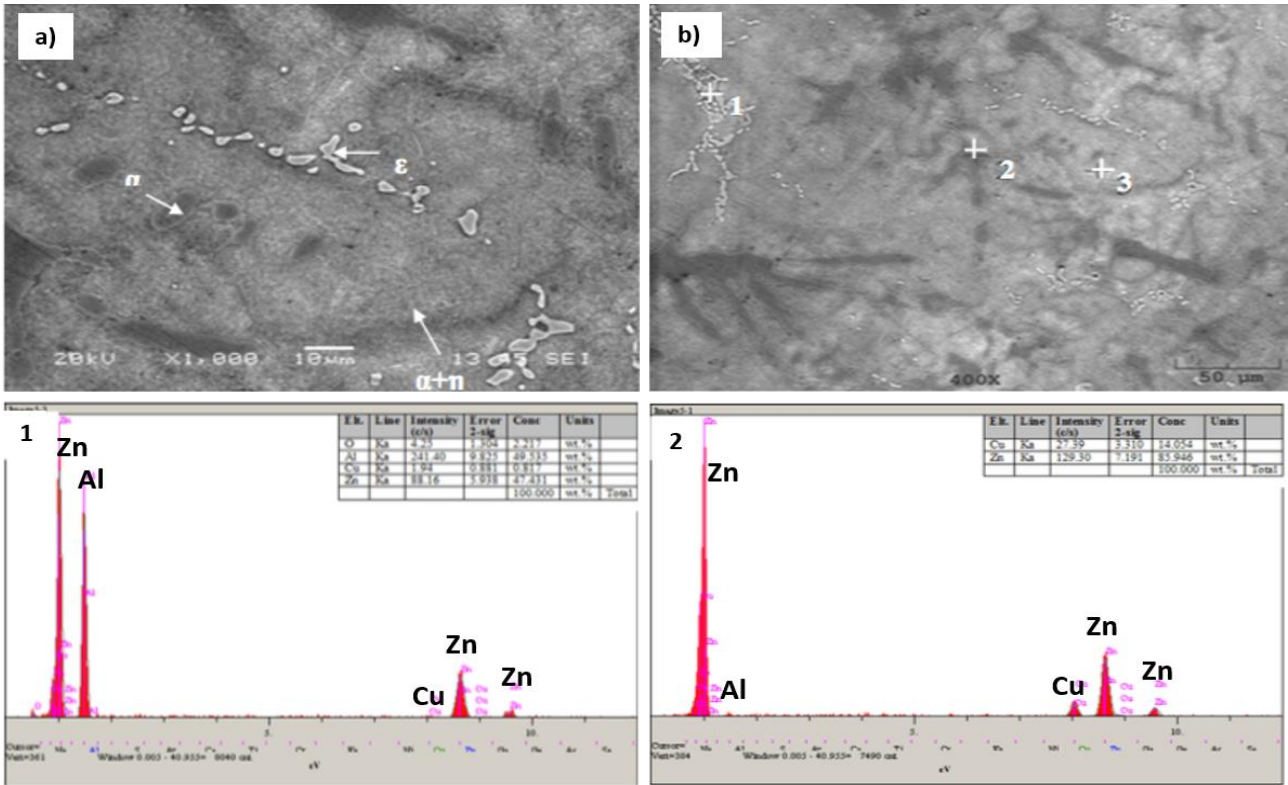


Figure 13 SEM structure of ZA 27 alloy a-b) heat treated state state 1-2-) EDS analysis of the ZA 27 alloy

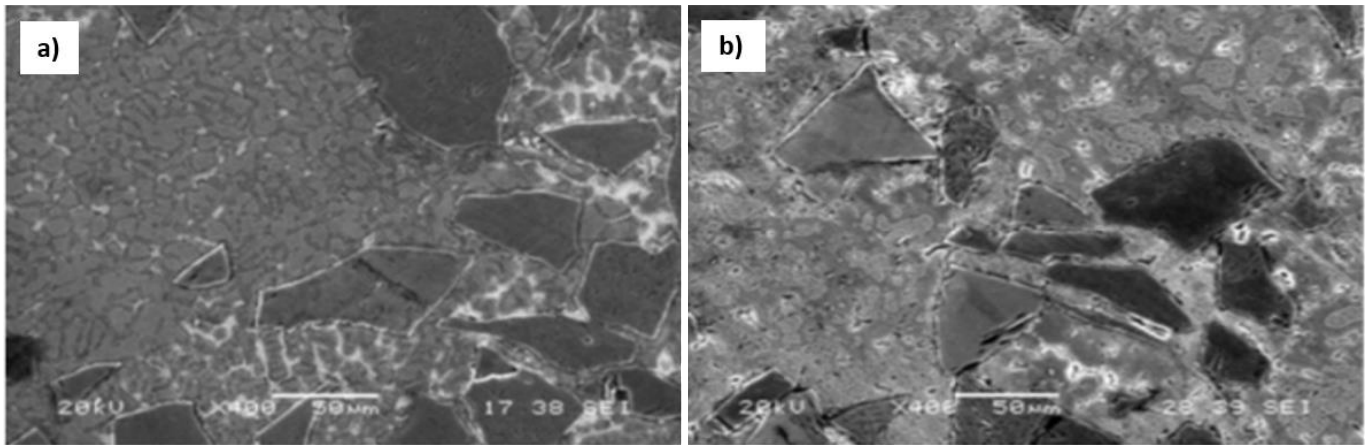


Figure 14 SEM structure of 10% SiC by weight reinforced composite material (SRC) a) casting state b) heat treatment state

In Figure 15–19, it is seen in SEM images that it consists of islet-shaped primary  $\alpha$  phases and surrounding  $\alpha+\eta$  phase structure as in standard

ZA 27 alloys. After the heat treatment in the structure, the  $\epsilon$  phases remain intact.

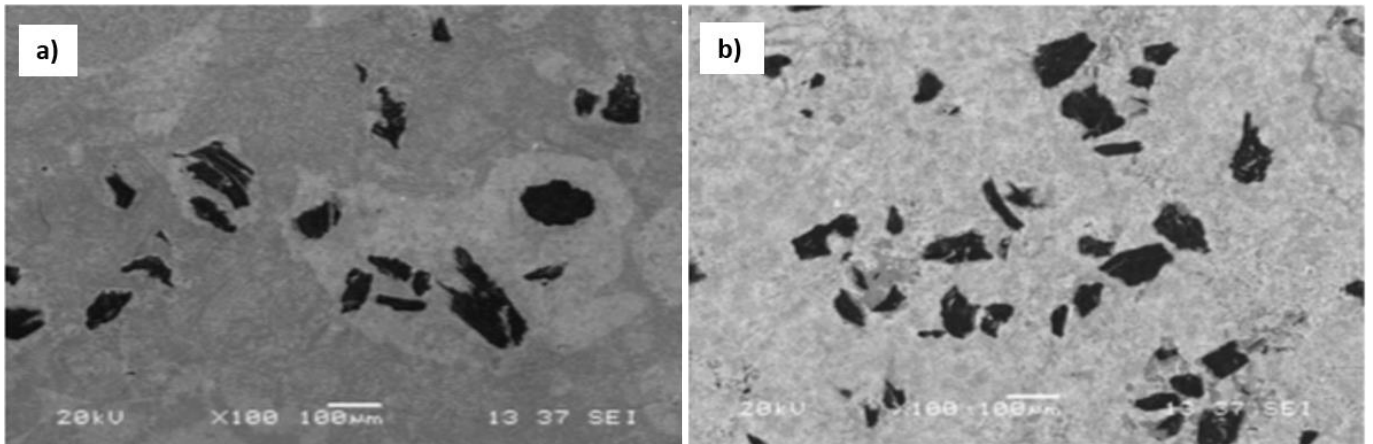


Figure 15 SEM structure of 2.5% by weight graphite reinforced composite material (GRC) a) casting state b) heat treated state

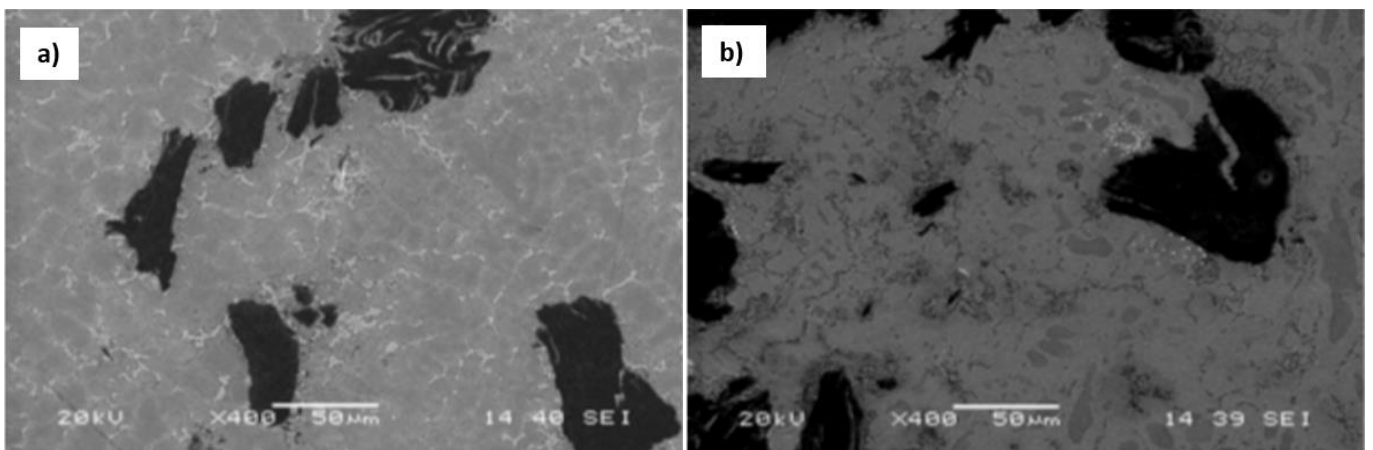


Figure 16 SEM structure of 5% graphite by weight reinforced composite material (GRC): a) Casting state, b) Heat treated state

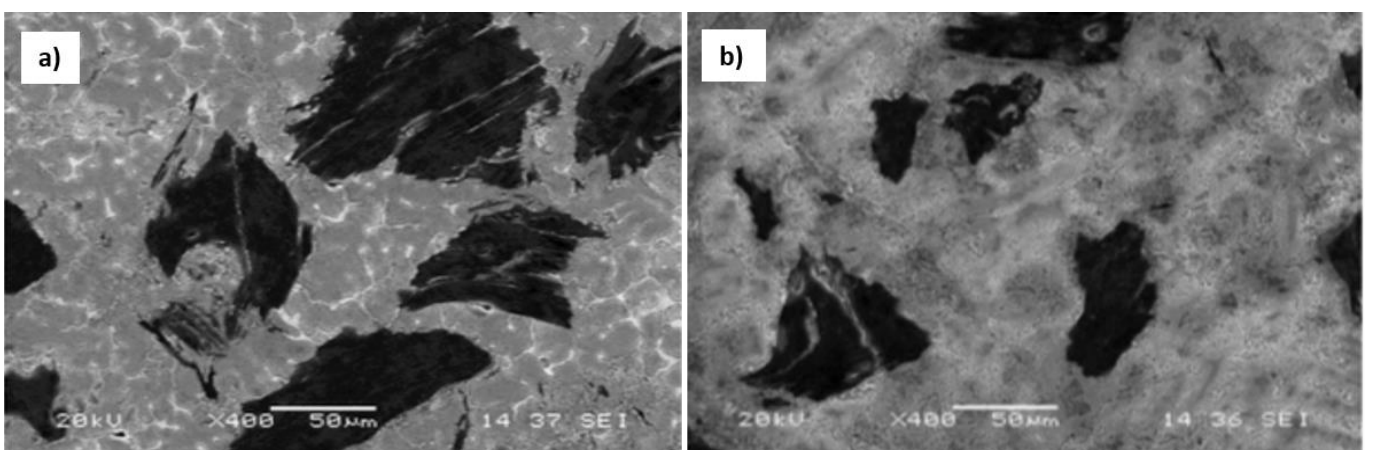


Figure 17 SEM structure of 7.5% Graphite by weight reinforced composite material (GRC): a) casting state b) heat treatment state

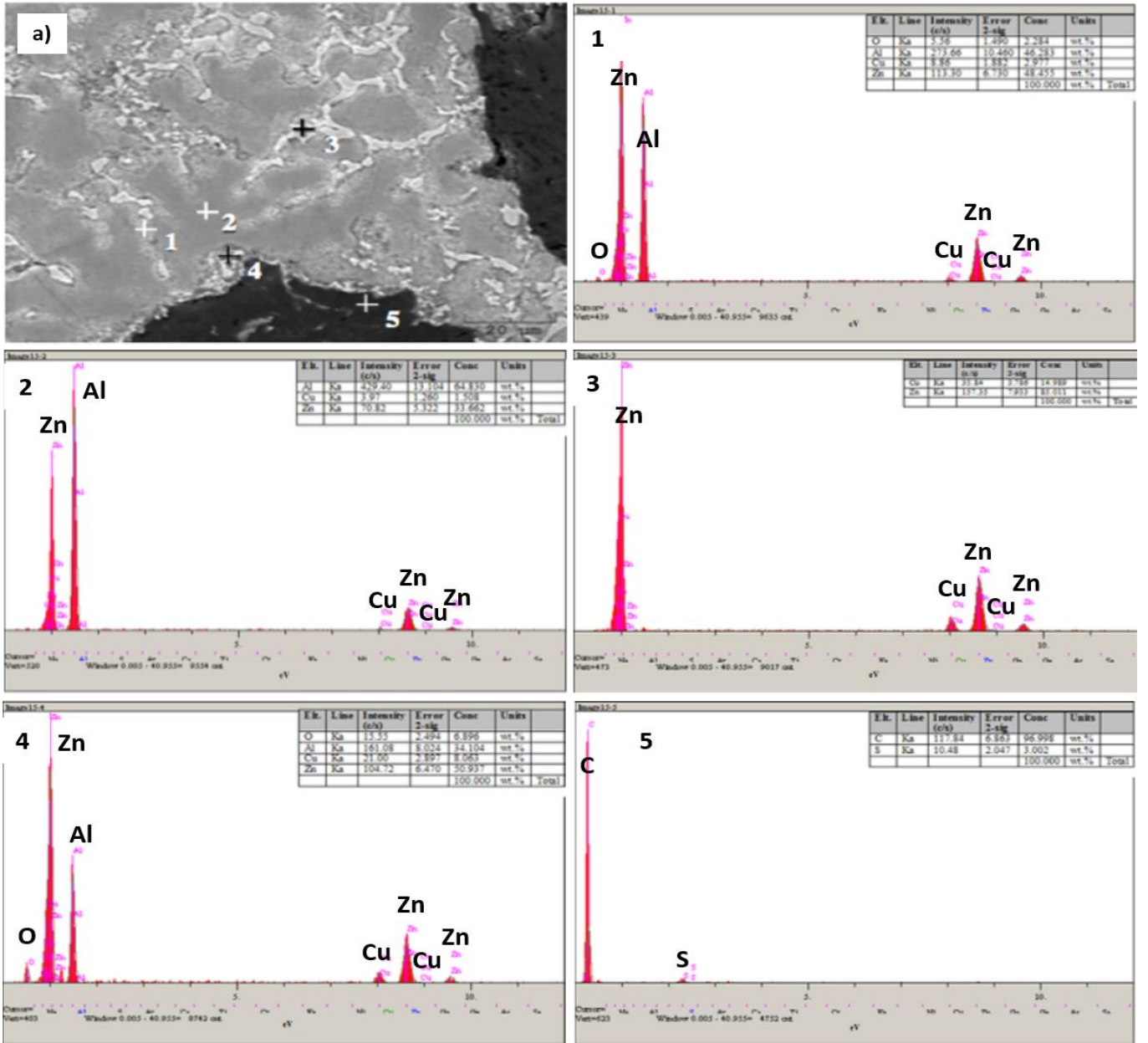


Figure 18 SEM structure of 10% graphite by weight reinforced composite material (GRC) a-b) cast state, 4-5) EDS analysis

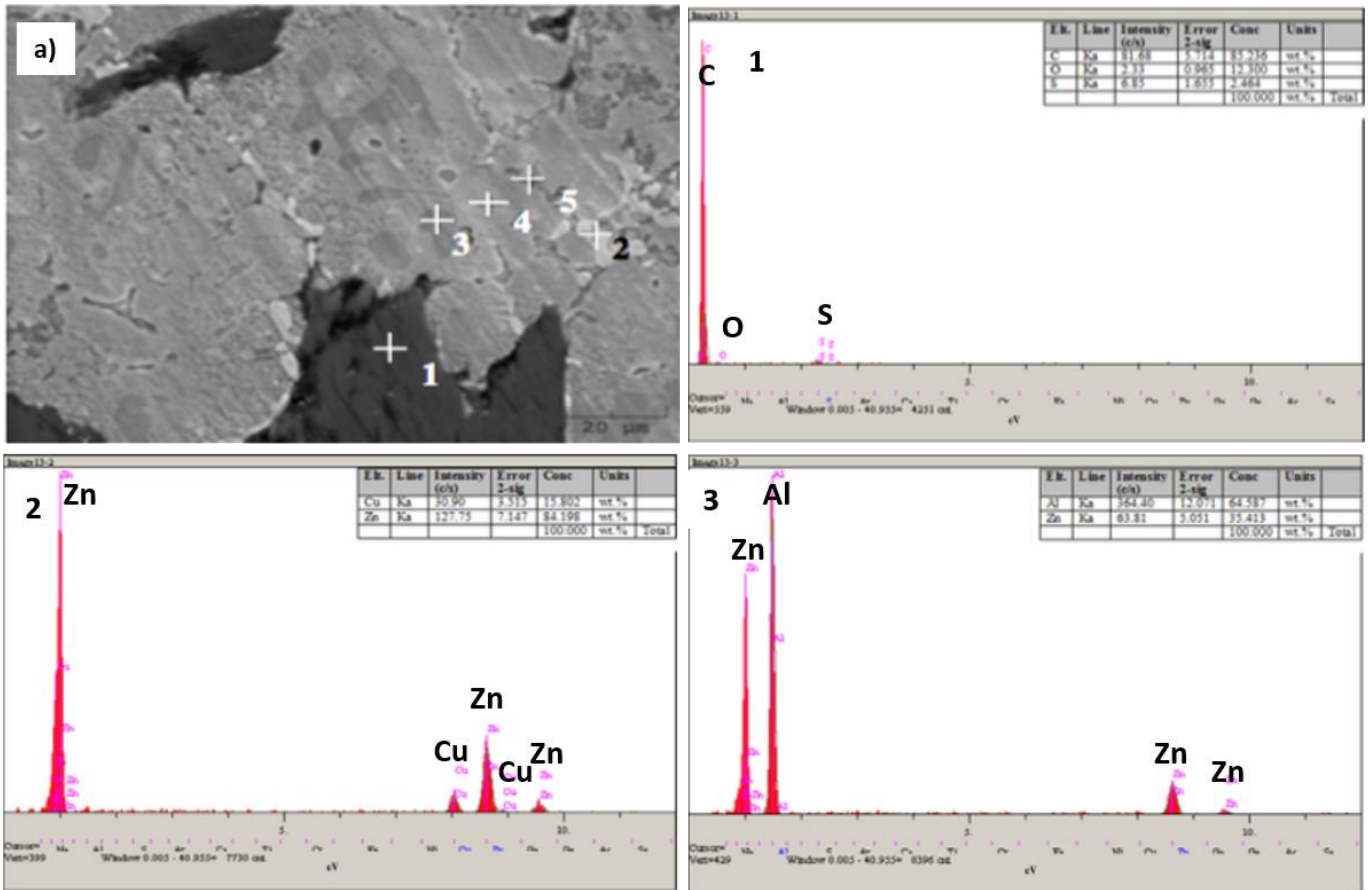


Figure 19 SEM structure of 10% graphite by weight reinforced material (GRC) b) heat treated state 1-3) EDS analysis

Electron microscope images and EDS analyzes of hybrid composite materials (HCM) containing 10% SiC and 2.5-5-7.5-10% graphite, respectively, are given in Figure 20-24. The matrix shows the same properties as in the ZA 27 alloy, SRC and GRC. When the HCM structures are examined, it is seen that the graphite and SiC particles are homogeneously dispersed in the matrix and the matrix and particle interface is very good. Hibrit kompozit malzemelere ilave edilen grafitler aynen As with GRC composites, it is very well wetted by the matrix. The images that prove this are the matrix phase infiltrating the

graphite in Figure 21 and 22. The high strength bearing feature of the SiC reinforcement phase in the hybrid composites has preserved its physical stability during the vortex method and compression casting production. When both SRC and HCM are examined, it is seen that most of the SiC particles remain in the matrix without deformation. However, it was determined that very little SiC and graphite were fragmented during the production of the composite by vortex and during the production by high pressure compression casting method.

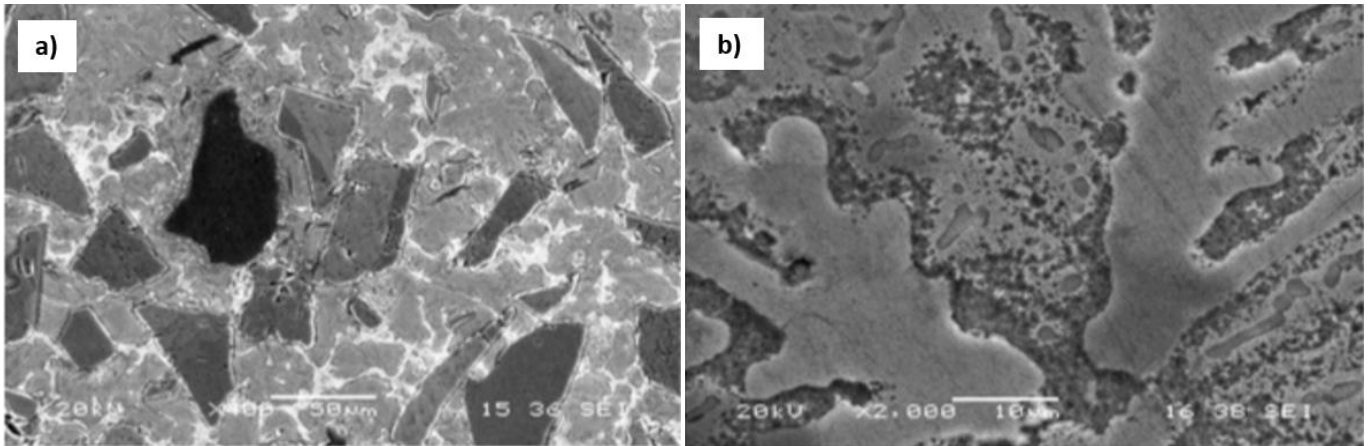


Figure 20 SEM structure of 10% SiC and 2.5% graphite by weight reinforced hybrid composite material (HCM) a) casting state b) heat treated state

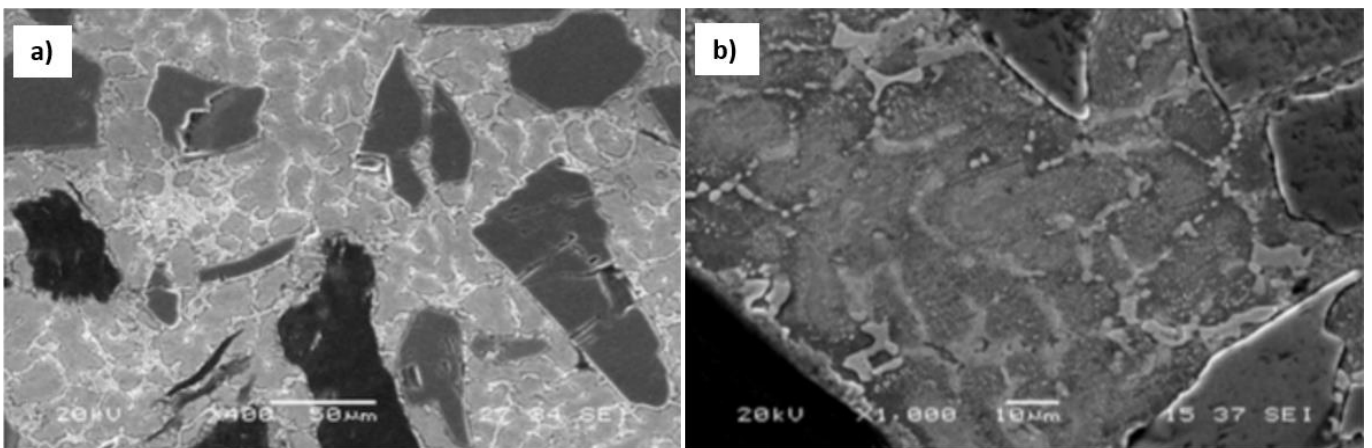


Figure 21 SEM microstructure of 10%SiC and 5% graphite by weight reinforced hybrid composite material (HCM) a) casting state b) heat treated state

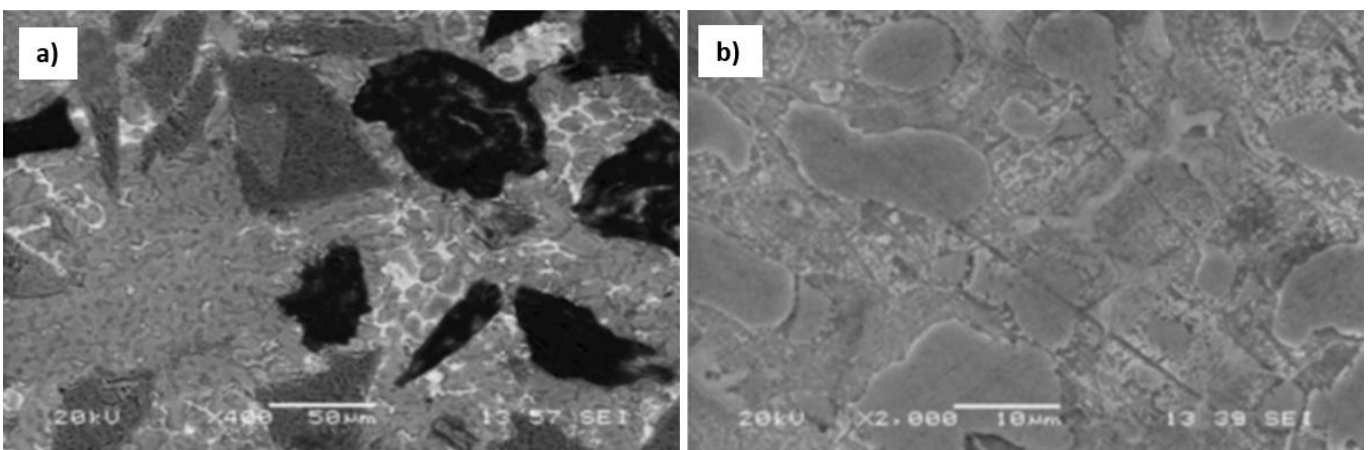


Figure 22 SEM structure of 10% SiC and 7.5 % graphite by weight reinforced hybrid composite material (HCM) a) casting b) heat treated state

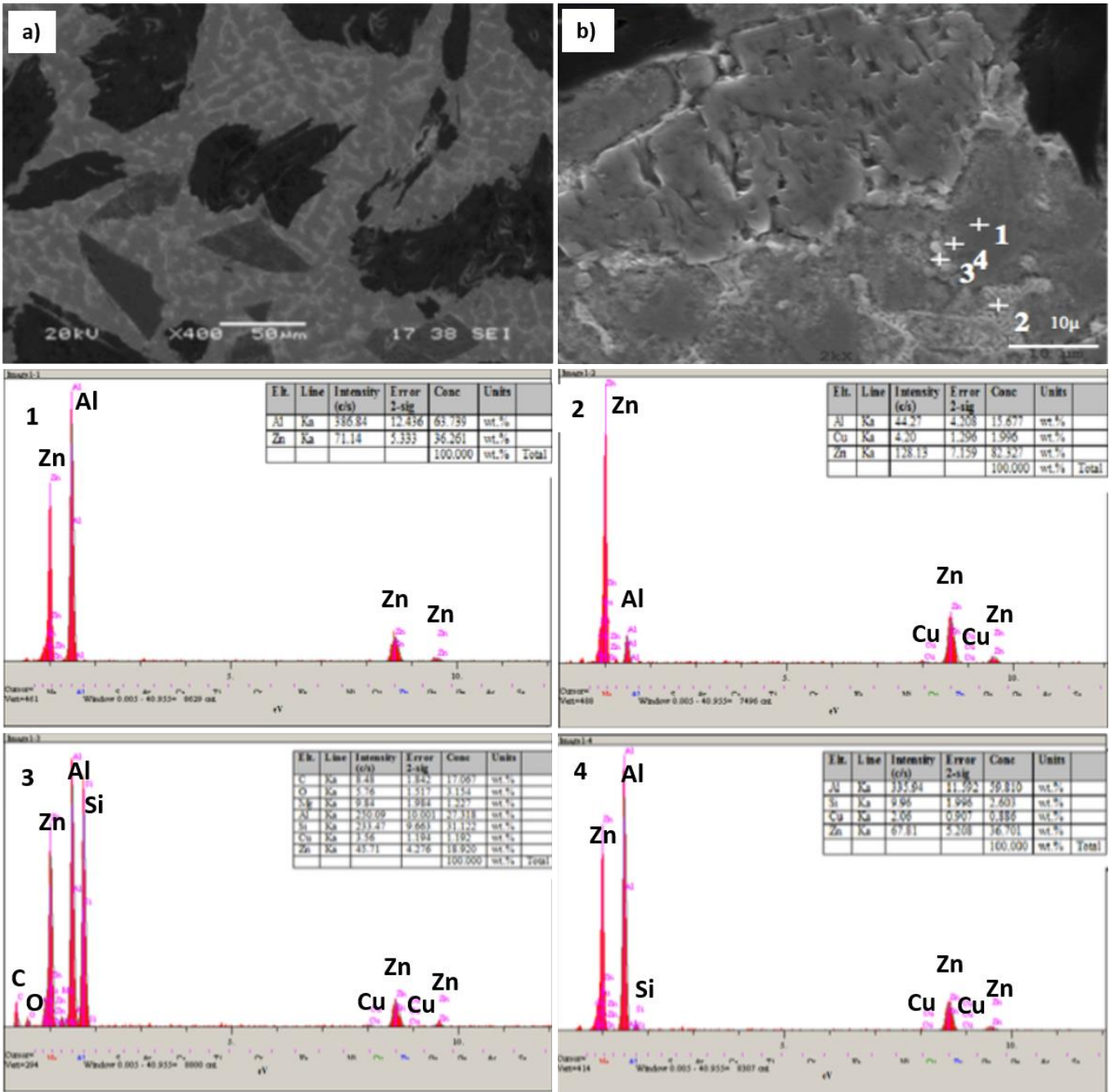


Figure 23 SEM microstructure of a-b) cast hybrid composite material containing 10%SiC and 10% graphite by weight 1-4) EDS analysis

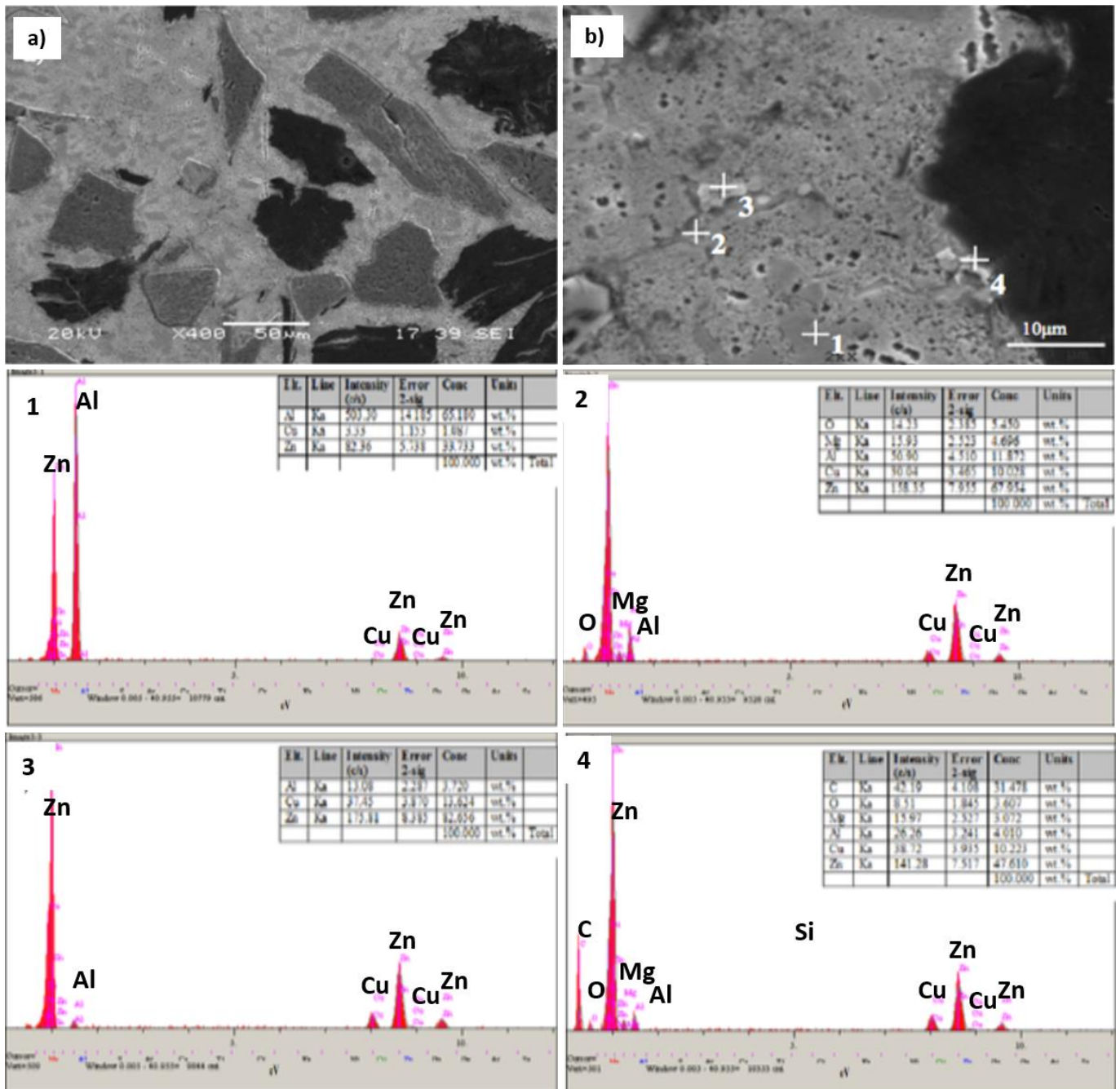


Figure 24 SEM microstructure of the hybrid composite material (HCM) a-b) heat treated state containing 10%SiC and 10% graphite by weight 1-4) EDS analyzes

#### 4. CONCLUSION

1- The ZA-27 metal matrix alloy and hybrid composite materials with an addition of SiC and graphite particles produced by the vortex method and casted by the compression casting method which allows reinforcements generally homogeneously distributed in the matrix. In the optical investigation, it was determined that very little particle segregation occurred in 2.5%

graphite reinforced composite (GRC), and this segregation disappeared with an increase in graphite addition.

2- SiC and graphite particles added to the 2-ZA-27 alloy which had a heterogeneous nucleating effect during solidification.

3- Thin dendrites tend to become a spheroid shape after heat treatment.

3-Thin dendrites tend to spheroid after heat treatment.

### **Acknowledgments**

We would like to thank Prof. Dr. Hatem Akbulut and Assoc. Prof. Dr.. Mehmet Uysal for providing laboratory facilities.

### **Funding**

The author (s) has no received any financial support for the research, authorship or publication of this study.

### **The Declaration of Conflict of Interest/ Common Interest**

No conflict of interest or common interest has been declared by the authors.

### **Authors' Contribution**

The first author contributed 80%, the second author 20%.

### **The Declaration of Ethics Committee Approval**

This study does not require ethics committee permission or any special permission.

### **The Declaration of Research and Publication Ethics**

The authors of the paper declare that they comply with the scientific, ethical and quotation rules of SAUJS in all processes of the paper and that they do not make any falsification on the data collected. In addition, they declare that Sakarya University Journal of Science and its editorial board have no responsibility for any ethical violations that may be encountered, and that this study has not been evaluated in any academic publication environment other than Sakarya University Journal of Science.

## **REFERENCES**

[1] Demirkesen, E., Kompozit Malzemeler, İTÜ Kimya Fakültesi, 1.Baskı s.1-5, 1991.

- [2] S.S. Owoeye, D.O. Folorunso, B. Oji, S.G. Borisade, “Zinc-Aluminum (ZA-27)-based metal matrix composites: a review article of synthesis, reinforcement, microstructural, mechanical, and corrosion characteristics,” *Int. J. Adv. Manuf. Technol.* 100 (2019) 373–380. <https://doi.org/10.1007/s00170-018-2760-9>
- [3] S. S. Owoeye, D. O. Folorunso, B. Oji, and S. G. Borisade, “Zinc-aluminum (ZA-27)-based metal matrix composites: a review article of synthesis, reinforcement, microstructural, mechanical, and corrosion characteristics,” *Int. J. Adv. Manuf. Technol.*, vol. 100, no. 1–4, pp. 373–380, 2019, doi: 10.1007/s00170-018-2760-9
- [4] S. Sastry, M. Krishna, and J. Uchil, “Study on damping behaviour of aluminite particulate reinforced ZA-27 alloy metal matrix composites,” *J. Alloys Compd.*, vol. 314, no. 1–2, pp. 268–274, 2001, doi: 10.1016/S0925-8388(00)01235-4
- [5] R. Arıkan, “Saffil ( $\eta$ -Al<sub>2</sub>O<sub>3</sub>) fiber takviyeli ZA-12 alaşımın sürtünme aşınma davranışları,” *J. Fac. Eng. Archit. Gazi Univ.*, vol. 22, no. 3, pp. 359–368, 2007
- [6] M. Gelfi, E. Bontempi, A. Pola, R. Roberti, D. Rollez, and L. E. Depero, “Microstructural and mechanical properties of zinc die casting alloys,” *Adv. Eng. Mater.*, vol. 6, no. 10, pp. 818–822, 2004, doi: 10.1002/adem.200400087
- [7] M.R. Monteiro, A.R.P. Ambrozın, A.O. Santos, P.P. Contri, S.E. Kuri, “Evaluation of Metallic Corrosion Caused by Alcohol Fuel and Some Contaminants,” *Materials Science Forum*, Vol 636 – 637, 1024-1029, 2010
- [8] A. Pola, R. Roberti, L. Montesano, ‘New Zinc alloys for semisolid applications’, *International Journal of Material Forming*, 2010, Volume 3, Supplement 1, 743-746.

- [9] Alüminyum Hibrit Kompozit Malzemelerin Aşınma Davranışlarının İncelenmesi, Doktora Tezi, Sakarya Üniversitesi Fen Bilimleri Enstitüsü, 2004.
- [10] S. C. Sharma, B. M. Girish, R. Kamath, and B. M. Satish, “Effect of SiC particle reinforcement on the unlubricated sliding wear behaviour of ZA-27 alloy composites,” *Wear*, vol. 213, no. 1–2, pp. 33–40, 1997, doi: 10.1016/S0043-1648(97)00185-3.
- [11] Sharma, S., C., Sastryb, S., Krishna, M., Effect of Aging Parameters on the Micro Structure and Properties of ZA-27/ Aluminite Metal Matrix Composites, *Journal of Alloys and Compounds* 346, 292– 301, 2002.
- [12] Miroslav, B., Vencl, A., Mitrovic, S.; Bobic, I., “Influence of T4 Heat Treatment on Tribological Behavior of Za27 Alloy Under Lubricated Sliding Condition,” *Tribol Lett*, 36:125–134, 2009
- [13] Metallography and Microstructures of Zinc and Its Alloys, *Metallography and Microstructures*, Vol 9, ASM Handbook, ASM International, ,p. 933– 941, 2004.
- [14] Jovanovic, M. T., Bobić, I., Djurcic, B. Grahovac, N., “Microstructural and Sliding Wear Behaviour of a Heat-Treated Zinc-Based Alloy”, *Tribology Letters*, Volume 25, Number 3, 173-184, 2007.
- [15] Pürçek, G., “Çinko-Alüminyum Esaslı Alaşımlardan Üretilen Kaymalı Yatakların Tribolojik Özelliklerinin incelenmesi”, Yüksek Lisans Tezi, Karadeniz Teknik Üniversitesi, 1994.
- [16] Akbulut, H., Altunpak, Y., “Alümina Kısa Fiber Takviyeli Al Esaslı LM 13 Alaşımında Yaşlandırma Isıl İşlem Özellikleri Optimizasyonu,” *Teknoloji*, Cilt 8, Sayı 4, 331-339, 2005.
- [17] Durman, M., Murphy, S., “An electron metallographic study of pressure die-cast commercial zinc–aluminum-based alloy ZA27,” *Journal of Materials Science*, 32, 1603-1611.



SAKARYA ÜNİVERSİTESİ

# FEN BİLİMLERİ ENSTİTÜSÜ DERGİSİ

Sakarya University Journal of Science  
SAUJS

e-ISSN: 2147-835X | Founded: 1997 | Period: Bimonthly | Publisher: Sakarya University |  
<http://www.saujs.sakarya.edu.tr/en/>

Title: Development of a Fluorescent Protein Based FRET Biosensor for Determination of Protease Activity

Authors: İbrahim İNCİR, Özlem KAPLAN, Sema BİLGİN, İsa GÖKÇE

Received: 2021-07-02 00:00:00

Accepted: 2021-09-29 00:00:00

Article Type: Research Article

Volume: 25

Issue: 5

Month: October

Year: 2021

Pages: 1235-1244

How to cite

İbrahim İNCİR, Özlem KAPLAN, Sema BİLGİN, İsa GÖKÇE; (2021), Development of a Fluorescent Protein Based FRET Biosensor for Determination of Protease Activity.

Sakarya University Journal of Science, 25(5), 1235-1244, DOI:

<https://doi.org/10.16984/saufenbilder.961026>

Access link

<http://www.saujs.sakarya.edu.tr/tr/pub/issue/65589/961026>

New submission to SAUJS

<http://dergipark.org.tr/en/journal/1115/submission/step/manuscript/new>

## Development of a Fluorescent Protein Based FRET Biosensor for Determination of Protease Activity

İbrahim İNCİR<sup>1</sup>, Özlem KAPLAN<sup>2</sup>, Sema BİLGİN<sup>3</sup>, İsa GÖKÇE\*<sup>4</sup>

### Abstract

Proteases are closely associated with many pathological conditions. Efficient detection of protease activity may be useful for diagnosis, prognosis, and the development of new therapeutic biomolecules. Fluorescent Resonance Energy Transfer (FRET) is defined as the non-radioactive energy transfer that occurs between two fluorophores. Fluorescent proteins are widely used in FRET biosensors because they can be genetically encoded and compatible with cells. Fluorescent Protein based FRET (FP-FRET) biosensors are used to monitor biological processes such as enzyme activity, intracellular ion concentration, conformational changes, protein-protein interactions. In this study, it was aimed to detect protease activity using an FP-FRET biosensor and TEV protease was chosen as a model enzyme. The plasmid encoding the mNeonGreen-TEV-mRuby3 fluorescent protein-based FRET biosensor was constructed. The gene of the designed FP-FRET biosensor was expressed in *Escherichia coli* DH5 $\alpha$  cells using recombinant DNA techniques and purified using Ni-NTA affinity chromatography. As a result, the activity of the TEV protease enzyme was determined by emission measurements performed in the spectrofluorometer using the produced FP-FRET biosensor. The usability of the designed FP-FRET biosensor in the determination of protease enzyme activity was demonstrated.

**Keywords:** Recombinant DNA Technology, Fluorescent Proteins, Fluorescent Resonance Energy Transfer (FRET), Biosensor, *E. coli*

\* Corresponding author: isa\_gokce@yahoo.co.uk

<sup>1</sup> Tokat Gaziosmanpaşa University, Tokat-Turkey, Faculty of Engineering and Natural Sciences / Department of Bioengineering. Karamanoğlu Mehmetbey University, Karaman-Turkey, Kazım Karabekir Vocational School, Department of Medical Services and Techniques / Environmental Health Program  
E-Mail: ibrahimincir@kmu.edu.tr

ORCID: <https://orcid.org/0000-0003-4599-6908>

<sup>2</sup> Istanbul University, Faculty of Science, Molecular Biology and Department of Genetic  
E-Mail: ozlem.kaplan@istanbul.edu.tr

ORCID: <https://orcid.org/0000-0002-3052-4556>

<sup>3</sup> Tokat Gaziosmanpaşa University, Tokat-Turkey, Tokat Vocational School of Health Services / Department of Medical Services and Techniques.

E-Mail: sema.bilgin@gop.edu.tr

ORCID: <https://orcid.org/0000-0001-5921-5434>

<sup>4</sup> Tokat Gaziosmanpaşa University, Tokat-Turkey, Faculty of Engineering and Natural Sciences / Department of Bioengineering.

ORCID: <https://orcid.org/0000-0002-5023-9947>

## 1. INTRODUCTION

Proteases have an important role in various biological processes such as cell proliferation, digestion and differentiation. Protease activity may be abnormal in pathological conditions such as cancer, neurodegenerative disorders, arthritis, allergies and infections [1]. New and improved protease detection systems may have a fundamental role in the diagnosis of these diseases and drug development.

Förster or fluorescent resonance energy transfer (FRET), first described by Theodor Förster in 1946; It is a mechanism by which a donor fluorophore in its excited state transfers its energy to an adjacent acceptor fluorophore, causing the acceptor to emit characteristic fluorescent light [2]. For energy transfer between fluorophores, the emission spectrum of the donor molecule and the absorption spectrum of the acceptor molecule must overlap [3]. Three main types of fluorophores are used in FRET biosensors: small organic dyes, fluorescent proteins, and quantum dots. Unlike organic dyes and quantum dots, fluorescent proteins are widely used because they can be genetically encoded and compatible with cells. Biosensor systems created using the FRET technique have occupied an important place in biotechnology and biological studies [4, 5]. These genetically encoded biosensors can be transferred to cells, tissues or the whole organism by transfection of plasmid DNA. The biggest advantage of such a biosensor approach is that it is a non-invasive method and does not damage cells. Fluorescent proteins are in most cases non-toxic to host cells and can remain stable in cells for a long time thanks to their high intracellular stability [2, 6]. In this context, fluorescent proteins and FRET-based biosensors have become powerful tools for *in vitro* and *in vivo* applications [6–8]. In FP-FRET sensors, the selection of the FRET pair (donor and acceptor fluorophores) is the most important parameter for the performance of the biosensors to be designed [9]. The diversity of FPs with improved optical properties has made it possible to select FRET pairs with high FRET efficiency and to develop high-sensitivity FRET biosensors [2]. The color

variety of monomeric FPs covers almost the entire visible spectrum, from violet to far red [10].

Shaner et al. obtained a tetrameric yellow fluorescent protein from *Branchiostoma lanceolatum* and later developed a monomeric protein called mNeonGreen, which is more photostable and has significant advantages in terms of rapid maturation. [11]. The mNeonGreen protein (26.6 kDa) has excitation wavelengths at 506 nm and emission wavelengths at 517 nm [11]. mNeonGreen is widely used to investigate biological processes in various organisms including bacterial and eukaryotic cells [12].

The brighter mRuby protein was developed as a result of continuous and intense optimization of the wild-type red fluorescent protein called EqFP611 (derived from *Entacmaea quadricolor*) [13]. Good performance in most fusion structures and resistance to acidic environments makes mRuby useful for many cell biology applications. mRuby has evolved into an effective fluorescent protein for imaging of mammalian cells, flow cytometry analyzers and FACS [14]. Studies in mammalian cells have shown that mRuby3 is the brightest and most photostable monomeric red fluorescent protein known and functions as an efficient FRET acceptor. The mRuby3 protein (26.6 kDa) has excitation and emission at 558 and 592 nm, respectively [15]. Bajar et al. showed that the mNeonGreen-mRuby3 pair is one of the best choices in terms of photostability, brightness and FRET dynamic range when used in cultured cells [2].

In this study, mNeonGreen-TEV-mRuby3 plasmid was designed as a model to determine TEV protease activity. These fluorescent proteins were linked by a 17 amino acids sequence (GGSLEENLYFQGEFSGG) that also contained the TEV protease recognition site. Expression of the designed FP-FRET biosensor was carried out in *E. coli* DH5 $\alpha$  cells. Using the produced FP-FRET biosensor, the activity of TEV protease enzyme was determined spectrofluorometrically. With this study, the usability of the produced recombinant mNeonGreen-mRuby3 FRET pair in the determination of protease activity has been clearly demonstrated.

## 2. MATERIALS AND METHODS

### 2.1. Plasmid design

The DNA sequence for the mNeonGreen protein was obtained from NCBI (KC295282.1). Then, the DNA sequence was codon optimization for *E. coli* K12 organism using JCat codon optimization program (<http://www.jcat.de/>). The DNA sequence of the mRuby3 protein was obtained from the Addgene database (plasmid catalog number: 74234). The DNA sequence of the

biosensor was designed as 5'-mNeonGreen-TEV protease recognition sequence-mRuby3-3' (mNG-TEV-mRuby3). The histidine tag (6x-His) and the stop codon were added to the 3' end of the mRuby3 DNA sequence, respectively. In addition, codons of serine and glycine amino acids were added to both sides of the TEV cleavage site for optimization of linker length, its flexibility and stabilization (Figure 1). The designed DNA sequence of FRET pair was purchased from Biomatik as cloned into the pET-30a vector.

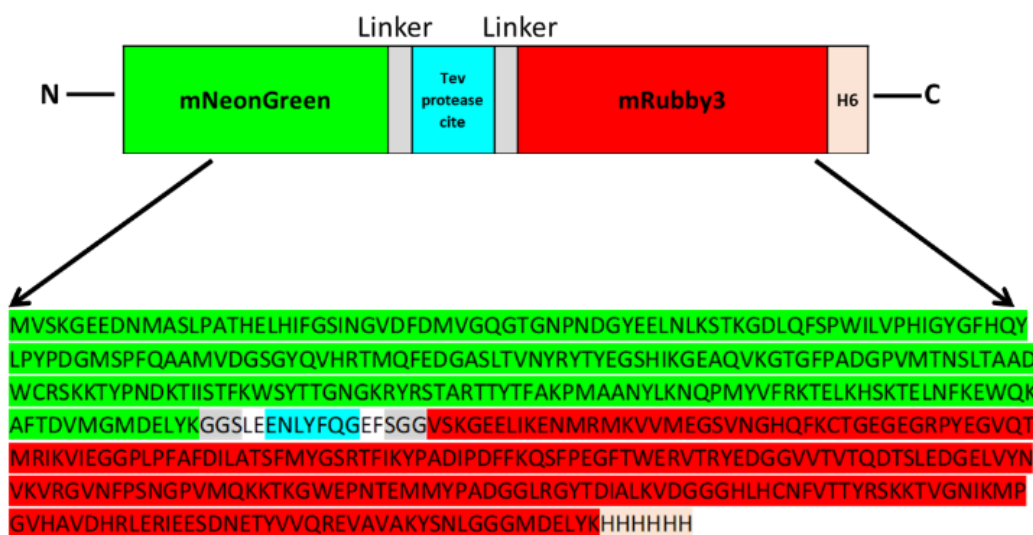


Figure 1 Modular organization and amino acid sequence of the mNG-TEV-mRuby3 protein

### 2.2. Expression and partial purification of recombinant proteins

The mNG-TEV-mRuby3 protein pair was expressed in *E. coli* DH5 $\alpha$  cells. The plasmid mNG-TEV-mRuby3 was used for transformation of *E. coli* DH5 $\alpha$  cells by heat shock. The cells were spread on LB agar medium containing 50  $\mu$ g/ml kanamycin. A single colony was taken and 4 ml of inoculated LB broth (containing 50  $\mu$ g/ml kanamycin) was grown overnight. The overnight culture was transferred into 600 ml of LB medium containing 50  $\mu$ g/ml kanamycin and was then incubated at 37  $^{\circ}$ C at 240 rpm for 20 hours. The cells were collected by centrifugation at 8 000 rpm for 10 minutes and suspended by adding lysis buffer (25 mM Tris-HCl and 300 mM NaCl and pH: 7.8). After the addition of lysozyme enzyme (1 mg/ml), PMSF (0.1 mM), and benzamidine

(0.1 mM), the cells were lysed with the help of a sonicator. The cell lysate was centrifuged at 30 000 rpm for 1 hour. The mNG-TEV-mRuby3 fusion protein was purified using Ni-NTA column. 12.5 mg of the mNG-TEV-mRuby3 fusion protein was obtained from 1 L of bacterial culture.

Wash buffer (10 mM imidazole, 25 mM Tris-HCl and 300 mM NaCl and pH: 7.8) and elution buffer (300 mM imidazole, 25 mM Tris-HCl and 300 mM NaCl and pH: 7.8) were used in the purification step. Samples taken at certain steps and purified protein were analyzed in 10% SDS-PAGE.

TEV protease protein was expressed in *E. coli* BL21 pLysE cells. The production and purification processes of TEV protease enzyme were carried out similar to the protocol detailed in

our previous studies [16, 17]. In summary, plasmid encoding TEV protease protein (pRK793) was used for transformation of *E. coli* BL21 pLysE cells by heat shock. These cells were grown in LB medium containing 100 µg/mL ampicillin and 34 µg/mL chloramphenicol. The cells were lysed with a sonicator and protein partial purification from lysate was performed by nickel affinity chromatography.

### 2.3. Analysis of TEV protease enzyme activity

Purified the mNG-TEV-mRuby3 fusion protein and TEV protease were dialyzed against 1x TEV protease buffer (25 mM Tris-HCl and 150 mM NaCl and pH:8). Then, mNG-TEV-mRuby3 fusion protein (6 mg/ml) was incubated with TEV protease enzyme (3.5 mg/ml) at 30 °C for 3 hours as indicated in Table 1.

Table 1 Cleavage of the mNG-TEV-mRuby3 with TEV protease enzyme (A: 1x TEV protease buffer without mercaptoethanol, B: 1x TEV protease buffer containing β-mercaptoethanol)

	1	2	3	4	5	6
<b>TEV protease enzyme</b>	-	50 µl	65 µl	-	25 µl	25 µl
<b>1x TEV buffer</b>	165 µl A	150 µl A	100 µl A	140 µl A	140 µl A	140 µl B

				+ 25 µl B		
<b>mNG-TEV-mRuby3 protein</b>	35 µl	-	35 µl	35 µl	35 µl	35 µl

After the protease cleavage process was completed, the color change in the microtubes was observed. Samples of TEV protease cleavage products were analyzed in SDS-PAGE. The emission wavelengths of the reaction mixtures obtained after incubation of the mNG-TEV-mRuby3 FRET sensor with the TEV enzyme were recorded in a spectrofluorometer (Jasco FP-8300) at 37 °C. TEV protease cleavage products were excited at 506 nm (5 nm bandwidth) and emission wavelengths between 510-700 nm were shown.

The experimental steps of this study are summarized in Figure 2.

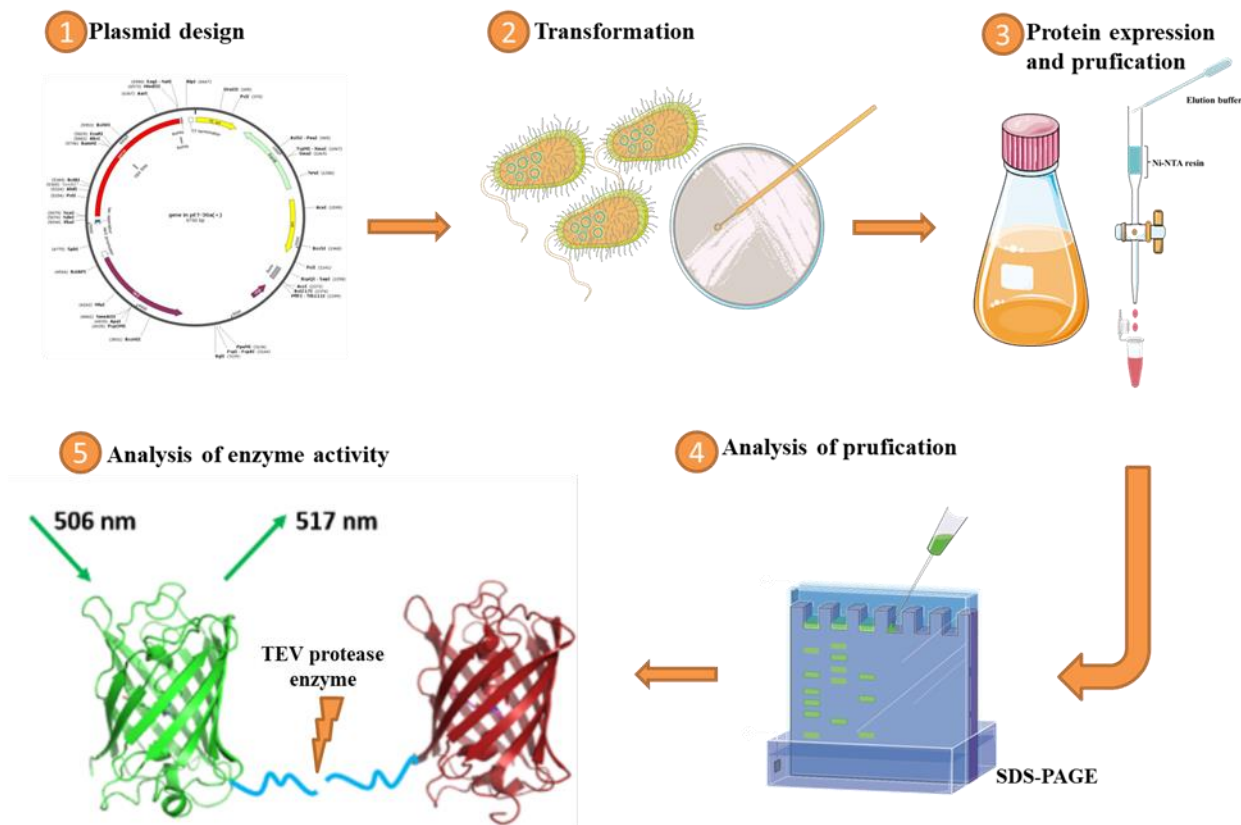


Figure 2 A summary of the experimental steps used in the development of a fluorescent protein-based FRET biosensor for determination of protease activity

### 3. RESULTS AND DISCUSSION

#### 3.1. Expression and partial purification of the mNG-TEV-mRuby3 FRET sensor

The mNG-TEV-mRuby3 fusion protein was produced in *E. coli* DH5 $\alpha$  cells and purified by nickel affinity chromatography. Samples taken during production and partial purification were analyzed in SDS-PAGE. As expected, the 55 kDa mNG-TEV-mRuby3 fusion protein was obtained (Figure 3).

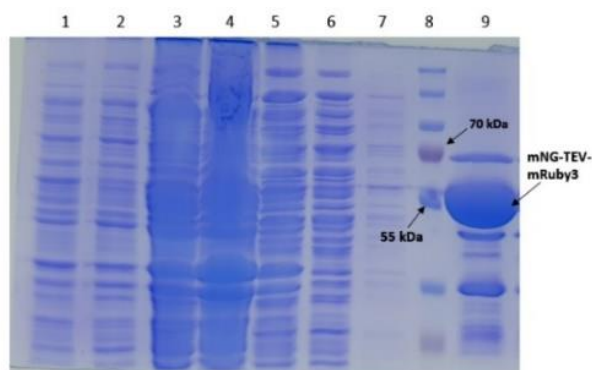


Figure 3 Analysis of the production and partial purification of the mNG-TEV-mRuby3 FRET pair in SDS-PAGE. Lanes 1 and 2 are cell culture samples 2 hours and 4 hours after cell inoculation, respectively. Lane 3, sample of pellet after sonicator. Lanes 4 and 5 sample pellet and supernatant after ultracentrifugation, respectively. Lane 6, flowing filtrate after passing the supernatant through the column. Lane 7, sample obtained by passing wash buffer through the column. Lane 8, protein marker (Thermo Scientific Prestained). Lane 9, sample obtained by passing elution buffer through the column.

#### 3.2. Analysis of TEV protease activity with the mNG-TEV-mRuby3 FRET sensor

The mNG-TEV-mRuby3 FRET sensor was incubated with the TEV protease enzyme in the amounts given in Table 1. When the TEV protease cleavage site in the mNG-TEV-mRuby3 FRET sensor is cleaved by the TEV protease enzyme, it is expected to cause a color and emission change in this FP-FRET biosensor. In addition, a reaction was prepared to examine

whether  $\beta$ -Mercaptoethanol in the TEV protease buffer has an effect on the color change in the mNG-TEV-mRuby3 FRET sensor (example number 4 in Table 1). No direct effect of  $\beta$ -Mercaptoethanol on color change was observed. As expected, the color change in the FP-FRET sensor occurred after the related region was cleaved by the TEV enzyme (Figure 3B). After cleavage with TEV protease, the reaction mixture was analyzed by 10% SDS-PAGE. As indicated in Table 1, where the protease degradation reaction components are shown, there was only

the mNG-TEV-mRuby3 FRET pair (approximately 55 kDa) in lanes 1 and 4. In lane 2, only TEV protease enzyme with a molecular weight of approximately 27 kDa was observed. In lanes 3, 5 and 6, as a result of cleavage of the mNG-TEV-mRuby3 FRET pair (55 kDa) with TEV protease added to the microtubes, mNeonGreen (28 kDa) and mRuby3 (27 kDa) fragments were obtained (Figure 4A).

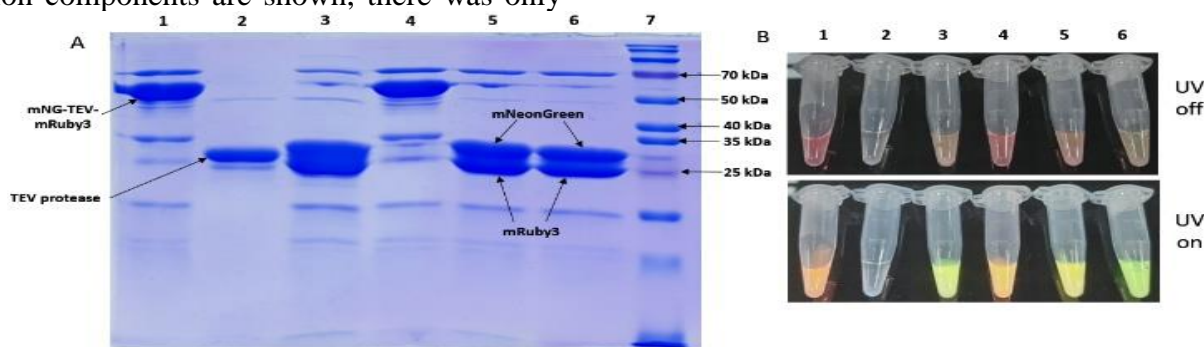


Figure 4 A. Analysis of mNG-TEV-mRuby3 FRET sensor cleavage by TEV protease enzyme in SDS-PAGE. Lanes 1 and 4 contain only FP-FRET biosensor, lane 2 contains only TEV protease enzyme. Lanes 3, 5 and 6 are the products of the FP-FRET biosensor after cleavage with TEV protease. Lane 7, Protein marker (Bio Basic Prestained). B. Image under UV light after mNG-TEV-mRuby3 FRET sensor cleavage by TEV protease enzyme after applying the protocols given in Table 1.

After the mNG-TEV-mRuby3 FRET sensor was cleaved with the TEV enzyme, measurements of emission wavelengths were carried out in the spectrofluorometer. In reactions without TEV protease enzyme, the TEV protease binding site between the mNG-TEV-mRuby3 FRET pair was preserved. As shown in Figure 5, the mNG-TEV-mRuby3 FRET sensor excited at 506 nm wavelength peaks at two wavelengths, 517 nm and 572 nm. The peak at 517 nm is the emission wavelength of the mNeonGreen fluorescent protein. Then, the excited mNeonGreen uses some of its energy as emission energy and transfers the rest to the mRuby3 fluorescent protein, causing the mRuby3 protein to be excited. In this way, the induced mRuby3 fluorescent protein emits at a wavelength of 572 nm (Figure 5A).

In reactions involving the TEV protease enzyme, the connection between the mNG-TEV-mRuby3 FRET pair was cleaved, resulting in two separate fluorescent proteins, mNeonGreen and mRuby3. This indicates that direct resonance energy transfer between the two fluorescent proteins will not occur. In other words, it was observed that resonance energy transfer did not occur by emitting at 517 nm wavelength as a result of excitation of the mNG-TEV-mRuby3 FRET sensor at 506 nm wavelength. In summary, if resonance energy transfer had occurred, a significant peak at 572 nm would be expected. In addition, a weak peak at 572 nm is seen in the graph. This situation can be evaluated as some mNG-TEV-mRuby3 FRET sensors in the reaction tube not cutting with the TEV enzyme or the cutting process is not completed (Figure 5B).

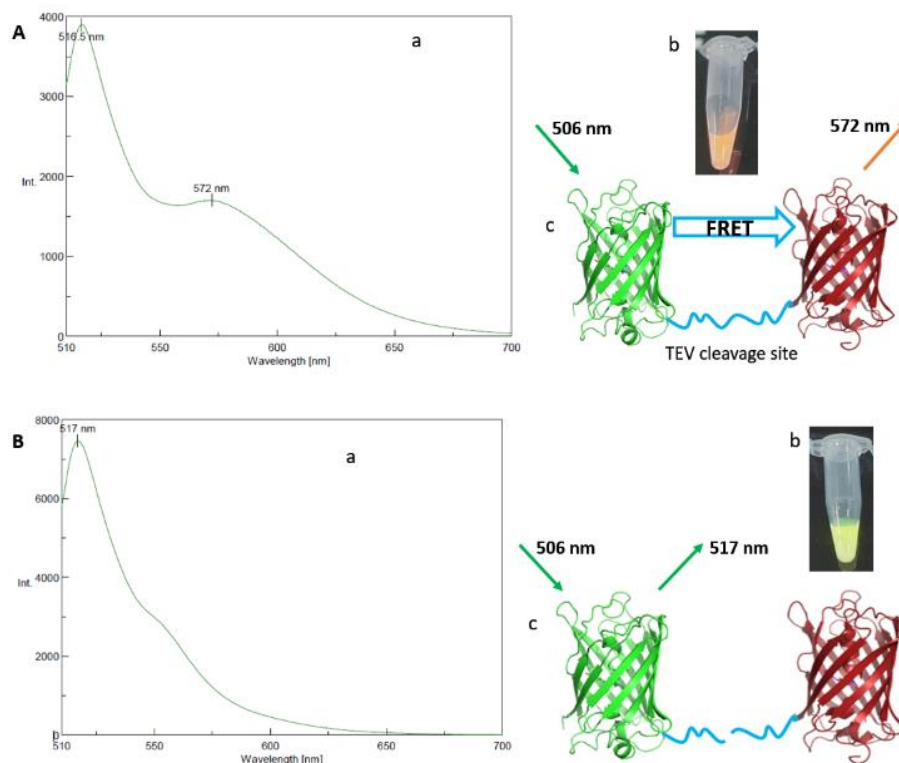


Figure 5 A. Images of the produced mNG-TEV-mRuby3 FRET sensor. Emission wavelength graph of the produced FP-FRET sensor (a), image of the FP-FRET sensor under UV light (b), schematized version of biosensor (c). B. Images of the mNG-TEV-mRuby3 FRET sensor after the TEV protease activity. Emission wavelength graph of the FP-FRET sensor after protease activity (a), image of the biosensor under UV light after the TEV protease activity (b), schematized version after the TEV protease activity (c).

In all FRET biosensors, the selection of the optimum FRET pairs is the most important parameter for the performance of the biosensors to be designed [9]. Bajar et al. (2016) demonstrated that the mClover3-mRuby3 or mNeonGreen-mRuby3 pair is one of the best choices in terms of photostability, brightness, and FRET dynamic range when used in cultured cells [2]. In addition, linker length is one of the important parameters in FP-FRET biosensors. In most cases, steric hindrance or folding interaction between the proteins of interest can occur when the linker joining the fluorescent pairs is not long and flexible enough. Therefore, the linker should be flexible, soluble and resistant to proteolysis and should not have a secondary structure or aggregate [18].

The design of genetically encoded FP-FRET biosensors shows some differences according to the intended use. In general, a large number of different biosensors have been developed for various cellular targets, such as changes in ions,

molecules, enzymatic activity, oxidation-reduction events, membrane potential and channel conformation, or stages of the cell cycle [19]. Therefore, there is no ideal linker length used in FP-FRET biosensors. Different linker lengths are used according to the purpose of the study. For example, 20 amino acids for Factor Xa protease activity [20], 25 amino acids for trypsin enzyme activity [21], 20 amino acids for Caspase-3 [22] and 12 amino acids length linker for MMP-2 [23] were used. In a study using the mNeonGreen and mRuby3 proteins, a linker consisting of 8 amino acids was used to examine the FRET activity [24]. Also, when it comes to linker flexibility, the amino acid that gives the greatest flexibility to a peptide chain is glycine with the smallest side chain. Therefore, the linker region between the fluorescent protein pairs was designed to contain the glycine sequence [18]. Flexible polypeptide linkers composed of glycine and serine amino acids are important components of engineered fusion proteins. Some studies have been done on linkers containing glycine and

serine repeats. It was observed that FRET activity decreased with increasing linker length, and FRET activity decreased in linkers containing less glycine. In addition, flexibility was reduced in linkers with low glycine content [25].

In this study, a linker containing 17 amino acids (GGSLEENLYFQGEFSGG) was used in the designed mNG-TEV-mRuby3 biosensor. Within this linker length there were the sequences of the TEV protease cleavage site and restriction enzymes. In addition, the GGS sequence was added to both ends of the linker symmetrically in order to obtain linker stabilization, flexibility and effective linker length. It has been clearly demonstrated that the designed structure is effective in generating FRET pairs. By genetically modifying the protease recognition sequence, a different FP-FRET biosensor that can be used to determine the activity of other protease enzymes can be simply designed.

#### 4. CONCLUSION

There are standard approaches to looking at enzymes, such as analysis of transcripts (i.e. mRNAs) or protein levels, but these cannot reflect the specific activity of the enzyme under certain conditions. Activity-based probes have been designed for the detection of enzyme activity. However, activity-based probes negatively affect enzyme activity due to covalent binding. This situation limits the visibility of dynamic processes [26]. Dynamic and continuous detection of enzyme activity in living cells is possible with FRET sensors. FRET can visualize relevant molecular events in living or fixed cells that are difficult to image for other molecular techniques, thanks to its unique functional distance range. Therefore, FRET has become a key technique for studying the activity of enzymes in cells. Continuous detection of enzyme activities (proteases, phosphatases, polymerase, kinases, telomerase, etc.) is an important parameter in medical diagnosis [27].

Genetically encoded FP-FRET sensors allow the monitoring of certain biochemical or biological recognition processes in the cell by preserving the data flow of time and space [28]. This makes

fluorescent proteins and FP-FRET sensors powerful tools for *in vivo* and *in vitro* applications [6].

In this study, the mNG-TEV-mRuby3 FRET sensor designed to monitor TEV protease activity was expressed in *E. coli* DH5a cells. The TEV protease enzyme used in the study was also expressed in *E. coli* BL21 pLysE cells using recombinant DNA techniques. TEV protease activity was analyzed in SDS-PAGE and spectrofluorometer using the mNG-TEV-mRuby3 FRET sensor as a target. With this study, the utility of the mNeonGreen-mRuby3 FRET pair in the determination of protease activity was demonstrated. These findings provide strong evidence that mNG-mRuby3 FRET sensors can be developed that can be used in new protease activity assays. If needed, protease recognition sites can be changed by genetically modifying, and versatile new mNG-mRuby3 FRET sensors can be easily developed.

#### *Funding*

This work was supported by grants from Tokat Gaziosmanpaşa University, Foundation of Scientific Researches Projects (Project number: 2019/71).

#### *The Declaration of Conflict of Interest/ Common Interest*

The authors confirm that this article content has no conflicts of interest

#### *Authors' Contribution*

İbrahim İncir, Özlem Kaplan, Sema Bilgin and İsa Gökçe formed the research idea and designed the experiments. İbrahim İncir performed the experiments. İbrahim İncir, Özlem Kaplan, Sema Bilgin and İsa Gökçe analyzed the data. İbrahim İncir created the first draft of the manuscript which was edited by all the authors.

#### *The Declaration of Ethics Committee Approval*

This study does not require ethics committee permission or any special permission.

## REFERENCES

- [1] J. S. Bond, "Proteases: History, discovery, and roles in health and disease," *Journal of Biological Chemistry*, vol. 294, no. 5, pp. 1643–1651, 2019, doi: 10.1074/jbc.TM118.004156.
- [2] B. T. Bajar, E. S. Wang, S. Zhang, M. Z. Lin, and J. Chu, "A guide to fluorescent protein FRET pairs," *Sensors (Switzerland)*, vol. 16, no. 9, 2016, doi: 10.3390/s16091488.
- [3] M. P. Maria-Chantal Chirio-Lebrun, "Fluorescence resonance energy transfer (FRET): theory and experiments," *Biochemical Education*, vol. 26, no. 4, pp. 320–323, 1998.
- [4] A. Kaur, P. Kaur, and S. Ahuja, "Förster resonance energy transfer (FRET) and applications thereof," *Analytical Methods*, vol. 12, no. 46. Royal Society of Chemistry, pp. 5532–5550, Dec. 14, 2020. doi: 10.1039/d0ay01961e.
- [5] A. Masharina, L. Reymond, D. Maurel, K. Umezawa, and K. Johnsson, "A Fluorescent Sensor for GABA and Synthetic GABA," *Journal of the American Chemical Society*, vol. 134, pp. 19026–19034, 2012, doi: 10.1021/ja306320s.
- [6] H. Wang, E. Nakata, and I. Hamachi, "Recent Progress in Strategies for the Creation of Protein-Based Fluorescent Biosensors," *ChemBioChem*, vol. 10, no. 16, pp. 2560–2577, Nov. 2009, doi: 10.1002/cbic.200900249.
- [7] V. Trümper *et al.*, "Flow cytometry-based FRET identifies binding intensities in PPAR $\gamma$ 1 protein-protein interactions in living cells," *Theranostics*, vol. 9, no. 19, pp. 5444–5463, 2019, doi: 10.7150/thno.29367.
- [8] D. Zhang, E. Redington, and Y. Gong, "Rational engineering of ratiometric calcium sensors with bright green and red fluorescent proteins," *Communications Biology*, vol. 4, no. 1, Dec. 2021, doi: 10.1038/s42003-021-02452-z.
- [9] D. W. Piston and G. J. Kremers, "Fluorescent protein FRET: the good, the bad and the ugly," *Trends in Biochemical Sciences*, vol. 32, no. 9, pp. 407–414, 2007, doi: 10.1016/j.tibs.2007.08.003.
- [10] D. M. Chudakov, M. V. Matz, S. Lukyanov, and K. A. Lukyanov, "Fluorescent Proteins and Their Applications in Imaging Living Cells and Tissues," *Physiological Reviews*, vol. 90, no. 3, pp. 1103–1163, Jul. 2010, doi: 10.1152/physrev.00038.2009.
- [11] N. C. Shaner *et al.*, "A bright monomeric green fluorescent protein derived from *Branchiostoma lanceolatum*," *Nat Methods*, vol. 10, no. 5, pp. 407–409, 2013, doi: 10.1038/nmeth.2413.A.
- [12] I. Stockmar *et al.*, "Optimization of sample preparation and green color imaging using the mNeonGreen fluorescent protein in bacterial cells for photoactivated localization microscopy," *Scientific Reports*, vol. 8, no. 1, pp. 1–11, 2018, doi: 10.1038/s41598-018-28472-0.
- [13] S. Kredel *et al.*, "mRuby, a Bright Monomeric Red Fluorescent Protein for Labeling of Subcellular Structures," *PLoS ONE*, vol. 4, no. 2, p. e4391, Feb. 2009, doi: 10.1371/journal.pone.0004391.
- [14] K. D. Piatkevich and V. V. Verkhusha, "Guide to red fluorescent proteins and biosensors for flow cytometry.," *Methods in cell biology*, vol. 102, pp. 431–61, 2011, doi: 10.1016/B978-0-12-374912-3.00017-1.

- [15] B. T. Bajar *et al.*, “Improving brightness and photostability of green and red fluorescent proteins for live cell imaging and FRET reporting,” *Scientific Reports*, vol. 6, no. October 2015, pp. 1–12, 2016, doi: 10.1038/srep20889.
- [16] H. Kuduğ, B. Ataman, R. İmamoğlu, D. Düzgün, and İ. Gökçe, “Production of red fluorescent protein (mCherry) in an inducible E. coli expression system in a bioreactor, purification and characterization,” *International Advanced Researches and Engineering Journal*, vol. 3, no. 1, pp. 20–25, 2019.
- [17] Ö. Kaplan, R. İmamoğlu, İ. Şahingöz, and İ. Gökçe, “Recombinant production of *Thermus aquaticus* single-strand binding protein for usage as PCR enhancer,” *International Advanced Researches and Engineering Journal*, vol. 5, no. 1, pp. 42–46, 2021, doi: 10.35860/iarej.766741.
- [18] S. Shimosono and A. Miyawaki, “Engineering FRET Constructs Using CFP and YFP,” *Methods in Cell Biology*, vol. 85, no. 08, pp. 381–393, 2008, doi: 10.1016/S0091-679X(08)85016-9.
- [19] A. E. Palmer, Y. Qin, J. G. Park, and J. E. McCombs, “Design and application of genetically encoded biosensors,” *Trends in Biotechnology*, vol. 29, no. 3, pp. 144–152, 2011, doi: 10.1016/j.tibtech.2010.12.004.
- [20] R. D. Mitra, C. M. Silva, and D. C. Youvan, “Fluorescence resonance energy transfer between blue-emitting and red-shifted excitation derivatives of the green fluorescent protein,” *Gene*, vol. 173, no. 1, pp. 13–17, 1996, doi: 10.1016/0378-1119(95)00768-7.
- [21] R. Heim and R. Y. Tsien, “Engineering green fluorescent protein for improved brightness, longer wavelengths and fluorescence resonance energy transfer,” *Current Biology*, vol. 6, no. 2, pp. 178–182, Feb. 1996, doi: 10.1016/S0960-9822(02)00450-5.
- [22] A. W. Nguyen and P. S. Daugherty, “Evolutionary optimization of fluorescent proteins for intracellular FRET,” *Nature Biotechnology*, vol. 23, no. 3, pp. 355–360, 2005, doi: 10.1038/nbt1066.
- [23] J. Yang *et al.*, “Detection of MMP activity in living cells by a genetically encoded surface-displayed FRET sensor,” *Biochim Biophys Acta*, vol. 1773, no. 3, pp. 400–407, 2007, doi: 10.1016/j.bbamcr.2006.11.002.
- [24] T. W. McCulloch, D. M. MacLean, and P. J. Kammermeier, “Comparing the performance of mScarlet-I, mRuby3, and mCherry as FRET acceptors for mNeonGreen,” *PLoS ONE*, vol. 15, no. 2, pp. 1–22, 2020, doi: 10.1371/journal.pone.0219886.
- [25] M. Van Rosmalen, M. Krom, and M. Merckx, “Tuning the Flexibility of Glycine-Serine Linkers to Allow Rational Design of Multidomain Proteins,” *Biochemistry*, vol. 56, no. 50, pp. 6565–6574, 2017, doi: 10.1021/acs.biochem.7b00902.
- [26] H. Y. Hu *et al.*, “FRET-based and other fluorescent proteinase probes,” *Biotechnology Journal*, vol. 9, no. 2, pp. 266–281, Feb. 2014, doi: 10.1002/biot.201300201.
- [27] X. Qiu and N. Hildebrandt, “A clinical role for Förster resonance energy transfer in molecular diagnostics of disease,” *Expert Review of Molecular Diagnostics*, vol. 19, no. 9. Taylor and Francis Ltd, pp. 767–771, Sep. 02, 2019. doi: 10.1080/14737159.2019.1649144.
- [28] A. Ibraheem and R. E. Campbell, “Designs and applications of fluorescent protein-based biosensors,” *Current Opinion in Chemical Biology*, vol. 14, no. 1, pp. 30–36, 2010, doi: 10.1016/j.cbpa.2009.09.033



SAKARYA ÜNİVERSİTESİ

# FEN BİLİMLERİ ENSTİTÜSÜ DERGİSİ

Sakarya University Journal of Science  
SAUJS

e-ISSN: 2147-835X | Founded: 1997 | Period: Bimonthly | Publisher: Sakarya University |  
<http://www.saujs.sakarya.edu.tr/en/>

Title: The Investigation of Physical Properties of Composite Fertilizer Including Boron  
Micro Element

Authors: Havva MUMCU ŞİMŞEK, Rövsen GULİYEV

Received: 2021-01-04 00:00:00

Accepted: 2021-09-30 00:00:00

Article Type: Research Article

Volume: 25

Issue: 5

Month: October

Year: 2021

Pages: 1245-1252

How to cite

Havva MUMCU ŞİMŞEK, Rövsen GULİYEV; (2021), The Investigation of Physical  
Properties of Composite Fertilizer Including Boron Micro Element. Sakarya  
University Journal of Science, 25(5), 1245-1252, DOI:

<https://doi.org/10.16984/saufenbilder.853343>

Access link

<http://www.saujs.sakarya.edu.tr/tr/pub/issue/65589/853343>

New submission to SAUJS

<http://dergipark.org.tr/en/journal/1115/submission/step/manuscript/new>

## The Investigation Of Physical Properties of Composite Fertilizer Including Boron Micro Element

Havva MUMCU ŞİMŞEK\*<sup>1</sup>, Rövsen GULİYEV<sup>2</sup>

### Abstract

Fertilization is one of the most common applications in agricultural fields for achieving high yield. Fertilizer is the important input of agriculture. Raw material costs are nearly 80% of the production costs in chemical fertilizers. Because of high prices, fertilizer usage has started to decrease. The utilization of industrial wastes in the production reduces the costs. Not only is fertilizer expenditure significant, but also the physical properties should be considered. In this study, the physical characteristics of composited fertilizer containing boron which was obtained from the reaction between the diammonium phosphate and borogypsum industrial waste were examined. Under laboratory conditions, diammonium phosphate was composited with borogypsum at the mole ratio of 1:1 and during this process, the solid/liquid (S/L) ratio, temperature, time, pH of the pulp and speed were 1/3, 40°C, 90 min, 5.5 and 500 rpm respectively. The moisture content, grain (granule) size, tight and loose volume weights, granular fracture resistance and the agglomeration angle of the new product including boron were evaluated. As a consequence, the grain size was in range of 3 and 4 mm, loose volume weight was 1363.32 kg/m<sup>3</sup>, the granular fracture resistance was 2.92 kg/granule, agglomeration angle was 89.9 kg/granule and Granulometric Spread Index (GSI) and Uniformity Index (UI) were recorded as 16 and 76.9. These findings were compatible with National and International Standards.

**Keywords:** Borogypsum, ammonium sulfate fertilizer, physico-mechanical properties of fertilizer, industrial waste

### 1. INTRODUCTION

Recently, the global population has started to increase enormously and thus, the usage of composited fertilizers in agricultural areas has gained importance in order to raise production yields. Both conducting development studies about effective and proper use of fertilizers and the utilization of them which contain macro and micro elements together, play a significant role in

supplying nutritional requirements of increasing population. The soil properties, food stuffs in soil, plant types, climate, application procedures and so on should be known for achieving the desired yield from fertilizer [1-2].

The macro and micro nutrition elements are needed for plant growth and boron is one of the crucial micro substances. Boron is a structural mineral which acts as cement and helps consolidate the plant wall [3-4]. Related

\* Corresponding author: havvamumcu@osmaniye.edu.tr

<sup>1</sup> Osmaniye Korkut Ata University, Faculty of Engineering, Department of Chemical Engineering.  
ORCID: <https://orcid.org/0000-0002-8396-3771>

<sup>2</sup> Ardahan University, Faculty of Engineering, Department of Environmental Engineering  
E-Mail: rovsenguliyev@ardahan.edu.tr  
ORCID: <https://orcid.org/0000-0003-2396-8201>

semimetal has influences on fruit and seed formations rather than leaf and shoot. Plant diseases and reductions in plant yields could be appeared in the lack of boron [5]. Besides, it decreases the occurrence of empty fruit in cherry [6], boron is useful in enhancing the nicotine amount of tobacco [7]. Increasing pollination, fruit yields and fruit sets are observed in plant areas where the fertilizer with boron is used [8]. Boron fertilizer is applied to soil and plant leaves. Considering plant types and soil properties, 50-400 g boron is suggested per decare of field [9]. The concentration of solution that will be given to soil ought not to exceed 0.5% [8]. The impact factors on plant beneficialness are pH and organic molecule content of soil and washing and climate conditions. Hence, the application of boron fertilizer to leaves in growing period is proposed thrice [8]. In Turkey, soil analysis were conducted by Soil, Fertilizer and Water Resources Central Research Institute and the boron amounts were declared as insufficient, sufficient, much and excessive in the 46.2%, 31.1%, 19.4% and 3.3% of our country respectively. The insufficient level of boron was reported in 33.72% of Black sea region [10]. Borax decahydrate, sodium pentaborate, disodium octaborate, anhydrous borax and borax pentahydrate are fertilizers for eliminating boron absence in Turkey. But, aforementioned fertilizers are not economic, thus composited ones which involves boron are more suitable [11-12]. Boric acid, which is produced in our country by the General Directorate of Eti Maden Enterprises, is produced because of the reaction of colemanite with sulfuric acid. As can be seen from the equation below, boric acid and gypsum are formed as a result of the reaction [13].



Due to its very low solubility,  $\text{CaSO}_4 \cdot 2\text{H}_2\text{O}$  (gypsum) is easily separated from the solution and boric acid is crystallized from the remaining solution.

Environmental problems that occur during the operation of mineral deposits in Turkey are storage problems caused by air, soil, water pollution and increasing wastes [14]. In the USA, the precautions to be taken to minimize the

negative effects of the wastes generated during the operation of boron mines on the environment are a priority study [15].

Environmental problems caused by pollution are one of the most important problems affecting the progress and growth of mining in our country. Therefore, there are limitations imposed by various standards, regulations, and laws in order to dispose wastes and minimize their damage to the environment [16-17].

During the annual production of 385 thousand tons of boric acid in Turkey, approximately 1155 thousand tons of borogypsum is formed [11].

The usability of borogypsum in the production of diammonium phosphate was investigated in line with this purpose and composited fertilizer containing 0.75% boron was manufactured [18].

On the other hand, physical features of fertilizer are substantial and parameters like sprinkling fertilizer onto soil and storage and delivering of it are critical in the application technique [19-20]. The physical properties are also strictly contributed to the design of fertilizing machines and their settings [21]. Hence, the conformity to National and International Standards of newly formulated products or previous solid mineral fertilizers whose composition was changed, should be checked carefully.

The aim of this research was to analyze the physical specialties of composited fertilizer consisted of plant nutrients and boron which was procured from borogypsum. The tight and loose volume weights, grain (granule) size, granular fracture resistance, dimensional analysis and the agglomeration angle were the parameters evaluated. The compatibility of data to TS 2832 Fertilizer Regulation was also checked. It is thought that, this study which scrutinizes the valuable methods and devices in determining the quality indices of a composited fertilizer, will be a guide for scientists and engineers.

## 2. EXPERIMENTAL

### 2.1. Material and methods

As a raw material, borogypsum was used which was supplied from Eti Holding, Solid Waste Facility of Emet Boric Acid Fabric, Kütahya. Moist borogypsum was waited at room conditions firstly and then dried at 100°C in an oven (Gemo DT104), until no weight changes were observed. Dried sample was subjected to both particle and composition analysis and 100 mesh size (under sieve) of borogypsum was utilized.

Table 1 and Figure 1 represent the chemical composition and X-ray diffractogram of borogypsum respectively. Chemical composition was revealed by ICP-MS (Spectro blue ICPOS) and the brand of X-ray diffraction was XRD-Rigaku Smartlab.

Table 1 Chemical constituents of borogypsum

Compound	Composition(%)*
B <sub>2</sub> O <sub>3</sub>	6.52
SiO <sub>2</sub>	7.14
SO <sub>3</sub>	43.40
CaO	26.38
MgO	1.15
Fe <sub>2</sub> O <sub>3</sub>	0.72
Al <sub>2</sub> O <sub>3</sub>	0.83
Na <sub>2</sub> O	0.16
SrO	0.95
As <sub>2</sub> O <sub>3</sub>	0.15
H <sub>2</sub> O	12.60

\*percentage by weight

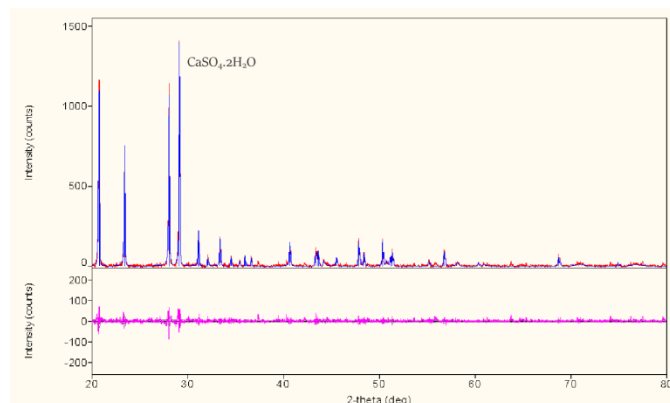


Figure 1 X-ray diffractogram of raw material Diammonium phosphate (DAP) (contained 46% of P<sub>2</sub>O<sub>5</sub>, 18% N) was obtained from Apaydın Fertilizer Fabric, Osmaniye.

DAP was put into a 1 L reactor (Dragonlab OS20-S) with a mechanical mixer and water was added into medium keeping the solid/liquid rate of 1:3. Heating was applied to 40°C. After that, DAP was composited with borogypsum at equal moles and mixing process was continued. Time, pH of the pulp and mixing speed were 90 min, 5.5 and 500 rpm respectively. Finally, the temperature of the product was kept at 90-100°C in the oven (Gemo DT104) for 2-3 hours.

#### 2.1.1. The determination of grain (granule) size (Screening test)

Particle size is an important factor in the usage of fertilizer distribution machines and packaging. Furthermore, particle size has an impact on the style of fertilizer sprinkling in related equipments. Trials were performed according to TSE EN 1235 standard by using a mechanical screening machine including a sieve set. Several measurement techniques are available in specifying the particle sizes and their distributions. Generally, particle size is reported by means of an average particle size (d<sub>50</sub>) or a particle guide number (PGN). When d<sub>50</sub> is multiplied with 100, PGN value is obtained. For instance, a fertilizer whose d<sub>50</sub> value is 2.5, has a PGN of 250 [22].

The distribution of particle size could be expressed as either Granulometric Spread Index (GSI) or Uniformity Index (UI). Some companies may give both of them in specification forms. GSI

and UI enable to test the distribution of diameter size as shown in Figure 2. Information and mathematical expressions which are useful for calculations are given in the following;

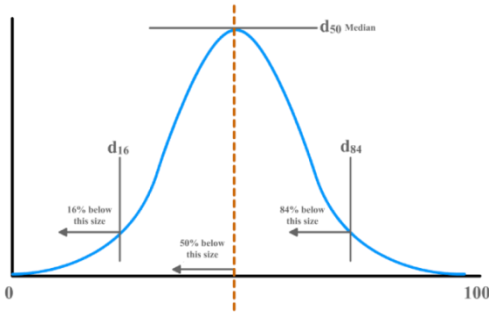


Figure 2 Particle size distribution that demonstrates d16, d50 and d84 for a fertilizer sample [22]

d50 value could be identified with the aid of GSI (Equation 2) [23-24], UI (Equation 3) [21] or screening analysis.

$$GSI = \frac{(d_{84} - d_{16})}{2 \times d_{50}} \times 100 \quad (2)$$

$$UI = \frac{d_{95}}{d_{50}} \times 100 \quad (3)$$

**2.1.2. The determination of loose volume weight**

This test is based on measuring the weight of fertilizer which is transferred from a standard funnel to a graduated cylinder (Equation 4) (TS 3740 EN 1236-1, Fig 3, [25]).

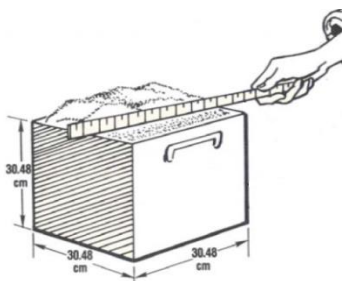


Figure 3 Equipment used to find the heap angle of fertilizer

$$\rho = \frac{LW}{V} \quad (4)$$

$\rho$  : Loose volume weight (kg/m<sup>3</sup>)

LW : The weight of sample (kg)

V : The brimming volume of graduated cylinder (m<sup>3</sup>)

**2.1.3. The determination of tight volume weight**

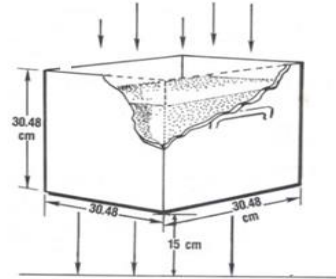


Figure 4 Compacted volume weight measurement (Box volume 0,0283 m<sup>3</sup>)

Tight volume weight is described as the weight of any material per unit volume, after filling it to a container and pressing under specific conditions (Fig 4). This parameter is usually stated as kg/m<sup>3</sup> (TS 6801 TSEN 1237). While measuring, fertilizer is piled into a can up to the brim and a linear ruler is used for slipping excessive amounts on the top. Then, can is thrown from a height of 15 cm to the concrete floor, so the sample in the can is able to be pressed. Failing amount in the can is fulfilled, slipped and thrown from the same height again until pressing process is completed. Equation 5 is valid for calculating tight volume weight.

$$\rho_L = \frac{SW}{V} \quad (5)$$

$\rho_L$  : Tight volume weight (kg/m<sup>3</sup>)

SW : The weight of pressed sample (kg)

V : The brimming volume of graduated cylinder (m<sup>3</sup>)

**2.1.4. The specification of agglomeration angle**

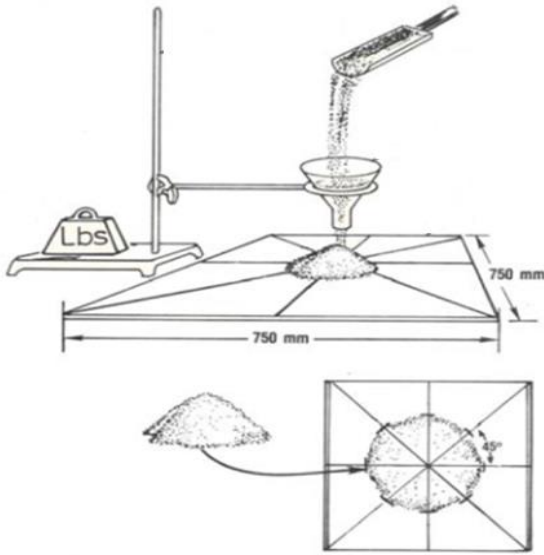


Figure 5 Equipment used to find the heap angle of fertilizer

The stacking angle, is calculated from equation 6 in degrees, [23-25](Fig 5).

$$\alpha = \arctan \frac{2h}{d-d_i} \quad (6)$$

h : The height of cone (mm). 120 mm is a generally accepted value.

d : The arithmetic mean of measured four diameters which form right angles of 90 degrees each other at the bottom (mm)

d<sub>i</sub> : The outlet diameter of funnel (25 mm)

**2.1.5. The specification of granular fracture resistance**

At least, 25 pieces of fertilizer granule are broken by hardness measurement device (Chalton measuring instrument) and results are recorded [1].

**2.1.6. The specification of moisture content**

Moisture analysis was conducted according to TS 2832-1 (Equation 7).

$$M = \frac{m_2 - m_3}{m_2 - m_1} \times 100 \quad (7)$$

M: Moisture level (%)

m<sub>1</sub>: The mass of empty container (g)

m<sub>2</sub>: Total mass of empty container and initial sample (g)

m<sub>3</sub>: Total mass of empty container and dried sample (g)

**3. RESULTS AND DISCUSSION**

Nine sieves calibrated previously were used for screening analysis and average diameter (d<sub>50</sub>) was calculated. Granulometric distribution is given with GSI and the mean diameters of fertilizers usually change between 2.5 and 4.5 mm [26]. Figure 6 depicts the results of screening test and it can be inferred from the figure that the average diameters are in range of 3 and 4 mm.

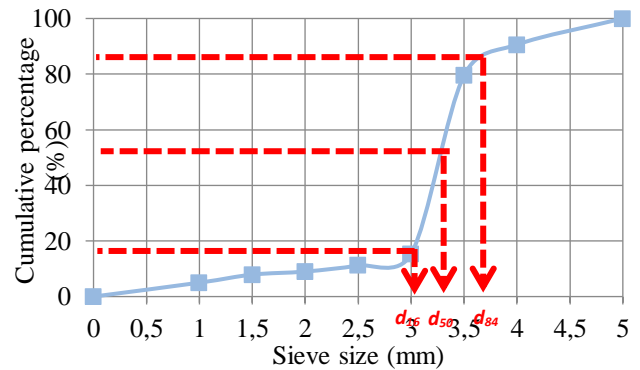


Figure 6 Granulometric distribution of composited fertilizer produced from borogysum

During the formation of composited fertilizer, the effect of washing process were also assessed. The unwashed and washed were composited fertilizer evaluated with scanning electron microscope (SEM) and energy dispersive X-ray analysis (EDX). The SEM images shows the surface morphology of the composited fertilizer as shown in Fig.7a and 7c, respectively. The grain sizes are still in good agreements with the granulometric distribution. The EDX analysis show that after washing process Nitrogen (N) peak was disappeared which is due to water solubility of Ammonium Sulfate ((NH<sub>4</sub>)<sub>2</sub>SO<sub>4</sub>).

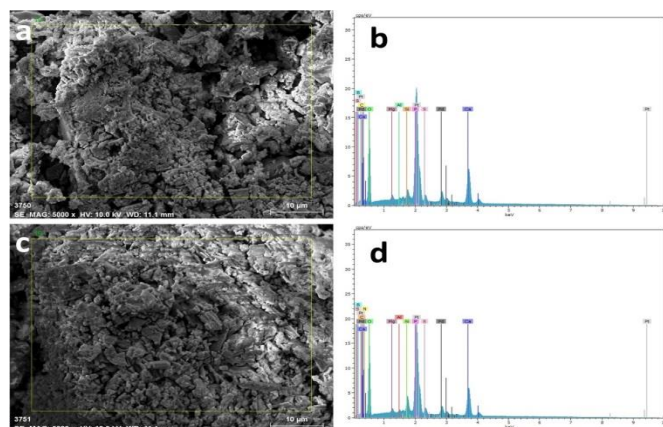


Figure 7 Scanning electron microscope (SEM) with energy dispersive X-ray analysis (EDX) analysis of composited fertilizer produced from borogypsum after (a, b) and before (c, d) washing step

Table 2 expressed the chemical properties of DAP and composited fertilizer and the contents of nitrogen and phosphorus in new product were lower than DAP. On the contrary, boron, sulphur and calcium were only detected in aforementioned fertilizer. The quantities of total plant nutrients were close to each other in both of them, but the level of these elements in composited one, were a bit higher than the commercial. It is thought that, this will contribute the effectiveness of new fertilizer positively. Same results were reported by [27] in the production of triple superphosphate with borogypsum.

Table 2 The moisture, mineral and phosphorus pentoxide amounts of fertilizers

	DAP	Composited Fertilizer
Moisture (%)	1.5	0.80
Nitrogen (%)	18.1.1	12.84
Phosphorus (%)	46.1.1	31.40
Sulphur (%)	-	10.22
Boron (%)	-	0.47
Calcium (%)	-	10.15
P <sub>2</sub> O <sub>5</sub> soluble in water and neutral ammonium citrate	46.1.1	31.40

The tight and loose volume weights of fertilizers with and without borogypsum were calculated as 1370.87, 1363.32 kg/m<sup>3</sup> and 1258.23, 1253.43 kg/m<sup>3</sup> respectively (Table 3). As is known, having high density makes the shipping of a product easier and correspondingly, the transportation

costs reduce. When considered from this point of view, novel product has an advantage. Moreover, volume weights are directly related to the spreading width of fertilizer machine. Because, granules owning high densities are able to spread on a large area and dust particles do not occur at high rates of rotating discs [28]. As GSI value is low and UI is high, so the particles of fertilizer are smooth and homogenous, and hence uniform spreading is ensured.

Table 3 The physical qualifications of commercial and new products

	DAP	Composited Fertilizer	Aim
Particle size (% , 1-4 mm)	Minimum 90	91	Ensuring effective use of fertilizer distribution machines
Particle size (% , 1 mm, under sieve)	Maximum 3	3	Ensuring proper storage of fertilizer
Loose volume weight (kg/m <sup>3</sup> )	1253.43	1363.32	Ensuring proper storage and transportation of manure
Tight volume weight (kg/m <sup>3</sup> )	1258.23	1370.87	To prevent slipping in the storage area
Agglomeration angle (°)	89.91	89.55	Determine granule resistance
Granular fracture resistance (kg/granule)	2.92	2.85	Keeping the fertilizer in granular form
GSI	16.00	17.60	Granulometric Spread Index
UI	76.90	75.00	Uniformity Index

Granular fracture resistance is defined as the resistance of granules against deformation or fraction under pressure. Fracture resistance is useful for designating pressure boundaries during fertilizing, transport and delivering facilities of granule material which can be attributed to the particle volume weight and size. If a substance has a low fracture resistance, aforementioned operations will cause negative effects on granules

and thus, they will be crashed and converted into dust.

#### 4. CONCLUSION

The physical as well as chemical properties of fertilizers in agriculture are significant. The factors which have enhancing effects on fertilizer costs are the high price of raw materials and being imported from abroad. For this reason, local raw materials could be an alternative. The usage of borogypsum, a material which comes out as a result of boric acid production in fertilizer manufacturing, reduce dramatically the waste storage costs and environmental pollution. High nutritional value for plants in this newly formed product is another key parameter.

In this study, a previously obtained composited fertilizer [10] which included boron, phosphor, sulphur and calcium together was developed and the physical quality indices were evaluated. At the same time, a commercial sample was compared with newly formed product and advantages and disadvantages were clearly revealed. The utility of composited fertilizer in cultivated areas were investigated as well as a consequence, fertilizer with boron is superior and could be preferable in fertilizer production. Being compatible to national and international standards will step forward this fertilizer in the market.

#### REFERENCES

- [1] F.A. Alayunt, İ. Önal, E. Aykas, “Kati Mineral Gübrelerin Bazı Fiziksel Özelliklerinin Belirlenmesinde Kullanılan Yöntemler,” 25.Tarımsal Mekanizasyon Ulusal Kongresi,s. 225-233, 2009.
- [2] C. A. Bayram, G. Büyük, “Toprak İşleme ve Gübreleme Yapılmayan Meyve Ağaçlarında Bitki Besin Elementi Düzeylerinin Belirlenmesi”, Avrupa Bilim ve Teknoloji Dergisi, vol.23, pp.1-8, 2021.
- [3] H. Polat, “Türkiye’de Kimyasal Azotlu Gübre Tüketim Durumunun ve Toprak Analizi Zorunluluğunun Azotlu Gübre Kullanımına Etkilerinin Değerlendirilmesi”, Toprak Su Dergisi, vol.9, no.2, pp.60-71, 2020.
- [4] R. Hajiboland, S. Bahrami-Rad, S. Bastani, “Phenolics Metabolism In Boron-Deficient Tea [*Camellia Sinensis* (L.) O. Kuntze] Plants,”*Acta Biologica Hungarica*, vol.64, no.2, pp. 196-206, 2013.
- [5] M. Ganie, A. Akhter, F. Bhat, M.A. Malik, A.R. Junaid, J. Shah, A.M. Bhat, A.H. Bhat, “Boron-a critical nutrient element for plant growth and productivity with reference to temperate fruits,” *Current Science*, vol.104, no.1, 2013.
- [6] A. İkinci, Ş. Aldanmaz, İ. Bolat, “Bor ve Çinko İçerikli Yaprak Gübresi Uygulamalarının Kiraz (*Prunus avium* L.) Meyvelerinin Bazı Kalite Özellikleri Üzerine Etkileri”, *Türk Tarım ve Doğa Bilimleri Dergisi*, vol.8, no.3, pp.557-566, 2021.
- [7] T. Mauhammad, A. Ali, K. Amanullah Hak Lataf, “Comparing application methods for boron fertilizer on the yield and quality of tobacco (*Nicotiana tabacum* L.),”*Communications in Soil Science and Plant Analysis*, vol.41, pp.1525–1537, 2010.
- [8] Ulusal Bor Araştırma Enstitüsü. (Boren). (2019). Bor Bitkiler İçin Neden Çok Önemli .[www.boren.gov.tr](http://www.boren.gov.tr)
- [9] U. C. Gupta, “ Boron nutrition of crops”, *Adv. Agronomy*, 31, 273-307, 1979.
- [10] Toprak, Gübre ve Su kaynakları Merkez Araştırma Enstitüsü 2016 faaliyet raporu.
- [11] R. Guliyev, “Borojips endüstriyel atığının bor içerikli diamonyum fosfat üretiminde kullanılabilirliğinin incelenmesi,” *Bor Dergisi*, ,vol.3, no.2, 87-92, 2018.

- [12] R. Yüzbaşıoğlu, Üreticilerin kimyasal gübre kullanım bilinç düzeylerinin incelenmesi: Tokat Merkez ilçe örneği. *Turkish Journal of Agricultural Engineering Research*, vol.1, no.2, pp.452-465, 2020.
- [13] N. Taylan, H. Gürbüz, B. Cenk, N. Bulutcu, "Sulu ortamda kolemanitin sülfürik asit ile reaksiyon kinetiğinin incelenmesi", İTÜ Kimya - Metalurji Fakültesi, İstanbul. 2004.
- [14] M. Karadeniz., Cevher zenginleştirme tesis atıklarının çevreye etkilerinin önlenmesi. Maden Tetkik Arama Daire Başkanlığı, 332, Ankara. 1996.
- [15] T. S. Griffin, T. L. Downing, Rio Tinto Borax's pond reprocessing and sustainable development. *New Developments in Mineral Processing*, 9. Balkan Mineral Processing Congress. pp.319-324, İstanbul. 2001.
- [16] M. Çolak, "Etibank Kırka Boraks İşletmesi atıklarının Turgutlu killeri İle tuğla-kiremit denemesi". 8. Ulusal Kil Sempozyumu, Kütahya. 1997.
- [17] B. Kuşkay, A. N. Bulutcu, Kolemanitten Yeni Bir Yöntemle Borik Asit Üretim Prosesinin Geliştirilmesi. İTÜ dergisi, vol.9, no.2, pp.15-26. 2010.
- [18] H. Mumcu Şimşek, "Diamonyum Hidrojen Fosfat Çözeltisinde Borojipsin Çözünme Kinetiği, Optimizasyonu ve Kompleks Gübre Üretimi," Atatürk Üniversitesi, Fen Bilimleri Enstitüsü, 2018, Erzurum.
- [19] J. W. Hofstee and W. Huisman, "Handling and spreading of fertilizers. Part 1: physical properties of fertilizer in relation to particle motion," *Journal of Agricultural Engineering Research*, vol. 47, pp. 213–234, 1990.
- [20] P. C. H. Miller, "The measurement and classification of the flow and spreading characteristics of individual fertilisers," *Proceeding no. 390, The International Fertiliser Society, York, UK. 1996.*
- [21] İ. Önal, "Ekim, bakım, gübreleme makinaları", Ders kitabı, Ege Üniversitesi yayınları, 2006, 623s.
- [22] K. Port, J. Fulton, "Physical Properties of Granular Fertilizers and Impact on Spreading." *Agricultural and Environmental Sciences. United States of America, 2016.*
- [23] O. Miserque, E. Pirard, Y. Schenkel, O. Mostade and B Huyghebaert, "Spreading segregation of blended fertilizers: influence of the particles properties," *Applied, Engineering in Agriculture*, vol. 24, no. 2, pp.137–144, 2008.
- [24] J. Fulton, K. Port, "Physical Properties of Granular Fertilizers and Impact on Spreading. College of Food," *Agricultural and Environmental, Sciences, 1-9, 2016.*
- [25] D. W. Rutland, "Manual for Determining Physical Properties of Fertilizer. Reference Manual IFDC-R-6. International Fertilizer Development Center Muscle Shoals," Alabama, USA. 1986.
- [26] E. Pirard, O. Miserque, V. Chapeau, *Physical Properties of Fertilizers, 2005.*
- [27] R. Guliyev. "An investigation of borogypsum utilization for the production of triple superphosphate containing boron fertilizers," *Fresenius Environmental Bulletin*, vol. 24, no.3, 748-754, 2015.
- [28] M. C. Pare, S. E. Allaire, L. Khiari, and C. Nduwamungu, "Physical properties of organo-mineral fertilizers Short Communication," *Canadian Biosystems Engineering*, vol. 51, no. 3, pp. 21–27. 2009.